

1999

## Additives for Increased Atomic Oxygen Resistance in Cyanate Ester Resins

Sandeep Amar Saggar  
*College of William & Mary - Arts & Sciences*

Follow this and additional works at: <https://scholarworks.wm.edu/etd>



Part of the [Polymer Chemistry Commons](#)

---

### Recommended Citation

Saggar, Sandeep Amar, "Additives for Increased Atomic Oxygen Resistance in Cyanate Ester Resins" (1999). *Dissertations, Theses, and Masters Projects*. William & Mary. Paper 1539626216.  
<https://dx.doi.org/doi:10.21220/s2-nett-nt17>

This Thesis is brought to you for free and open access by the Theses, Dissertations, & Master Projects at W&M ScholarWorks. It has been accepted for inclusion in Dissertations, Theses, and Masters Projects by an authorized administrator of W&M ScholarWorks. For more information, please contact [scholarworks@wm.edu](mailto:scholarworks@wm.edu).

# **Additives for Increased Atomic Oxygen Resistance in Cyanate Ester Resins**

---

A Thesis

Presented to

The Faculty of the Department of Chemistry

The College of William and Mary

In Partial Fulfillment

of the Requirements for the Degree of

Master of Arts

---

by

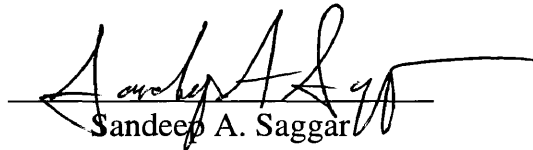
Sandeep Amar Saggar

December 1999

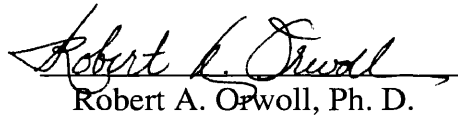
APPROVAL SHEET

This thesis is submitted in partial fulfillment of  
the requirements for the degree of

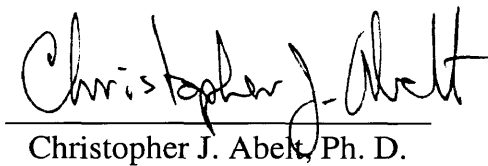
Master of Arts

  
Sandeep A. Saggari

Approved, December 1999

  
Robert A. Orwoll, Ph. D.

  
Richard L. Kiefer, Ph. D.

  
Christopher J. Abelt, Ph. D.

## Table of Contents

<u>Section</u>	<u>Page</u>
Acknowledgments.....	vi
List of Tables.....	vii
List of Figures.....	viii
Abstract.....	xiii
I Background.....	2
I.1. Purpose.....	2
I.2. Spacecraft in Low Earth Orbit Environment.....	2
I.3. Polymeric Materials/Composites in Spacecraft Design.....	6
I.4. Atomic Oxygen Interactions with Polymeric Spacecraft Materials.....	8
I.5. Materials.....	11
I.5.i. Motivation for Use of Additives.....	11
I.5.ii. Boron.....	12
I.5.iii. Boron Carbide and Whisker Technology.....	12
I.5.iv. Organoclays.....	13
I.5.v. Cyanate Resin.....	15
I.6. Experimental Methods.....	20
I.6.i. Scanning Electron Microscopy.....	20
I.6.ii. Thermogravimetric Analysis.....	22
I.6.iii. X-ray Photoelectron Spectroscopy.....	24
References.....	27
II. Experimental.....	29

II.1.	Materials.....	29
II.1.i.	Bisphenol A-based Cyanate Ester Resin.....	29
II.1.ii.	Hexcel 954-3 Cyanate Ester Resin.....	32
II.2.	Ground-based Atomic Oxygen Plasma Generator.....	34
II.3.	Atomic Oxygen Exposures and Mass Loss Determinations.....	37
II.4.	X-ray Photoelectron Spectroscopy.....	38
II.5.	Scanning Electron Microscopy.....	38
II.6.	Thermogravimetric Analysis.....	39
II.7.	Summary of Studies.....	40
	References.....	40
III.	Results.....	41
III.1.	Atomic Oxygen Exposures and Mass Losses.....	41
III.2.	TGA Analysis.....	46
III.3.	SEM Analysis.....	47
III.4.	XPS Analysis.....	47
IV.	Discussion.....	51
IV.1.	Polymer + Additive Preparation Success.....	51
IV.2.	Analysis of BPA-based CE + Boron Samples.....	51
IV.2.i.	Mass Loss.....	51
IV.3.	Analysis of BPA-based CE + B <sub>4</sub> C Samples.....	52
IV.3.i.	Mass Loss.....	52
IV.3.ii.	SEM Analysis.....	52
IV.3.iii.	XPS Analysis.....	54

IV.4.	Deviations in Flux on Sample Holder.....	56
IV.4.i.	First Method of Correction.....	57
IV.4.ii.	Second Method of Correction.....	58
IV.5.	Analysis of the Third and Fifth Sets of AO Exposures.....	58
IV.5.i.	Mass Loss.....	58
IV.6.	Analysis of the Sixth Set of AO Exposures.....	64
IV.6.i.	Mass Loss.....	64
IV.6.ii.	XPS Analysis.....	65
IV.7.	TGA Analysis.....	68
	References.....	69
V.	Conclusion.....	70
	Appendix.....	72
	Vita.....	155

## Acknowledgements

The research performed in this study was made possible by a NASA cooperative agreement, NCC-1-327. I would like to heartily thank Dr. Orwoll for his guidance and assistance in the undertaking of this project, as well as for advising me through my undergraduate and graduate career at The College of William and Mary. I would also like to thank Dr. Kiefer and Dr. Sheila Thibeault at NASA for getting me oriented with the Langley Research Center. Thanks to Dr. Abelt for his advice regarding graduate studies and to Dr. Cromer for his XPS analysis. In addition, I would like to thank William Gray at NASA LaRC for conducting the atomic oxygen exposures and teaching me about the atomic oxygen plasma generator. Finally, I would like to thank my family and close friends for their support.

## List of Tables

Table 1: Fluences experienced at different surface orientations	6
Table 2: Bisphenol A-based Cyanate Ester Samples	31
Table 3: Hexcel 954-3 Cyanate Ester Samples	33
Table 4: Samples for XPS Analysis	38
Table 5: Summary of Studies	40
Table 6: Abbreviations for sample locations on sample holder	41
Table 7: Mass Losses for BPA-based CE {first set of AO exposures}	41
Table 8: Mass Losses for BPA-based CE {second set of AO exposures}	42
Table 9: Mass Losses for Hexcel 954-3 CE {third set of AO exposures}	43
Table 10: Mass Losses for Hexcel 954-3 {fourth set of AO exposures}	44
Table 11: Mass Losses for Hexcel 954-3 CE {fifth set of AO exposures}	11
Table 12: Abbreviations used in the sixth set of AO exposures	45
Table 13: Mass Losses for Hexcel 954-3 CE {sixth set of AO exposures}	46
Table 14: XPS pure BPA-based CE Control and AO Exposed	47
Table 15: XPS BPA-based CE + 10 wt. % B <sub>4</sub> C Back Control and Back AO Exposed	48
Table 16: XPS BPA-based CE + 10 wt. % B <sub>4</sub> C Front Control and Front AO Exposed	48
Table 17: XPS Pure Hexcel 954-3 CE Control and AO Exposed 18 and 104 hours	49
Table 18: XPS Hexcel 954-3 CE + 5 wt. % Boron AO Exposed 18, 36, 68, & 104 hrs	50
Table 19: Corrected Mass Losses for the Third Set of AO Exposures	59
Table 20: Corrected Mass Losses for the Fifth Set of AO Exposures	61
Table 21: Corrected Mass Losses for the Sixth Set of AO Exposures	64

## List of Figures

Figure 1: Atmospheric Composition in Low Earth Orbit	3
Figure 2: Seasonal and Inclinal Effects on Fluence	5
Figure 3: Surface Orientation Effects on Fluence	7
Figure 4: Spacesuit Components and Cross-Section	72
Figure 5: Organoclay Depiction	15
Figure 6: Preparation of Stable Aryl Cyanates	15
Figure 7: Cyanate Synthesis via Thiatriazole Thermolysis	16
Figure 8: Cyclopolymerization of Aryl Cyanate to s-triazine	16
Figure 9: BPA dicyanate Synthesis	17
Figure 10: A Cyanurate	18
Figure 11: A Polycyanurate network	19
Figure 12: Schematic of SEM Instrument	73
Figure 13: Schematic of TGA Instrument	74
Figure 14: Schematic representation of the XPS process	26
Figure 15: Schematic of XPS Instrument	75
Figure 16: Viscosity Profile for Hexcel 954-3 Cyanate Ester	76
Figure 17: Neat Resin Moisture Absorption Plot for Hexcel 954-3 CE	77
Figure 18: Configuration of Oxygen Plasma Apparatus	78
Figure 19: Upgraded Atomic Oxygen Generator	79
Figure 20: Diagram of the Oxygen Plasma Apparatus Console	80

Figure 21: Picture of the Oxygen Plasma Apparatus Console	81
Figure 22: Components of Quartz AO Chamber	82
Figure 23: Chamber Positioned within the Oxygen Plasma Tube Enclosure	83
Figure 24: Chamber during Atomic Oxygen Exposure	84
Figure 25: Quartz sample holder in AO chamber	35
Figure 26: Quartz sample holder	36
Figure 27: Thermogram of Pure Hexcel 954-3 CE	85
Figure 28: Thermogram of Pure Hexcel 954-3 CE (N <sub>2</sub> )	86
Figure 29: Thermogram of Hexcel 954-3 + 5 wt. % Boron	87
Figure 30: Thermogram of Hexcel 954-3 + 10 wt. % Boron	88
Figure 31: Thermogram of Hexcel 954-3 + 5 wt. % Cloisite-15A	89
Figure 32: Thermogram of Hexcel 954-3 + 10 wt. % Cloisite-15A	90
<b>SEM Photographs</b>	
Figure 33: Pure BPA-based CE Control x150	91
Figure 34: Pure BPA-based CE AO Exposed x150	91
Figure 35: Pure BPA-based CE AO Exposed x600	92
Figure 36: BPA-based CE + 10 wt. % B <sub>4</sub> C Back Control x150	92
Figure 37: BPA-based CE + 10 wt. % B <sub>4</sub> C Back Control x600	93
Figure 38: BPA-based CE + 10 wt. % B <sub>4</sub> C Back AO Exposed x150	93
Figure 39: BPA-based CE + 10 wt. % B <sub>4</sub> C Back AO Exposed x600	94
Figure 40: BPA-based CE + 10 wt. % B <sub>4</sub> C Front Control x150	94
Figure 41: BPA-based CE + 10 wt. % B <sub>4</sub> C Front Control x600	95
Figure 42: BPA-based CE + 10 wt. % B <sub>4</sub> C Front AO Exposed x20	95

Figure 43: BPA-based CE + 10 wt. % B <sub>4</sub> C Front AO Exposed x60	96
Figure 44: BPA-based CE + 10 wt. % B <sub>4</sub> C Front AO Exposed x150	96
Figure 45: BPA-based CE + 10 wt. % B <sub>4</sub> C Front AO Exposed x200	97

### **XPS Spectra**

Figure 46: Pure BPA-based CE Control	98
Figure 47: Pure BPA-based CE AO Exposed	99
Figure 48: BPA + 10 wt. % B <sub>4</sub> C Back Surface Control	100
Figure 49: BPA + 10 wt. % B <sub>4</sub> C Back Surface AO Exposed	101
Figure 50: BPA + 10 wt. % B <sub>4</sub> C Front Surface Control	102
Figure 51: BPA + 10 wt. % B <sub>4</sub> C Front Surface AO Exposed	103
Figure 52: Pure BPA-based CE Carbon Peak Control	104
Figure 53: Pure BPA-based CE Oxygen Peak Control	105
Figure 54: Pure BPA-based CE Nitrogen Peak Control	106
Figure 55: Pure BPA-based CE Carbon Peak AO Exposed	107
Figure 56: Pure BPA-based CE Oxygen Peak AO Exposed	108
Figure 57: Pure BPA-based CE Nitrogen Peak AO Exposed	109
Figure 58: BPA + 10 wt. % B <sub>4</sub> C Back Surface Carbon Peak Control	110
Figure 59: BPA + 10 wt. % B <sub>4</sub> C Back Surface Oxygen Peak Control	111
Figure 60: BPA + 10 wt. % B <sub>4</sub> C Back Surface Nitrogen Peak Control	112
Figure 61: BPA + 10 wt. % B <sub>4</sub> C Back Surface Boron Peak Control	113
Figure 62: BPA + 10 wt. % B <sub>4</sub> C Back Surface Carbon Peak AO Exposed	114
Figure 63: BPA + 10 wt. % B <sub>4</sub> C Back Surface Oxygen Peak AO Exposed	115
Figure 64: BPA + 10 wt. % B <sub>4</sub> C Back Surface Nitrogen Peak AO Exposed	116

Figure 65: BPA + 10 wt. % B <sub>4</sub> C Back Surface Boron Peak AO Exposed	117
Figure 66: BPA + 10 wt. % B <sub>4</sub> C Front Surface Carbon Peak Control	118
Figure 67: BPA + 10 wt. % B <sub>4</sub> C Front Surface Oxygen Peak Control	119
Figure 68: BPA + 10 wt. % B <sub>4</sub> C Front Surface Nitrogen Peak Control	120
Figure 69: BPA + 10 wt. % B <sub>4</sub> C Front Surface Boron Peak Control	121
Figure 70: BPA + 10 wt. % B <sub>4</sub> C Front Surface Carbon Peak AO Exposed	122
Figure 71: BPA + 10 wt. % B <sub>4</sub> C Front Surface Oxygen Peak AO Exposed	123
Figure 72: BPA + 10 wt. % B <sub>4</sub> C Front Surface Nitrogen Peak AO Exposed	124
Figure 73: BPA + 10 wt. % B <sub>4</sub> C Front Surface Boron Peak AO Exposed	125
Figure 74: Pure Hexcel 954-3 CE Control	126
Figure 75: Pure Hexcel 954-3 CE AO Exposed 18 hours	127
Figure 76: Pure Hexcel 954-3 CE AO Exposed 104 hours	128
Figure 77: Hexcel 954-3 CE + 5 wt. % Boron AO Exposed 18 hours	129
Figure 78: Hexcel 954-3 CE + 5 wt. % Boron AO Exposed 36 hours	130
Figure 79: Hexcel 954-3 CE + 5 wt. % Boron AO Exposed 68 hours	131
Figure 80: Hexcel 954-3 CE + 5 wt. % Boron AO Exposed 104 hours	132
Figure 81: Pure Hexcel 954-3 CE Carbon Peak AO Exposed 18 hours	133
Figure 82: Pure Hexcel 954-3 CE Oxygen Peak AO Exposed 18 hours	134
Figure 83: Pure Hexcel 954-3 CE Nitrogen Peak AO Exposed 18 hours	135
Figure 84: Pure Hexcel 954-3 CE Carbon Peak AO Exposed 104 hours	136
Figure 85: Pure Hexcel 954-3 CE Oxygen Peak AO Exposed 104 hours	137
Figure 86: Pure Hexcel 954-3 CE Nitrogen Peak AO Exposed 104 hours	138
Figure 87: Hexcel 954-3 CE + 5 wt. % Boron Carbon Peak AO Exposed 18 hours	139

Figure 88: Hexcel 954-3 CE + 5 wt. % Boron Oxygen Peak AO Exposed 18 hours	140
Figure 89: Hexcel 954-3 CE + 5 wt. % Boron Nitrogen Peak AO Exposed 18 hours	141
Figure 90: Hexcel 954-3 CE + 5 wt. % Boron Boron Peak AO Exposed 18 hours	142
Figure 91: Hexcel 954-3 CE + 5 wt. % Boron Carbon Peak AO Exposed 36 hours	143
Figure 92: Hexcel 954-3 CE + 5 wt. % Boron Oxygen Peak AO Exposed 36 hours	144
Figure 93: Hexcel 954-3 CE + 5 wt. % Boron Nitrogen Peak AO Exposed 36 hours	145
Figure 94: Hexcel 954-3 CE + 5 wt. % Boron Boron Peak AO Exposed 36 hours	146
Figure 95: Hexcel 954-3 CE + 5 wt. % Boron Carbon Peak AO Exposed 68 hours	147
Figure 96: Hexcel 954-3 CE + 5 wt. % Boron Oxygen Peak AO Exposed 68 hours	148
Figure 97: Hexcel 954-3 CE + 5 wt. % Boron Nitrogen Peak AO Exposed 68 hours	149
Figure 98: Hexcel 954-3 CE + 5 wt. % Boron Boron Peak AO Exposed 68 hours	150
Figure 99: Hexcel 954-3 CE + 5 wt. % Boron Carbon Peak AO Exposed 104 hours	151
Figure 100: Hexcel 954-3 CE + 5 wt. % Boron Oxygen Peak AO Exposed 104 hours	152
Figure 101: Hexcel 954-3 CE + 5 wt. % Boron Nitrogen Peak AO Exposed 104 hrs	153
Figure 102: Hexcel 954-3 CE + 5 wt. % Boron Boron Peak AO Exposed 104 hours	154
Figure 103: Mass Losses per Surface Area of Pure Hexcel 954-3 CE Samples	57
Figure 104: Mass Losses for 3rd Set of AO Exposures (First Correction Method)	59
Figure 105: Mass Losses for 3rd Set of AO Exposures (Second Correction Method)	60
Figure 106: Mass Losses for 5th Set of AO Exposures (First Correction Method)	62
Figure 107: Mass Losses for 5th Set of AO Exposures (Second Correction Method)	62

## Abstract

In addition to ultraviolet radiation, charged particle radiation, thermal cycling, and space debris, spacecraft materials in low earth orbit must withstand the effects of atomic oxygen. This highly reactive species erodes the surface of polymeric materials. The utility of polymeric materials in present and future spacecraft design motivates the study of methods that will reduce this erosion.

This study focuses on the ability of boron and organic clay additives to protect the surfaces of cyanate ester resins from erosion. Polymer and additive combinations were prepared, exposed to atomic oxygen in a ground-based atomic oxygen plasma generator. Mass loss data were obtained from these exposures, and corrections were made for deviations in atomic oxygen flux at different locations within the generator. Samples were analyzed by x-ray photoelectron spectroscopy and scanning electron microscopy.

The research performed here supports boron and organic clay additives and Hexcel 954-3 cyanate ester resin as the best combination of polymer and additive to reduce erosion by atomic oxygen.

## **Additives for Increased Atomic Oxygen Resistance in Cyanate Ester Resins**

## **CHAPTER 1: BACKGROUND**

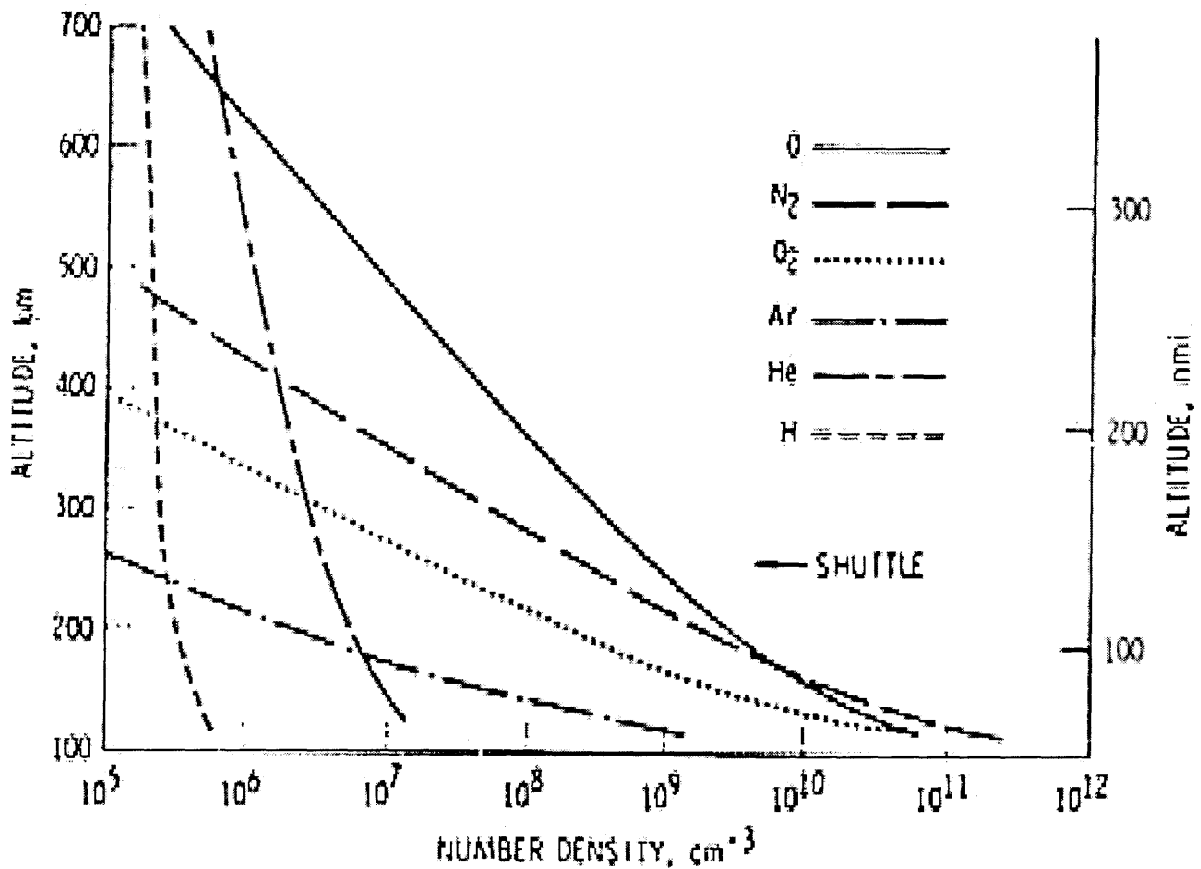
### **I.1. Purpose**

In Low Earth Orbit, polymeric spacecraft materials must withstand the environmental effects of atomic oxygen, ultraviolet radiation, charged particle radiation, thermal cycling, and space debris, including micrometeoroids. This work focuses on the surface erosion caused by impinging atomic oxygen (AO). In the studies reported here studies were undertaken to impart AO resistance to a polymer with the aid of additives. It is the author's intent to show that polymers with uniformly dispersed additives will lose less mass than their pure counterparts. The amount of mass lost will be shown to be proportional to the amount of additive in the polymer. In addition, the formation of an additive oxide layer that protects underlying polymer from reaction with AO will be discussed. Experimental methods include processing of the composites, exposure to atomic oxygen in a ground laboratory, mass loss determinations, and XPS, TGA, and SEM analyses.

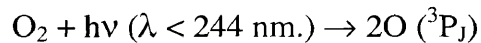
### **I.2. Spacecraft in Low Earth Orbit Environment**

The composition, density, and temperature of the upper atmosphere are all functions of altitude, latitude, solar flare activity, local time, and season. While all of these factors share importance, the easiest relationship to make between any two of these parameters is between altitude and average composition of the upper atmosphere. It is evident from Figure 1 that atomic oxygen (AO) is the predominant species in the 200 to 700 kilometer range of the upper atmosphere<sup>1</sup>. This range, known as Low Earth Orbit (LEO), happens to include the altitudes at which most orbiting spacecraft fly to reduce drag effects and minimize requirements for re-boost propulsion systems.

Figure 1<sup>1</sup>: Atmospheric Composition in Low Earth Orbit



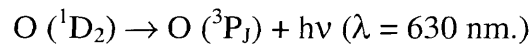
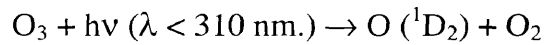
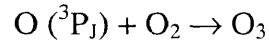
AO is generated in this region by a photo-dissociation reaction:



Solar photons in the stratosphere have sufficient energy to induce this reaction, while those in the troposphere, the lowest part of the atmosphere, do not. The predominant electronic state of AO in LEO is the ground state (<sup>3</sup>P<sub>J</sub>)<sup>\*</sup>. Ground state AO can undergo

<sup>\*</sup> The energy levels of the three triplet ground states, <sup>3</sup>P<sub>2</sub>, <sup>3</sup>P<sub>1</sub>, and <sup>3</sup>P<sub>0</sub>, are, respectively, 0.0, 0.45, and 0.65 kcal/mol. Because the energy differences between these states are so small, it is widely acceptable to jointly refer to them as the <sup>3</sup>P<sub>J</sub> ground state.

other reactions that produce excited singlet states of AO, but these prove short-lived by relaxation:

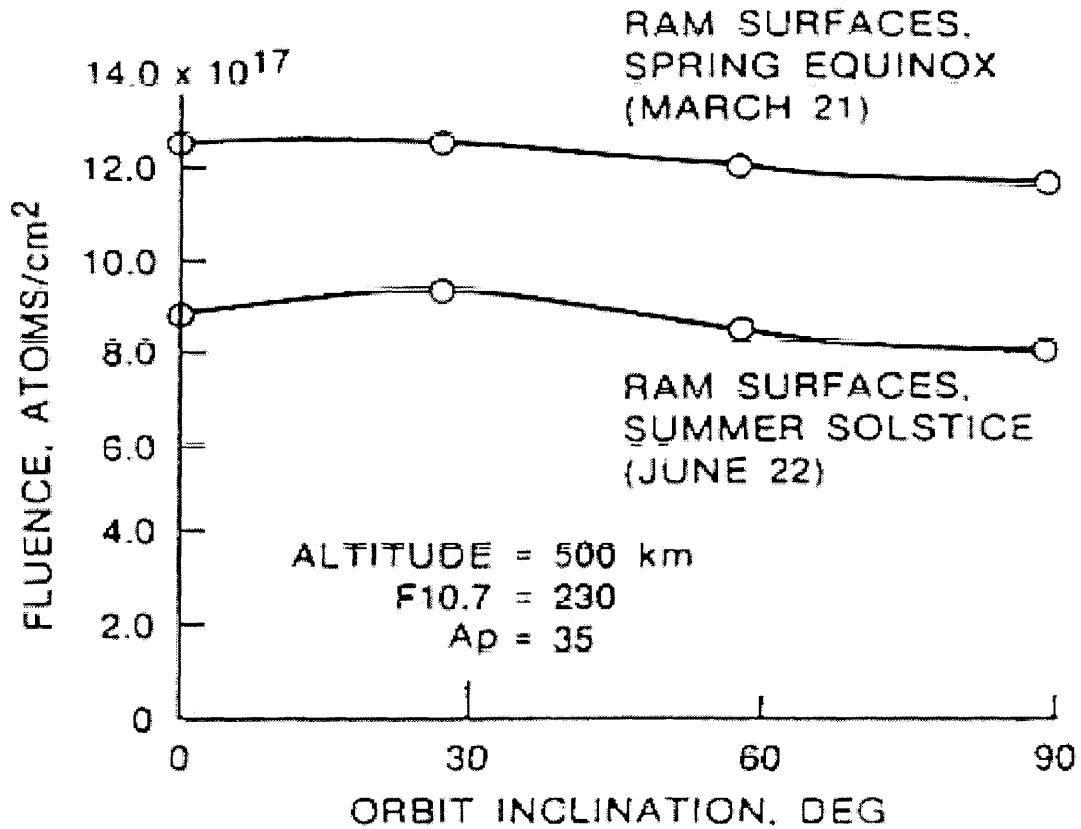


Because the AO radicals have a large amount of translational energy, the probability that they will come together and recombine is small. Thus dissociation is favored over recombination, accounting for the high concentrations of AO relative to molecular oxygen. Above 200 km., the AO density decreases exponentially with increasing altitude, and the atmosphere at orbital altitudes of 200-700 km. consists mainly of 80% AO and 20% molecular nitrogen. Although the typical number density of atomic oxygen is low at spacecraft altitudes ( $\sim 10^9$  atoms/cm<sup>3</sup>), the high orbital velocities ( $\sim 8$  km/sec) cause the impinging AO flux ( $\sim 10^{15}$  atoms/cm<sup>2</sup> • sec) to be sufficiently high for interaction with spacecraft materials. In addition to these high flux levels, the interaction is aided by the 5.0-8.0 eV AO gains from collisions with spacecraft surfaces.

The total integrated flux, or fluence, of AO on the surface of a spacecraft is mainly dependent on altitude, inclination (changes in the impinging angle – angle between incoming flux and surface), spacecraft orientation, solar activity, and season. A parametric study by Leger and Visentine shows the nature of these relationships<sup>2</sup>. AO fluence was shown to increase with decreasing altitude (e.g. as altitude drops from 900 km. to 150 km., fluence on ram-oriented surfaces increases from  $3.1 \times 10^{18}$  to  $4.4 \times 10^{23}$  atoms/cm<sup>2</sup> per year) and increase with solar flare activity. The effects of the seasonal and

inclination parameters are interconnected. As shown in Figure 2, a density bulge created by solar heating lies along the equator during the fall and spring equinoxes<sup>2</sup>.

Figure 2<sup>2</sup>: Seasonal and inclinational effects on fluence



As a result, orbiting spacecraft experience a maximum fluence at inclination angles of 0° during these times of year. Similarly, this area of increased AO density is 23.5° above the equator during the summer solstice, and a maximum fluence is apparent at an inclination angle of 23.5°. Perhaps the most interesting parametric relationship observed is between AO fluence and spacecraft surface orientation. Four predominant orientations were evaluated: ram, wake, solar and anti-solar. Ram surfaces face the direction of flight while wake surfaces conversely oppose the direction of flight.

Likewise, solar oriented surfaces face toward the sun and anti-solar oriented surfaces face away from the sun. At a circular orbit of 500 km. during a period of nominal solar activity the following fluencies were observed:

Table 1: Flux experienced at different surface orientations

Surface	Flux x 10 <sup>-20</sup> (atoms/cm <sup>2</sup> per year)
Ram	7.4
Wake	3.3
Anti-solar	2.7
Solar	1.5

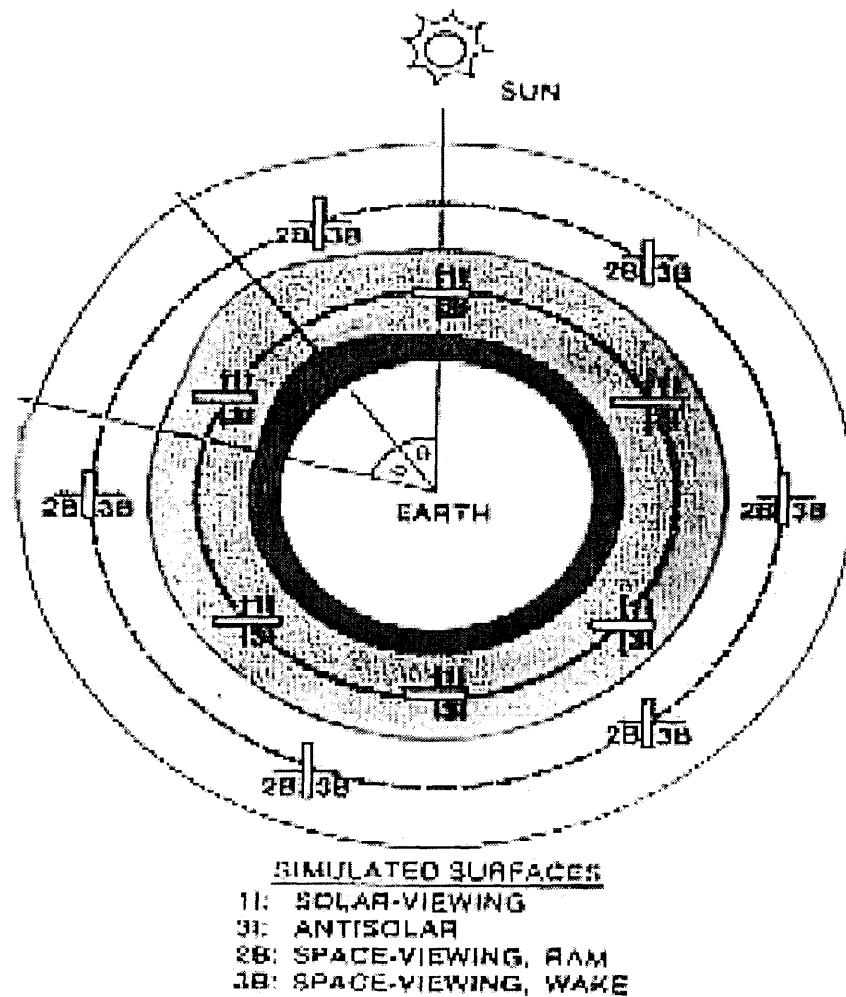
Seen in Table 1, ram surfaces experienced the greatest fluence because they were oriented toward direct collision with impinging energetic AO. The disparity between fluencies of solar and anti-solar surfaces is less obvious. Shown in Figure 3, solar heating effects create a bulge in AO number density at approximately 40° east of solar noon<sup>2</sup>. In general, spacecraft are launched in an eastward direction so the momentum generated by the earth's rotation aids them. As a result, anti-solar surfaces lead toward the ram direction, while solar viewing surfaces look towards the wake direction. During orbit anti-solar surfaces fly through this bulge of heightened AO number density while wake effects protect solar viewing surfaces from it, explaining the greater fluence experienced by the former. Although the relative orientations of these two surfaces are reversed at night, the nighttime AO density drops sharply (from 4.2x10<sup>7</sup> to 1.4x10<sup>8</sup> atoms/cm<sup>3</sup> at 500km.) so that the solar noon effect is not compensated for.

### **I.3. Polymeric Materials/Composites in Spacecraft Design**

Polymers are used as spacecraft materials because they are strong, lightweight, and can be modified in numerous ways to impart specific properties to a structure. Perhaps the most important applications for polymers and composites in space

are as thermal control materials and solar array interconnects. For example, polyimide films are used as substrates for lightweight, large-area solar arrays. Polyurethane paints are used to suppress stray light within astronomical telescopes and absorb thermal radiation on parabolic communication antennae.

Figure 3<sup>2</sup>: Surface orientation effects on fluence



Graphite epoxy composites are utilized for lightweight truss members in large space structures.

In addition to spacecraft structural materials, polymers have use in materials needed for extravehicular activity (EVA), such as the spacesuit. The basic components of a spacesuit are a helmet with an extravehicular visor assembly (EVVA), a hard upper torso unit (HUT), and a lower torso assembly (LTA). Figure 4 in the Appendix shows these components as well as a cross-section of the materials lay-up for the arms and legs of the spacesuit<sup>3</sup>.

The outer layer of the helmet, HUT, and LTA is an orthofabric cover made of a combination of Teflon, Nomex, and Kevlar (Teflon is AO blocker). These three units are all insulated by 5 plies of reinforced aluminized Mylar. The helmet and EVVA are composed of polycarbonate and polysulfone. Spacesuits feature an inner-liquid cooling ventilation garment (LCVG) composed of spandex, water, and ethylvinyl acetate. Other polymeric materials used in spacesuit construction include Dacron, fiberglass, and neoprene coated nylon ripstop. Average EVA events last 6-7 hours, and current spacesuits are currently designed to withstand approximately 7.5 hours of maximum EVA. While spacesuits offer thermal, atmospheric, and micrometeoroid protection, their effectiveness in blocking space ionizing radiation is limited.

#### **I.4. Atomic Oxygen Interactions with Polymeric Spacecraft Materials**

As evidenced by the Advanced Composites Materials Exposure to Space Experiment (ACOMEX) aboard STS 41-G, interaction of atomic oxygen with polymeric spacecraft materials can lead to surface recession/erosion, loss of surface gloss, and discoloring<sup>1</sup>. The efficiency with which spacecraft materials react with atomic oxygen proves varied. Test materials aboard STS-5 (300km, fluence= $1.0 \times 10^{20}$  atoms/cm<sup>2</sup>) and STS-8 (205 km, fluence= $3.5 \times 10^{20}$  atoms/cm<sup>2</sup>) that contained C, H, N, and O experienced

high reaction rates ( $2.5 \times 10^{-24}$  to  $3.0 \times 10^{-24}$  cm<sup>3</sup>/atom) while most metals, with the exception of osmium, silver, and to a lesser degree copper, were stable to AO exposure<sup>2</sup>. The reaction rates of filled organic materials depended on the oxidative stability of the fillers. For example, materials filled with carbon reacted with AO much more efficiently than those filled with metal oxides. On the other hand, perfluorinated and silicone polymers were fifty times more stable towards AO than their organic neighbors. In addition, aromatic polymers such as Kapton displayed lower reactivity with AO than those of aliphatic hydrocarbons. These results suggest a strong relationship between molecular structure and AO reactivity\*.

Unlike with smaller molecules, the mechanism of polymer degradation by AO is elusive and yet to be completely understood. The preliminary steps of oxidation are primary bond dissociation reactions. When AO impacts the surface of a polymeric material, there are three basic routes it can follow. On the surface of the polymer, impinging AO can react with either organic material or condensed nitrogen compounds, or it can diffuse into the bulk of the polymer. With thick materials, diffusion is limited and the concentration of AO is greater at the surface. This disparity results in faster reaction rates and a greater changes in surface properties than bulk properties. For example, the degradation of Kapton films in LEO is due to a chain reaction involving hydroperoxide formation and free-radical initiation. Rapid surface oxidation occurs, dramatically changing the surface properties of the Kapton film. Oxidation resistance is imparted to the surface of Kapton films with the aid of a protective coating, typically

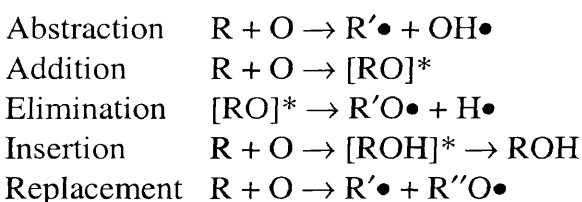
---

\*In these flight experiments surface recession/thickness loss was determined from mass changes in the specimens and was shown to be proportional to fluence. Reaction efficiencies were then determined by:  $\Delta x = F_T \times R_e$ ;  $\Delta x$  = surface recession,  $F_T$  = accumulated fluence,  $R_e$  = reaction efficiency.

composed of Teflon or siloxane. In this case, diffusion-limited oxidation is the main erosion reaction. Changes in the bulk properties of a material can still affect the surface in the forms of surface cracking and crazing.

According to the work of Jellinck and Lipovac, there is an induction time before the onset of erosion during which oxygen transforms from a gas phase to a film phase<sup>4</sup>.

This slow step is followed by fast oxidation reactions of many types:



While the exact mechanisms of AO erosion of polymers require a case-by-case analysis, some generalizations can be made about this interaction. For one, hydrogen abstraction is the preferred pathway for ground state AO. O (<sup>3</sup>P<sub>1</sub>) abstracts hydrogen from saturated organic molecules and adds to carbon-carbon double bonds resulting in the formation of carbonyl compounds and epoxides. On the other hand, O (<sup>1</sup>D<sub>2</sub>) tends to form alcohols by inserting into carbon-hydrogen bonds. In either case, secondary fragmentation reactions follow, governed by the relative thermodynamic stabilities of the possible products<sup>5,6,7</sup>.

The fragmentation of high molecular weight polymer chains is problematic for a variety of reasons. Aside from surface erosion and loss of functional groups in the polymer that can lead to polymer failure, fragmentation leads to formation of volatile condensable materials that can deposit on sensitive surfaces as contamination. For example, mass spectrometry characterized the gaseous products formed by the reaction of AO with C<sup>13</sup> labeled Kapton as a part of the EOIM-III flight experiment aboard the STS-46 mission<sup>8</sup>. The gaseous products included CO, CO<sub>2</sub>, H<sub>2</sub>O, NO, and NO<sub>2</sub>.

Since the primary reactions of polymer erosion by AO are bond dissociation reactions, the dissociation energies of polymeric bonds is a large contributor to reaction rates. Comparisons of reactive efficiencies and dissociation energies of different polymers can suggest probable degradation mechanisms. For example, if the mechanism of erosion of FEP Teflon is carbon-carbon bond breakage, then FEP Teflon should be as reactive as polyethylene towards AO. But the well-observed smaller reactivity of FEP Teflon with AO suggests another mechanism of erosion, such as carbon-fluorine bond dissociation. The dissociation energy of this bond is 5.5eV, an amount only thirty percent of AO in LEO have. Therefore FEP Teflon, as well as other fluorinated polymers, is more stable to AO attack. Similarly, the dissociation energy of the Si-O bond in SiO<sub>2</sub> is 8.3 eV, explaining why SiO<sub>2</sub> is commonly used as a protective coating on spacecraft materials. Relative to aliphatic polymers, aromatic polymers exhibit higher dissociation energies for hydrogen abstraction. For this reason the use aromatic polymers in space is preferable.

Physical factors have also been shown to influence the reactivity of a polymer towards AO. These factors include degree of crystallinity, presence of amorphous regions, and permeability to oxygen. In addition, the surface-to-volume ratio of the polymer structure has shown to be important to the rate of oxidative degradation.

## **I.5. Materials**

### **I.5.i. Motivation for Use of Additives**

Different additives were mixed into a polymer precursor with hopes that, upon curing, those additives would be held in the matrix of the polymer. Exposure to atomic oxygen would then form chemically stable additive oxide layers, and therefore protect the

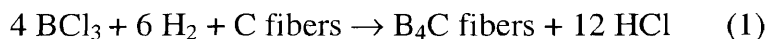
underlying polymer from further oxidation. Hence, the additive would have conferred a certain level of resistance to oxidation to the polymer.

### **I.5.ii. Boron**

Boron, a main group metalloid, was chosen as an additive because of its high melting temperature of 2075°C, low density of 2.34 g/cm<sup>3</sup>, and its use in atomic oxygen protection is novel. Space shuttle flight STS-46 conducted AO erosion studies that included exposure of six types of carbon and carbon-boron nitride (C-BN) composites. Not only did degradation resistance increase with BN composition, but exposure of C-BN and graphite composites resulted in preferential etching of graphite, leaving BN domains. This observation suggests boron has a low AO reaction efficiency, relative to the polymer in which it is dispersed<sup>9</sup>. In addition, 19.9% of natural boron exists as <sup>10</sup>B, which has proven effective in capturing thermal neutrons in space environments that result from the interaction of galactic cosmic radiation with space materials<sup>10</sup>.

### **I.5.iii. Boron Carbide and Whisker Technology**

Boron carbide, B<sub>4</sub>C, has many appealing qualities in a fibrous form, including high strength, high modulus of elasticity, low density, and high chemical stability. In particular, boron carbide has shown strong resistance to air oxidation up to temperatures of 750 - 800°C<sup>11</sup>. Boron carbide can be synthesized by the chemical conversion of multi-filament carbon precursor fibers, as shown:



This reaction takes place in two steps at temperatures of 1600 - 1900°C:



The reaction between boron and carbon was shown to be the rate-limiting step. Under isothermal conditions, the initially flexible and unfused carbon fibers became brittle and fused as flow rates of boron trichloride and hydrogen were increased. Excess boron bridged the carbon fibers together at contact points, thereby decreasing its flexibility.

#### **I.5.iv. Organoclays**

Having great significance among industrial minerals, clays are utilized in many forms for a wide array of applications. Equally important, organically modified clays can impart specific rheological characteristics to polymeric materials. Smectite clay, mined from Bentonite ore, is commonly used in the production of organoclays. Smectite has two forms: montmorillonite and hectorite.

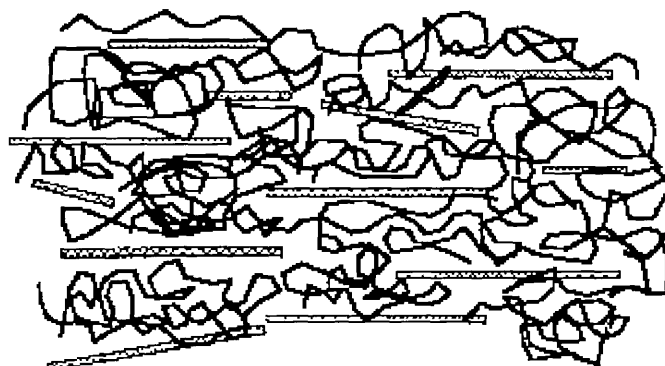
The base unit of the smectite clays consists of three octahedral spaces along with associated tetrahedral sheets. Montmorillonite, an aluminum silicate  $\text{Al}_2[(\text{OH})_2\text{Si}_4\text{O}_{10}] \cdot n\text{H}_2\text{O}$ , is a dioctahedral smectite with two of the octahedral spaces in the unit cell filled with aluminum while the third is empty. The most common of its uses is as an adsorbent because of its excellent ion exchange ability<sup>12</sup>. On the other hand, Hectorite, a magnesium silicate  $\text{Mg}_3[(\text{OH})_2\text{Si}_4\text{O}_{10}] \cdot n\text{H}_2\text{O}$ , is a trioctahedral smectite with all three spaces in the unit cell filled with magnesium. Differences in chemical composition between the two forms of Smectite manifest themselves in terms of morphology. Montmorillonite is made up of hexagonal plate-like particles, and assumes a sheet arrangement, while Hectorite has lath or strip morphology. Incidentally, Montmorillonite is vastly more commercially available than Hectorite.

Montmorillonite crystals have an internal net negative charge, with positive ions on the surface to render the crystals electrically neutral. The sodium and calcium ions

can be easily replaced by other cations via an ion exchange process. If the replacement is an organic cation, such as a quaternary ammonium cation, an organoclay results.

As mentioned, the primary motivation to use organoclays for atomic oxygen resistance is the formation of a chemically stable additive oxide layer that will protect underlying polymer from erosion. A secondary reason is now discussed. Polymers exhibit enhanced ordering near surfaces and interfaces, resulting in an enhancement of properties at those locations<sup>13</sup>. For example, a Japanese research group at Toyota Research Laboratories made composites consisting of single-layer silicates applied to the surface of a polyimide. Compared to the bulk of the polymer, the surface exhibited a 60% decrease in water permeability, a 25% decrease in its thermal expansion coefficient, as well as an enhanced modulus<sup>14</sup>. Generation of several interfaces is possible by homogeneously dispersing the clays in a polymer matrix. Giannelis proposed that the silicate layers of the clays would exist in a parallel fashion due to dipole-dipole interactions<sup>15</sup>. The composite structure is shown below in Figure 5, where the horizontal bars represent the silicate layers.

Figure 5: Organoclay depiction

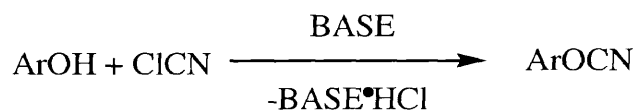


Property enhancement would then occur throughout the polymer, not just at the surface. The best matrix to use is that of a polymer with semi-rigid chains so that the effects of enhanced crystallinity are extended over a long distance. This specification would also aid processing because less organoclay is needed. The increase in crystalline regions will ultimately affect the polymer's reactivity with AO, presumably in a negative fashion.

#### I.5.v. Cyanate Resin

Although their chemical compositions are classified, commercial cyanate esters, or cyanates, of polyphenolic compounds have been well studied. In the early 1960s Grigat prepared stable aryl cyanates by reacting phenolic compounds with a cyanogen halide<sup>16</sup>. This finding is shown in Figure 6.

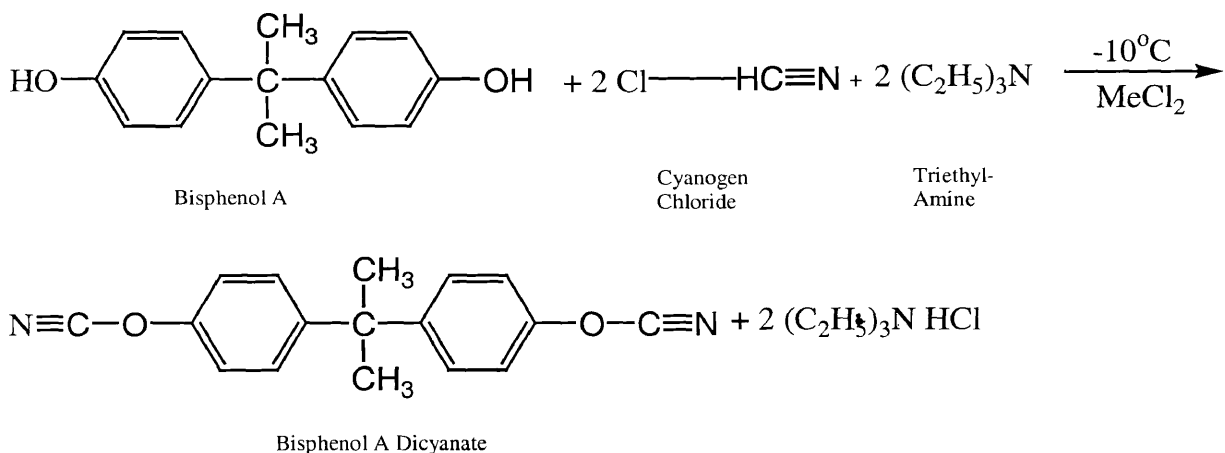
Figure 6: Preparation of stable aryl cyanates





dicyanates are commercially manufactured by reacting BPA with cyanogens chloride in the presence of a tertiary amine.

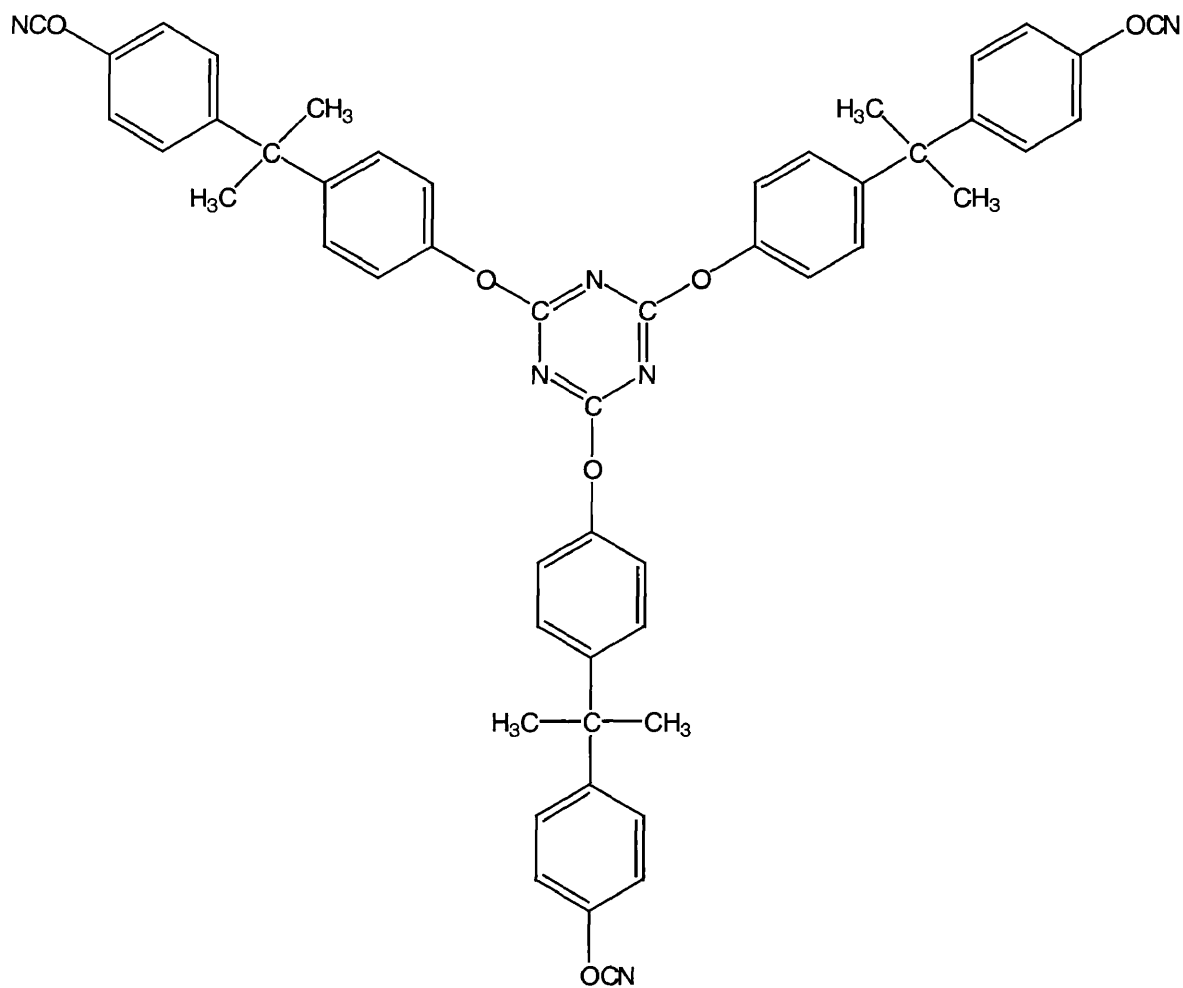
Figure 9: BPA dicyanate synthesis



These aryl dicyanate esters (NCO-Ar-OCN) are commercially important because they are crystalline solids of high purity, low melting point and toxicity, and are widely soluble and compatible.

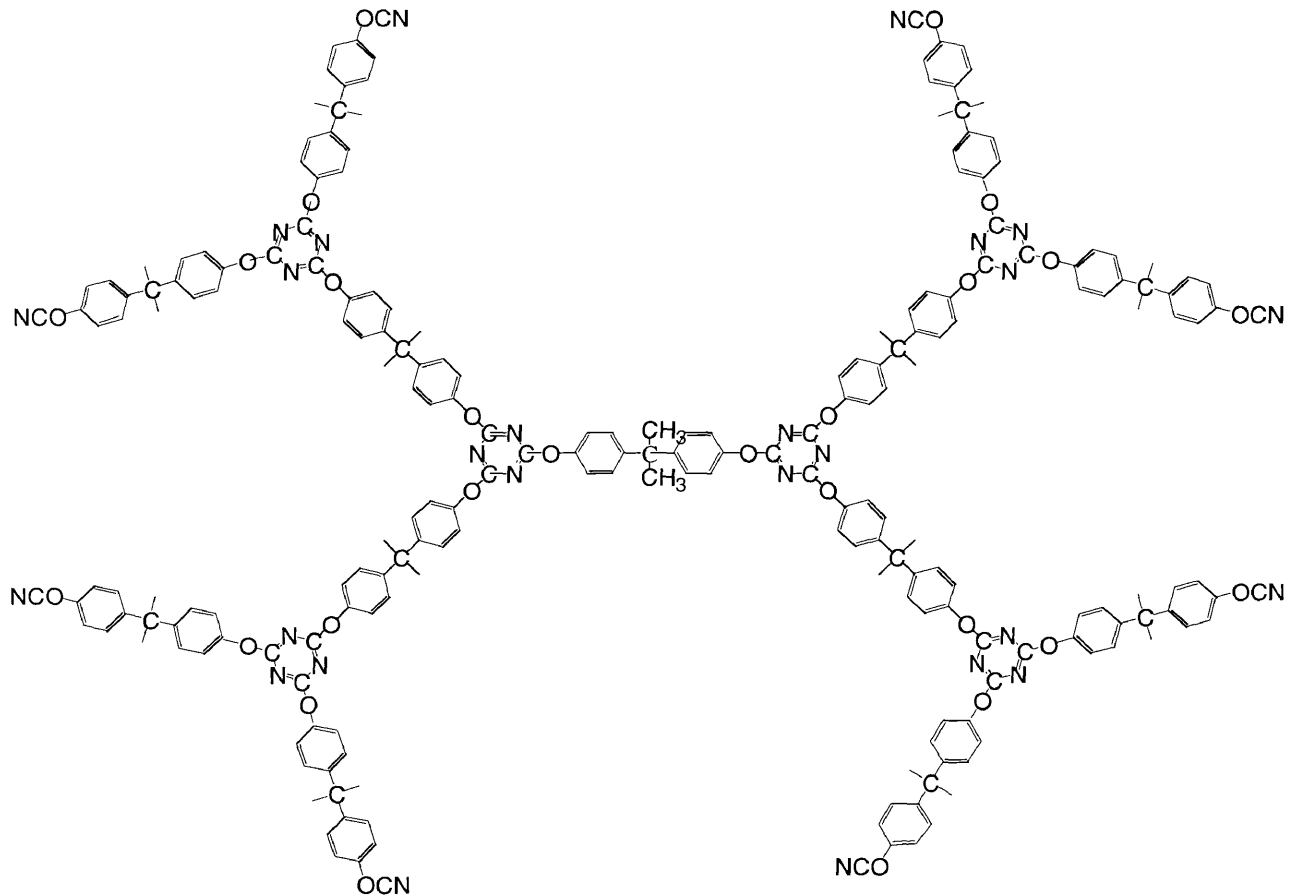
The cyanate esters used in this research are thermoset resins, meaning the prepolymers cure and harden under application of heat and pressure, after which they do not soften readily. According to Graver, the process by which BPA-based cyanate esters are cured is well studied. Aryl cyanate esters, such as the dicyanate previously mentioned, cyclotrimerize to s-triazine structures upon heating above 150°C. This structure, known as a cyanurate, is shown in Figure 10.

Figure 10: A Cyanurate



Cross-linking occurs in the thermoset matrix when the s-triazine rings connect other aryl cyanates. The result is a completely cross-linked matrix that is referred to as a polycyanurate network<sup>19</sup>. This network is shown in Figure 11.

Figure 11: A Polycyanurate network



The benefits of cyanate ester networks are numerous, including low shrinkage, high adhesion, void-free structures, and the absence of volatile polymerization by-products. Because of these properties, cyanate resins are often compared with epoxy resins. A study by Delano on the use of cyanate esters in carbon fiber prepegs for advanced structural composites revealed that, when fully crosslinked, cyanate systems outperformed epoxy resins in mechanical, electrical, thermal, toughness and moisture resistance properties<sup>20</sup>.

## **I.6. Experimental Methods**

### **I.6.i. Scanning Electron Microscopy**

Scanning electron microscopy (SEM) is an analytical technique used to obtain surface information of materials at high resolution. In this process, the surface of a solid sample is swept in a raster pattern with a finely focused electron beam. A raster is a scanning pattern in which the electron beam is first swept across the surface in the x direction, then returned to its starting position, and finally shifted downward in the y direction by a standard increment. During the scanning process, signals in the form of backscattered and secondary electrons are received above the sample surface in the z direction, which are stored and converted into an image by a computer. Figure 12 in the Appendix shows a schematic of a SEM<sup>21</sup>.

The condenser lens system modifies the electron beam emitted from the electron gun (source) so that a finely focused electron beam reaches the objective lens system. This latter lens system regulates the size of the electron beam incident on the surface of the sample. Two pairs of electromagnetic coils are located within the objective lens system, one that deflects the electron beam in the x direction (x coils) across the sample surface, and another that deflects it in the y direction (y coils). The application of an electrical signal to the x coils causes the electron beam to strike the sample surface on one side of the center axis of the lens system. Hence, varying the electrical signal with time produces a line scan in which the electron beam moves across the sample surface in the x direction, and then returns to its initial position. The application of an electric signal to the y coils shifts the electron beam downward in the y direction an amount proportional to the applied signal. Therefore, alternating the application of electrical

signals to the two pairs of coils results in the raster scanning pattern across the surface sample.

The sample holder is a movable stage that can be rotated about the x, y, and z-axes, allowing for many viewing perspectives. The incident electron beam interacts with the sample surface in two ways. Elastic interactions occur when an electron collides with an atom on the sample surface and then changes direction without a significant change in speed. Therefore the kinetic energy of the electron is constant. The electrons that are emitted from the sample surface as a result of elastic scattering are referred to as backscattered electrons. The other method of interaction is inelastic in nature, meaning there is energy transfer or flow from the incident electron to the atoms in the sample surface. In this process, weakly bound conduction electrons in the metal surface are emitted with low energy. These electrons are referred to as secondary electrons.

Scintillation devices are used as transducers for these emitted electrons. The signal they receive above the sample surface is driven into a cathode-ray tube (CRT), which forms an image by using a detector to observe differences in intensity of each scan point. Ultimately, every point on the image corresponds to a particular location on the sample surface at which a signal was produced. The magnification of the image is equal to the ratio of the width of the CRT display and the width of a single line scan across the sample surface. While decreasing the width of the line scans can increase magnification, many factors limit the degree of magnification to a range from 10x to 100,000x.

In SEM, flooding the specimen with electrons produces images. Because the sample is a poor conductor, it would accumulate negative charge from the electron

flooding, resulting in image distortion. To remedy this occurrence, plating them with gold or palladium heightens the conductivity of specimens. There are two general methods used for metal-plating SEM specimens: evaporative coating and sputter coating.

In the evaporative coating process, system conditions are high temperature and vacuum. As sublimation takes place, metal vapor adheres to the surface of the specimen. There are three well-defined drawbacks to this procedure. Firstly, the coating is directional; meaning the degree of plating physically depends on the motions of the metal apors. As a result, physical rotation or tilting of the specimen may be required to insure total coverage of the specimen's surface. Secondly, the system conditions require high temperatures, imposing possible damage to the specimen. Lastly, evaporative coating is a macroscopic process; so metal particle size and plating thickness are uncontrollable by the operator.

Sputter coating involves the liberation of metal atoms from the specimen by n impact. Atom dispersion takes place in a chamber, allowing clouds of metal atoms to coat the specimen. The advantages of this process are obvious. First of all, dispersion ensures that specimen coating is thorough, so physical manipulation is not needed. In addition, the metal atoms are thermally cool so damage to the polymer sample by heat is avoided. Finally, sputter coating is a microscopic process, so coating thickness and uniformity are controllable parameters.

#### **I.6.ii. Thermogravimetric Analysis**

Thermogravimetric analysis (TGA) is a method of thermal analysis that can provide information about decomposition and oxidation reactions of a material, as well as physical processes such as sublimation, vaporization, and desorption. In TGA

experiments, the mass of a sample in a controlled atmosphere is monitored as a function of temperature. The output, called a thermogram, is a plot of mass percent as a function of temperature.

Instrumentation includes a sensitive analytical balance, a furnace, a purge gas system that provides the desired inert or reactive atmospheric conditions, and a computer/processor for instrument control, data acquisition and display.

The balances commonly have a range of 5 to 20 milligrams. Shimadzu provides a schematic of a thermogravimetric analyzer in Figure 13, found in the Appendix.

The sample is put in a platinum sample cell that is then placed on a sample pan hanging down in the atmosphere-controllable reaction tube. Weights are placed in another pan opposite the sample pan to almost balance the beam, supported by a taut band, that connects them. Changes in sample mass due to heating cause the beam to incline, which is detected by photoelectric elements and amplified. A current flows to a feedback coil to provide a uniform magnetic field to balance with the moment of rotation based on the mass change of the sample. Known as the zero-position method, the beam position is thus kept at a fixed position. Because the torque of the beam is in direct proportion to the current, mass changes of the sample can be measured continuously with accuracy by a data acquisition system that monitors the current and transforms its signal into mass loss information.

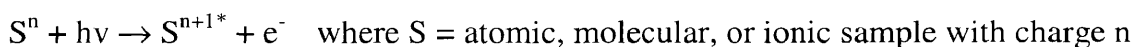
The furnace in a TGA instrument is capable of a temperature range from room temperature to over 1500°C. Heating and cooling rates can range from between zero and 200°C per minute. The exterior of the furnace is insulated and cooled to prevent heat transfer to the analytical balance. As mentioned, a purge gas system is connected to the

furnace to allow for controlled atmospheric conditions. Common purge gases are nitrogen, argon, oxygen, and air.

A thermocouple is utilized to obtain sample temperatures within the furnace. For reasons of sample contamination, decomposition, and mass measurement errors, the thermocouple cannot be placed directly in the sample holder. Therefore it is placed as close as possible to the sample holder, causing the recorded temperatures to slightly lag or lead the true sample temperatures. This deviation is minimized in modern instruments that use computerized programs to adjust the voltage of the heater to match the voltage output of the thermocouple.

### **I.6.iii. X-ray Photoelectron Spectroscopy**

X-Ray Photoelectron Spectroscopy (XPS) is an analytical technique that provides information on a sample such as atomic composition, structure, and oxidation state. The general reaction that occurs during the XPS process is:



$h\nu$  = monochromatic X-Ray beam of known energy

$S^{n+1*}$  = electronically excited sample with positive charge  $n+1$

$e^-$  = emitted electron \*

Excitation typically involves inner shell K and L electrons. Figure 14 shows how X-ray beams excite some of these electrons to the energy levels of the outer shell or valence electrons. In Figure 14,  $E_b$  refers to the energy levels of inner shell electrons, while  $E_v$  refers to the energy levels of valence electrons. An electron spectrometer is used to

---

\* Emitted electrons can pass through only 10 to 50 Angstroms of a solid specimen.

measure the kinetic energy of the emitted electron. The binding energy of the emitted electron is then calculated by the equation:

$$E_b = h\nu - E_k - W \quad \text{where } E_b = \text{binding energy of the emitted electron}$$

$h\nu$  = monochromatic incident X-Ray beam of known energy

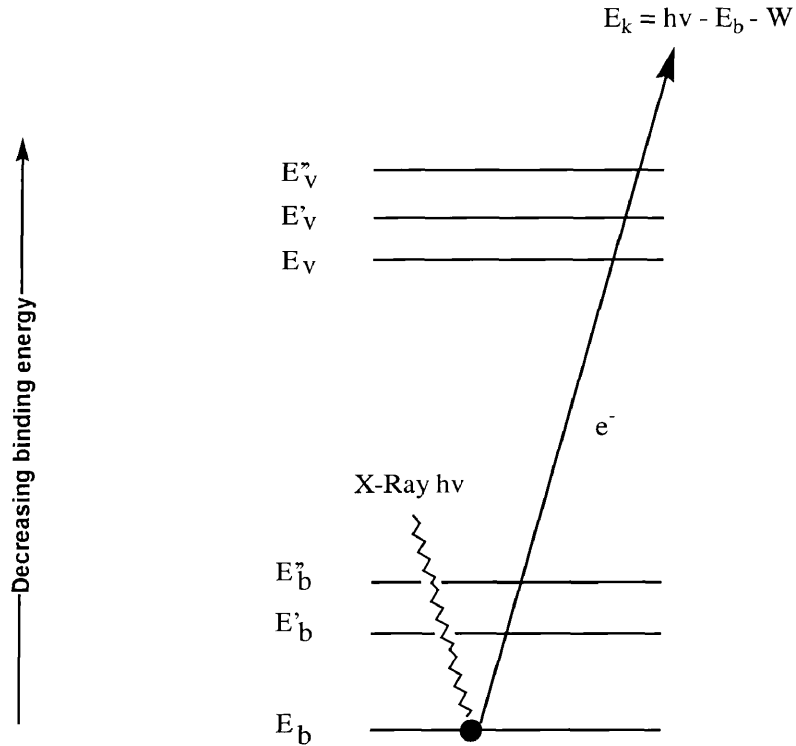
$E_k$  = kinetic energy of the emitted electron

$W$  = work function of the electron spectrometer

The binding energy of the electron is useful because it specifies the atom and orbital from which it was emitted. The work function is a correction for the electrostatic environment in which the emitted electron is formed and measured.

As found in most optical spectroscopic instruments, the instrumentation for XPS includes a source, sample holder, analyzer, detector, and signal processor and readout. A schematic for a modern XPS instrument is provided in Figure 15 in the Appendix<sup>21</sup>. Typical X-ray sources are X-ray tubes with magnesium or aluminum targets and corresponding filters. More sophisticated XPS instruments utilize a crystal monochromatic source to provide X-rays with fine bandwidth on the order of 0.3 eV.

Figure 14: Schematic representation of the XPS process



The benefits of this more expensive source is the enhancement of signal-to-noise ratios via elimination of Brehmsstrahlung background, as well as the capability to study much smaller areas on the sample surface.

Solid specimens are placed in a fixed sample holder located as close to the X-Ray source as possible. A vacuum pump is used to lower the pressure in the sample compartment to an order of  $10^{-5}$  torr or smaller. The high vacuum reduces both attenuation of the X-ray beam and contamination of the sample surface by oxygen and water.

In the majority of XPS instruments, a hemispherical electrostatic magnetic field is used to deflect the electrons of the X-ray beam in a curved path towards the transducer

and analyzer. The radius of curvature of the electrons is dependent on their kinetic energy as well as the field strength. Therefore electrons with different kinetic energies can be selectively analyzed by varying the magnitude of the hemispherical field.

The multi-channel transducer consists of an array of small photosensitive elements arranged on a semi-conductor chip. The application of a potential on the order of many kilovolts across the transducer incurs a cascade pulse of  $10^6 - 10^8$  electrons per incident electron. The pulses are then counted electronically. A plot of the counting rate versus the binding energy of the emitted electron generates the X-ray photoelectron spectrum. A survey spectrum is commonly achieved by specifying low resolution and a scan wide enough to encompass a binding energy range of 0 to 1250 eV. When using a magnesium or aluminum  $K_{\alpha}$  source, all elements except hydrogen and helium emit core electrons with characteristic binding energies that will provide peaks in this region.

Oxidation states are assigned to spectral peaks by the chemical shifts they exhibit under higher resolution. The correlation between the position of the peak maximum and the chemical environment of the atom that gives rise to the peak is based on the ability of outer electrons to shield core electrons from the attraction of the nucleus. When an electron is emitted, the effective charge experienced by the core electron is increased, resulting in a shift to a higher binding energy. Hence as oxidation states become more positive, binding energies increase accordingly.

---

<sup>1</sup> D.G. Zimcik, "Advanced Composite Materials Exposure to Space Experiment (ACOMEX) on STS 41-G", *Canadian Aeronautics and Space Journal*. **1985**, 31, p 250.

<sup>2</sup> L.J. Leger and J.T. Visentine, "A Consideration of Atomic Oxygen Interactions with the Space Station", *Journal of Spacecraft and Rockets*. **1986**, 23, 5, pp 507-510.

- 
- <sup>3</sup> A.J. Ross, B. Webbon, L.C. Simonsen, and J.W. Wilson In *Spacesuits*; J.W. Wilson, J. Miller, A. Kouradi, and F.A. Cucinotta, Ed.; NASA Shielding Strategies for Human Space Exploration, **1997**, pp 293-295.
- <sup>4</sup> H.H.G. Jellinek and S.N. Lipovac, "Diffusion Controlled Oxidative Degradation of Isotactic Polystyrene at Elevated Temperatures", *Macromolecules*. **1970**, Vol 3, No 2.
- <sup>5</sup> R.J. Cvetanovic and D.L. Singleton, *Reviews of Chemical Intermediates*; **1984**, 5, p 183.
- <sup>6</sup> J.T. Herron and R.E. Huie, *J. Phys. Chem. Ref. Data* 2, **1974**, p 467.
- <sup>7</sup> A.C. Luntz, *J. Chem. Phys.* **1980**, 73, p 1143.
- <sup>8</sup> S.L. Koontz, L.G. Leger, J.T. Visentine, D.E. Hunton, J.B. Cross, C.L. Hakes. An Overview of the Evaluation of Oxygen Interactions with Materials III Experiment: Space Shuttle Mission 46, July-August 1992; Proceedings of the Third Post-Retrieval Symposium on LDEF-69 Months in Space; Sponsored by the National Aeronautics and Space Administration and the American Institute of Aeronautics and Astronauts, Washington D.C., in Williamsburg, VA, 1993; p 869.
- <sup>9</sup> B.R. Spady, A.W. Moore, and M. Lake. LEO Degradation of Graphite and Carbon – Based Composites Aboard Space Shuttle Flight STS-46; Proceedings of the Third Post-Retrieval Symposium on LDEF-69 Months in Space; Sponsored by the National Aeronautics and Space Administration and the American Institute of Aeronautics and Astronauts, Washington D.C., in Williamsburg, VA, 1993; p 869.
- <sup>10</sup> Scott Pugh, M.A. Thesis, The College of William and Mary, 1999.
- <sup>11</sup> L.G. Sneddon In *Boron Polymers and Materials*; W. Siebert, Ed.; Proceedings of the Ninth International Meeting on Boron Chemistry, Germany, 1996; p 497.
- <sup>12</sup> C. Breen, J.O. Rawson, and B.E. Mann, "Adsorption of polycations on clays; an in-situ study using <sup>133</sup>Cs NMR," *J. Mater. Chem.*, **1996**, 6, pp 253-60.
- <sup>13</sup> B.S. Hsiao and E.J.H. Chen, *Controlled Interfaces in Composite Materials*, ed. H. Ishida. New York: Elsevier, 1990. pp. 613-622.
- <sup>14</sup> K. Yano et al. , *Polymer Preprint*, **1991**, p 65.
- <sup>15</sup> E.P. Giannelis, "A New Strategy for Synthesizing Polymer-Ceramic Nanocomposites", *JOM*, **1992**, p 28.
- <sup>16</sup> E. Grigat and R. Putter, *Angew Chem. Internat. Edit* 6, **1967**, p 206.
- <sup>17</sup> D. Martin, *Angew Chem. Internat. Edit* 3, **1964**, p 311.
- <sup>18</sup> K.A. Jenson and A. Holm, *Acta Chem. Scand.* **1964**, 18, p 826.
- <sup>19</sup> R. Graver In *Cyanate Esters – High Performance Resins*; R.B. Seymour and G.S. Kirsherbaum, Ed.; Proceedings of the Symposium on the History of High Performance Polymers at the American Chemical Society Meeting, New York, 1986; pp 309-312.
- <sup>20</sup> C. B. Delano, A. H. Mcleod, C. J. Kiskiras, NASA Contract Final Report FR-80-42/AS (Contract NAS3-22025).
- <sup>21</sup> D.A. Skoog, F.J. Holler, T.A. Nieman. Principles of Instrumental Analysis; Harcourt Brace and Company: Philadelphia, 1998; pp 540, 551.

## CHAPTER 2: EXPERIMENTAL

### II.1. Materials

Samples were prepared from two polymers with four different additives. The two polymers were a Bisphenol-A based cyanate ester resin and Hexcel 954-3 cyanate ester resin.

The two metal-based additives were amorphous boron powder (B) and boron carbide ( $B_4C$ ). Both were from Alfa Aesar: a dark brown amorphous boron powder, -325 mesh, and dark grayish-black boron carbide whiskers of 300 microns in length and 5-8 microns in diameter, giving an average aspect ratio close to 46. Because there are four boron atoms per carbon, boron makes up 80 percent of a boron carbide molecule. The boron carbide used had a formula weight of 55.26 grams per mole, a density of 2.52 grams per cubic centimeter, and a melting point of 2350°C.

Southern Clay Products, Inc. (TX) provided Cloisite-15A, an alkyl quaternary ammonium montmorillonite, and Hectorite on a proprietary basis. The Cloisite-15A is a solid tan powder with a mild odor, while the Hectorite is slightly darker and is odorless. The exact atomic structures of these organoclays are unknown.

#### II.1.i. Bisphenol-A based Cyanate Ester Resin

The YLA Corporation supplied a Bisphenol A-based cyanate ester (CE). The chemical composition of this polymer is proprietary. The uncured polymer contained a pre-mixed curing agent, necessitating storage in a freezer to prolong the resin's shelf life. Additionally, the polymer becomes sticky at room temperature, so freezing facilitated sample preparation. Initially a pale green solid, the BPA-based CE turns amber upon curing.

### Bisphenol A-based CE Curing Procedure

The following instructions were used to prepare the Bisphenol A-based cyanate ester:

- Store uncured polymer at temperatures below 0°C.
- Chip off small pieces of the frozen uncured polymer with the aid of a hand tool. Free enough polymer from the bulk solid so that total sample mass approaches 8 grams.
- Heat the polymer in a circular aluminum dish (diameter and depth needed) on a heating plate until the solid liquefies and flows readily.
- Stir additive into polymer with aid of glass stirring rod. All additives are kept dry in an oven (100°C) prior to use. This step is skipped when processing pure samples.
- Place sample(s) in vacuum oven, and then apply both vacuum and heat.
- Once system reaches 30mm Hg, close vacuum so that system is no longer being pumped on. This limits the extent of bubbling that can occur during heating, due to additives. Purge system at approximately 125°C.
- Continue heating to 177°C, and then hold at this temperature for 1.5 hours to cure.
- Heat sample(s) to 232°C, and then hold at this temperature for 2 hours to post-cure.
- Remove sample from vacuum oven and peel the aluminum dish off of the cured polymer. Running water aids removal.

This procedure was utilized for the preparations of all the BPA-based CE samples.

Variations, shown in Table 2, were introduced by changing the temperatures at which the samples were placed in the oven and at which the system was purged.

Table 2: Bisphenol A-based Cyanate Ester Samples

Additive	% Additive (weight basis)	Start Temp. (°C)	Purge Temp. (°C)	Appearance
Pure x 5	0	25	125	Translucent amber
B	3	100	170	Bubbles/rough surface
B	5	25	125	Homogeneous
B	5	25	125	Homogeneous
B	6	25	170	Rough surface
B	7	100	125	Bubbles/rough surface
B	10	25	125	Homogeneous
B	10	25	125	Homogeneous
B <sub>4</sub> C	5	25	125	Additive mostly settles
B <sub>4</sub> C	5	25	125	Additive mostly settles
B <sub>4</sub> C	10	25	125	Additive mostly settles
B <sub>4</sub> C	10	25	125	Additive mostly settles
Hectorite	5	25	125	Additive mostly settles
Hectorite	10	25	125	Additive mostly settles
Cloisite	2	25	125	Homogeneous
Cloisite	5	25	125	Homogeneous
Cloisite	10	25	125	Homogeneous

Samples were made with all of the additives listed in Table 2. Those with B<sub>4</sub>C and Hectorite showed evidence of settling. This is attributable to two main factors: the large

difference in density of the additive compared to that of the CE and more importantly the viscosity drop exhibited by the CE. Although a graph of viscosity versus time was unavailable for the BPA-based CE, it is assumed to behave similarly to the Hexcel 954-3 CE whose viscosity decreases with time (heating) as shown in Figure 16 in the Appendix. This dramatic decrease complicated attempts to suspend an additive in the matrix of the polymer. The CE samples with B<sub>4</sub>C and Hectorite appeared homogeneous at temperatures up to 125°C. However, on further heating toward the curing temperature, viscosity dropped and these additives sank to the bottom of the sample. After cure and post-cure, these additives remained at the bottom of the polymer. A cross-section of these samples showed some of the B<sub>4</sub>C and Hectorite at the top and middle of the sample, so uniform samples with these additives may be creatable by other means. The samples with boron and Cloisite 15A appeared homogenous and were therefore preferable for AO exposure.

### **II.1.ii. Hexcel 954-3 Cyanate Ester Resin**

Hexcel Satellite Products (Pheonix, AX) provided on a consignment basis a one pound quantity of hot melt 954-3 cyanate resin. The resin contained a pre-mixed curing agent, necessitating storage in a freezer to prolong the resin's shelf life. As with the BPA-based CE, keeping the 954-3 CE frozen also aided the processing ability in sample preparation. A non-analysis agreement was signed as requested by Hexcel, keeping the molecular structure of the resin classified. According to Hexcel, the 954-3 cyanate resin shows excellent resistance to moisture absorption, seen in Figure 17 in the Appendix, as well as resistance to outgassing, and micro-cracking. This CE resin follows a similar curing procedure to the BPA-based CE. Initially a dark brown solid, the Hexcel

resin turns an opaque light brown upon curing, while its surface exhibits a dark reddish-brown.

Hexcel 954-3 CE Curing Procedure

The curing procedure for the Hexcel 954-3 CE is identical to the curing procedure of the BPA-based CE with the following exception:

- Continue heating to 177°C, and then hold at this temperature for 2 hours to cure (as opposed to 1.5 hours for the BPA-based CE).

This procedure was utilized for the preparations of all the BPA-based CE samples.

Variations, shown in Table 3, were introduced by changing the temperatures at which the samples were placed in the oven and at which the system was purged.

Table 3: Hexcel 954-3 Cyanate Ester Samples

Additive (# samples)	% Additive (weight basis)	Start Temp. (°C)	Purge Temp. (°C)	Appearance
Pure (8)	0	25	125	Homogeneous, dark surface
B	3	25	125	Homogeneous
B	5	25	125	Homogeneous
B	5	100	170	Bubbles/rough surface
B	10	25	125	Homogeneous
B	15	25	125	Porous surface
B (5)	5	25	125	Homogeneous
B <sub>4</sub> C	2	25	125	Additive mostly settles
B <sub>4</sub> C	5	25	125	Additive mostly settles
B <sub>4</sub> C	10	25	125	Additive mostly settles
Hectorite	2	25	125	Smooth, mostly settles
Hectorite	5	25	125	Smooth, mostly settles
Hectorite	5	100	170	Porous, mostly settles
Cloisite	2	25	125	Smooth, homogeneous
Cloisite	4	25	125	Smooth, homogeneous
Cloisite	5	25	125	Smooth, homogeneous
Cloisite (2)	10	25	125	Smooth, homogeneous
Cloisite	15	25	125	Rough surface
Cloisite (3)	5	25	125	Smooth, homogeneous

Samples were made with all of the additives listed in Table 3. Those with B<sub>4</sub>C and Hectorite were not used in the studies to follow because the cured samples showed large variations in composition, apparently due to the settling of the additives. This occurrence is similar to that with the BPA-based CE samples with B<sub>4</sub>C and Hectorite and can be explained similarly. The samples with boron and Cloisite 15A appeared homogenous, and were therefore preferable samples to utilize in AO exposure.

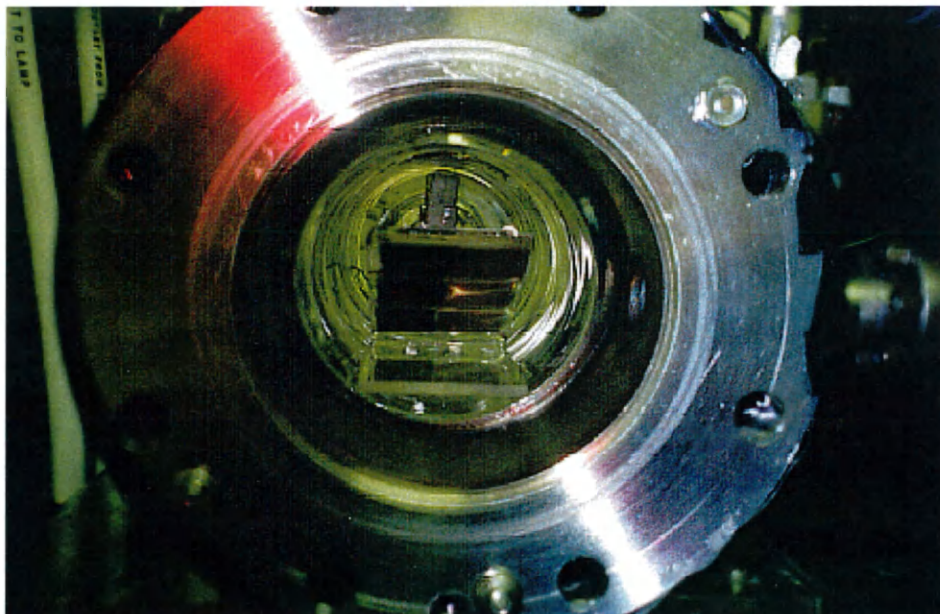
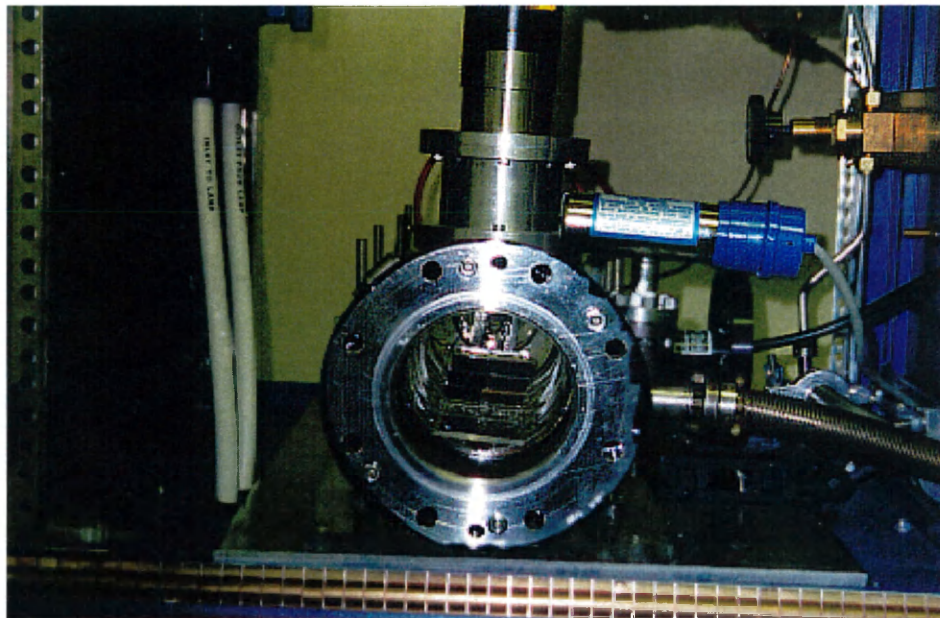
## **II.2. Ground-based Atomic Oxygen Plasma Generator**

While LEO Space Shuttle missions provide valuable information concerning AO, the high cost and time-consumption make alternative studies desirable. Ground-based oxygen plasma generators/reactors operating at low pressures allow for exposure results at less cost, and with a quicker turnaround time for data acquisition. In addition, the reactor's parameters can be controlled to simulate surface and bulk property changes experienced in LEO.

The oxygen plasma generator in the Structures and Materials Research Laboratory at NASA LaRC is a modified version of the system described and utilized by McCargo<sup>1,2</sup>. Both versions are shown in Figures 18 and 19 in the Appendix. A diagram and a picture of the oxygen plasma apparatus console are shown in Figures 20 and 21, respectively. The atomic oxygen plasma is generated in a 2-inch (diameter) x 6-inch (length) cylindrical quartz chamber. This plasma then passes through a 0.5-inch diameter opening into the quartz sample holder chamber that is 3-inches (diameter) x 7 inches (length). These two chambers are shown in Figures 22-24 in the Appendix. Figure 22 shows the components of the chambers, Figure 23 displays the chambers positioned within the oxygen plasma tube enclosure, and Figure 24 shows the chambers in use during an AO

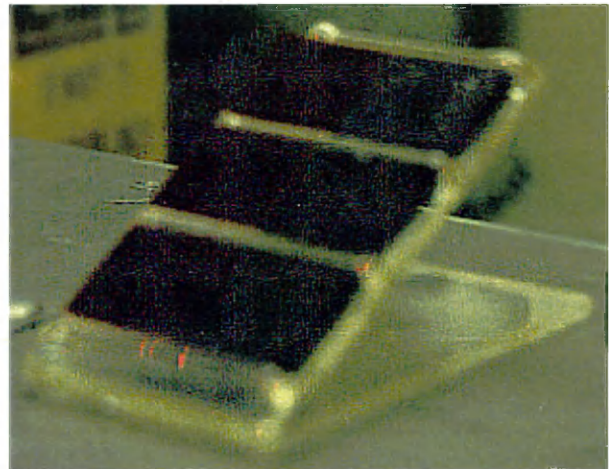
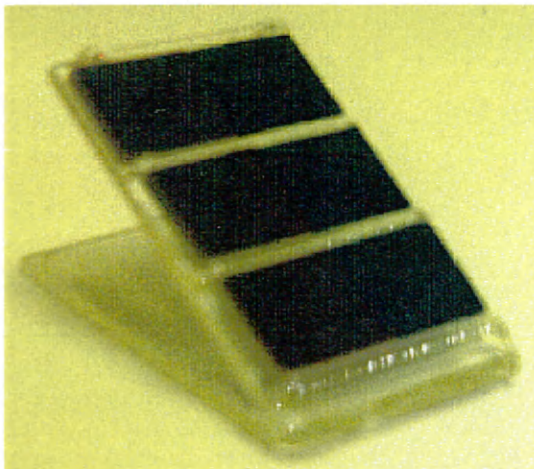
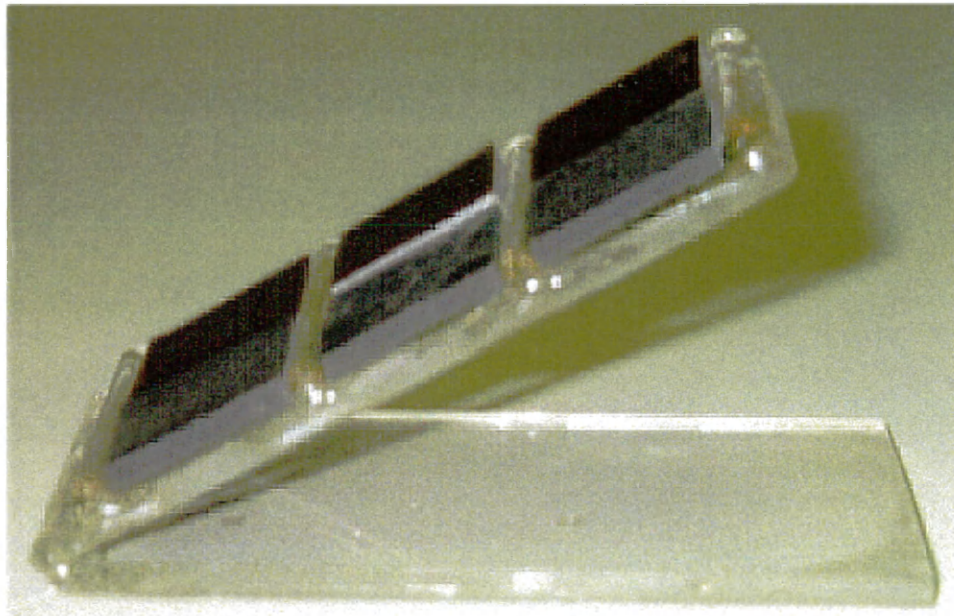
exposure. The cyanate ester resin samples lie on a flat quartz plate inclined about 30 degrees from the horizontal. The quartz plate is positioned near the center of the sample chamber, as shown in the pictures in Figure 25.

Figure 25: Quartz sample holder in AO chamber



This quartz structure can support 6 samples, 2 on each of the three rows. The length and width of the sample holder's base are 3 in. and 1.7 in. respectively. Pictures of the quartz sample holder are seen in Figure 26.

Figure 26: Quartz sample holder



The height of the sample holder is also approximately 1.7 inches, putting the top row of samples in the middle of the sample chamber. All surfaces of the sample holder

were cleaned with ethanol prior to placement into the chamber. AO was generated by a 13.56 MHz RF oscillator operating at 50 watts forward power and 0 watts reflected power. The AO flux output can be varied from  $10^{15}$  to  $10^{21}$  atoms/cm<sup>2</sup>•sec depending on the oxygen flow rate. A 150-Watt deuterium lamp with a magnesium fluoride vacuum window was positioned above the test specimen in the quartz sample chamber. This lamp can provide a UV output from 115nm to 400nm. Because only the effects of AO were studied in this research, the lamp was not utilized.

The reactor operating pressure, continuously monitored with a protected thermocouple gauge, was maintained at  $10^{-3}$  torr during all tests. The system temperature was measured by a thermocouple attached to the underside of the quartz sample chamber. After the completion of each exposure, the quartz reactor tubes were filled with dry nitrogen.

When the generator operated empty, a rose colored plasma was obtained, as shown in Figure 24 in the Appendix. When samples were exposed the plasma was blue with varying intensity. Knopf et al. made the same observation and determined the intensity of the plasma's color to be dependent on the rate of the degradation reaction and material outgassing<sup>2</sup>.

### **II.3. Atomic Oxygen Exposures and Mass Loss Determinations**

A Felker-Bay State Dresser Buehler Continuous Rim Diamond Blade wet saw was used to cut the samples into squares to fit the quartz sample holder. While all samples were approximately 0.2 cm thick, their surface areas differed due to the dimensions of the rows on the sample holder. Surface dimensions of the samples were recorded using a MAX-CAL Electronic Digital Caliper. All samples were cleaned with

ethanol prior to placement on the sample holder, which was also cleaned prior to placement in the AO generator. A Kimwipe tissue was dabbed with ethanol and then used to wipe all surfaces of the quartz plate and the unexposed samples. Between exposures, only the quartz plate was cleaned. Mass measurements were made with a Mettler Toledo Balance Model AT-201.

#### II.4. X-ray Photoelectron Spectroscopy

Dr. Frank Cromer of the Surface Analysis Laboratory at Virginia Tech (Blacksburg, VA) performed XPS analysis on two sets of samples with Mg  $K_{\alpha}$  x-rays using a Perkin Elmer 5400 instrument. Both survey and multiplex scans were done for all samples. The first set consisted of pure and 10% B<sub>4</sub>C BPA-based CE samples. The second set consisted of pure and 5%B Hexcel 954-3 CE samples. A control survey scan of the pure Hexcel 954-3 CE was obtained from a previous study<sup>3</sup>. These sets are listed in Table 4.

Table 4: Samples for XPS analysis

Set 1 (BPA-based CE)	Set 2 (Hexcel 954-3 CE)
Pure CE – Control	Pure CE – Exposed to AO for 18 hours
Pure CE – Exposed to AO	Pure CE – Exposed to AO for 104 hours
CE 10% B <sub>4</sub> C Front – Control	CE 5% B – Exposed to AO for 18 hours
CE 10% B <sub>4</sub> C Front – Exposed to AO	CE 5% B – Exposed to AO for 36 hours
CE 10% B <sub>4</sub> C Back – Control	CE 5% B – Exposed to AO for 68 hours
CE 10% B <sub>4</sub> C Back – Exposed to AO	CE 5% B – Exposed to AO for 104 hours

#### II.5. Scanning Electron Microscopy

SEM analysis of the polymer samples was conducted at the NASA Langley Research Center using a Hitachi S-510 Scanning Electron Microscope. All specimens

were coated with 5 nm of gold using an Anatech LTD Hummer VII Sputtering System. Images were captured on Polaroid Polapan 53 4x5 Black and White Instant Sheet Film. The samples investigated by SEM were those in Set 1 of the XPS samples.

## **II.6. Thermogravimetric Analysis**

The amorphous boron and Cloisite-15A additives in Hexcel 954-3 CE were investigated using TGA. Analysis was performed using a Shimadzu TGA-50 Thermogravimetric Analyzer with sample chamber environments of air and nitrogen. All samples were heated to a maximum temperature of 600°C.

It is common for smectite clays to retain water in their structure. Adsorbed, bound, and crystalline water are associated with the clay's structure by different means. Adsorbed water is found on the surface of clays in defect sites or at sites of bond breaks in the silicate structure. This type of water is held by relatively weak attractions and is present in small quantities proportional to the surface area of the clay. Surface water was eliminated by heating to temperatures of 80-90°C in a dry oven prior to TGA analysis. Bound water is found between smectite sheet layers, coordinated to cations. This type of water leaves the structure at temperatures ranging between 100-200°C. Crystalline water is found within the sheet layers, as hydroxyl (OH) units. Naturally, this type of water is firmly bound to the structure at temperatures up to 500°C.

## II.7. Summary of Studies

A summary of the different experimental methods by which the samples were studied, and their abbreviations are shown in Table 5. These abbreviations are used in the next section.

Table 5: Summary of Studies

Abbreviation	Sample	AO Exposure	TGA	SEM	XPS
<i>BPA-based Cyanate Ester Samples</i>					
BPA0	Pure	X		X	X
BPA3B	3 wt. % boron	X			
BPA7B	7 wt. % boron	X			
BPA10BC	10 wt. % B <sub>4</sub> C	X		X	X
<i>Hexcel 954-3 Cyanate Ester Samples</i>					
H0	Pure	X	X		X <sup>3</sup>
H5B	5 wt. % boron	X	X		X
H10B	10 wt. % boron	X	X		
H5C	5 wt. % Cloisite-15A	X	X		
H10C	10 wt. % Cloisite-15A	X	X		

<sup>1</sup> M. McCargo, R.E. Dammon, J.C. Robinson and R.J. Milligan, *Effects of Combined Ultraviolet and Oxygen Plasma Environment of Spacecraft Thermal Control Materials*, Proceedings, International Symposium on Environmental and Thermal Systems for Space Vehicles; October 1983.

<sup>2</sup> P.W. Knopf, R.J. Martin, R.E. Dammon, and M. McCargo, *Correlation of Laboratory and Flight Data for the Effects of Atomic Oxygen on Polymeric Materials*, AIAA paper 85-1066, 20<sup>th</sup> Thermophysics Conference; January 1985.

<sup>3</sup> J. L. Weisman, B.S. Thesis, The College of William and Mary, 1999.

## CHAPTER 3: RESULTS

### III.1. Atomic Oxygen Exposures and Mass Losses

To account for flux differences experienced on different positions on the sample holder, the following abbreviations, shown in Table 6, are used to note the location of experimental samples:

Table 6: Abbreviations for sample locations on sample holder

UL Upper Left	UR Upper Right
ML Middle Left	MR Middle Right
LL Lower Left	LR Lower Right

The first set of AO exposures involved three samples: pure BPA-based CE, BPA-based CE with 3 wt. % boron, and BPA-based CE with 7 wt. % boron. Unlike the following exposures, these samples were cut using a handsaw. As a result, the pure sample assumed an irregular shape due to chipping. The samples received 24 hours of exposure with an oxygen flow rate of .28 standard cubic centimeters per minute (SCCM), giving a fluence on the order of  $10^{15}$ . Table 7 shows the mass loss data for these samples.

Table 7: Mass Losses for BPA-based CE {first set of AO exposures}

Sample	Initial mass (grams)	Final mass (grams)	Mass loss (mg)
BPA0 - UL	0.51047	0.50537	5.1
BPA3B - MR	1.02376	1.01663	7.13
BPA7B - UR	0.98639	0.98013	6.26

The irregular shape of the pure sample evidently had an effect on the reaction between AO and the surface of the polymer. Therefore the surface areas of samples were measured in all subsequent exposures and mass losses were reported as mass loss per surface area in mg/cm<sup>2</sup>. The diminished mass loss of the 7 wt. % boron sample over the 3 wt. % boron sample is evidence that the additive offers some protection to the polymer from AO erosion.

The second set of AO exposures involved three samples: pure BPA-based CE, and two samples of BPA-based CE with 10 wt. % B<sub>4</sub>C. One of the two was exposed on the front surface, while the other was exposed on the back surface. This was done because the majority of the B<sub>4</sub>C visually appeared to have settled to the bottom of the sample. The samples received approximately 200 hours of exposure during which the AO plasma generator experienced difficulty in maintaining a consistent flux. When the apparatus was stabilized, another 168 hours of exposure was performed with an oxygen flow rate of .28 SCCM, giving a fluence on the order of 10<sup>15</sup>. Table 8 shows the mass loss data for these samples in addition to their surface areas (SA).

Table 8: Mass Losses for BPA-based CE {second set of AO exposures}

Sample	SA (cm <sup>2</sup> )	Mass loss (mg)	Mass loss/SA (mg/cm <sup>2</sup> )
BPA0 - MR	3.222	105	32.5
BPA10BC Front - UL	3.290	227	69.1
BPA10BC Back - UR	3.623	94	25.9

The contrast between the mass losses for the front and back exposed samples of the BPA-based CE with 10%B<sub>4</sub>C supports the visible evidence that the majority of the B<sub>4</sub>C settles to the bottom of the polymer during processing.

The third set of AO exposures involved six samples: 2 samples of pure Hexcel 954-3 CE, 2 samples of Hexcel 954-3 CE with 5 and 10% boron respectively, and 2

samples of Hexcel 954-3 CE with 5 and 10% Cloisite-15A respectively. In this set of samples, the formation of an oxidized protective layer was studied via successive exposures. The samples were exposed three times at 12-hour durations and masses were measured before and after each exposure. After the first 12-hour exposure, the middle row notch on the sample holder broke and had to be repaired by the glass laboratory at NASA LaRC. Once returned, the middle and lower rows had different dimensions, so the surface dimensions of the samples in these rows had to be altered to fit the sample holder. The samples received a total of 36 hours of exposure with an oxygen flow rate of .28 SCCM giving a fluence on the order of  $10^{15}$ . Table 9 shows the mass loss data for these samples in addition to their surface areas.

Table 9: Mass Losses for Hexcel 954-3 CE {third set of AO exposures}

Sample	SA (cm <sup>2</sup> )		Mass loss/SA (mg/cm <sup>2</sup> )		
	1st Exposure	2nd and 3rd Exposures	1st Exposure (0-12 hrs)	2nd Exposure (12-24 hrs)	3rd Exposure (24-36 hrs)
H5B - UL	4.080	4.080	2.48	2.47	0.93
H10B - UR	4.123	4.123	2.51	2.44	0.55
H0 - ML	3.142	1.933	2.23	5.22	1.62
H5C - MR	3.010	1.805	0.69	3.87	1.27
H0 - LL	3.170	2.455	1.85	6.80	1.80
H10C - LR	3.546	2.461	0.64	5.07	1.05

The fourth set of AO exposures involved six pure Hexcel 954-3 CE samples. In this set of samples, the differences in flux experienced on the six positions of the sample holder were studied. The samples received 12 hours of exposure with an oxygen flow rate of .28 SCCM giving a fluence on the order of  $10^{15}$ . Table 10 shows the mass loss data for these samples as well as their surface areas.

Table 10: Mass Losses for Hexcel 954-3 {fourth set of AO exposures}

Sample	SA (cm <sup>2</sup> )	Mass loss/SA (mg/cm <sup>2</sup> )
H0 - UL	3.470	3.66
H0 - UR	3.722	3.61
H0 - ML	3.183	3.11
H0 - MR	2.857	3.19
H0 - LL	3.856	2.94
H0 - LR	3.622	2.59

The fifth set of AO exposures involved six samples: 2 samples of pure Hexcel 954-3 CE, 2 samples of Hexcel 954-3 CE with 5 and 10 wt. % boron, respectively, and 2 samples of Hexcel 954-3 CE with 5 and 10 wt. % Cloisite-15A, respectively. This exposure, identical to the third exposure, was done because the change in surface dimensions mentioned in the third exposure seemed to have a variable effect on the degree of surface recession those samples experienced. The samples were exposed twice at 18-hour durations and masses were taken before and after each exposure. The samples received a total of 36 hours of exposure with an oxygen flow rate of .28 SCCM giving a fluence on the order of 10<sup>15</sup>. Table 11 shows the mass loss data and SA for these samples.

Table 11: Mass Losses for Hexcel 954-3 CE {fifth set of AO exposures}

Sample	SA (cm <sup>2</sup> )	Mass loss/SA (mg/cm <sup>2</sup> )	
		1st Exposure (0-18 hrs)	2nd Exposure (18-36 hrs)
H5B - UL	3.603	1.86	1.16
H10B - UR	3.724	1.31	0.41
H0 - ML	3.293	2.31	1.74
H5C - MR	3.097	1.53	0.88
H0 - LL	3.716	2.00	1.50
H10C - LR	3.661	1.07	0.51

The sixth set of AO exposures involved ten samples: 5 samples of pure Hexcel 954-3 CE and 5 samples of Hexcel 954-3 CE with 5 wt. % boron. In this set of samples, the formation of an oxidized protective layer was studied via successive exposures. In addition, some of these samples were analyzed by XPS to would provide insight on the nature of the reaction of AO with boron over an extended period of time. Four individual exposures were conducted of variable durations. The first lasted 18 hours, the second 36, the third 22, and the fourth and final exposure lasted 45 hours. Masses of all samples were measured before and after each exposure. Table 12 shows abbreviations for the samples and their respective locations on the sample holder to simplify the data presentation.

Table 12: Abbreviations used in the sixth set of exposures

UL: 1 and 1' Pure Hexcel 954-3 CE	UR: 4 and 4' Hexcel 954-3 + 5 wt. %B
ML: 2 and 2' Pure Hexcel 954-3 CE	MR: 5 and 5' Hexcel 954-3 + 5 wt. %B
LL: 3 Pure Hexcel 954-3 CE	LR: 6 Hexcel 954-3 + 5 wt. %B

Samples 1,2,3,4,5,6 were all initially exposed for 18 hours. Samples 1 and 4 were then removed and the remaining samples were exposed for another 18 hours. Therefore, samples 1 and 4 received a total of 18 hours AO exposure. After the second 18-hour exposure, samples 2 and 5 were removed and replaced with samples 2' and 5'. Therefore, samples 2 and 5 received a total of 36 hours AO exposure. In addition samples 1' and 4' were placed in the empty upper row. This set of samples was then exposed for 23 hours. After the 23-hour exposure, the masses of all the samples were determined, and then the samples were returned for a final 45 hours of AO exposure. After the 45-hour exposure, all samples were removed from the AO chamber. Samples 1', 2', 4', and 5' received a

total of 68 hours AO exposure, while samples 3 and 6 received a total of 104 hours of AO exposure.

During all of these exposures, the oxygen flow rate was stepped up to .48 SCCM, giving a fluence on the order of  $10^{21}$ . Table 13 shows the mass loss data for these samples. All mass losses have units of  $\text{mg}/\text{cm}^2$ , and all time frames of AO exposures are in hours.

Table 13: Mass Losses for Hexcel 954-3 CE {sixth set of AO exposures}

Sample	SA ( $\text{cm}^2$ )	Total Hours Exp.	Mass loss/SA ( $\text{mg}/\text{cm}^2$ ) and respective time frames (hrs)									
			Mass Loss	Time Frame	Mass Loss	Time Frame	Mass Loss	Time Frame	Mass Loss	Time Frame	Mass Loss	Time Frame
<b>Pure 954-3</b>												
1 UL	3.830	18	4.90	0-18	---	---	---	---	---	---	---	---
2 ML	3.377	36	13.30	0-36	---	---	---	---	---	---	---	---
3 LL	3.709	104	9.80	0-36	8.69	36-59	2.48	59-104	18.49	0-59	20.97	0-104
1' UL	3.108	68	16.02	0-23	2.73	23-68	18.75	0-68	---	---	---	---
2' ML	2.379	68	14.77	0-23	3.34	23-68	18.11	0-68	---	---	---	---
<b>5% B</b>												
4 UR	3.627	18	2.62	0-18	---	---	---	---	---	---	---	---
5 MR	3.317	36	7.92	0-36	---	---	---	---	---	---	---	---
6 LR	3.209	104	5.72	0-36	5.10	36-59	1.68	59-104	10.82	0-59	12.50	0-104
4' UR	2.670	68	10.63	0-23	2.03	23-68	12.66	0-68	---	---	---	---
5' MR	2.862	68	9.20	0-23	1.03	23-68	10.22	0-68	---	---	---	---

### III.2. TGA Analysis

The samples investigated by TGA include pure Hexcel 954-3 CE, Hexcel 954-3 CE + 5 wt. % boron, Hexcel 954-3 CE + 5 wt. % Cloisite-15A, Hexcel 954-3 CE + 10 wt. % boron and Hexcel 954-3 CE + 10 wt. % Cloisite-15A. The thermograms of the samples and their accompanying temperature programs are shown in Figures 27-32 in the Appendix. The additives in the matrices prove to have little effect on the thermal stability of the polymer. As expected, no differences in thermal decomposition resulted from switching between air and nitrogen environments.

### III.3. SEM Analysis

The samples investigated by SEM include pure BPA-based CE control and AO exposed, BPA-based CE+10 wt. % B<sub>4</sub>C back surface control and AO exposed, and BPA-based CE+10 wt. % B<sub>4</sub>C front surface control and AO exposed. Their respective SEM photographs are shown in Figures 33 through 45. All photographs were taken using 25 kV electrons. The degree of magnification is listed in each figure.

### III.4. XPS Analysis

Figures 46 through 51 show the full spectra of the first set of cyanate ester samples that were analyzed by Dr. Cromer of the Surface Analysis Center at Virginia Tech. The control and AO exposed carbon, oxygen, nitrogen, and boron peaks are shown on separate spectra, as seen in Figures 52 through 73. Tables 14, 15, and 16 show the elemental concentrations on the surfaces of pure BPA-based CE control and AO exposed, BPA-based CE+10 wt. % B<sub>4</sub>C back surface control and AO exposed, and BPA-based CE+10 wt. % B<sub>4</sub>C front surface control and AO exposed, respectively.

Table 14: XPS pure BPA-based CE Control and AO Exposed

Element	Control Concentration (%)	AO Exposed Concentration (%)
C 1s	76.87	57.01
O 1s	15.19	28.29
N 1s	1.51	8.92
Si 2p	6.44	0.00
B 1s	0.00	0.00
P 2p	0.00	2.81
F 1s	0.00	1.21
Co 2p	0.00	1.77

Table 15: XPS BPA-based CE + 10 wt. %B<sub>4</sub>C Back Control and Back AO Exposed

Element	Control Concentration (%)	AO Exposed Concentration (%)
C 1s	71.51	23.09
O 1s	19.09	33.72
N 1s	3.36	4.37
Si 2p	5.64	6.87
B 1s	0.00	18.61
P 2p	0.00	1.40
F 1s	0.40	8.36
Co 2p	0.00	0.00
Al 2p	0.00	2.27
Ca 2p	0.00	1.31

Table 16: XPS BPA-based CE + 10 wt. % B<sub>4</sub>C Front Control and Front AO Exposed

Element	Control Concentration (%)	AO Exposed Concentration (%)
C 1s	74.75	50.02
O 1s	15.66	29.07
N 1s	2.08	7.27
Si 2p	6.46	0.00
B 1s	0.00	7.04
P 2p	0.00	3.54
F 1s	1.05	0.81
Co 2p	0.00	2.25

Figures 74 through 80 show the full spectra of the second set of cyanate ester samples that were analyzed by Dr. Cromer of the Surface Analysis Center at Virginia Tech. The AO exposed carbon, oxygen, nitrogen, and boron peaks are shown on separate

spectra, as seen in Figures 81 through 102. Tables 17 and 18 show the elemental concentrations on the surfaces of pure Hexcel 954-3 CE control and AO exposed 18 and 104 hours, and Hexcel 954-3 CE+5 wt. % boron exposed 18, 36, 68, and 104 hours, respectively.

Table 17: XPS Pure Hexcel 954-3 CE Control and AO Exposed 18 and 104 hours

Element	Concentration (%) - Control	Concentration (%) - 18 hours AO Exposed	Concentration (%) - 104 hours AO Exposed
C 1s	82.48	59.68	63.66
O 1s	11.78	24.21	21.11
N 1s	1.14	9.55	4.50
B 1s	0.00	0.00	0.00
Na 1s	0.00	2.45	2.06
F 1s	0.00	1.44	4.98
Cu 2p	0.00	1.37	1.75
Zn 2p3	0.00	0.03	0.27
S 2p	0.00	0.89	1.65
Si 2p	4.60	0.39	0.02

Table 18: XPS Hexcel 954-3 CE + 5 wt. % Boron AO Exposed 18, 36, 68, and 104 hours

Element	Concentration (%)			
	18 hours	36 hours	68 hours	104 hours
C 1s	49.38	56.38	47.34	49.57
O 1s	22.81	22.86	20.75	18.47
N 1s	5.74	4.38	4.61	4.09
B 1s	18.32	9.45	22.70	22.93
Na 1s	1.71	2.24	1.62	1.66
F 1s	0.32	1.70	0.77	1.50
Cu 2p	0.30	0.62	0.77	0.76
Zn 2p3	0.00	0.15	0.80	0.54
S 2p	0.69	1.39	0.35	0.31
Si 2p	0.73	0.81	0.28	0.18

## CHAPTER 4: DISCUSSION

### IV.1. Polymer + Additive Preparation Success

The Hexcel 954-3 Cyanate Ester samples with boron and Cloisite-15A, respectively, appear to be the most promising combinations. These samples were the most homogeneous of the lot, characterized by smooth surfaces and uniform dispersion of the additives through the polymer as evidenced by their cross-sections.

Both the Hexcel 954-3 CE and BPA-based CE samples with boron carbide and Hectorite proved unsuccessful. The large difference in density between these additives and the CE coupled with the low viscosity of the CE directly preceding the onset of cross-linking resulted in inhomogeneous samples in which the majority of the additive lay at the bottom surface.

BPA-based CE samples with boron and Cloisite-15A, respectively, were successful in terms of homogeneity. While those samples with Cloisite-15A were not exposed to AO, those with boron showed positive results in the first set of AO exposures. Although these samples were fit for further study, efforts were made to focus on the space-certified Hexcel 954-3 CE instead.

### IV.2. Analysis of BPA-based CE + Boron Samples

#### IV.2.i. Mass Loss

The first set of AO exposures involved three BPA-based CE samples, as shown in Table 7. The BPA-based CE sample with 3 wt. % boron lost 7.13 mg., while the BPA-based CE sample with 7 wt. % boron lost 6.26 mg. A greater difference in mass loss between these two samples was expected. Surprisingly, the pure BPA CE sample lost 5.1 mg., the least of the three samples. As mentioned, this pure sample assumed an irregular

shape due to chipping when it was cut to fit the sample holder. These numbers prove inconclusive, and would possibly have been more meaningful if the surface areas of the samples had been taken prior to exposure. This step was therefore taken in all subsequent exposures. In addition, the uniformity of flux experienced at the six positions on the sample holder was brought into question.

### **IV.3. Analysis of BPA-based CE + B<sub>4</sub>C Samples**

#### **IV.3.i. Mass Loss**

The second set of AO exposures involved three BPA-based CE samples, as shown in Table 8. In a pair of BPA-based CE samples with 10% B<sub>4</sub>C, one was exposed to AO on its front surface while the other was exposed on its bottom face. The former lost 2.7 times as much mass per surface area (mass/SA) as the latter. This is consistent with the visible observation that the majority of the B<sub>4</sub>C settled to the bottom of these samples. Although the pure BPA-based CE sample lost 1.25 times as much mass/SA as the sample with 10% B<sub>4</sub>C that was exposed on its back surface, it surprisingly lost about half the mass/SA that the 10% B<sub>4</sub>C sample that was exposed on its front surface did. SEM analysis was performed to see if surface morphology could explain this apparent disparity.

#### **IV.3.ii. SEM Analysis**

The pure BPA-based CE control sample, seen in Figure 33 in the Appendix, has a very smooth appearance, a stark contrast to the surface of the AO exposed pure BPA-based sample shown in Figure 34 in the Appendix. The exposed surface has a cracked appearance, indicative of erosion. The erosion, or 'etching' as it is commonly known, is more pronounced under higher magnification, shown in Figure 35 in the Appendix.

Like the pure control sample, the BPA-based CE + 10 wt. % B<sub>4</sub>C back surface control in Figure 36 in the Appendix appears smooth and homogeneous. There is a small mark present that is similar to the marks on the pure control that are likely attributable to dust. Under higher magnification in Figure 37 in the Appendix, the mark is seen more closely but its identity is not any clearer. The 10 wt. % B<sub>4</sub>C back exposed surface in Figures 38 and 39 is very different from the exposed surface of the pure BPA-based CE. While etching seems evident, it is not as uniform as the case was for the pure sample. The photographs in Figures 38 and 39 probably depict B<sub>4</sub>C particles in a variety of orientations. Based on its aspect ratio of 46, the dimensions of the B<sub>4</sub>C particles are on the order of 300 x 570 microns. These approximate dimensions agree with the images in Figures 38 and 39, taking into account that some of the B<sub>4</sub>C particles may be oriented towards the viewer. In addition, the cracked polymer domains that were seen in the pure exposed sample are not seen in these photographs. This once again suggests that B<sub>4</sub>C is the major component in the lower areas of the sample.

Once again, the appearance of the BPA-based CE + 10 wt. % B<sub>4</sub>C front surface control in Figures 40 and 41 is smooth, albeit the presence of more dust particles. A significant change is seen in the SEM photographs of the exposed 10 wt. % B<sub>4</sub>C front surfaces, shown in different magnifications in Figures 42 through 45 in the Appendix. It is evident in Figure 42 that there are two distinct components of the upper areas of the sample. Figure 43 further clarifies these constituents. The cracked appearance that characterized the pure exposed BPA-based sample is present in Figure 43, along with scattered large spheres, some of which exhibit voids on their surfaces. These spheres,

presumably bubbles, are better seen under higher magnification in Figures 44 and 45.

The surface voids may be areas on the bubbles that have popped open.

#### **IV.3.iii. XPS Analysis**

XPS analysis revealed the elemental concentrations of the control and exposed surfaces of the pure, 10 wt. % B<sub>4</sub>C back side, and 10 wt. % B<sub>4</sub>C front side BPA-based CE samples. The elemental concentrations are the primary focus of this analysis. The identity of the individual peaks is secondary because the chemical structure of the BPA-based CE is proprietary. In all cases, the strongest trend is a decrease in the carbon peak, and an increase in the oxygen peak, indicating that oxygen is incorporating itself into the polymer surface.

The AO exposed pure BPA-based CE surface, relative to the control, shows an increase in oxygen from 15% to 28%, and a decrease in carbon from 77% to 57% (Table 14). Comparisons of the oxygen peaks in the control (Figure 53) and exposed (Figure 56) spectra show a shift to a higher binding energy, correlating to a change in the nature of the oxygen bonding. This oxygen peak must represent the two types of oxygen that are present in cyanurates: O-C≡N and Ar-O-Ar. The shift to higher binding energies may represent more double bonded oxygens, such as those found in carbonyl groups. But a comparison of the carbon peaks in the control (Figure 52) and exposed (Figure 55) spectra proves more interesting. In both cases, there are two carbon peaks, one at 285 eV, and a second at 289 eV. The enhancement of the peak at 289 eV indicates an increase in a carbonyl type carbon, possibly N-C=O. This is consistent with the downfield shift exhibited by the oxygen peak.

The increase in nitrogen concentration is also of some significance. More than likely, the majority of the nitrogen stems from the dry nitrogen that flushes through the system after each exposure, which can deposit on the surface of the polymer. Another possibility is that the AO reaction with the polymer surface results in some nitrogen bond dissociation in the cyanate ester, evolving some nitrogenous compounds. These compounds can then re-deposit on the surface as contamination.

The presence of other elements such as phosphorous, fluorine, cobalt, silicon, aluminum, and calcium was unexpected. It is very likely that these elements were introduced during the AO exposures. For example, in the description of the ground-based AO plasma generator it was mentioned that a deuterium lamp with a magnesium fluoride vacuum window was positioned above the test specimens in the quartz sample chamber for available UV exposure. The vacuum window could be the source of fluorine, while other components of the AO chamber tube enclosure may give rise to the other miscellaneous peaks. For example, NASA LaRC researchers Bill Gray and Dr. Kyo Song believe the o-rings in the AO generator are possible contamination sources.

When comparing the control and exposed surfaces of the BPA-based CE + 10 wt. % B<sub>4</sub>C back side samples, the carbon concentration drops sharply from 72% to 23% (Table 15). From Figures 58 and 62, it is evident that a large change occurs in the relative sizes of the 285 eV and 289 eV peaks. The former has diminished relative to the latter. The oxygen concentration increases from 19% to 34%, and its peaks also show a slight shift to a higher binding energy (Figures 59 and 63). The behavior of the carbon and oxygen peaks once again supports carbonyl formation on the surface of the polymer. The boron peak proves to be interesting as well. Relative to the control, the boron

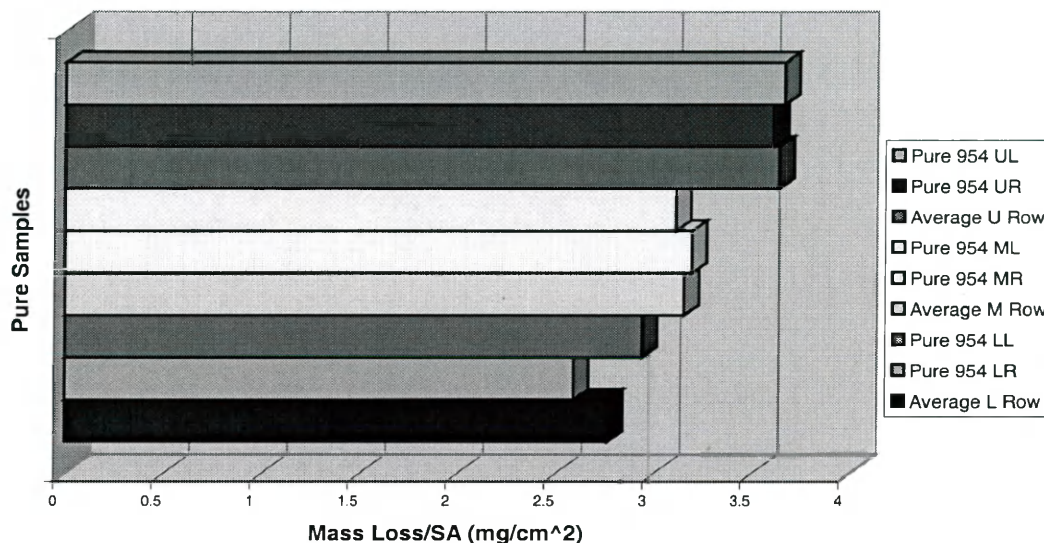
concentration increases from 0% to 19% (Figures 61 and 65). The initial absence of boron is consistent with the SEM photograph of the control sample in Figures 36 and 37. The formation of oxidized boron compounds could also explain the shift in the oxygen peaks.

The carbon concentration drops less sharply, from 75% to 50%, in the BPA-based CE + 10 wt. % B<sub>4</sub>C front side than it did in the back side sample. Figures 66 and 70 show the enhancement of the carbonyl carbon peak at 289 eV. The oxygen concentration increases from 16% to 29%, and exhibits a similar shift (Figures 67 and 71) to the samples mentioned already. Once again, the boron peak proves interesting (Figures 69 and 73). Its initial absence is consistent with the surface morphology depicted in Figures 40 and 41. The fact that the boron concentration after AO exposure is less on the front surface (7%) than the back surface (19%) is consistent with the settling of the boron carbide (Tables 15 and 16). In addition, the loss of carbon in the pure AO exposed sample is very similar to the loss of carbon in the 10 wt. % B<sub>4</sub>C front surface sample, yet strikingly different from the loss of carbon in the 10 wt. % B<sub>4</sub>C back surface sample. This also supports the assertion that boron carbide settles in the BPA-based CE.

#### **IV.4. Deviations in Flux on Sample Holder**

As shown in Table 10, the mass losses per surface area varied when all pure samples of the Hexcel 954-3 CE were placed on the sample holder. Figure 103 depicts this occurrence.

Figure 103: Mass Losses per Surface Area of Pure Hexcel 954-3 CE Samples



As seen in Figure 103, the greatest mass losses occurred in the top row of the sample plate. This may be due to the fact that the top row is vertically centered in the AO chamber tube, a region of maximum flux. Therefore the fluence experienced by a sample in the AO chamber during an exposure test has a dependence on its position on the sample plate. As a result, two methods of corrections were developed which both produced mass losses of arbitrary units.

#### IV.4.i. First Method of Correction

The first method entails two corrections, one for the difference in fluence experienced by the rows on the sample plate and another for the difference in fluence experienced by the columns on the sample plate. In the first step, the mass loss per surface area for a given sample is divided by the mass loss per surface area of the pure Hexcel 954-3 CE sample in the ML position of that set. This position was selected for

two reasons; firstly, all the exposures involving the Hexcel 954-3 CE had a pure sample in this position, and secondly, the middle row in the fourth set of exposures experienced a mass loss per surface area that approached an average between that experienced by the upper and lower rows (Figure 103). Therefore the first step involves data from the set of AO exposure in question. In the second step, the quotient from the first step is multiplied by the ratio of the average mass loss per surface of the middle row to the average mass loss per surface area of the respective row. Therefore the second step involves data from the fourth set of exposures only. As a result of these two steps, the pure Hexcel-954-3 CE in the ML position is a standard to which all the other samples in the set are relative.

#### **IV.4.ii. Second Method of Correction**

In the second method, the mass loss per surface area of a given sample is relative to the mass loss per surface area of the correspondingly positioned pure Hexcel 954-3 CE sample from the fourth set of AO exposures. This is done by dividing the mass loss per surface area of a given sample by the mass loss per surface area of the correlating pure sample in the fourth set of AO exposures.

#### **IV.5. Analysis of the Third and Fifth Sets of AO Exposures**

##### **IV.5.i. Mass Loss**

The third and fifth sets of AO exposures involved the same types of samples, so it is prudent to discuss them together. The samples exposed, shown in Tables 9 and 11, were all of Hexcel 954-3 CE: two pure, two with 5 wt. % and 10 wt. % boron, respectively, and two with 5 wt. % and 10 wt. % Closite-15A, respectively. The corrected mass losses for the third set of AO exposures are shown in Table 19.

Table 19: Corrected Mass Losses for the Third Set of AO Exposures

Sample	First Correction Method			Second Correction Method		
	1st Exposure (0-12 hours)	2nd Exposure (12-24 hours)	3rd Exposure (24-36 hours)	1st Exposure (0-12 hours)	2nd Exposure (12-24 hours)	3rd Exposure (24-36 hours)
H5B - UL	0.96	0.41	0.5	0.68	0.67	0.25
H10B - UR	0.97	0.41	0.29	0.70	0.68	0.15
H0 - ML	1	1	1	0.72	1.68	0.52
H5C - MR	0.31	0.74	0.78	0.22	1.21	0.40
H0 - LL	0.94	1.48	1.27	0.63	2.31	0.61
H10C - LR	0.33	1.1	0.74	0.25	1.96	0.40

The corrected mass losses are depicted in Figures 104 and 105.

Figure 104: Mass Losses for Third Set of AO Exposures Using the First Correction Method

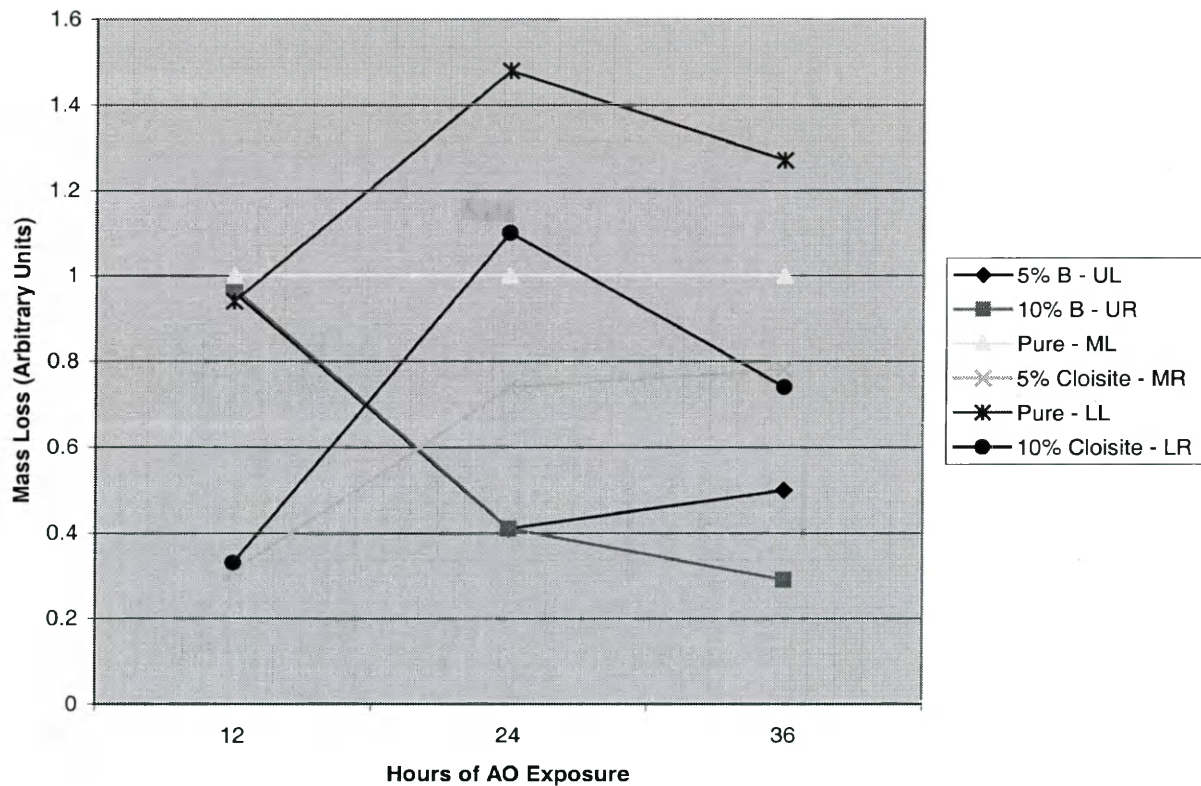
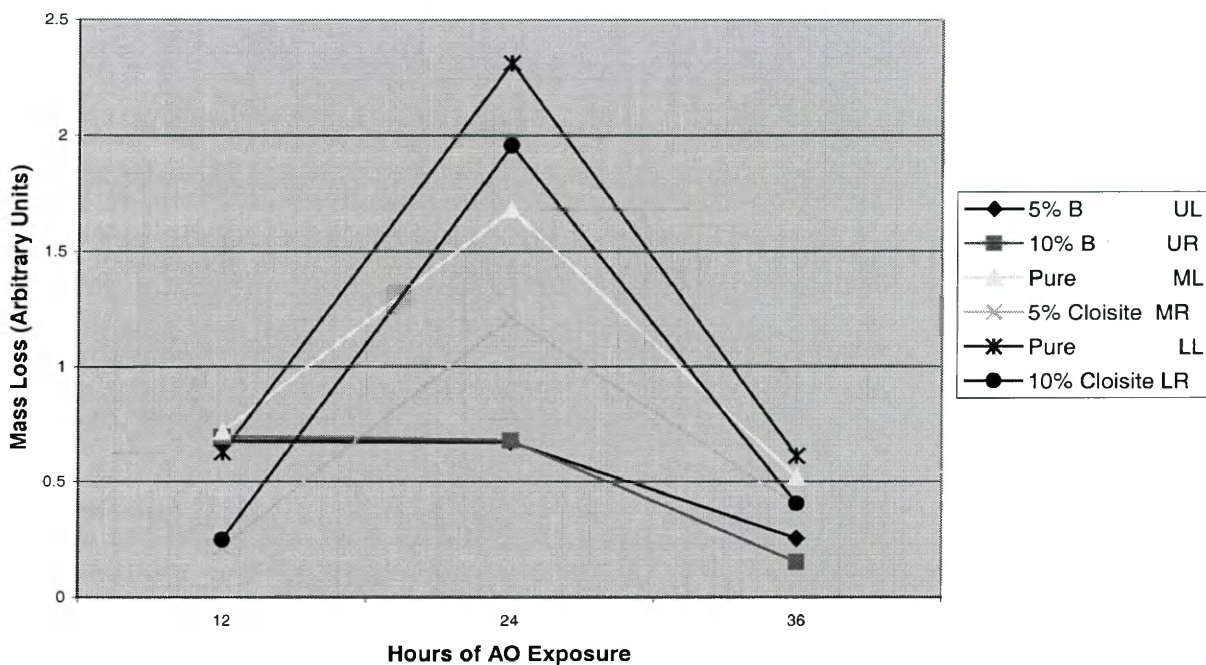


Figure 105: Mass Losses for Third Set of AO Exposures Using the Second Correction Method



The 5 and 10 wt. % boron samples exhibited similar mass losses to each other in the first and second AO exposures, as did the 5 and 10 wt. % Cloisite-15A samples. This was unexpected, because the increased additive composition should have offered more protection to the polymer. Similar mass losses indicate similar chemical compositions on the top surfaces of these polymers, possibly explained by the settling of additional boron past 5 wt. %. In the third 12-hour exposure, the 10 wt. % boron sample finally showed a smaller mass loss than the 5 wt. % boron sample. The other four samples are comparable only across the second and third exposures. The change in surface areas of these samples between the first and second exposures had a drastic effect; mass loss actually increased after the first exposure for the 5 and 10 wt. % Cloisite-15A samples.

The only other valuable information from this exposure is obtained by comparing the mass losses of the different samples across the first exposure. In each

method of correction, the Cloisite-15A samples lose the least mass of the lot. This trend does not hold in the other exposures, in which the boron samples lose the least mass. Because of the inconclusive results from this set of exposure, the experiment was performed again in the fifth set of AO exposures.

The fifth set of AO exposures involved the same type of samples in the same positions on the sample plate as the third set of AO exposures. The corrected mass losses are shown in Table 20.

Table 20: Corrected Mass Losses for the Fifth Set of AO Exposures

Sample	Corrected Mass Losses (unitless)			
	First Correction Method		Second Correction Method	
	1st Exposure (0-18 hrs)	2nd Exposure (18-36 hrs)	1st Exposure (0-18 hrs)	2nd Exposure (18-36 hrs)
H5B - UL	0.70	0.58	0.51	0.32
H10B - UR	0.49	0.20	0.36	0.11
H0 - ML	1.00	1.00	0.74	0.56
H5C - MR	0.66	0.50	0.48	0.28
H0 - LL	0.99	0.98	0.68	0.51
H10C - LR	0.53	0.33	0.41	0.20

The corrected mass losses are depicted in Figures 106 and 107.

Figure 106: Mass Losses for Fifth Set of AO Exposures Using First Correction Method

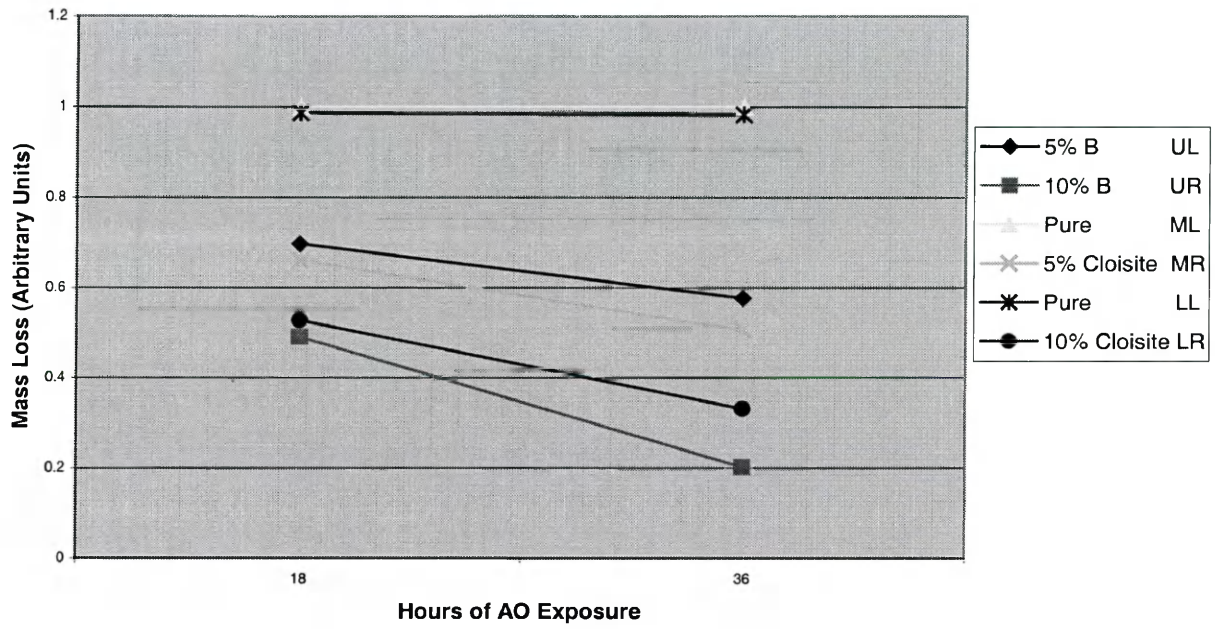
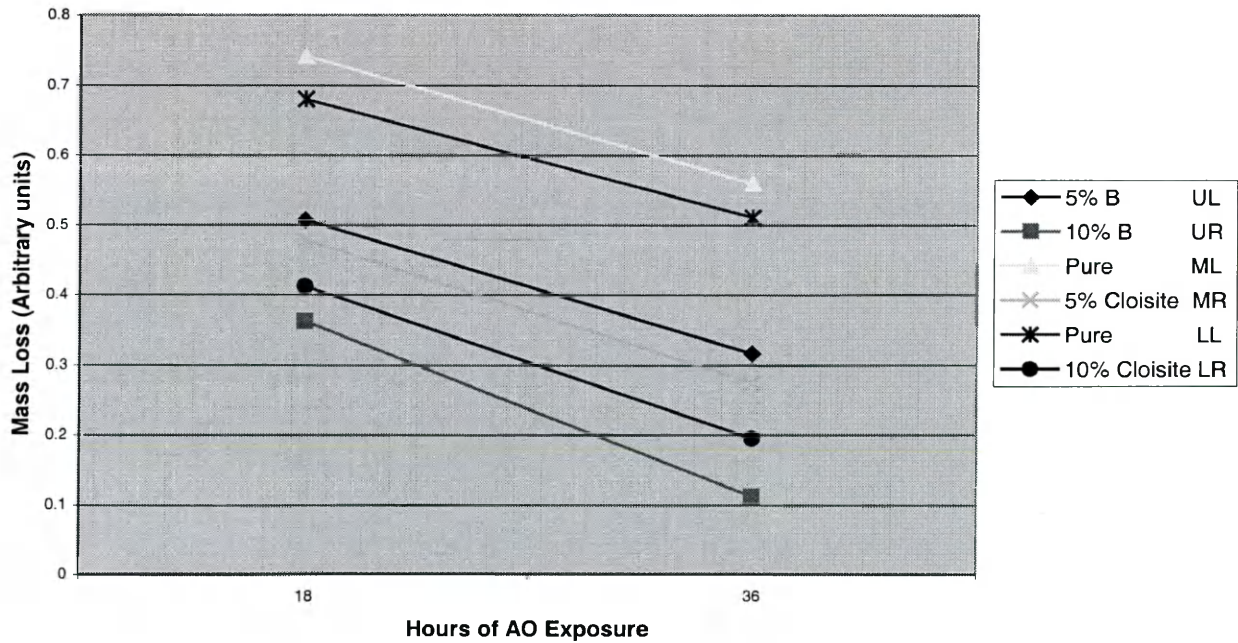


Figure 107: Mass Losses for Fifth Set of AO Exposures Using Second Correction Method



Relative to the third set of AO exposures, the mass losses observed in the fifth set of AO exposures look more significant. By the first method of correction, the pure samples agree very closely in their mass loss behaviors. The 5 and 10 wt. % boron and Cloisite-15A samples all show a decrease in mass loss after the first exposure. This supports the idea that the additive is protecting the underlying polymer by reacting with AO and forming a chemically stable additive oxide layer. In both pairs, the 10 wt. % samples lose less mass than the 5 wt. % samples, supporting the idea that the amount of protection from AO erosion is related to the concentration of the additive. Interestingly, the 5 wt. % Cloisite-15A sample outperforms the 5 wt. % boron sample, but the 10 wt. % boron sample outperforms the 10 wt. % Cloisite-15A sample in terms of diminished mass loss.

The mass losses from the second method of correction also show positive results. All of the samples with additives lost less mass than the pure samples in both exposures. In addition, the amount of mass lost decreased for each sample after the second exposure. While this was expected for the samples with additives, the pure samples were expected to lose approximately the same amount of mass in the two exposures. This expectation was met by the mass loss data from the first method of correction, but not the second. Since some of the pure polymer surface is oxidized during the first exposure, it is possible that regions of oxidation can protect underlying polymer during the subsequent exposures. In addition, the morphology of the eroded surface after the first exposure may affect the degree of reaction between AO and polymer in the second exposure. As found previously, the 10 wt. % samples lost less mass than the 5 wt. % samples, and the performance of the boron samples versus the Cloisite-15A samples was reversed upon increased additive composition as stated.

## IV.6. Analysis of the Sixth Set of AO Exposures

### IV.6.i. Mass Loss

Only the second method of correction was utilized to analyze the mass losses for the sixth set of AO Exposures. The first method of correction entails the relation of all samples on the plate to the sample in the ML position. Because new samples replaced some of the exposed samples between exposures, the identity of the sample in the ML position changed at a rate that did not match those of the other samples. For example, after the second exposure, the samples in the ML position and the LR had both received 36 hours of AO exposure. Prior to the third exposure, a new sample was placed in the ML position, such that afterwards, the sample in the ML position received 23 hours of AO exposure while the sample in the LR position had received 59 hours of AO exposure. Basing the mass loss of the latter sample on the former sample is inconsistent with the diminished mass losses exhibited by samples with previous AO exposure.

The mass losses corrected by the second method are shown in Table 21.

Table 21: Mass Losses for the Sixth Set of AO Exposures Using the Second Correction Method

Sample	Total Hours Exp.	Corrected Mass Losses and Respective Time Frames (hrs)									
		Mass Loss	Time Frame	Mass Loss	Time Frame	Mass Loss	Time Frame	Mass Loss	Time Frame	Mass Loss	Time Frame
<b>Pure 954-3</b>											
1 UL	18	1.34	0-18	---	---	---	---	---	---	---	---
2 ML	36	4.28	0-36	---	---	---	---	---	---	---	---
3 LL	104	3.33	0-36	2.96	36-59	0.84	59-104	6.29	0-59	7.13	0-104
1' UL	68	4.37	0-23	0.74	23-68	5.12	0-68	---	---	---	---
2' ML	68	4.75	0-23	1.07	23-68	5.82	0-68	---	---	---	---
<b>5% Boron</b>											
4 UR	18	0.73	0-18	---	---	---	---	---	---	---	---
5 MR	36	2.48	0-36	---	---	---	---	---	---	---	---
6 LR	104	2.21	0-36	1.97	36-59	0.65	59-104	4.18	0-59	4.83	0-104
4' UR	68	2.95	0-23	0.56	23-68	3.51	0-68	---	---	---	---
5' MR	68	2.88	0-23	0.32	23-68	3.20	0-68	---	---	---	---

The results of the sixth set of AO exposures are also significant. As expected, all the boron samples lost less mass than the pure samples. For example, 3 LL (no additive) experienced a mass loss of 7.13 in the total of 104 hours of AO exposure, while 6 LR (5 wt. % boron) experienced a mass loss of 4.83 during this time period. Of greater importance is the decreasing rate of mass loss exhibited by the boron samples during the exposures, supporting the formation of an oxidized boron layer on the surface of the sample that protects the underlying polymer.

**IV.6.ii. XPS Analysis**

XPS analysis revealed the elemental concentrations of the exposed surfaces of a set of Hexcel 954-3 CE samples. The elemental concentrations are the primary focus of this analysis. The identity of the individual peaks is secondary because the chemical structure of the Hexcel 954-3 CE is proprietary. The possible formation of a protective oxide layer was studied by the analysis of certain samples from the sixth set of AO exposures, listed in Table 4. The samples chosen to represent the set for XPS analysis were two samples of pure Hexcel 954-3 CE, exposed for 18 and 104 hours, and four samples of Hexcel 954-3 CE that contained 5 wt. % boron and were exposed for 18, 36, 68, and 104 hours, respectively. Expected changes in elemental concentrations included a decrease in carbon and increases in oxygen, boron, and nitrogen. Control samples for the polymers with boron were not run because an understanding of the effects of AO exposure on a previously unexposed polymeric material was studied already with the BPA-based CE samples.

When comparing the control, 18-hour exposed, and 104-hour exposed pure samples, the carbon concentration on the surface dropped from 82% to 60% and then rose to 64%, as shown in Table 17. While the initial decrease between the control and the 18-hour AO exposed sample was expected, the subsequent rise in carbon concentration at the end of all AO exposures in the set was not. This increase is likely attributed to experimental error in the performance of XPS analysis. Examination of the carbon peak of the 104-hour sample (Figure 84) shows a great reduction in the second carbon peak initially at 289.4 eV in the 18-hour sample (Figure 81). This peak may represent a carboxyl group carbon.

On the other hand, the oxygen concentration increased from 12% to 24% and then fell to 21%, as shown in Table 17. While the initial increase was expected, due to AO interaction with the polymer surface, the ensuing drop in oxygen concentration at the end of all AO exposures was not. This drop is small, but may suggest that changes in bonding on the surface of the polymer made it less reactive with AO over time. This is consistent with the diminished mass loss behavior exhibited by the pure samples in the Hexcel 954-3 CE exposures. Additionally, the peak at 532.3 eV (Figure 82), indicative of carbonyl group oxygen, experienced a downfield shift of 0.10 eV (Figure 85) due to prolonged exposure. This shift seems too small to be significant.

While the increase in nitrogen concentration between the control and the 18-hour AO exposed pure samples was expected, the decrease in nitrogen concentration at the end of all the AO exposures was not (Table 17). If the source of nitrogen was from the dry nitrogen used to purge the chamber after exposure, the sample that was exposed for 104 hours should have had a greater amount of nitrogen than the sample that was

exposed for 18 hours because it underwent more exposures, and therefore more system purging. Because this was not the case, it is possible that nitrogen exists in the surface of the Hexcel 954-3 CE samples in such a form that it is susceptible to AO attack. The other extraneous peaks are most likely due to contamination, although it is possible that the polymer, whose chemical structure is proprietary, may contain some of these elements.

The XPS analysis of the Hexcel 954-3 CE + 5 wt. % boron AO exposed samples is now considered. Based on the elemental concentrations, the amount of carbon on the surface fluctuated significantly in first three exposures, rising from 49% to 56% and then dropping to 47%, as shown in Table 18. After 104 hours of AO exposure the carbon concentration approached its 18-hour value by rising to 50%. Again, these fluctuations are likely attributable to experimental error in the performance of XPS analysis. In the 18-hour sample, the carbon peaks (Figure 87) are similar to those seen before: one peak at 285.1 eV and a second peak at 289.5 eV. These peaks show only insignificant changes in binding energy when compared to the 36, 68, and 104-hour samples in Figures 91, 95, and 99, respectively. Although the second carbon peak is not listed in Figures 91 and 99, this is more likely due to the operator's baseline selection rather than the absence of the peak.

As shown in Table 18, the oxygen concentration is fairly constant at 23% after the first two exposures, and then drops to 21% after the third. The largest drop is to 18% after the fourth exposure. The carbonyl group oxygen peaks at 532.5 eV are identical throughout (Figures 88, 92, 96, and 100), with the exception of a small shift downfield to 532.7 eV after the second exposure (Figure 92).

The boron composition shows a large decrease from 18% to 9% (Table 18) when the first two exposures are compared. The large decrease in boron is consistent with the accompanying sizeable increase in carbon. The boron content then jumps to 23% after the third and fourth exposures. These differences in boron content suggest the sample may have suffered from inhomogeneity. The peaks for boron, shown in Figures 90, 94, 98, and 102, are all very similar. There is a small shift after the second exposure (Figure 94) from 187.5 eV to 187.8 eV. This may suggest a change in the nature of boron bonding, possibly to a more electronegative species such as oxygen.

Nitrogen concentrations stay in the 4% to 6% range through the exposures, and are therefore not of any great significance, as is the case with the other extraneous peaks.

#### **IV.7 TGA Analysis**

TGA analysis was done on 6 Hexcel 954-3 CE samples. They are representative of those samples exposed to AO in the third, fourth, fifth, and sixth exposures. These samples include pure Hexcel 954-3 CE, Hexcel 954-3 CE with 5 and 10 wt. % boron, respectively, and Hexcel 954-3 CE with 5 and 10 wt. % Cloisite-15A, respectively. As shown in Figures 27 through 32, all of the polymers were thermally stable at 177° and 232°C, the respective cure and post-cure temperatures. They exhibited mass losses of less than 0.5% of their initial mass from 0°C to 232°C, probably due to loss of water. Significant mass loss did not occur until approximately 400°C. All of the thermograms list the percentage of the initial mass that was lost between approximately 400°C and 500°C. The pure, 5 wt. % boron, and 5 wt. % Cloisite-15A samples (Figures 27, 29, and 31, respectively) all lost between 56% and 58% of their initial mass in this temperature range. The 10 wt. % boron and 10 wt. % Cloisite-15A samples (Figures 30

and 32) both lost between 60% and 61% of their initial mass loss in this temperature. It can therefore be concluded that both the nature and the quantity of these additives had little effect on the thermal decomposition of the Hexcel 954-3 CE. While all of these samples were analyzed under air, an additional test was done on a pure sample under nitrogen (Figure 28). It can be concluded from Figures 27 and 28 that the atmosphere in which the tests were performed also had little effect on the thermal decomposition of the cyanate ester.

## CHAPTER 5: CONCLUSION

Additives can offer protection to a polymer from erosion by atomic oxygen. This was observed in the Hexcel 954-3 cyanate ester resin using boron and an organoclay as the additives. The formation of an additive oxide layer that protects the underlying polymer is suggested from these experiments, but needs further study to be firmly established.

The best combinations of polymer and additive found in this work were Hexcel 954-3 cyanate ester resin with boron and Cloisite-15A, respectively. These composites had smooth surfaces and were homogeneous. The boron carbide and Hectorite additives were not successfully held by the matrix of the cyanate ester, and resulted in inhomogeneous samples with rough, porous surfaces that would be unsuitable for use in spacecraft materials in low earth orbit.

The utility of the Bisphenol A-based cyanate ester resin showed promise based on mass loss data with boron, but was not investigated further with the organoclays once the space-certified Hexcel 954-3 cyanate ester resin was received. Mass loss data, SEM analysis, and XPS analysis were obtained for Bisphenol A-based cyanate ester resin samples with 10 wt. % boron carbide that were exposed on both their front and back surfaces. Again, the boron carbide and Hectorite additives were not successfully held by the matrix of the cyanate ester, and sometimes resulted in inhomogeneous samples that would be unsuitable for structural use.

After the first set of atomic oxygen exposures, it was determined that the surface area of the sample was an important factor to measure so that mass losses could be reported relative to their surface dimensions. The fourth atomic oxygen exposure

revealed disparities among the atomic oxygen fluences experienced at the different positions on the sample holder. Two correction methods were developed, and applied to the third, fifth, and sixth atomic oxygen exposures.

As a result, the corrected mass loss data of the pure Hexcel 954-3 CE, Hexcel 954-3 CE + 5 and 10 wt. % boron, respectively, and the Hexcel 954-3 CE + 5 and 10 wt. % Cloisite-15A samples support the assertion that boron and organoclay additives can offer protection to a polymer surface from atomic oxygen erosion. In addition, they support the hypothesis that the additive reacts with atomic oxygen in such a manner that mass losses are diminished over successive exposures. The sixth set of exposures focused on this idea. Mass loss data offers strong support, while XPS analysis was used to explain the differing elemental concentrations of the sample surfaces. These results support the need for further investigation of an additive oxide layer on the surface of the polymer. Future study should include SEM analysis of samples that are exposed in a successive fashion.

Figure 4: Spacesuit Components and Cross-Section

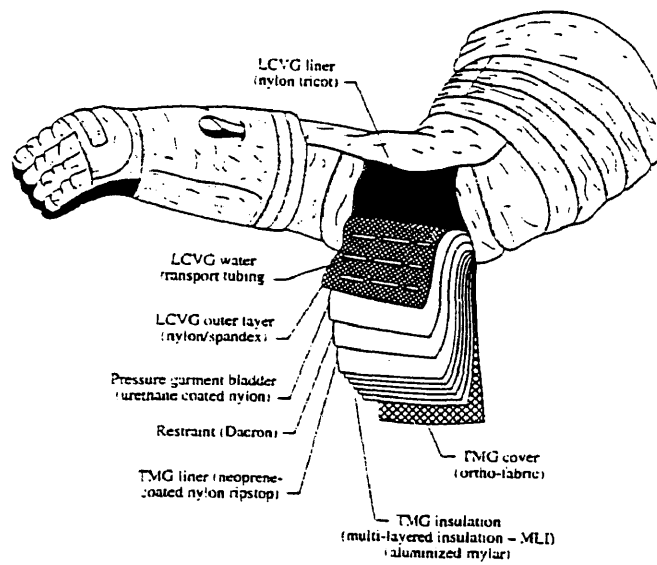
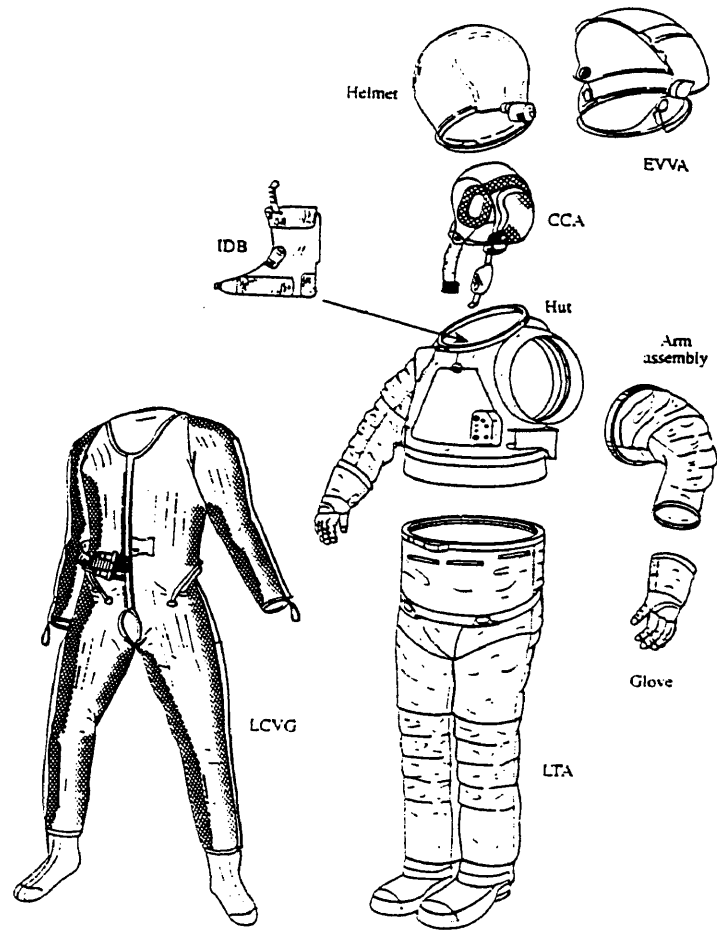


Figure 12: Schematic of SEM Instrument

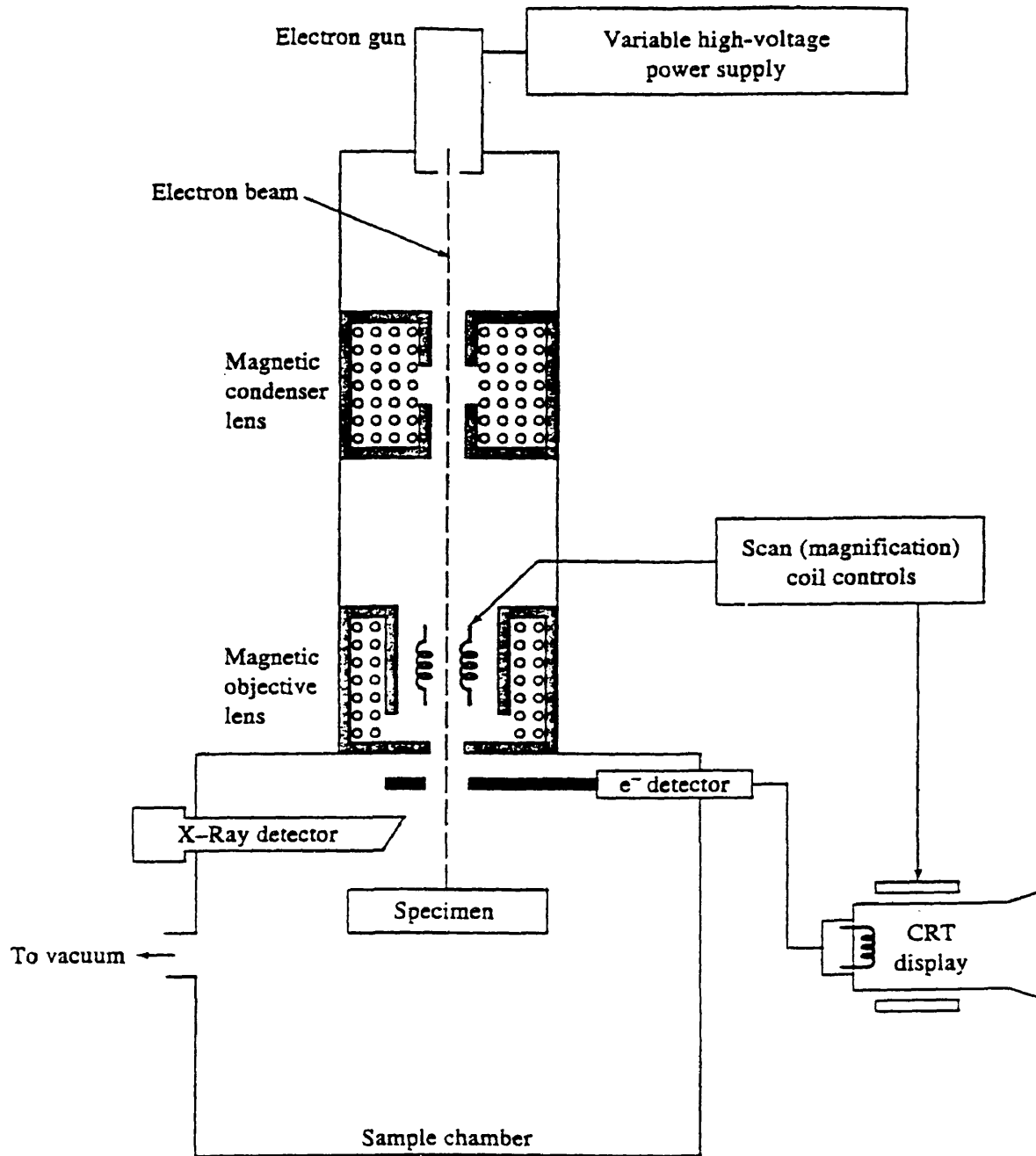


Figure 13: Schematic of TGA Instrument

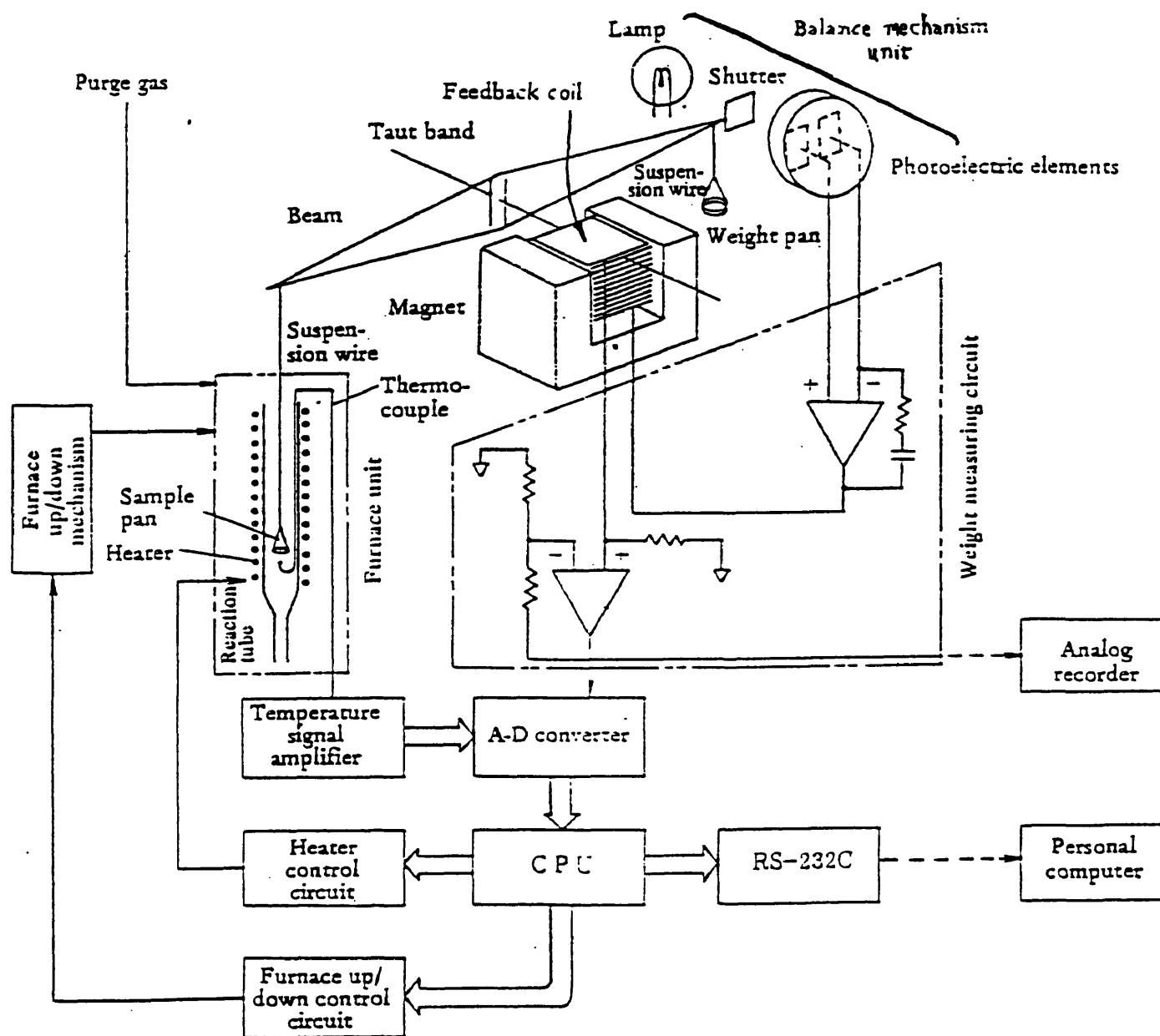


Figure 15: Schematic of XPS Instrument

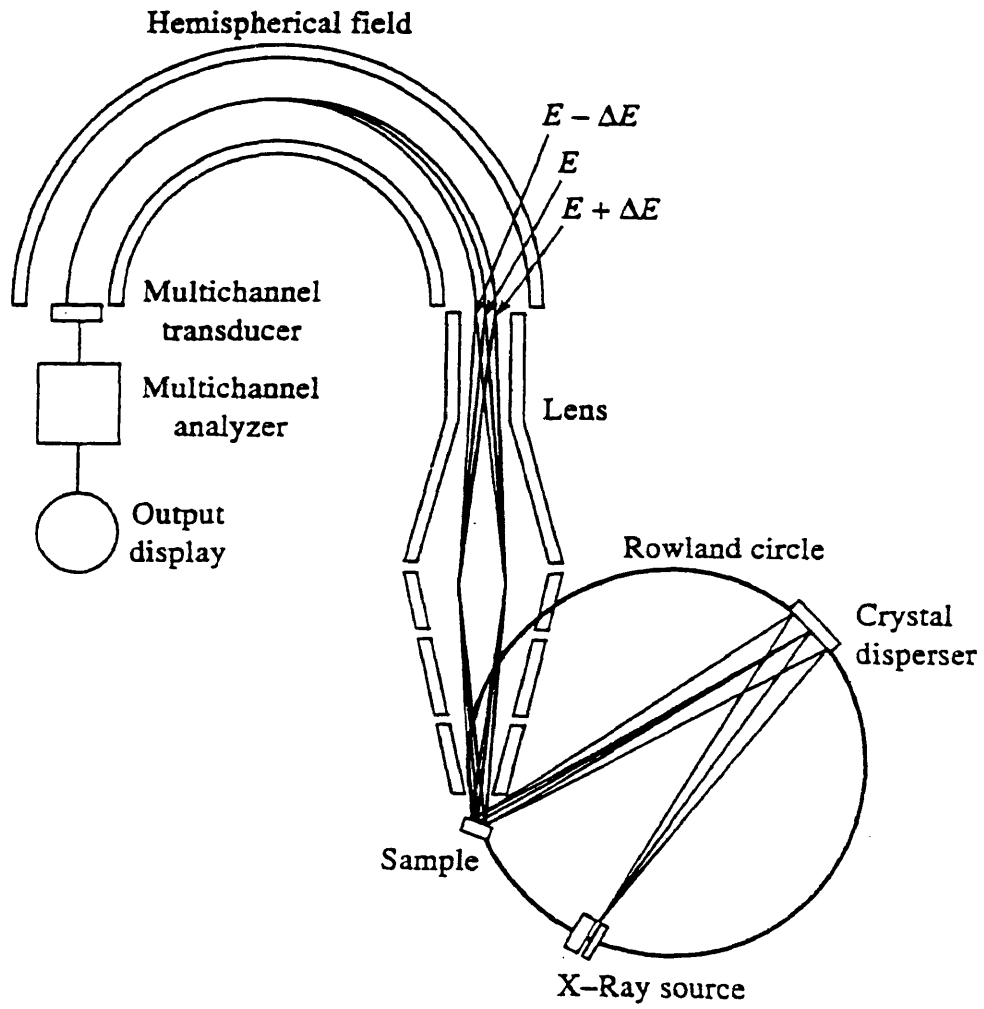


Figure 16: Viscosity Profile for Hexcel 954-3 Cyanate Ester

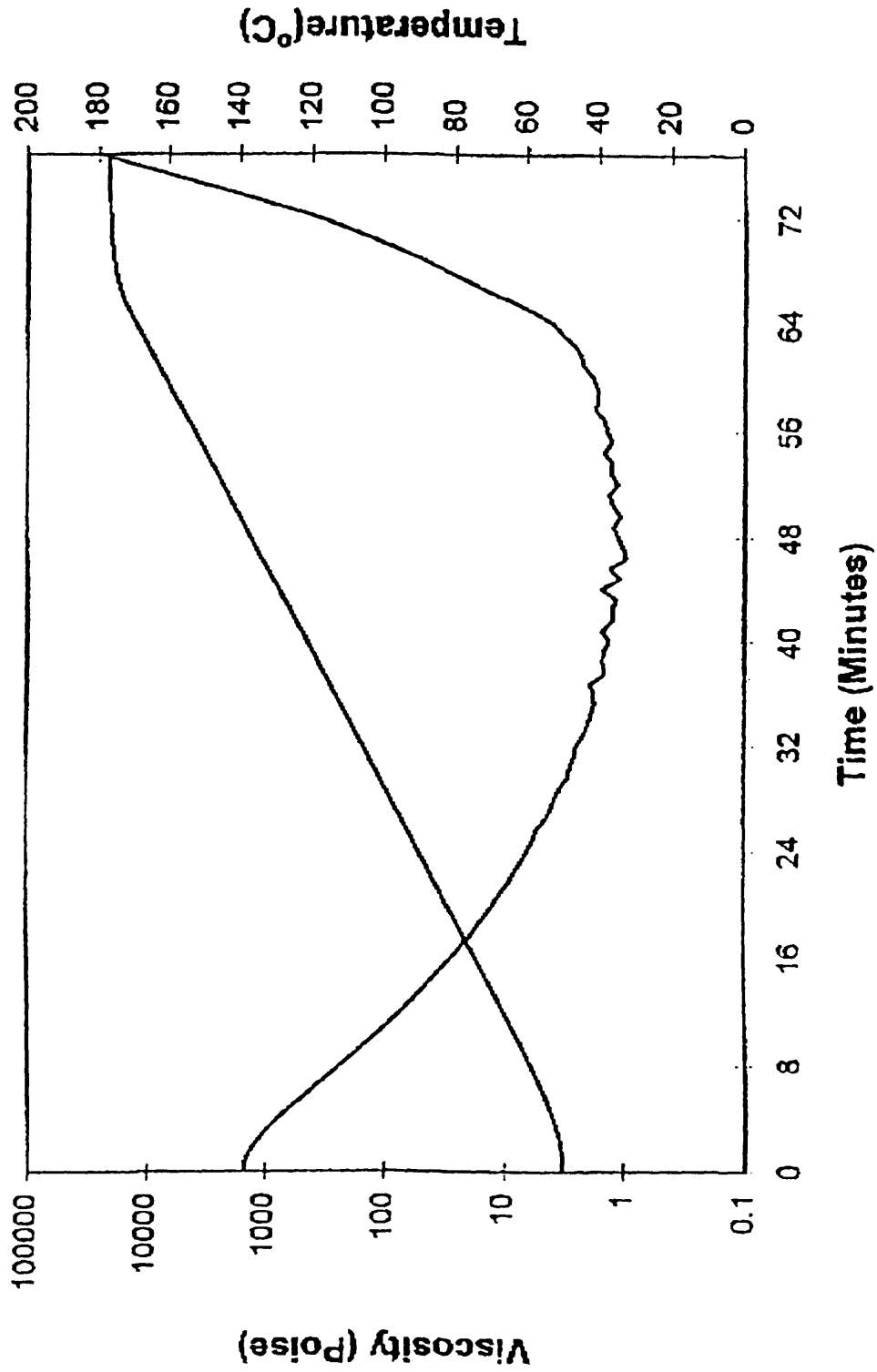


Figure 17: Neat Resin Moisture Absorption Plot for Hexcel 954-3 Cyanate Ester

### 954-3 Neat Resin Moisture Absorption @ RT/50% RH (compared to 934 epoxy)

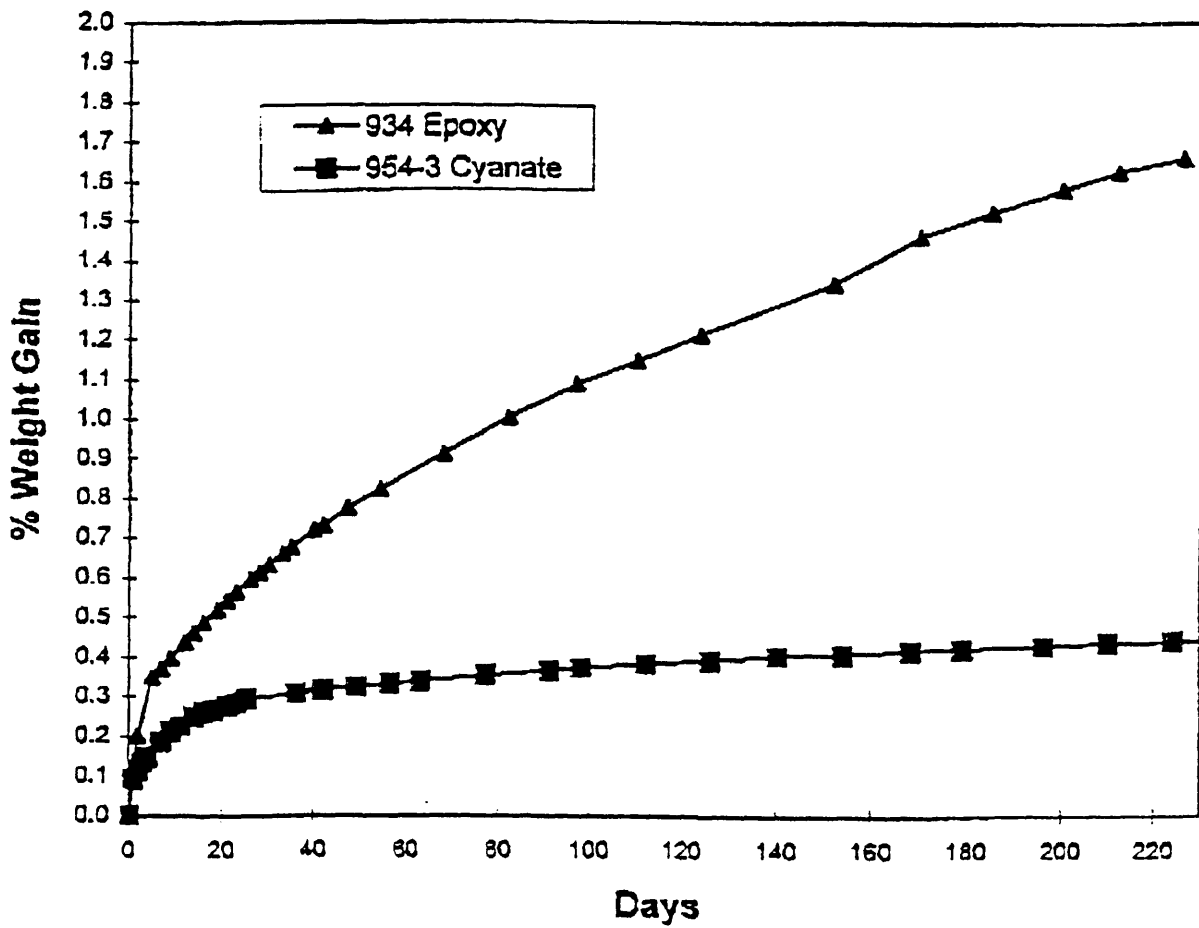
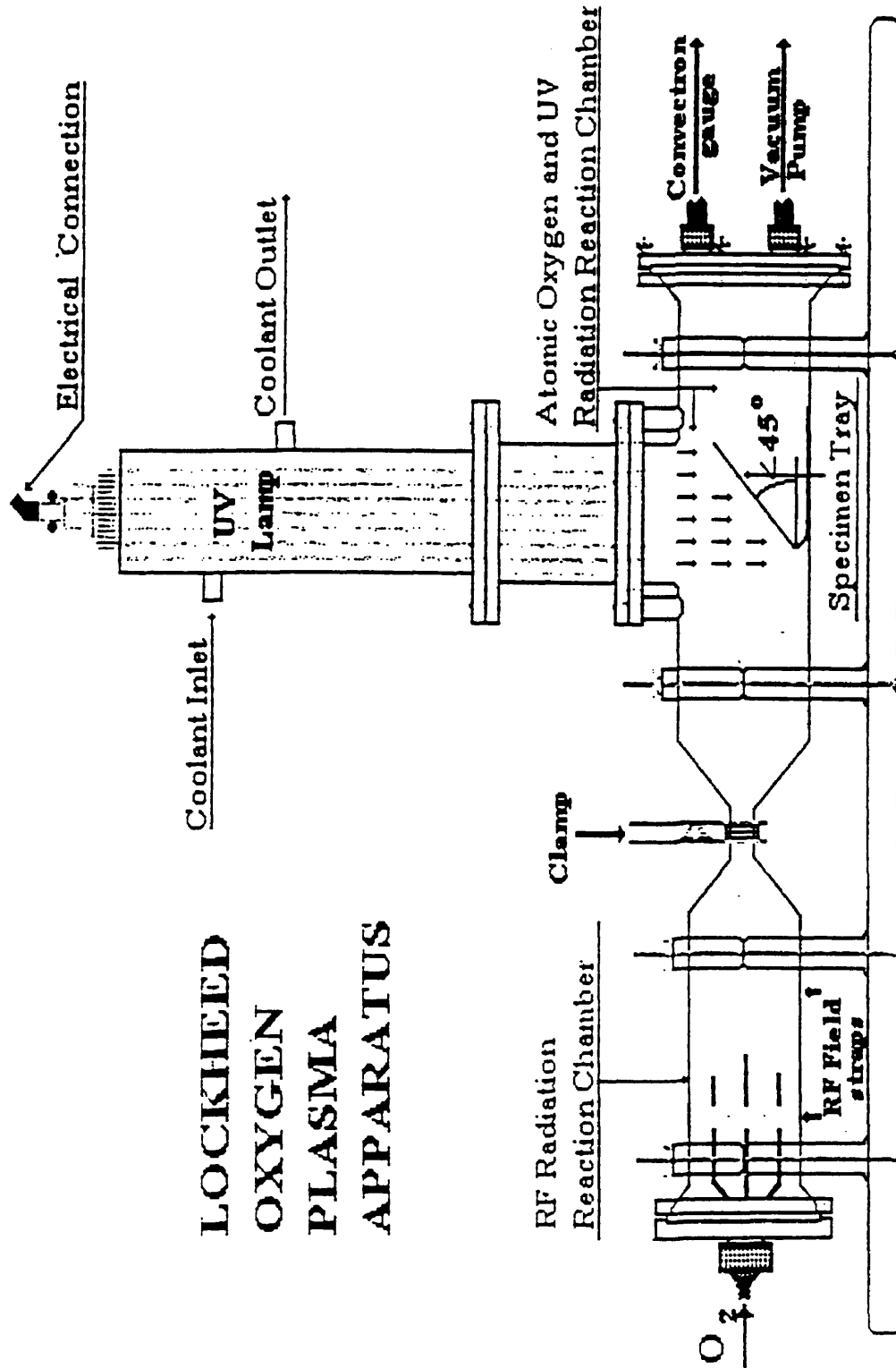


Figure 18: Configuration of Oxygen Plasma Apparatus (OPA)



**LOCKHEED  
OXYGEN  
PLASMA  
APPARATUS**

Figure 19: Upgraded Atomic Oxygen Generator

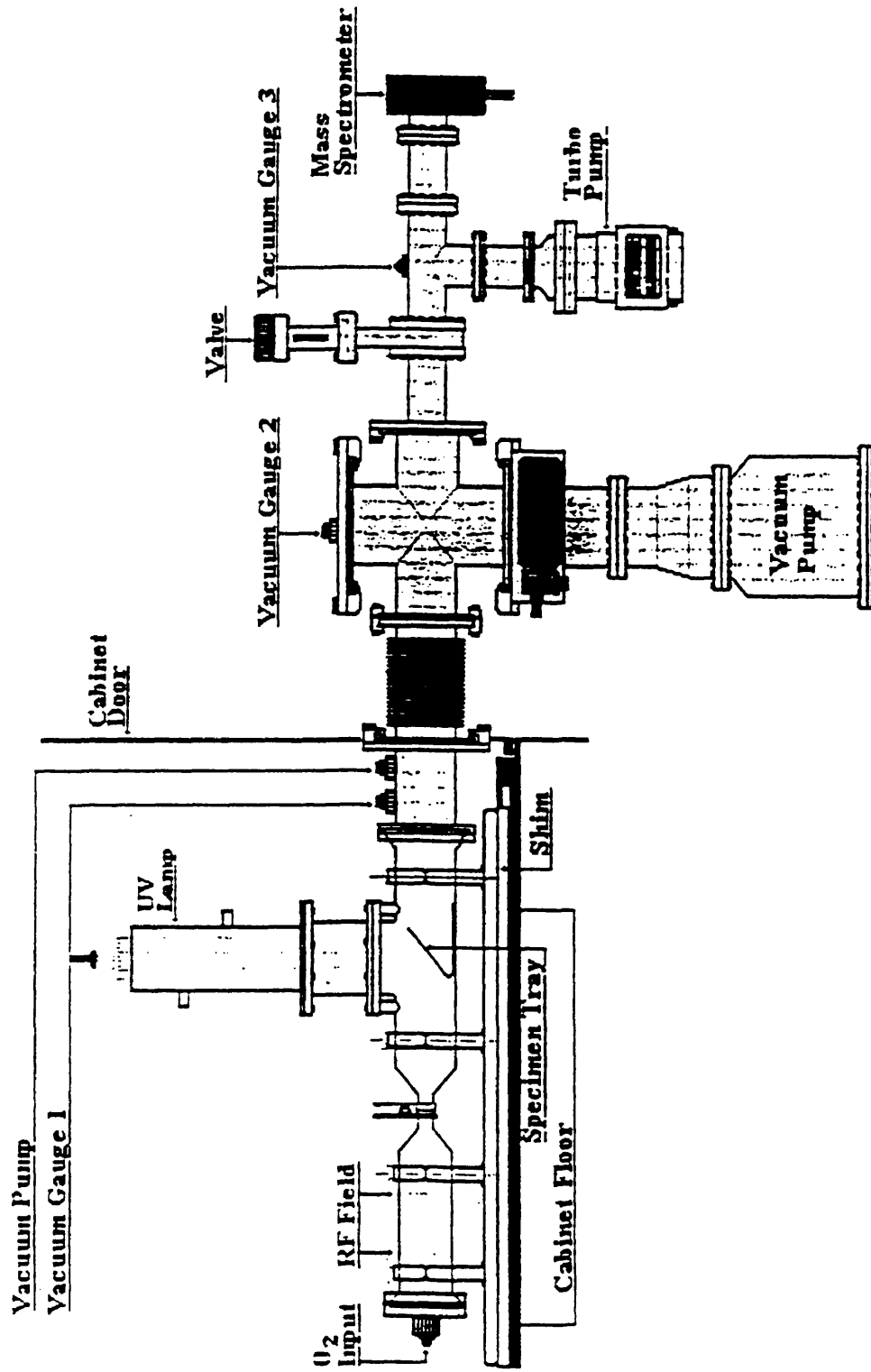


Figure 20: Diagram of the Oxygen Plasma Apparatus Console

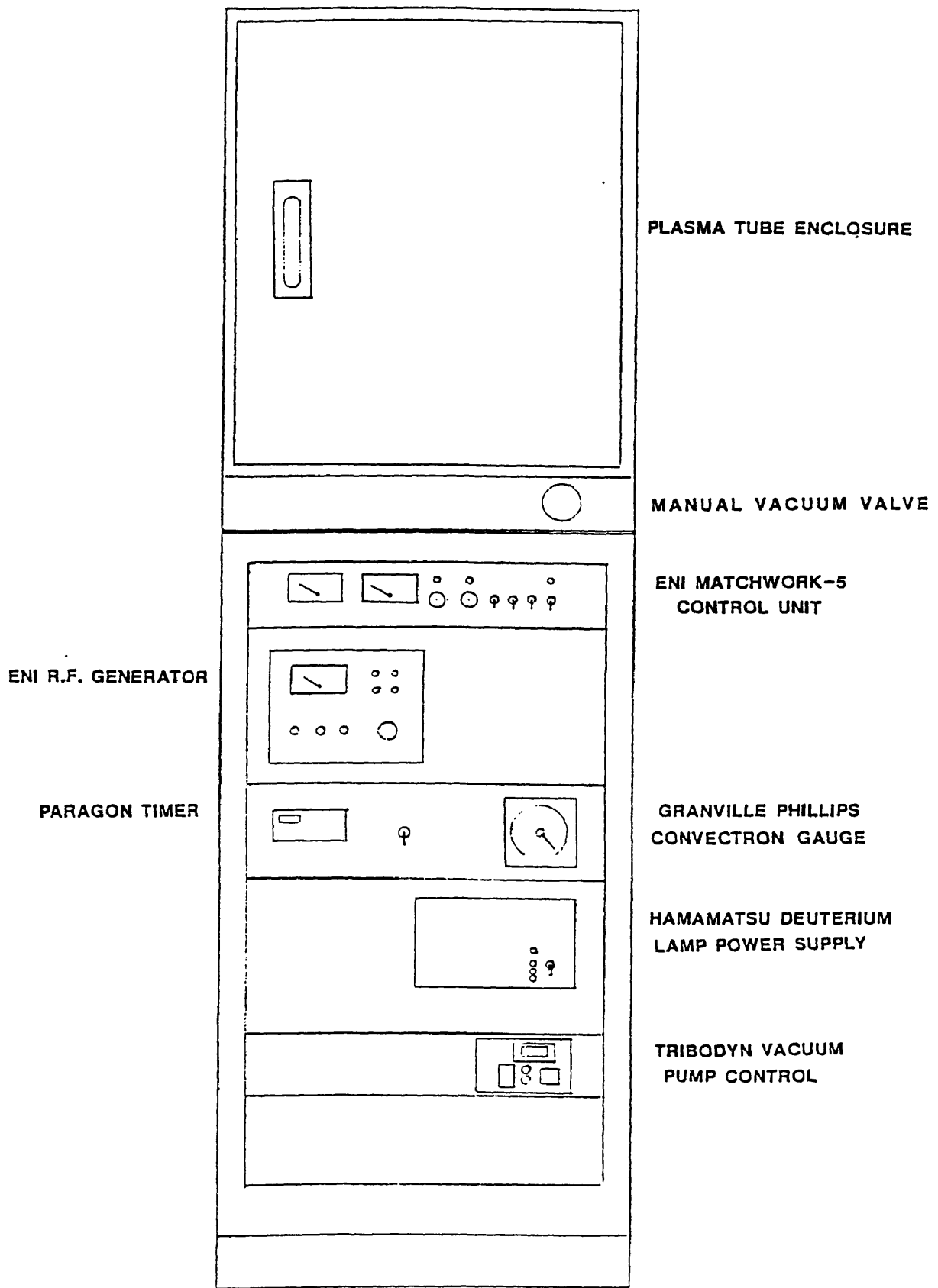


Figure 21: Picture of the Oxygen Plasma Apparatus Console



Figure 22: Components of Quartz AO Chamber



Figure 23: Chamber Positioned within the Oxygen Plasma Tube Enclosure

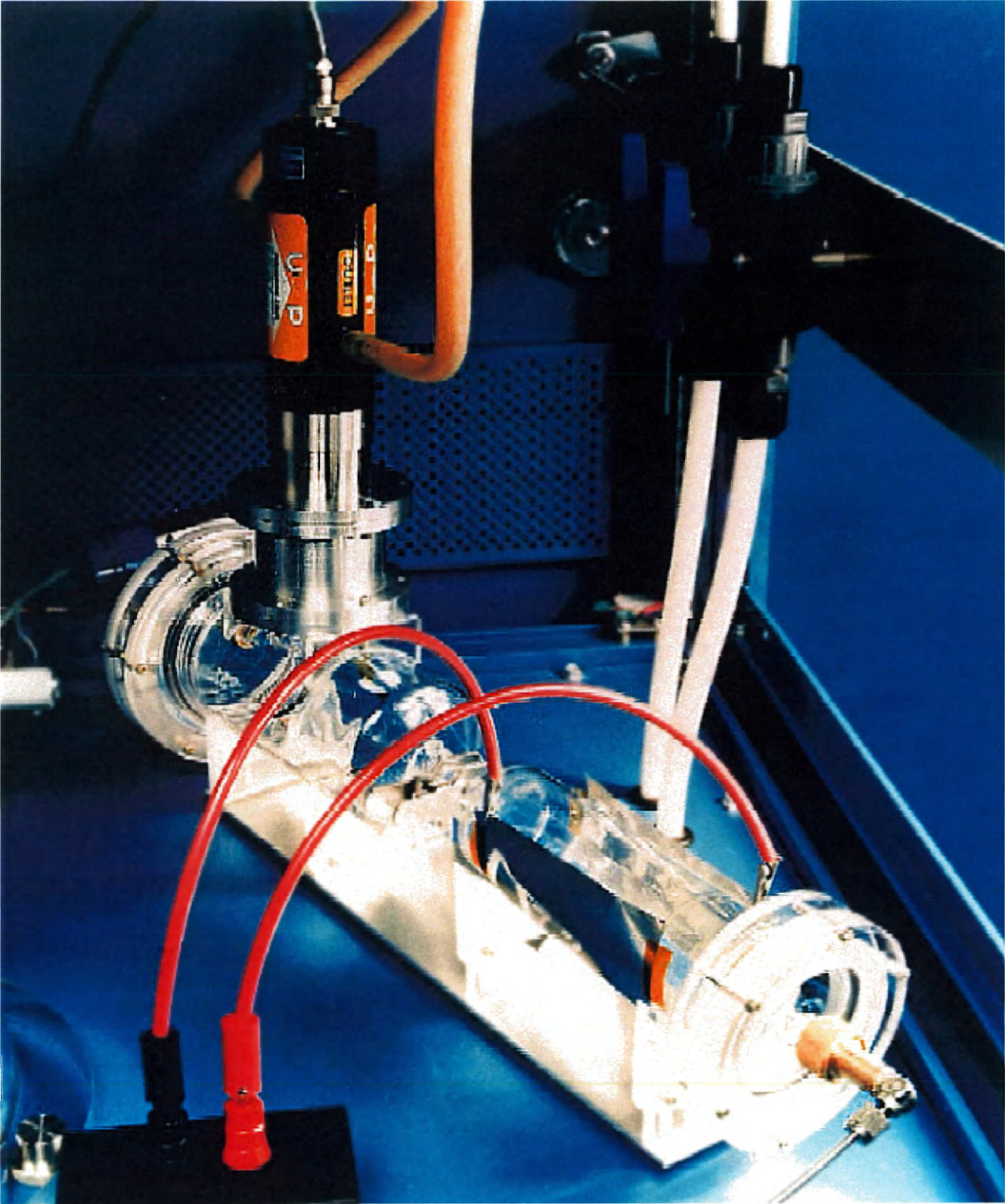


Figure 24: Chamber during Atomic Oxygen Exposure

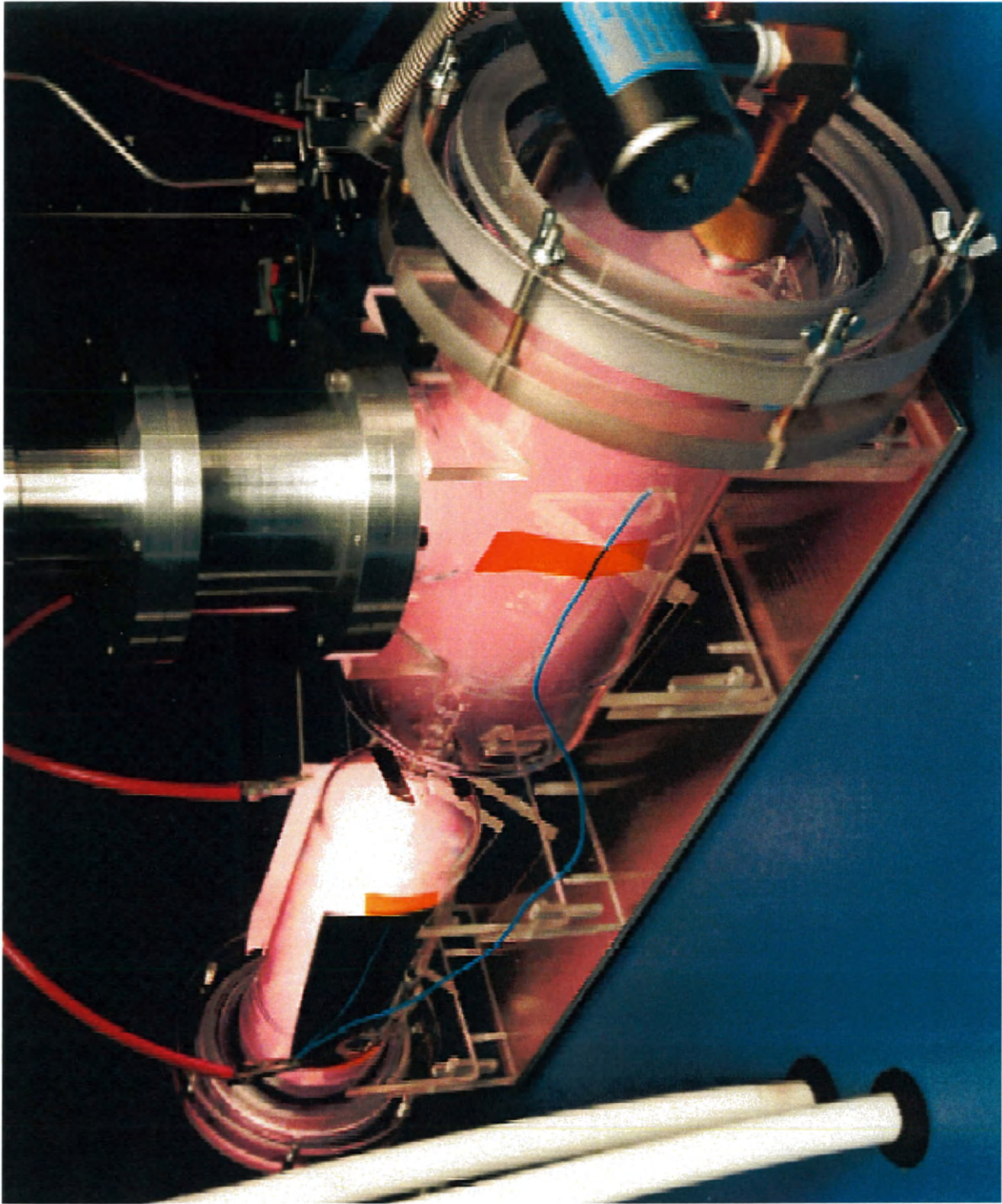


Figure 27: Thermogram of Pure Hexcel 954-3 CE

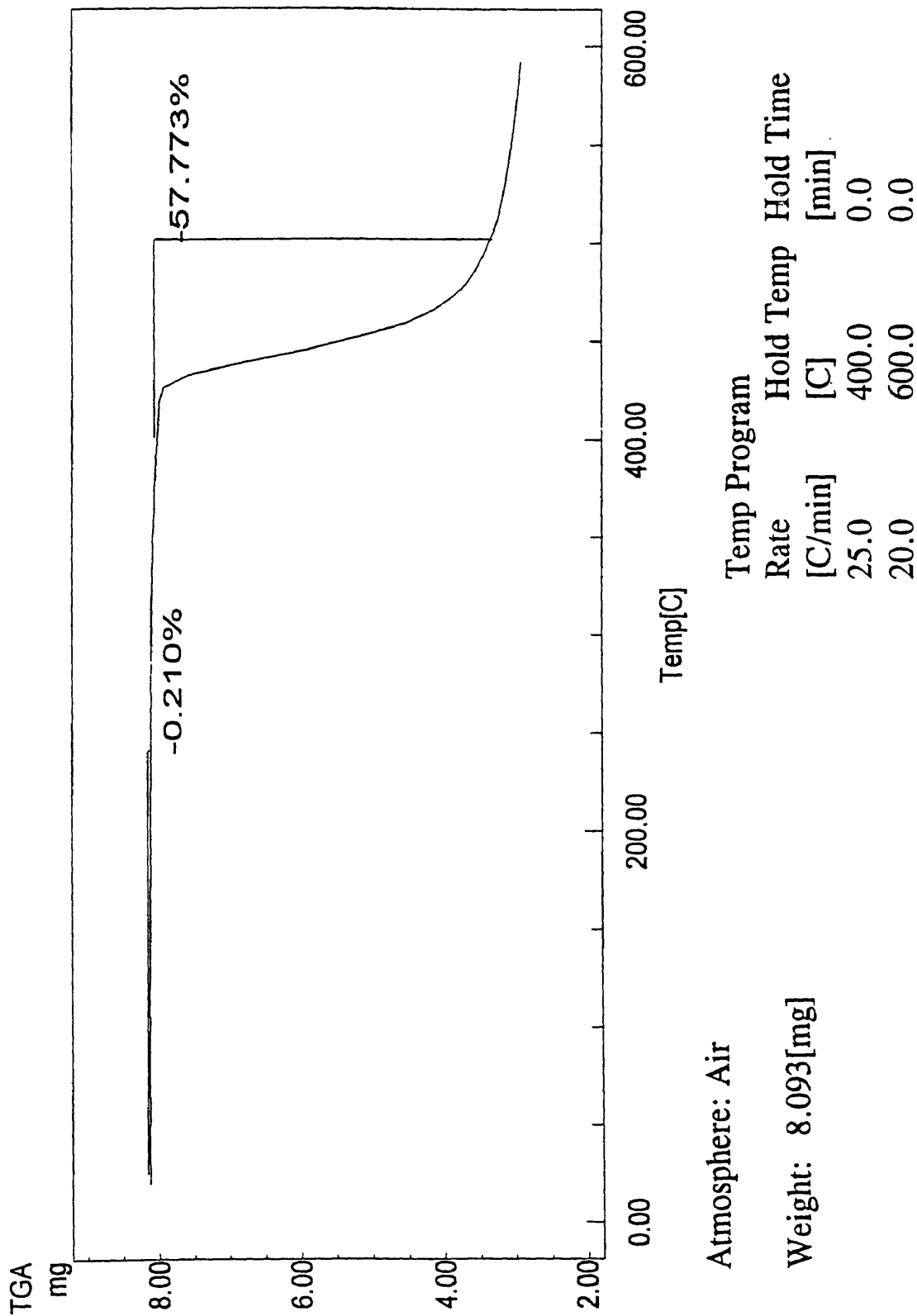


Figure 28: Thermogram of Pure Hexcel 954-3 CE (N<sub>2</sub>)

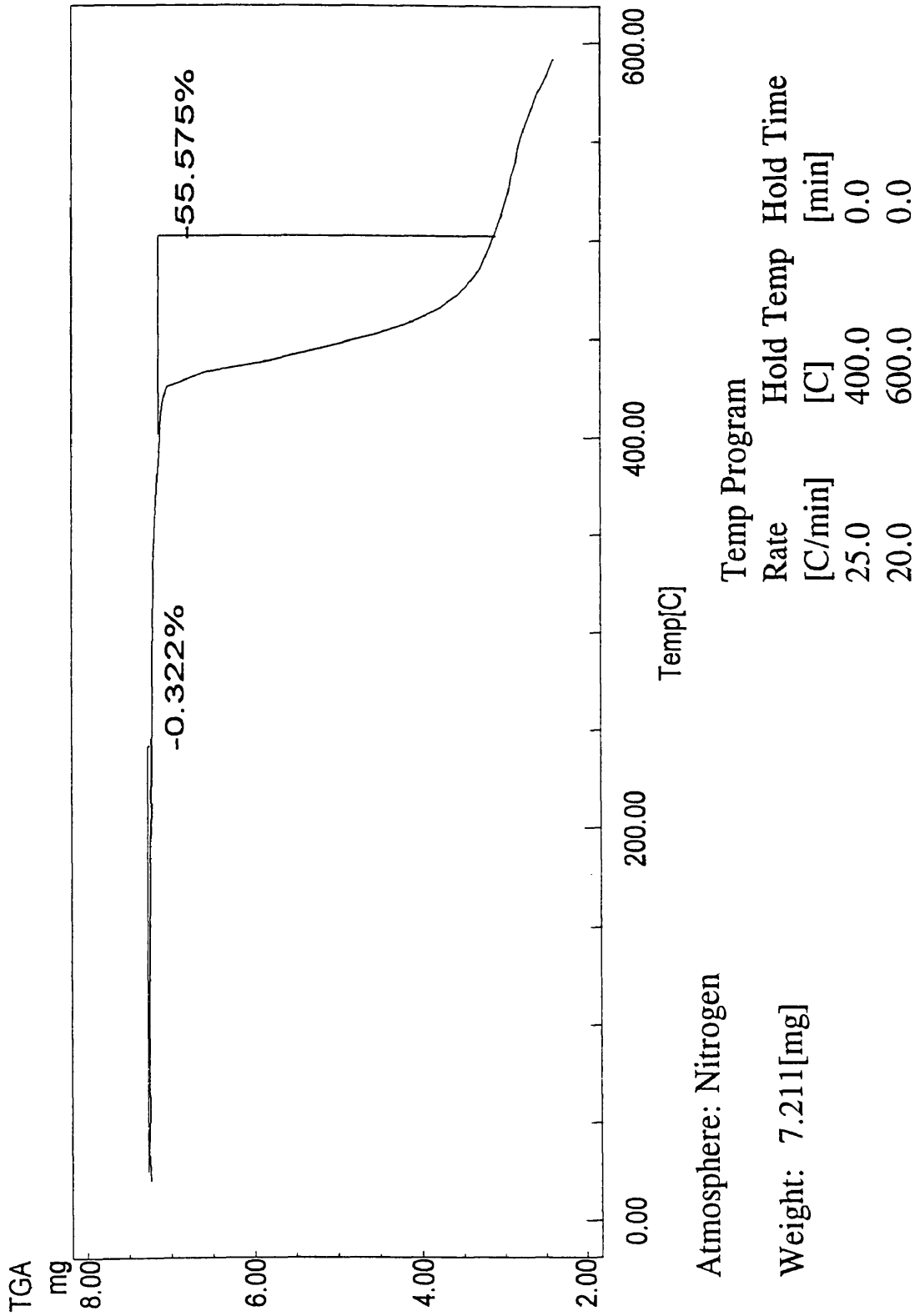


Figure 29: Thermogram of Hexcel 954-3 CE + 5% wt. Boron

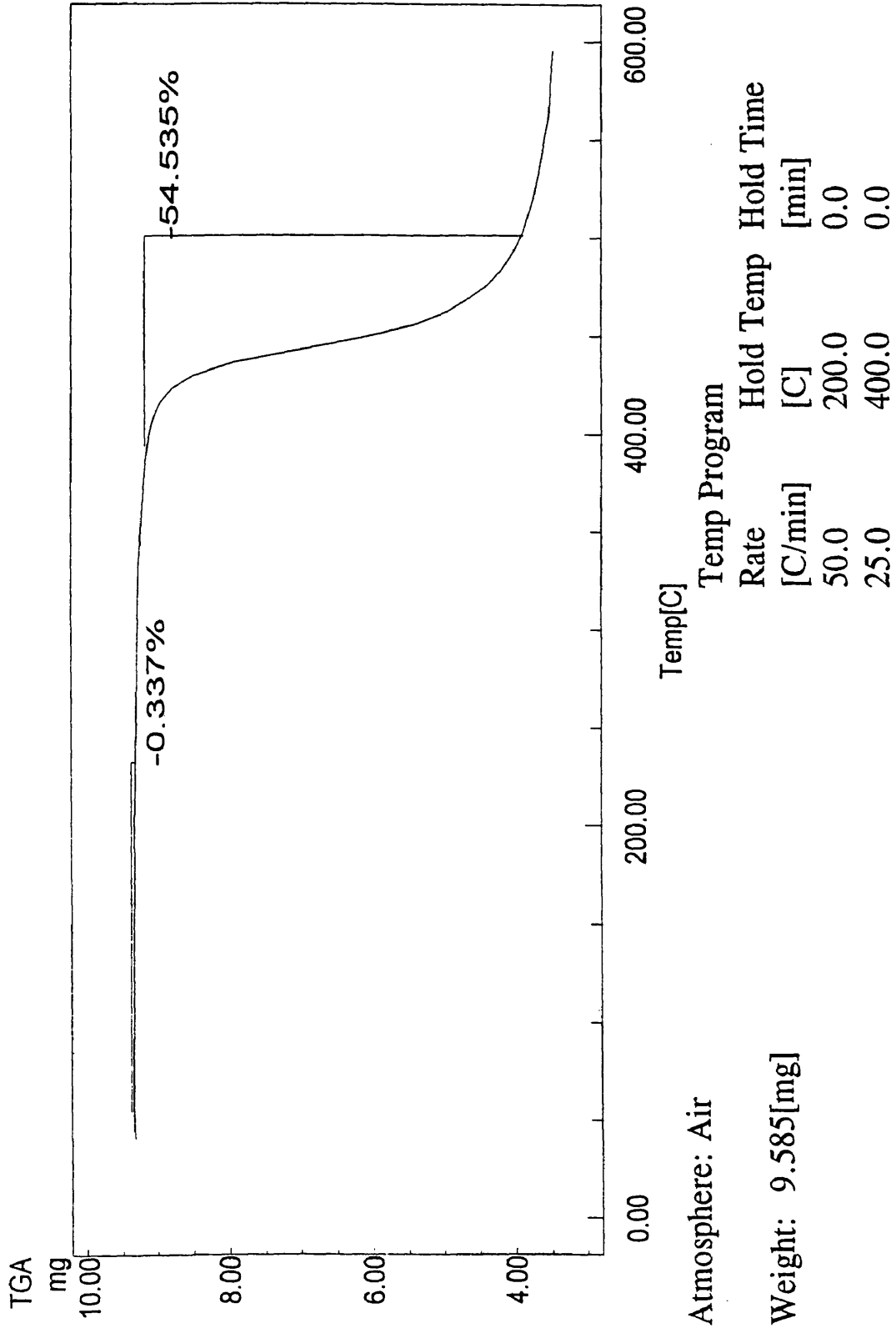


Figure 30: Thermogram of Hexcel 954-3 CE + 10 wt.% Boron

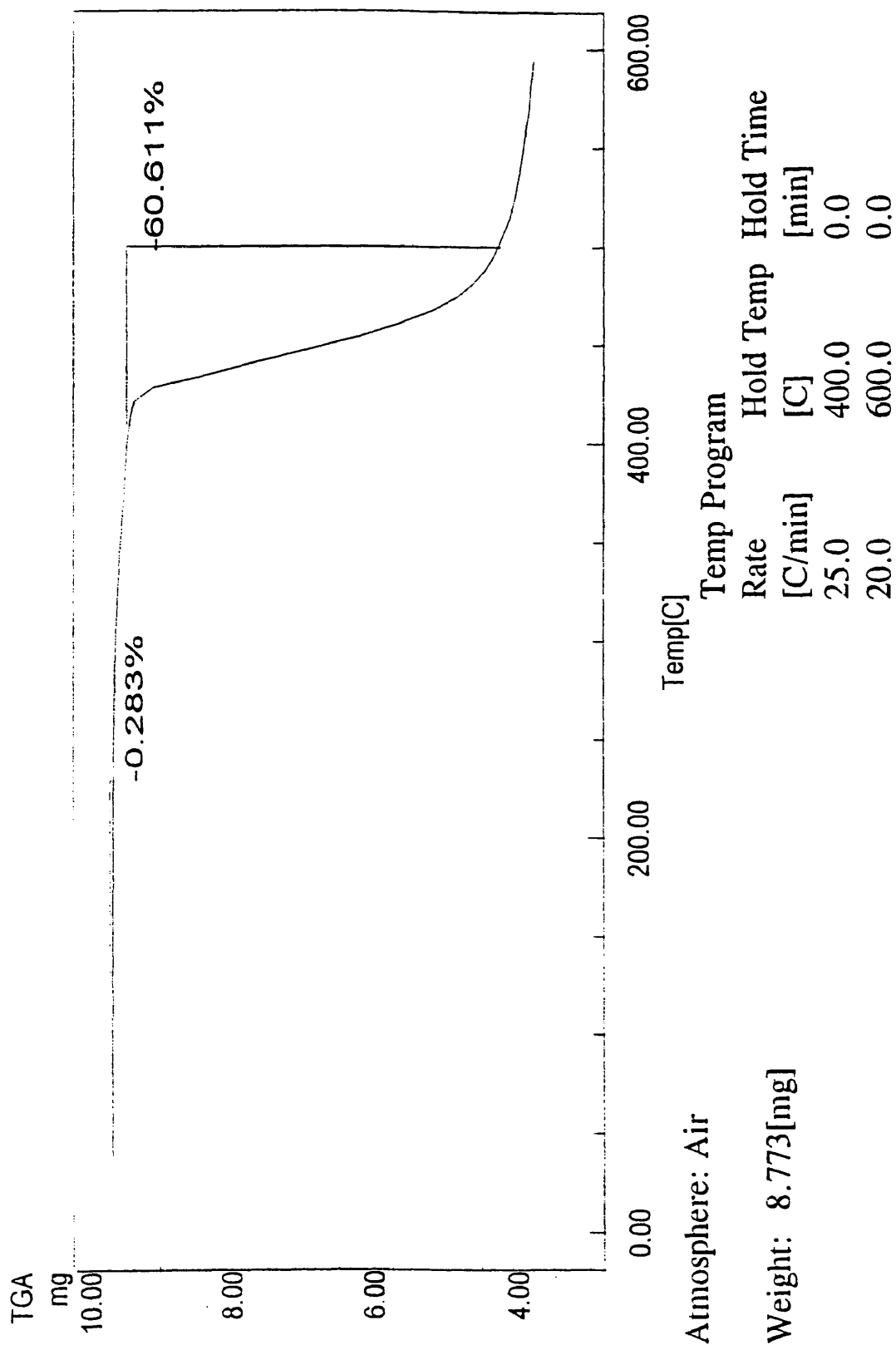


Figure 31: Thermogram of Hexcel 954-3 CE + 5% wt. Cloisite-15A

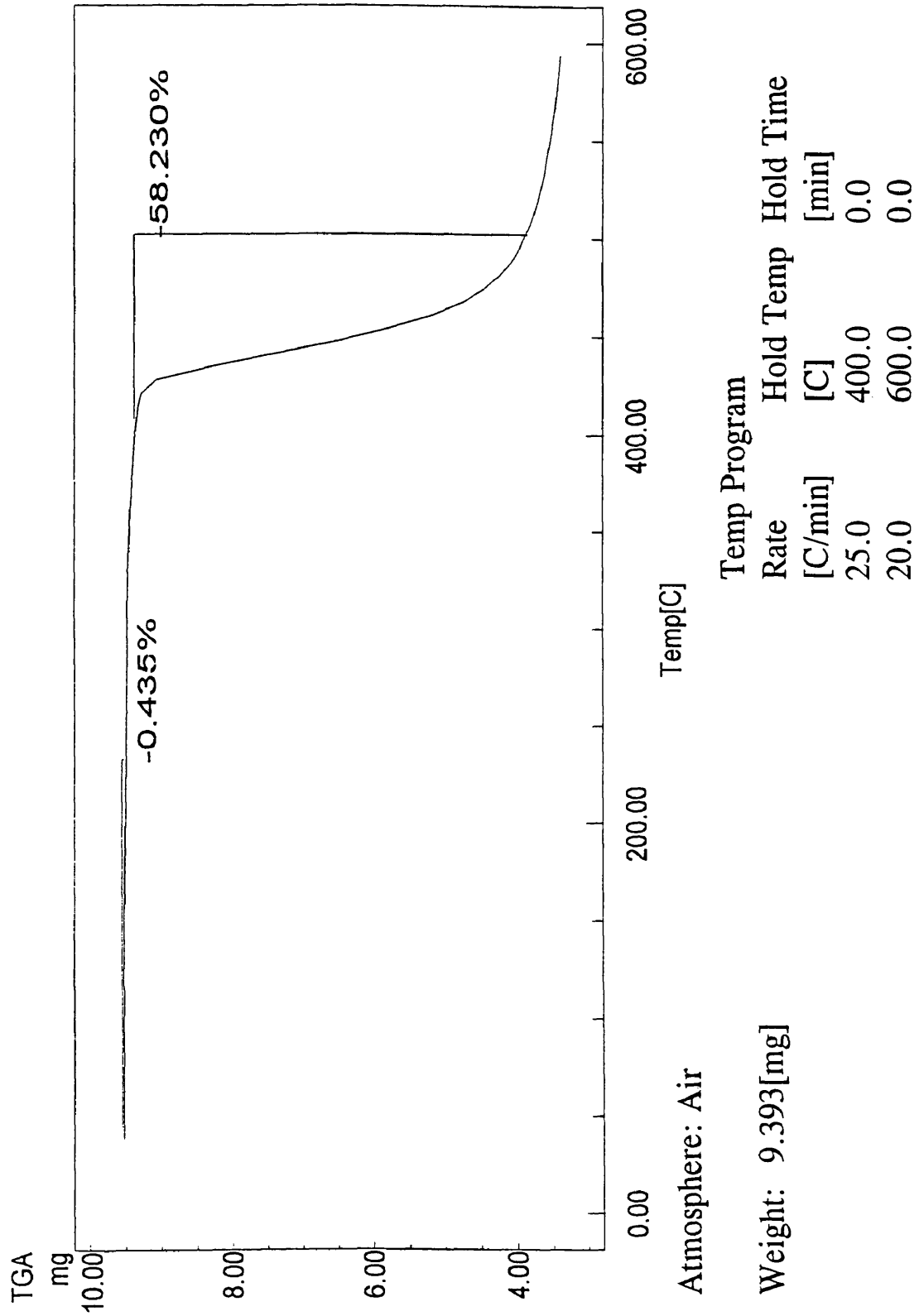
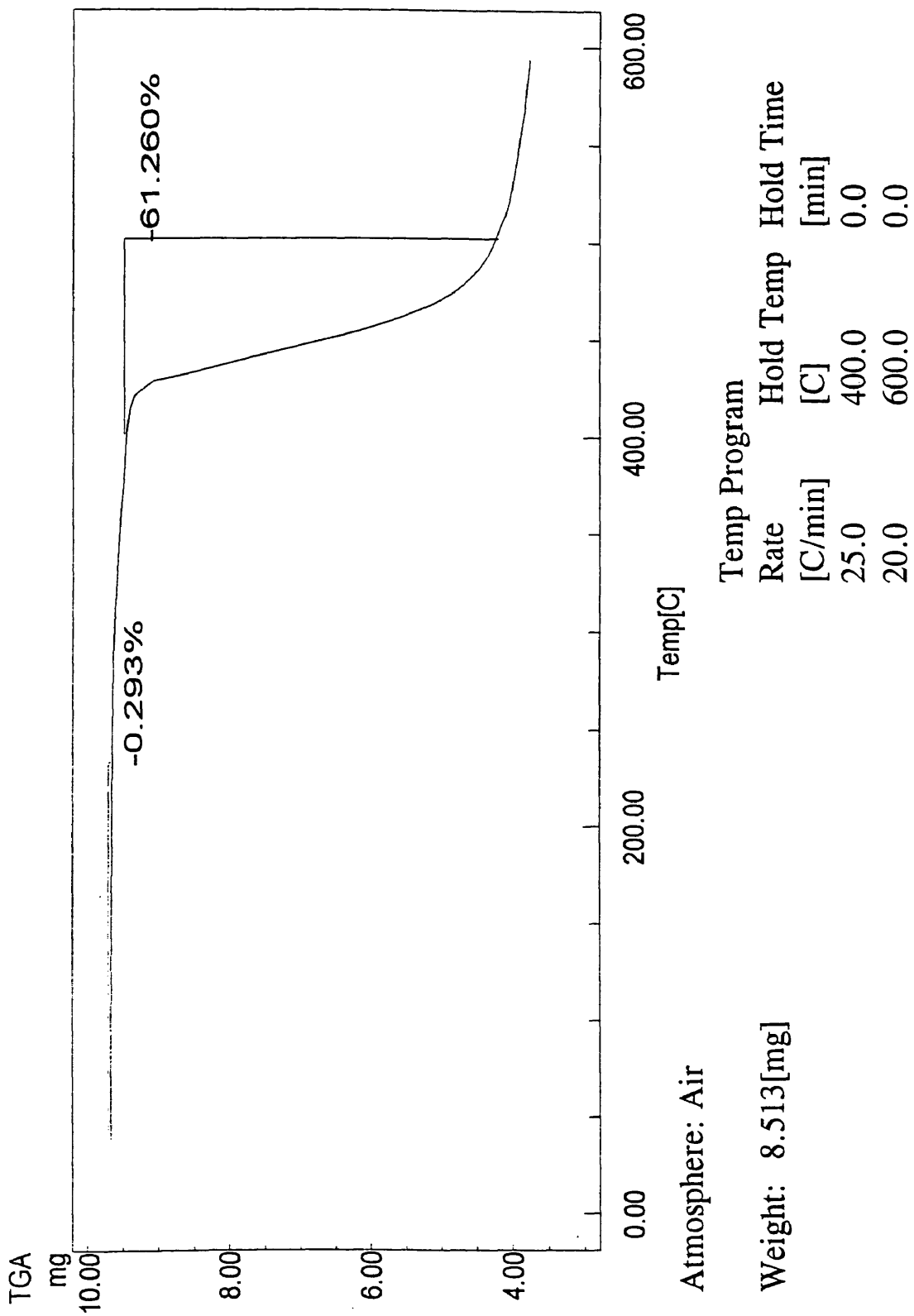


Figure 32: Thermogram of Hexcel 954-3 CE + 10% Cloisite-15A



## SEM Photographs

Figure 33: Pure BPA-based CE Control x150

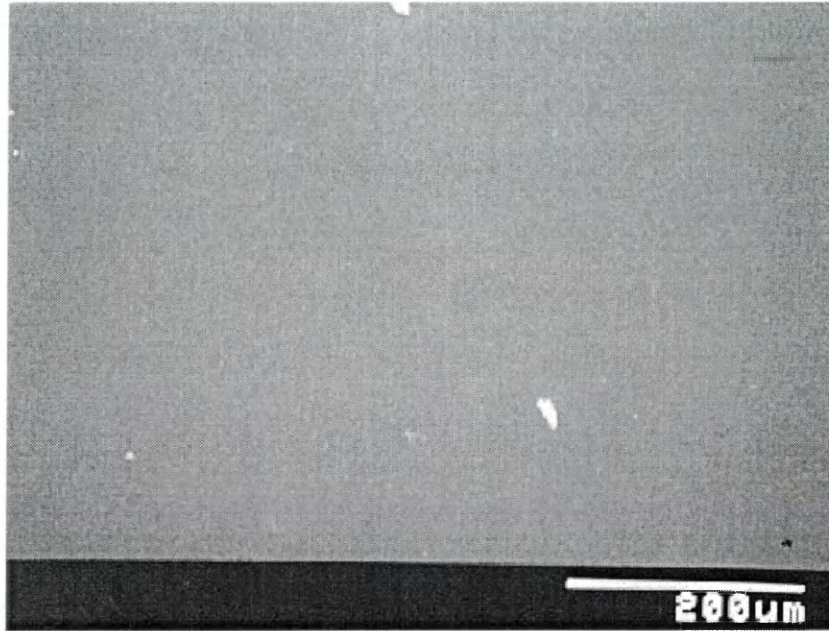


Figure 34: Pure BPA-based CE AO Exposed x150

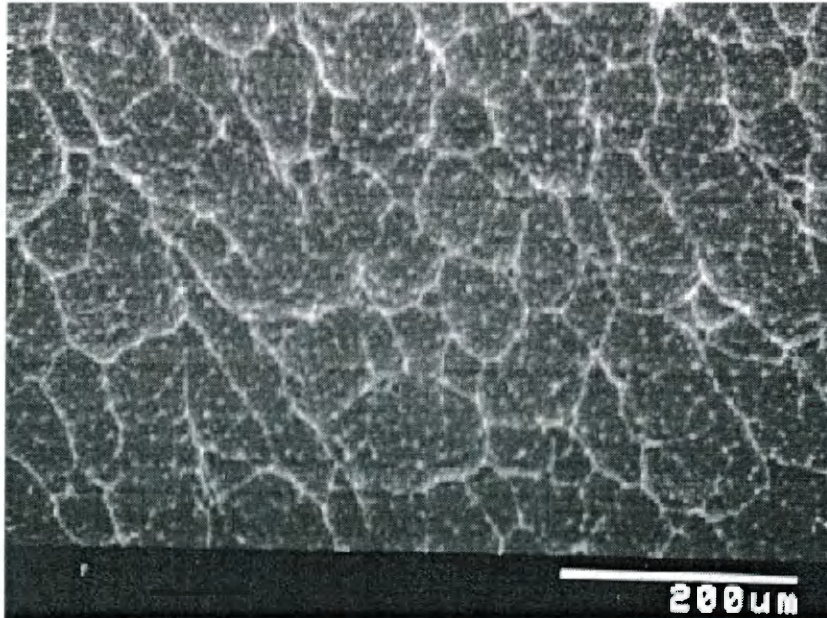


Figure 35: Pure BPA-based CE AO Exposed x600

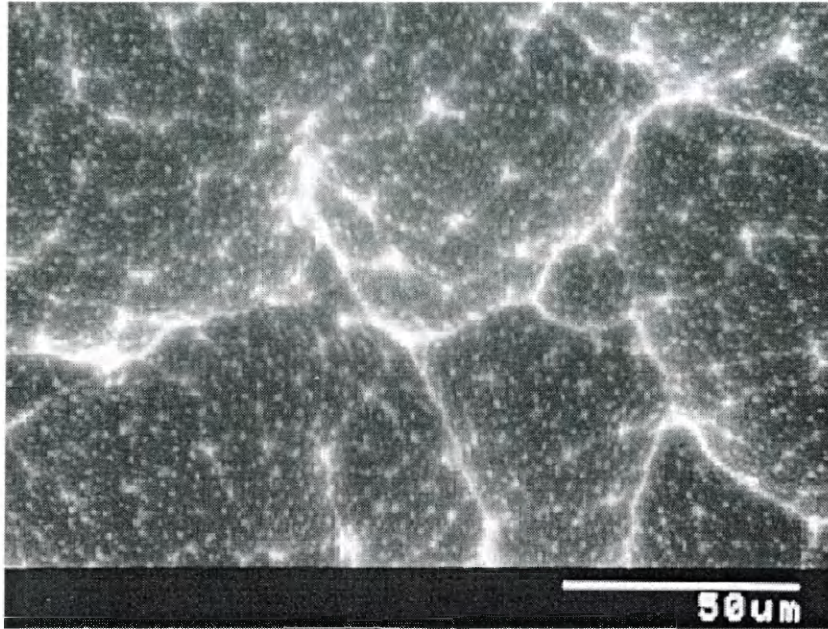


Figure 36: BPA-based CE + 10% Boron Carbide Back Control x150

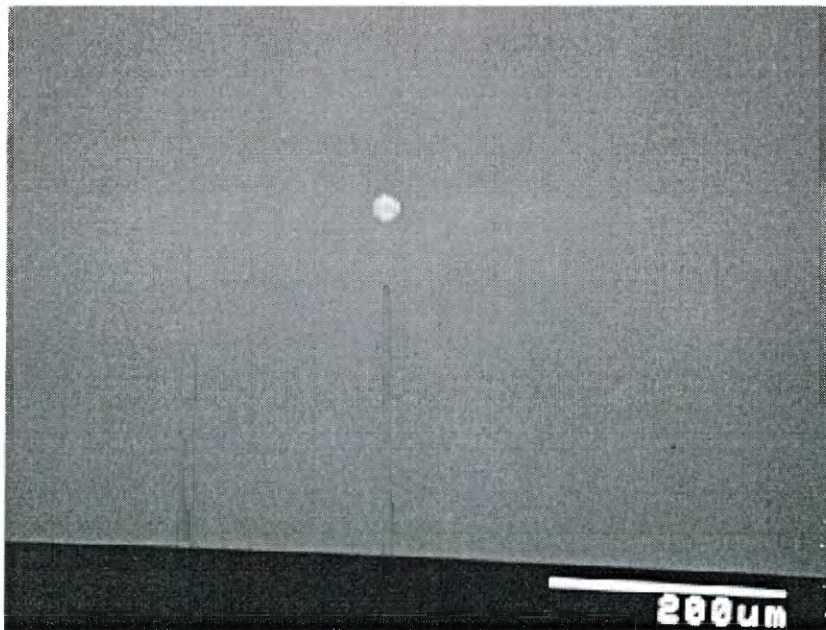


Figure 37: BPA-based CE + 10% Boron Carbide Back Control x600

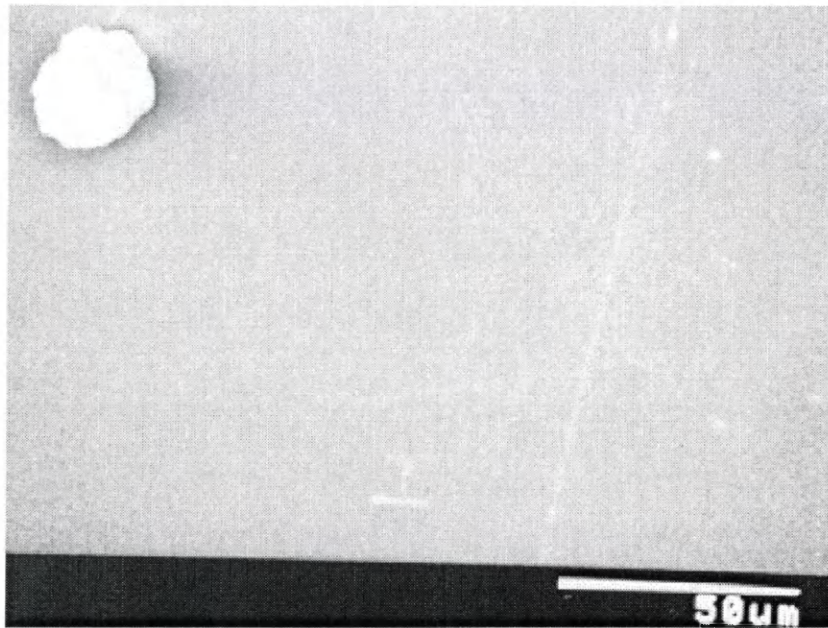


Figure 38: BPA-based CE + 10% Boron Carbide Back AO Exposed x150

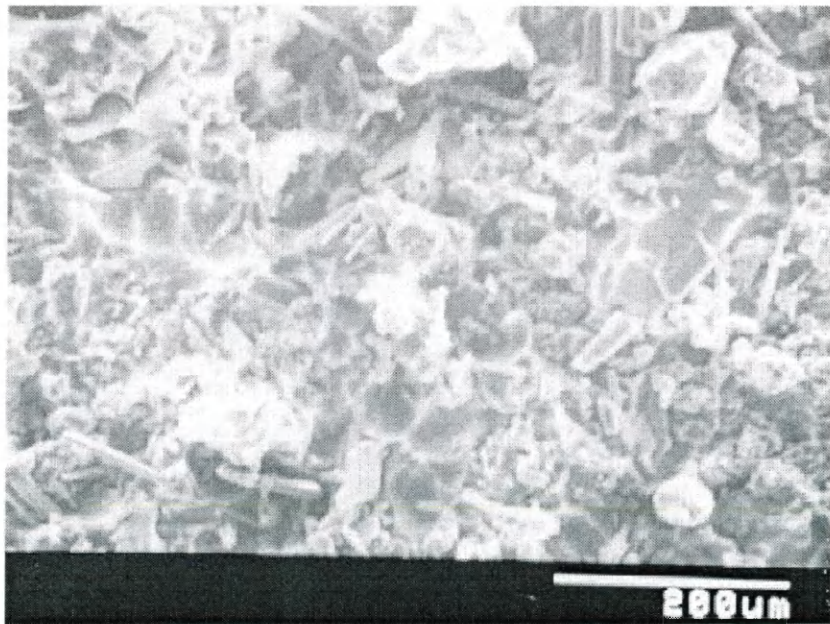


Figure 39: BPA-based CE + 10% Boron Carbide Back AO Exposed x600

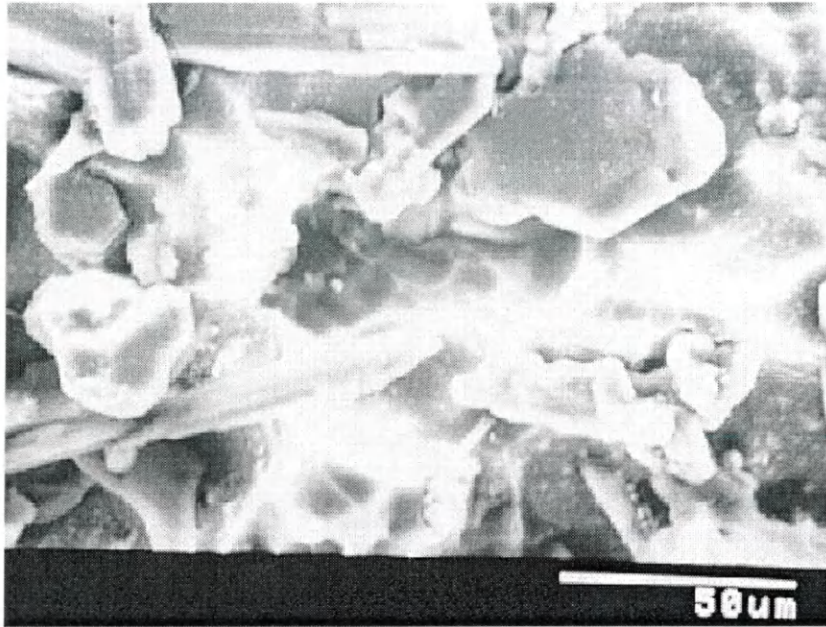


Figure 40: BPA-based CE + 10% Boron Carbide Front Control x150

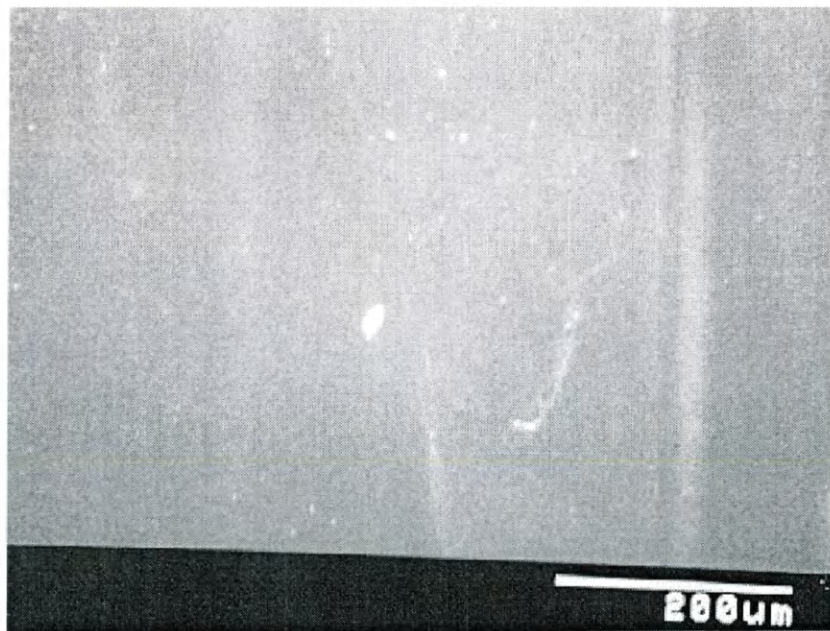


Figure 41: BPA-based CE + 10% Boron Carbide Front Control x600

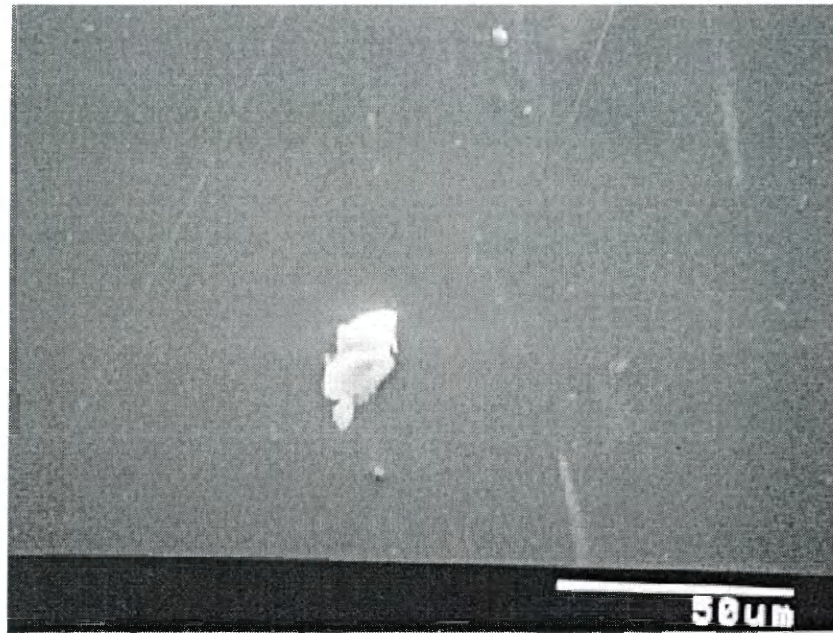


Figure 42: BPA-based CE + 10% Boron Carbide Front AO Exposed x20

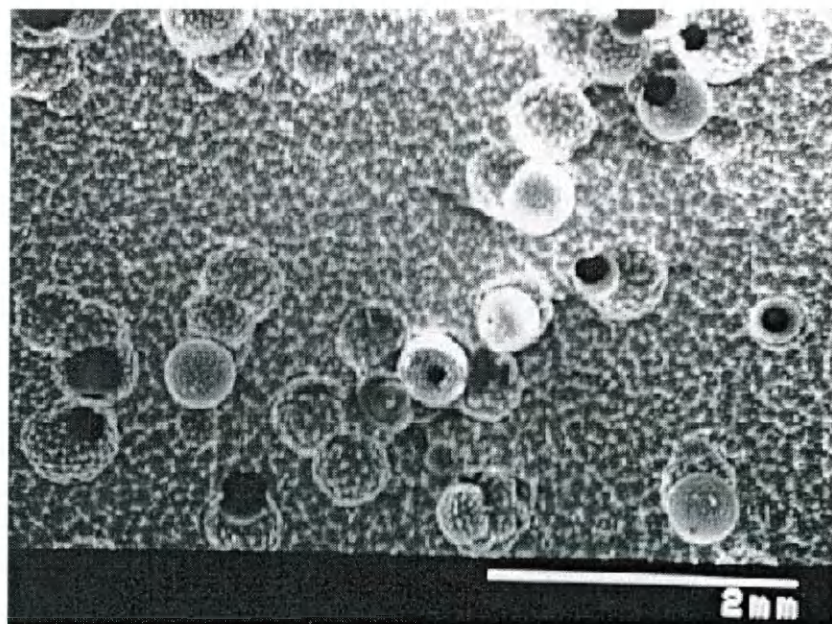


Figure 43: BPA-based CE + 10% Boron Carbide Front AO Exposed x60

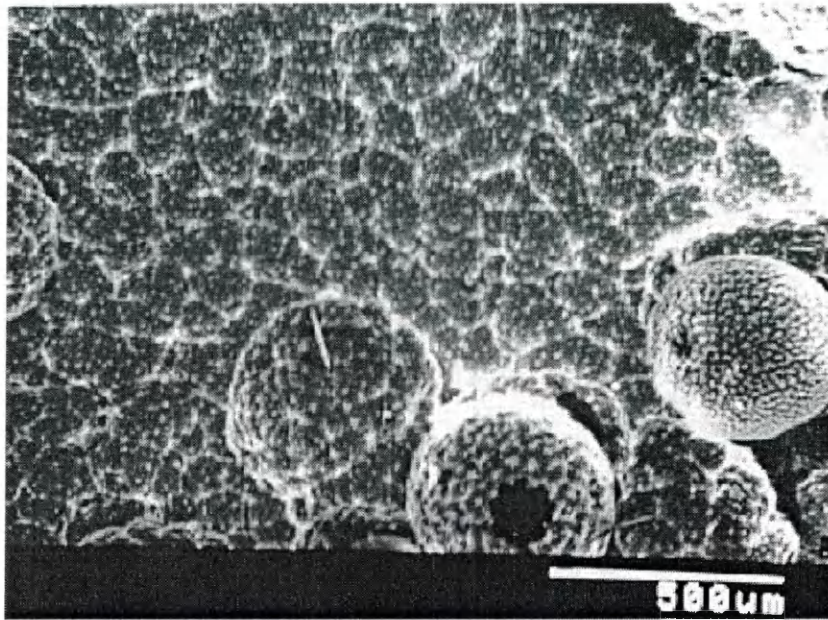


Figure 44: BPA-based CE + 10% Boron Carbide Front AO Exposed x150

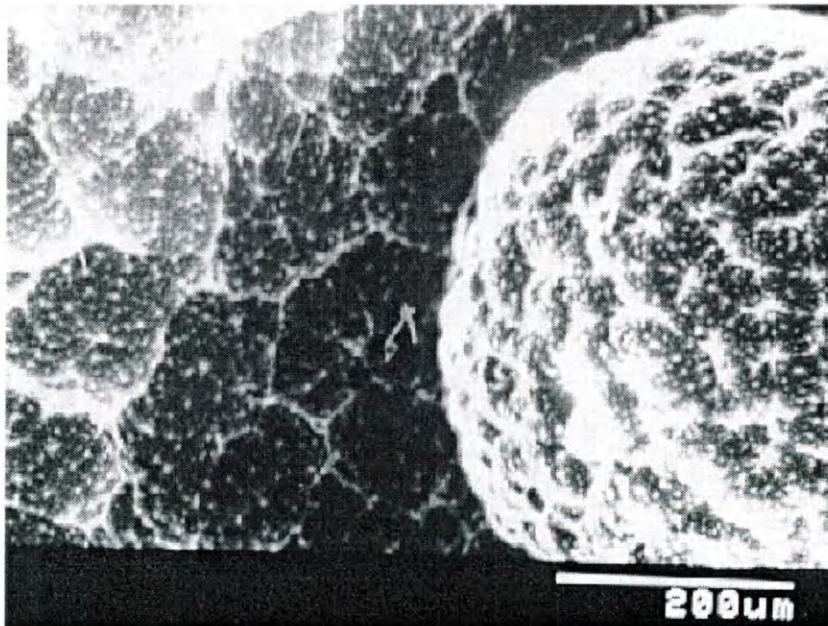
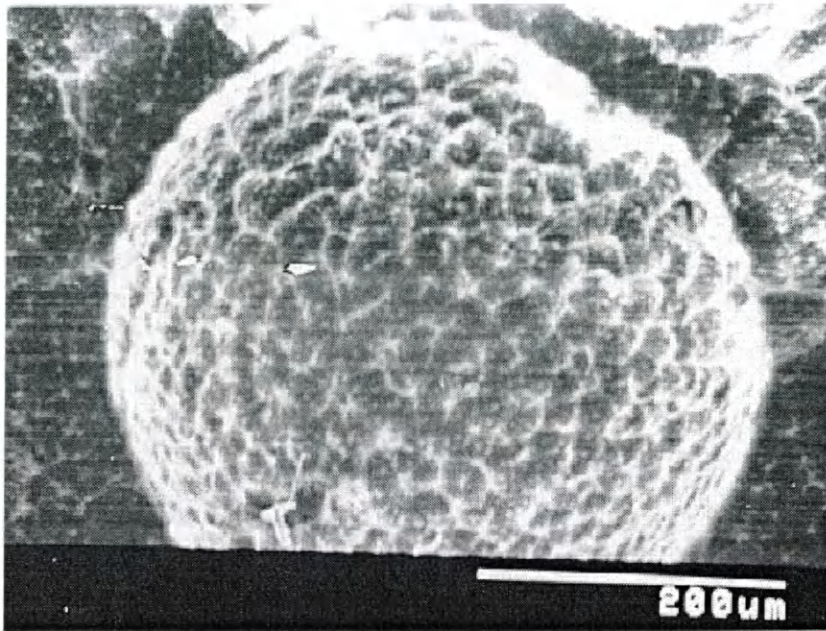


Figure 45: BPA-based CE + 10% Boron Carbide Front AO Exposed x200



# XPS Spectra

Figure 46: Pure BPA-based CE Control

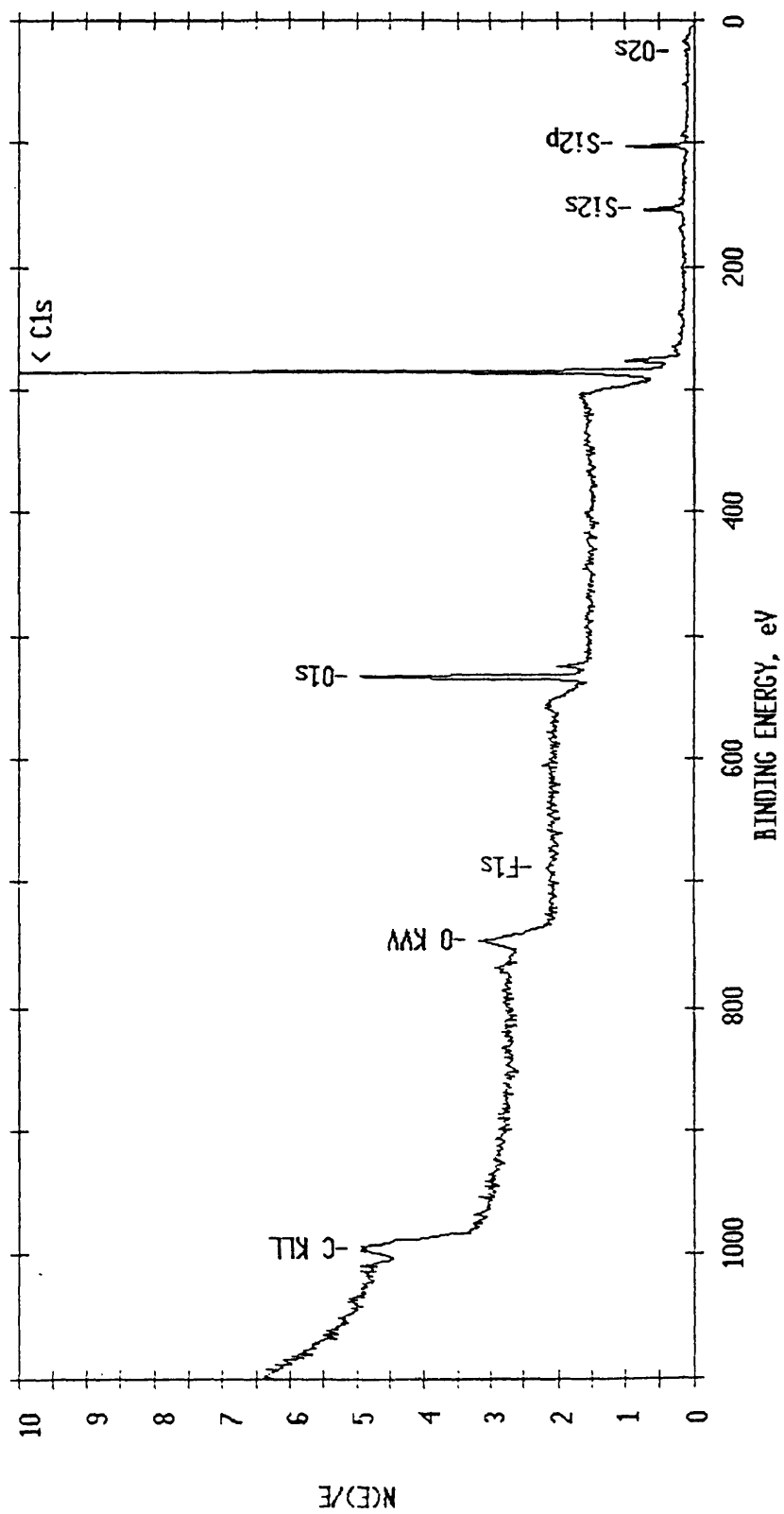


Figure 47: Pure BPA-based CE AO Exposed

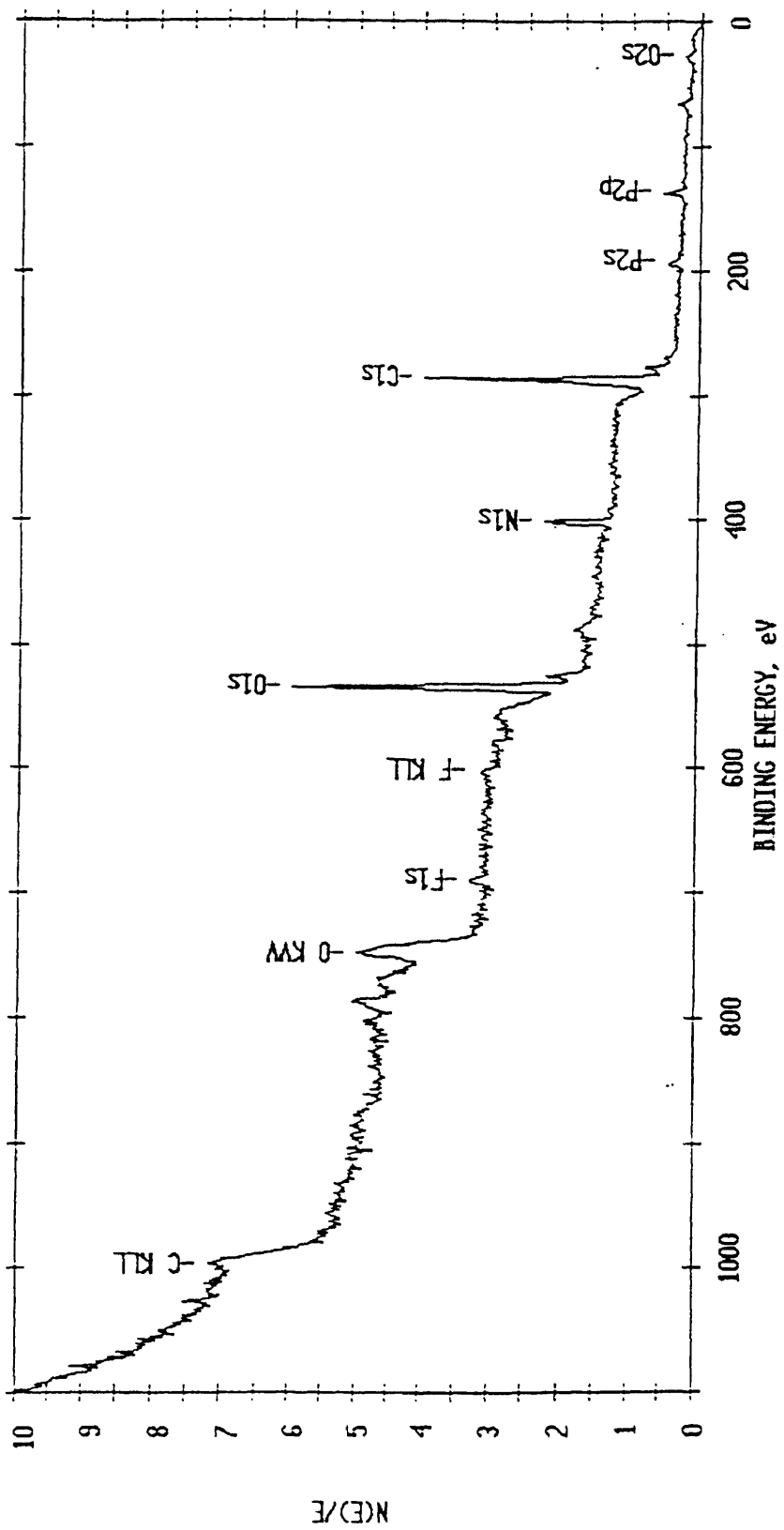


Figure 48: BPA + 10 wt. % B<sub>4</sub>C Back Surface Control

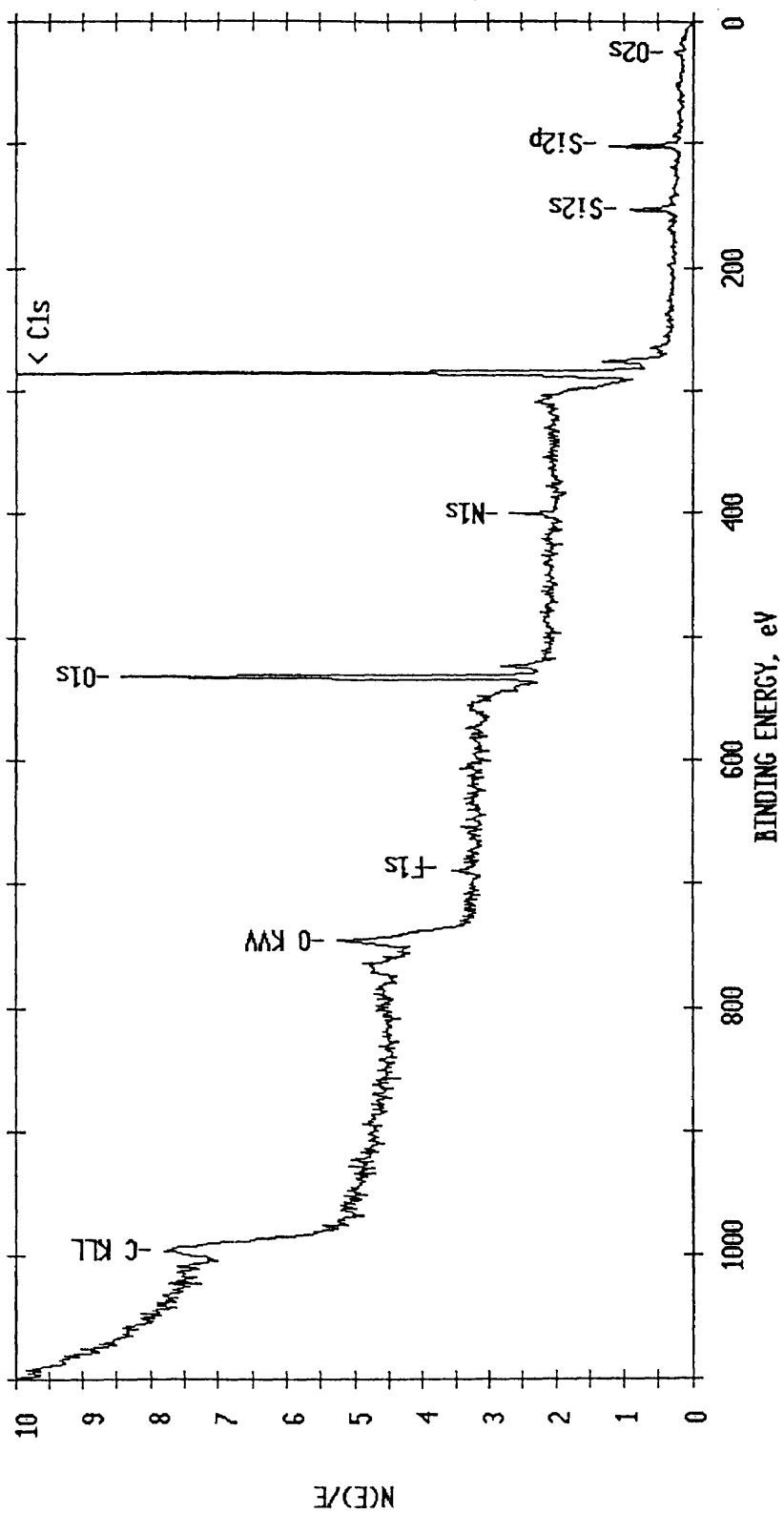


Figure 49: BPA + 10 wt. % B<sub>4</sub>C Back Surface AO Exposed

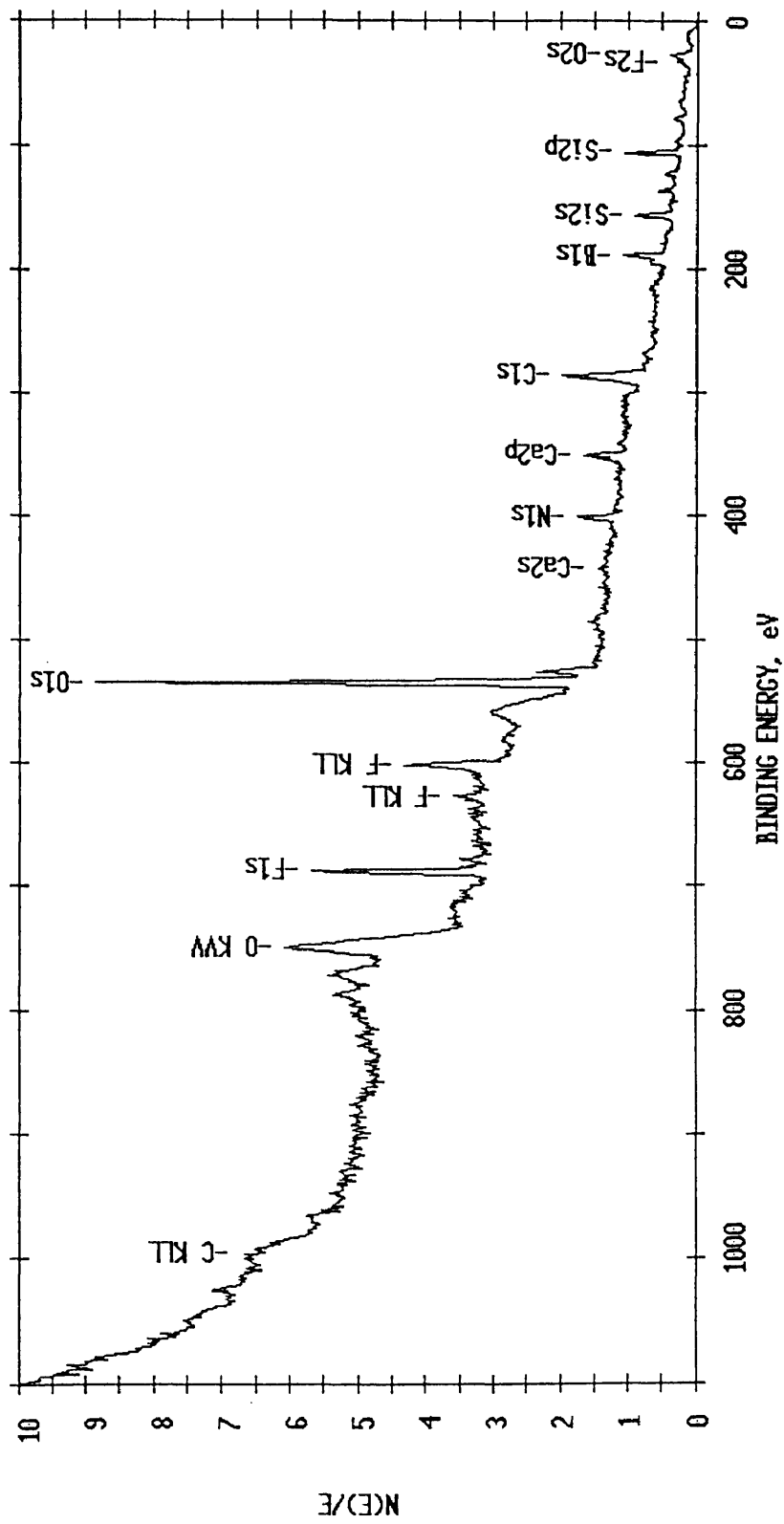


Figure 50: BPA + 10 wt. % B<sub>4</sub>C Front Surface Control

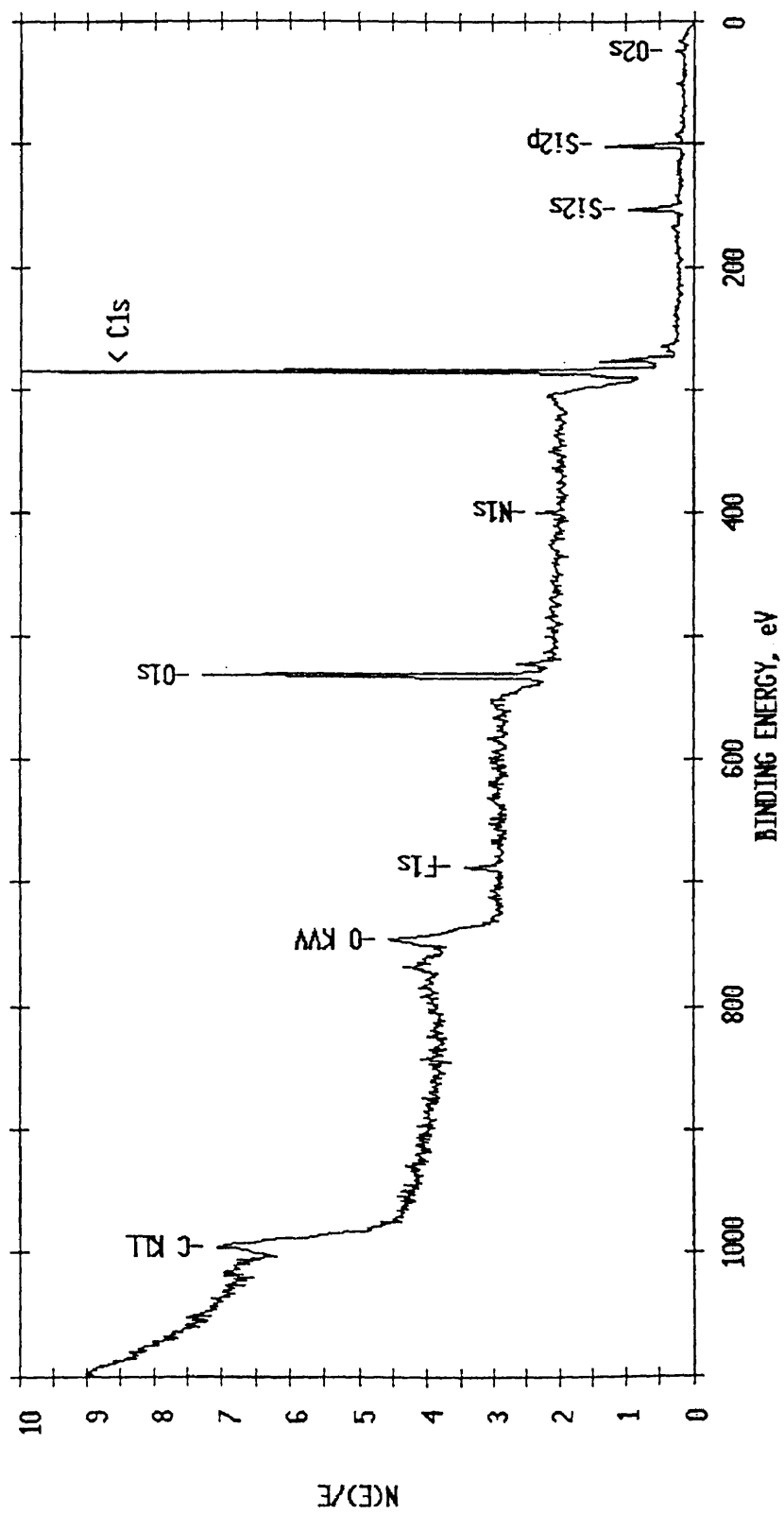


Figure 51 : BPA + 10 wt. % B<sub>4</sub>C Front Surface AO Exposed

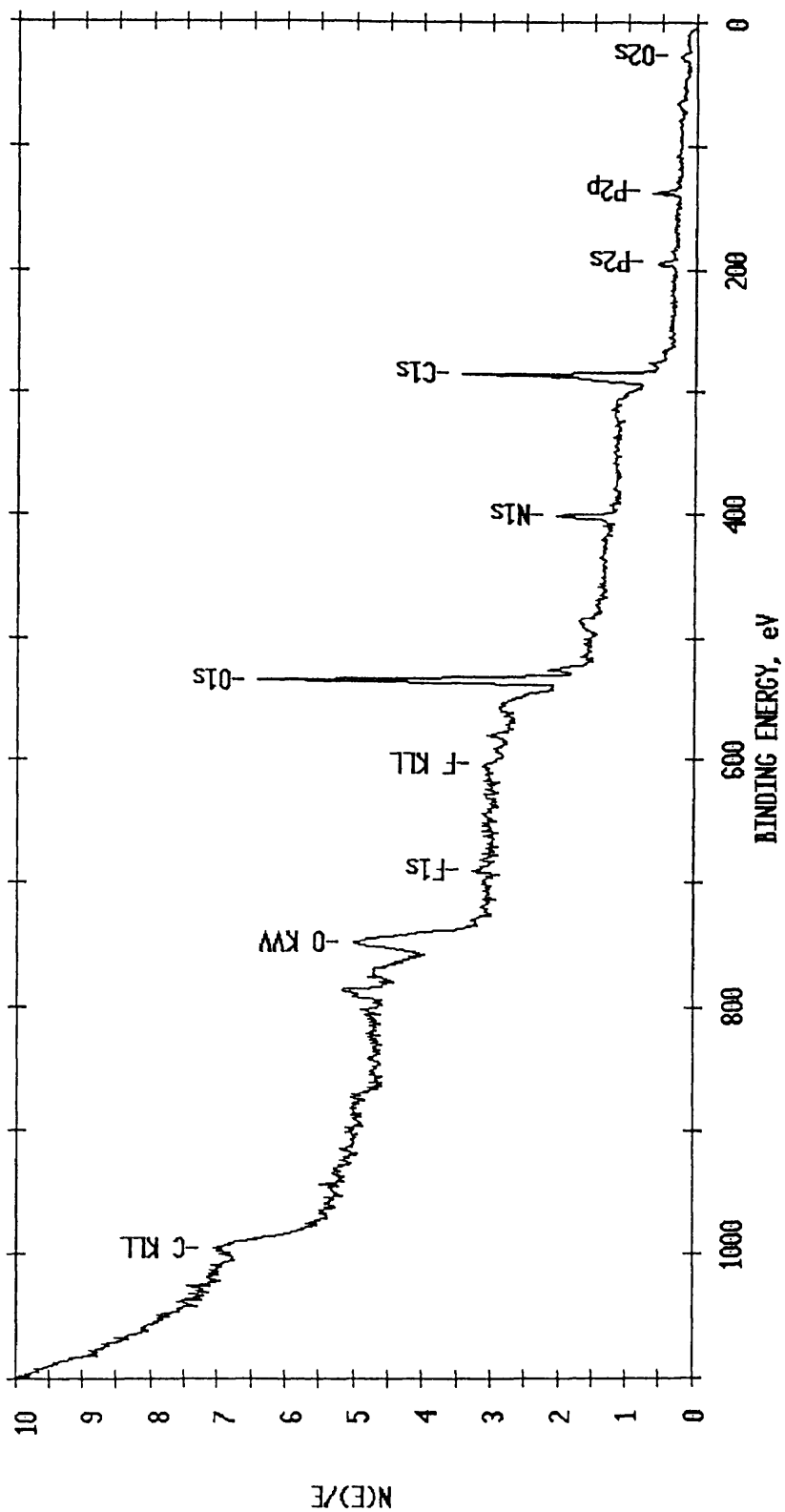


Figure 52 : Pure BPA-based CE Carbon Peak Control

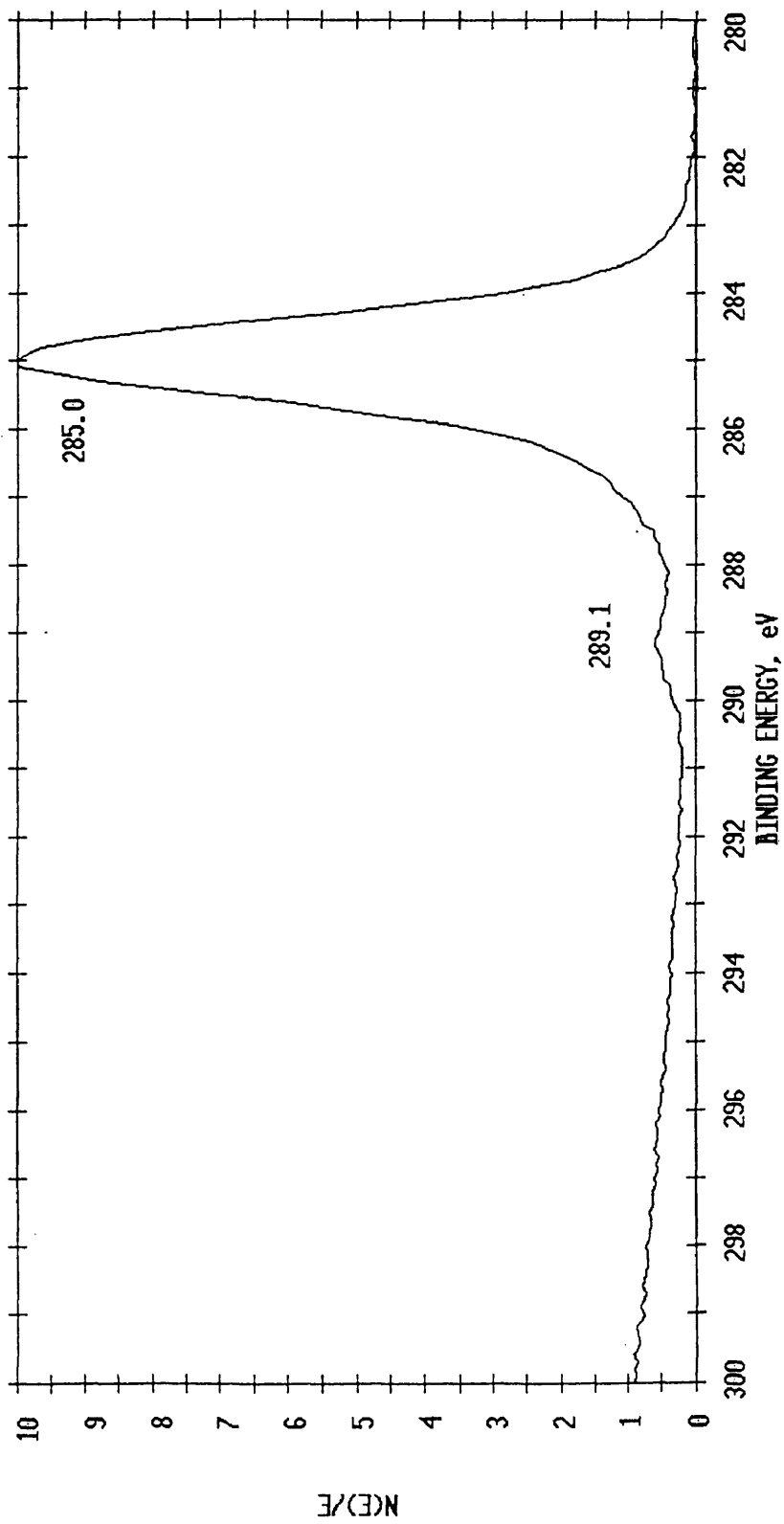


Figure 53: Pure BPA-based CE Oxygen Peak Control

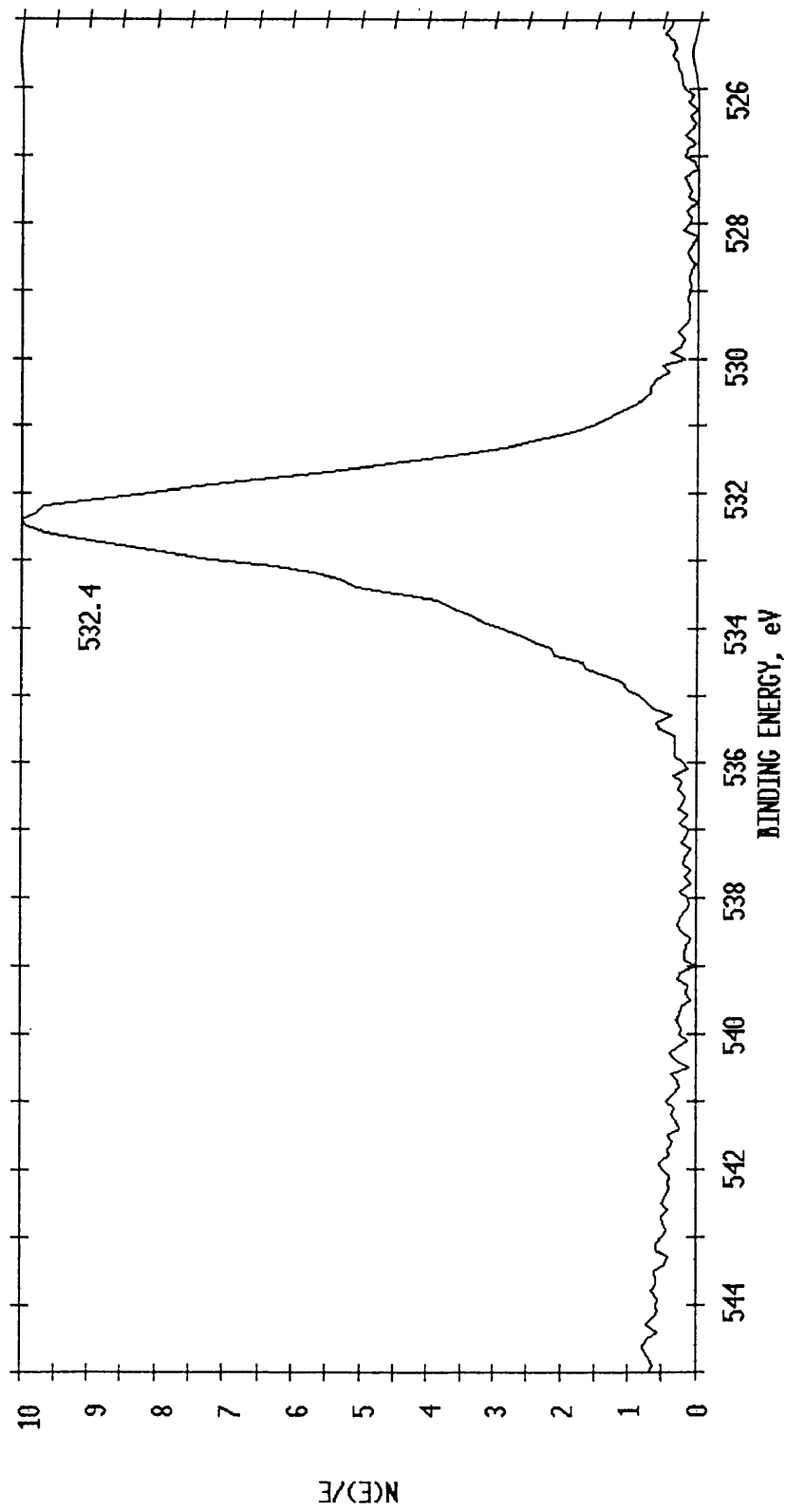


Figure 54: Pure BPA-based CE Nitrogen Peak Control

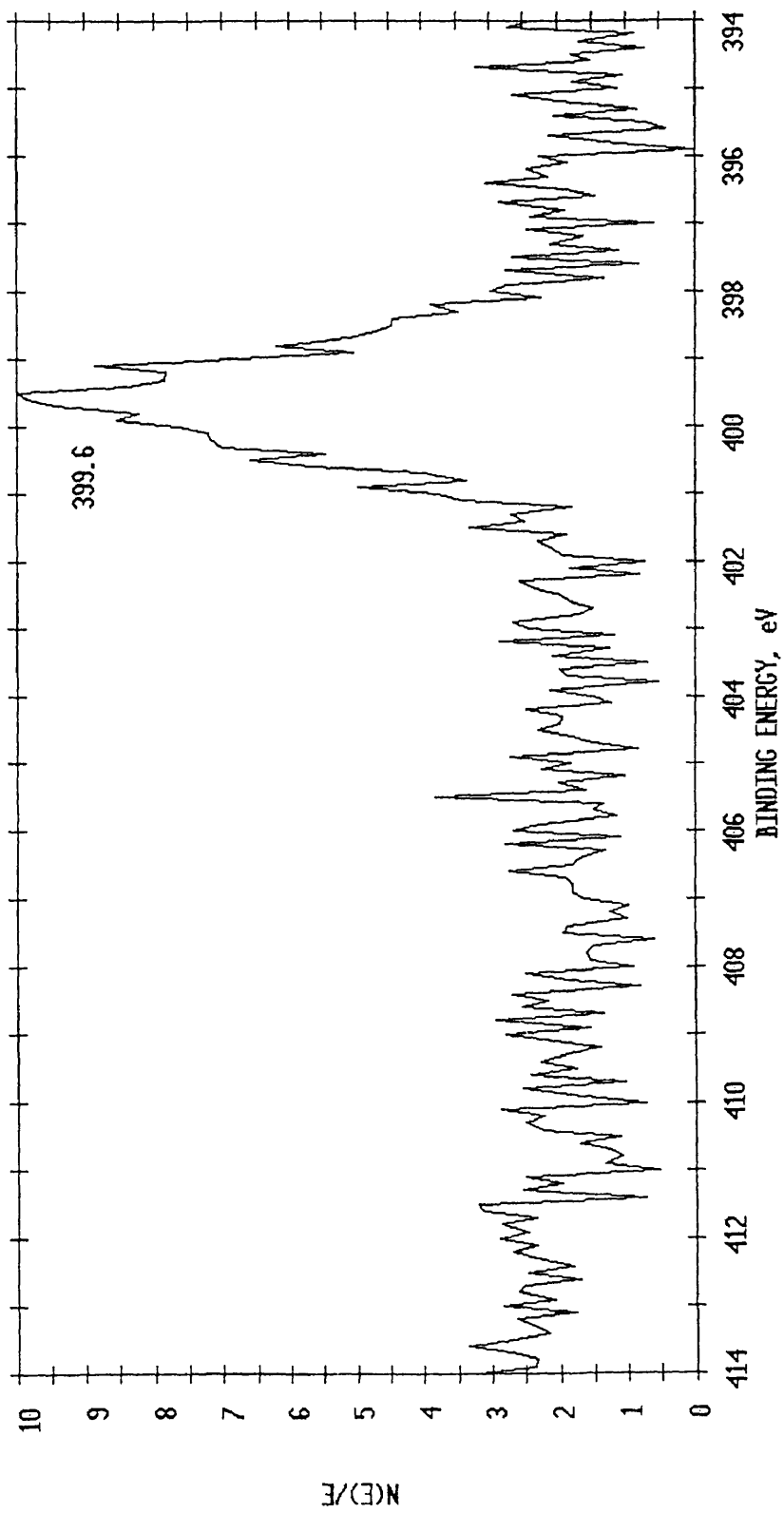


Figure 55: Pure BPA-based CE Carbon Peak AO Exposed

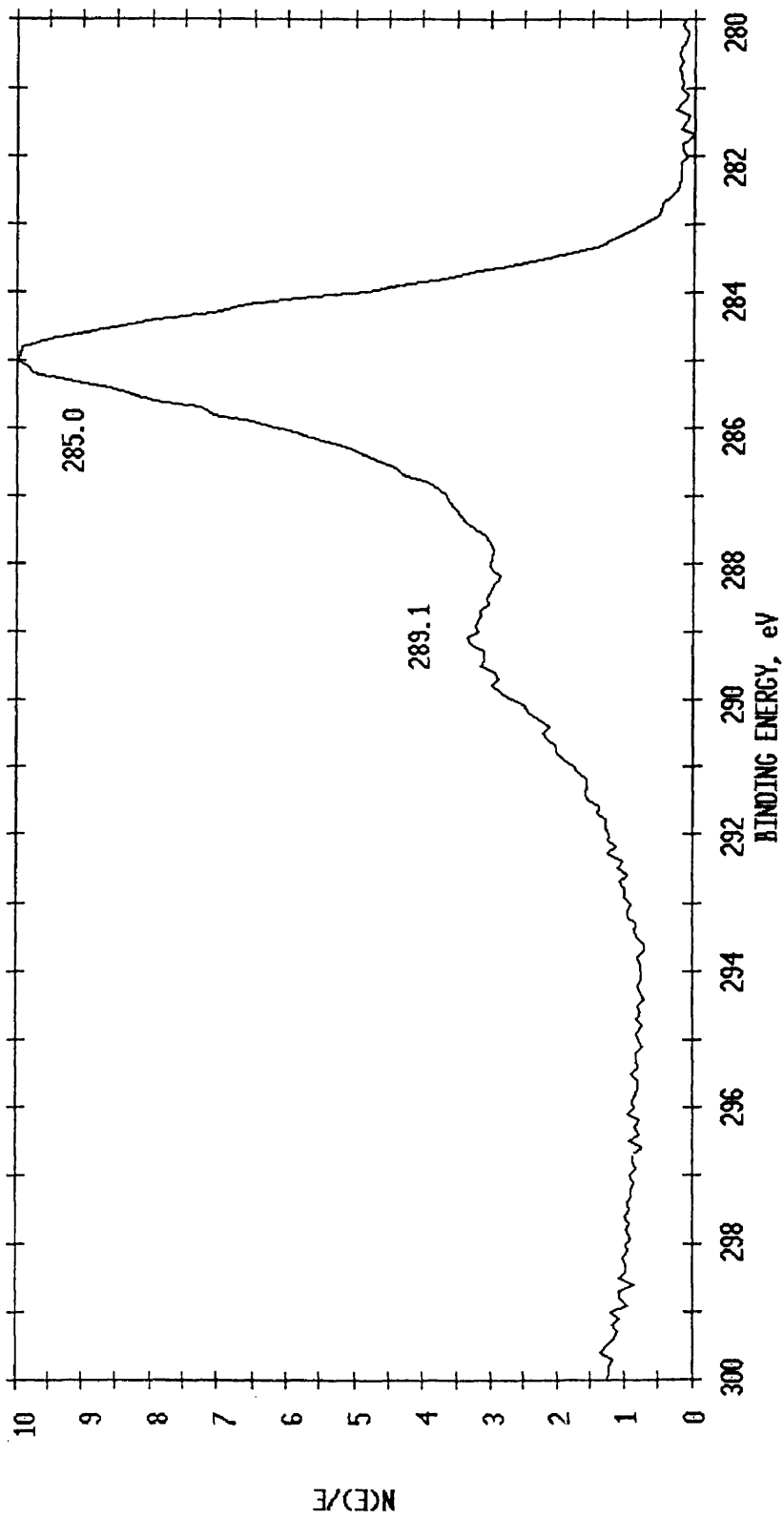


Figure 56: Pure BPA-based CE Oxygen Peak AO Exposed

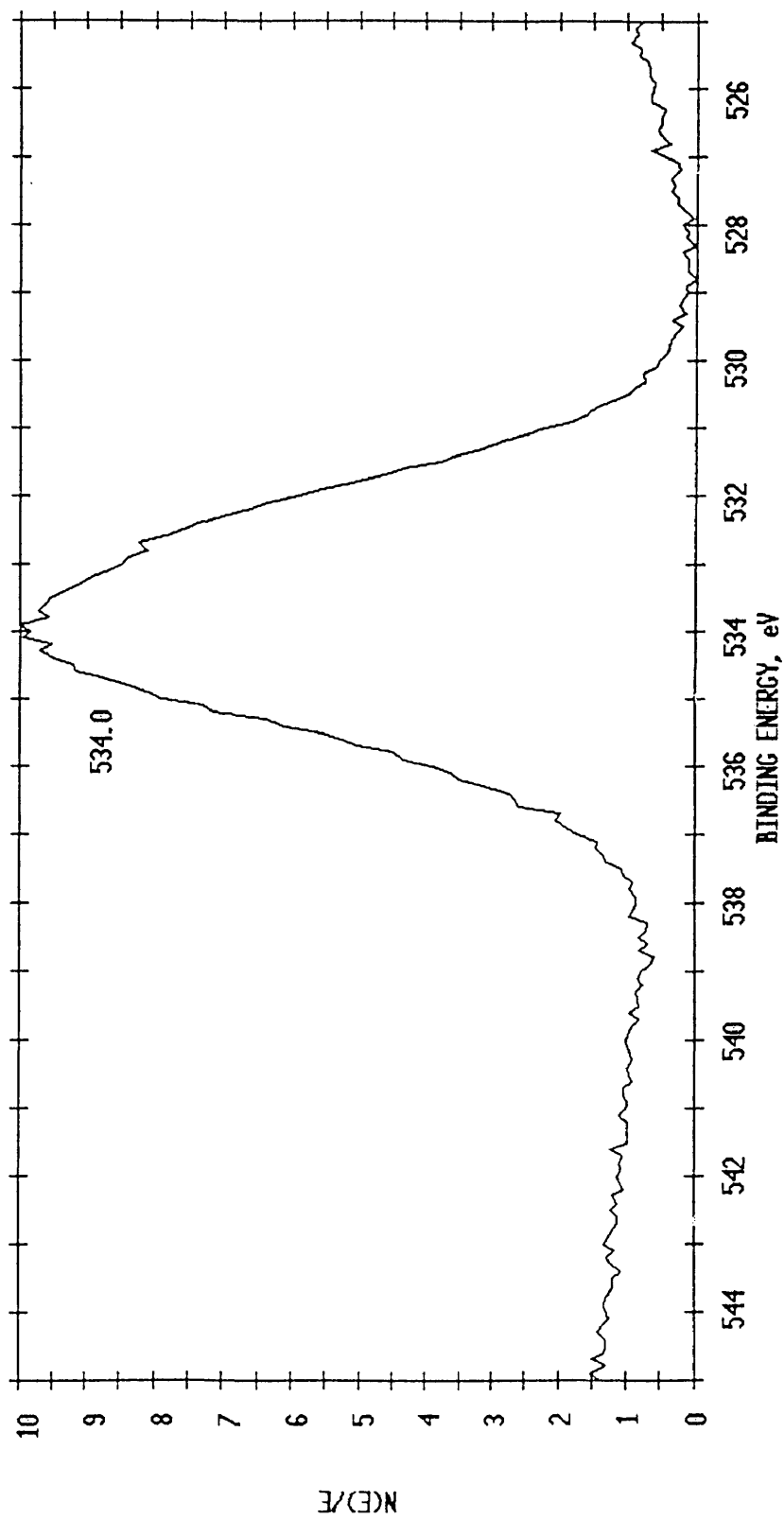


Figure 57: Pure BPA-based CE Nitrogen Peak AO Exposed

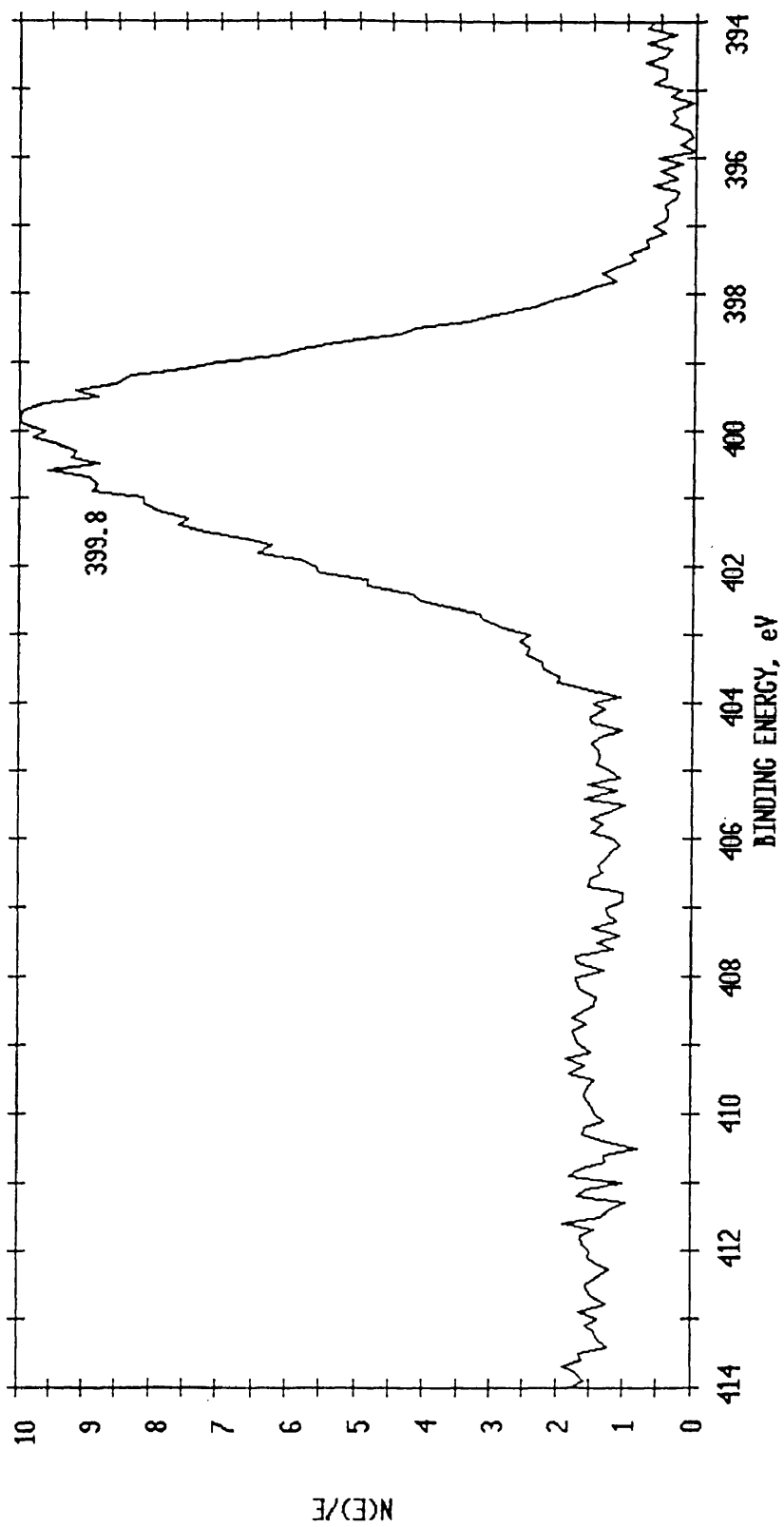


Figure 58: BPA-based CE + 10 wt. % B<sub>4</sub>C Back Surface Carbon Peak Control

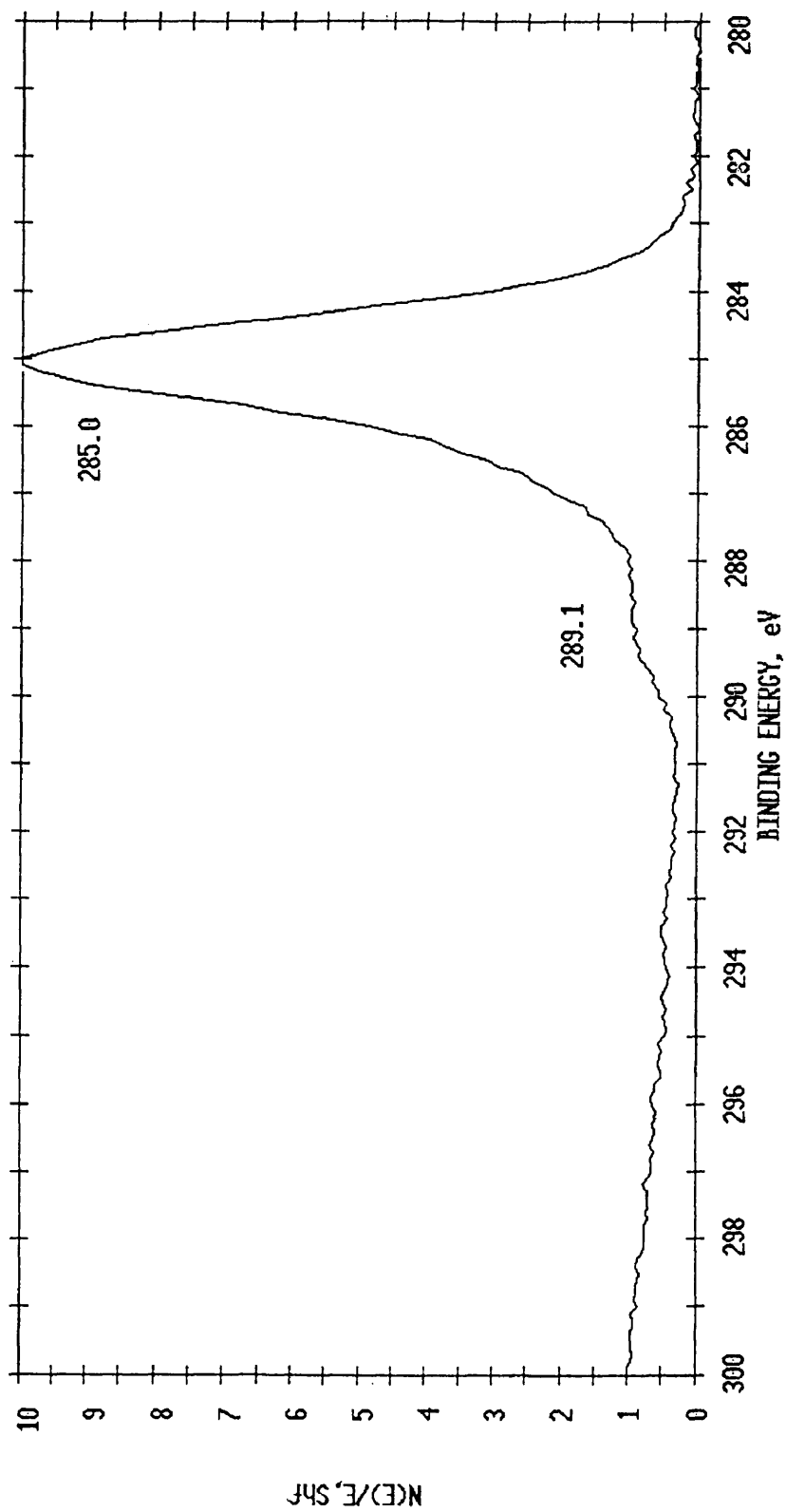


Figure 59: BPA-based CE + 10 wt. % B<sub>4</sub>C Back Surface Oxygen Peak Control

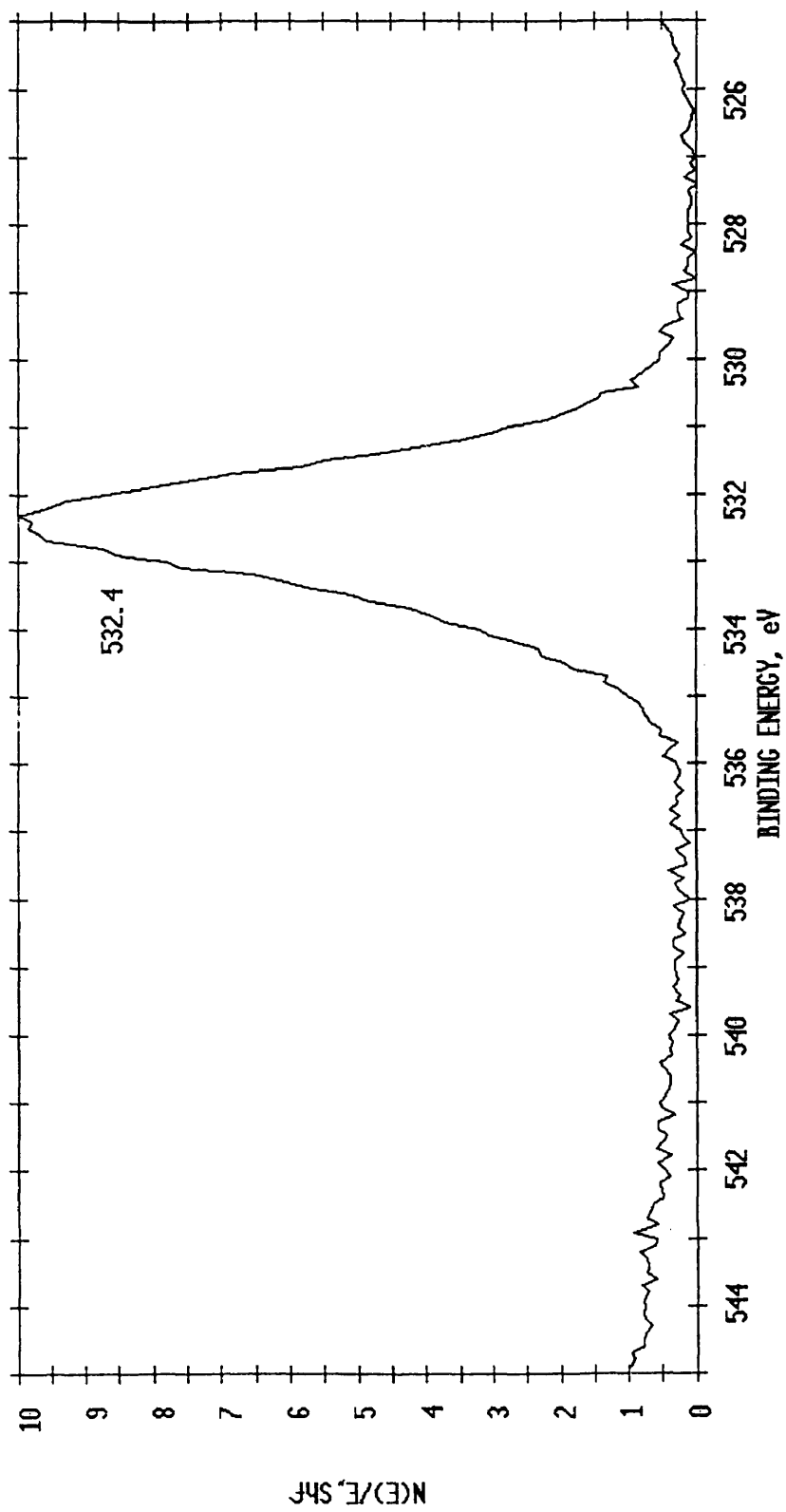


Figure 60: BPA-based CE + 10 wt. % B<sub>4</sub>C Back Surface Nitrogen Peak Control

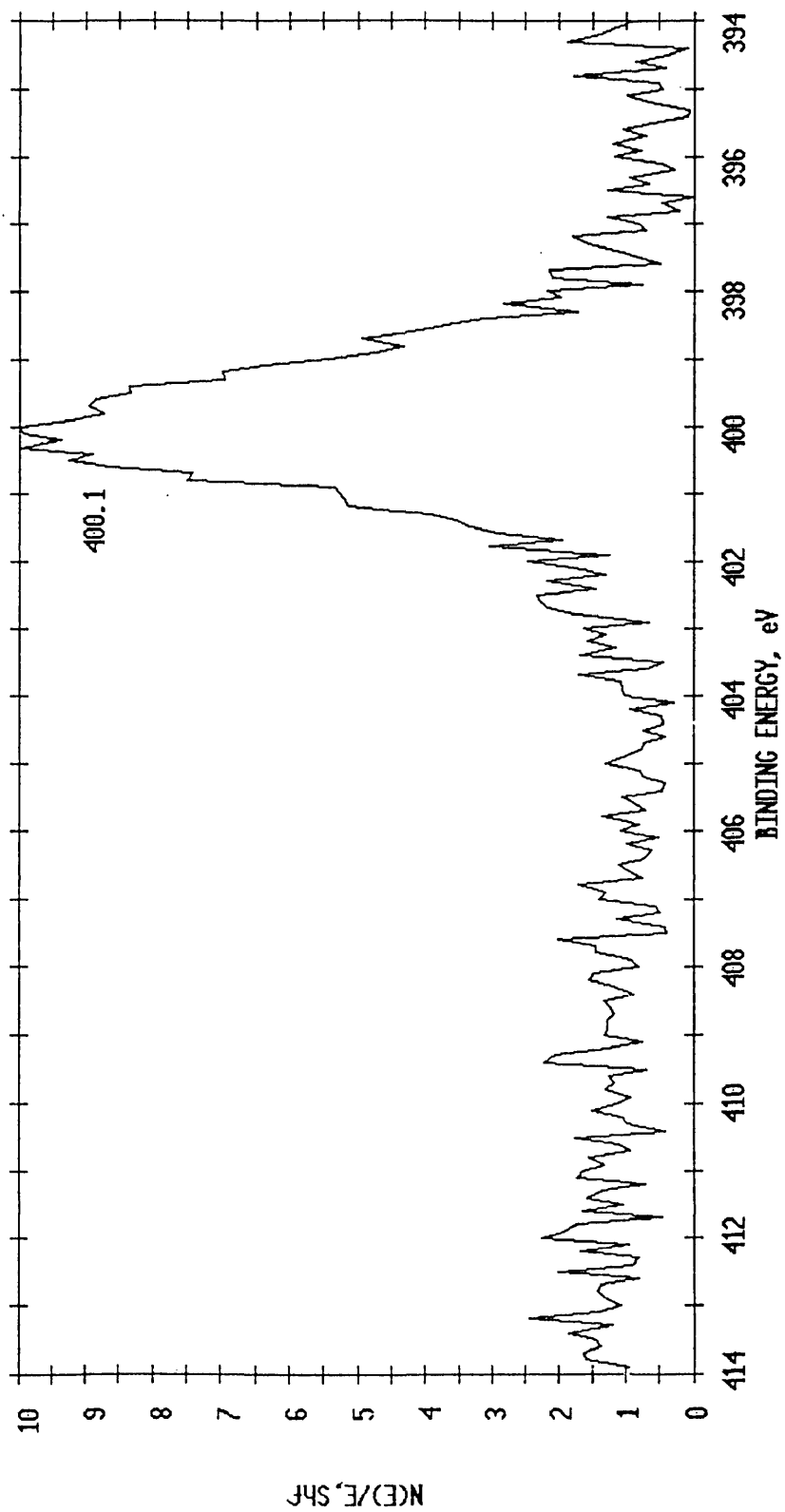


Figure 61: BPA-based CE + 10 wt. % B<sub>4</sub>C Back Surface Boron Peak Control

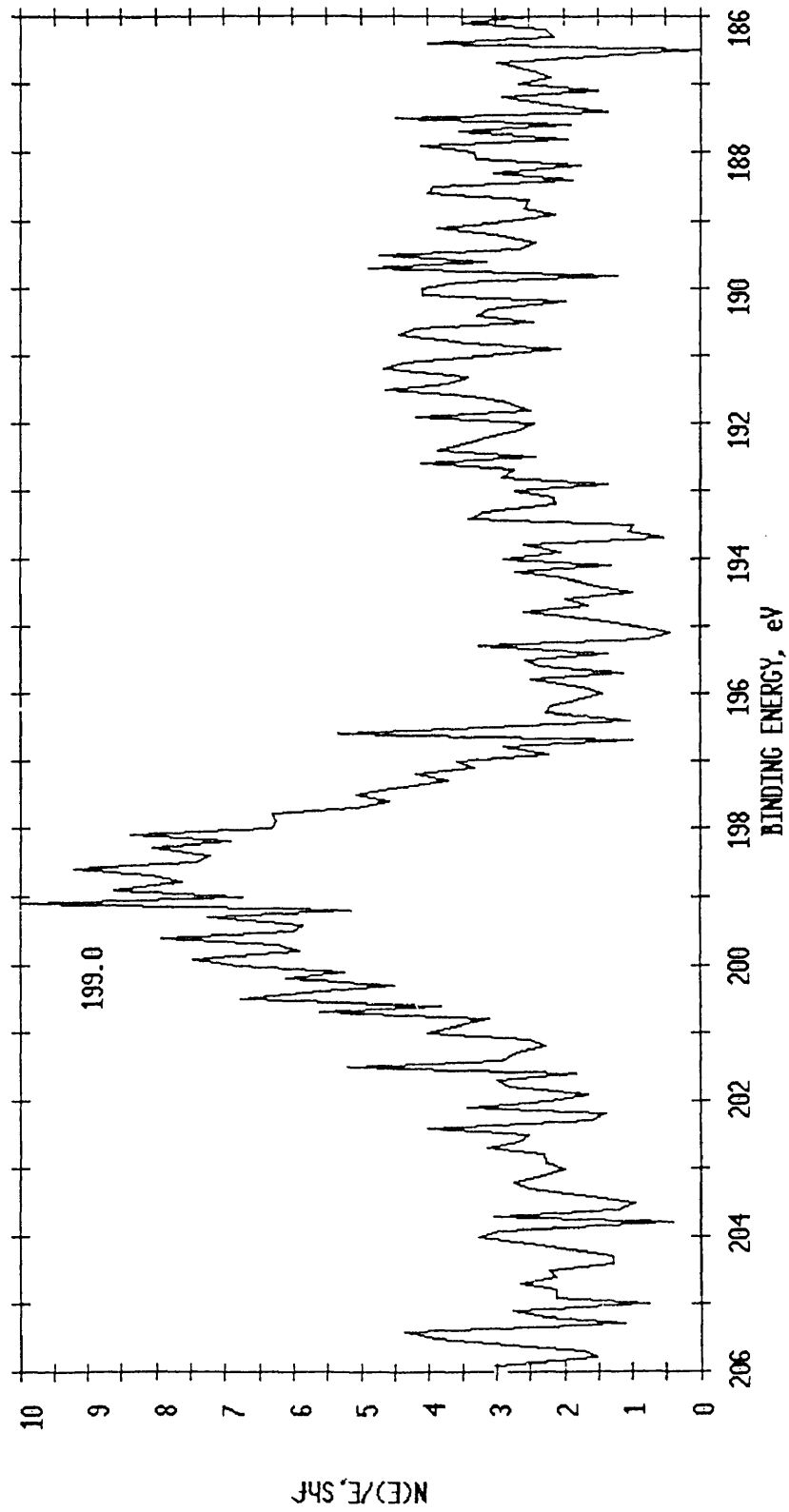


Figure 62: BPA-based CE + 10 wt. % B<sub>4</sub>C Back Surface Carbon Peak AO Exposed

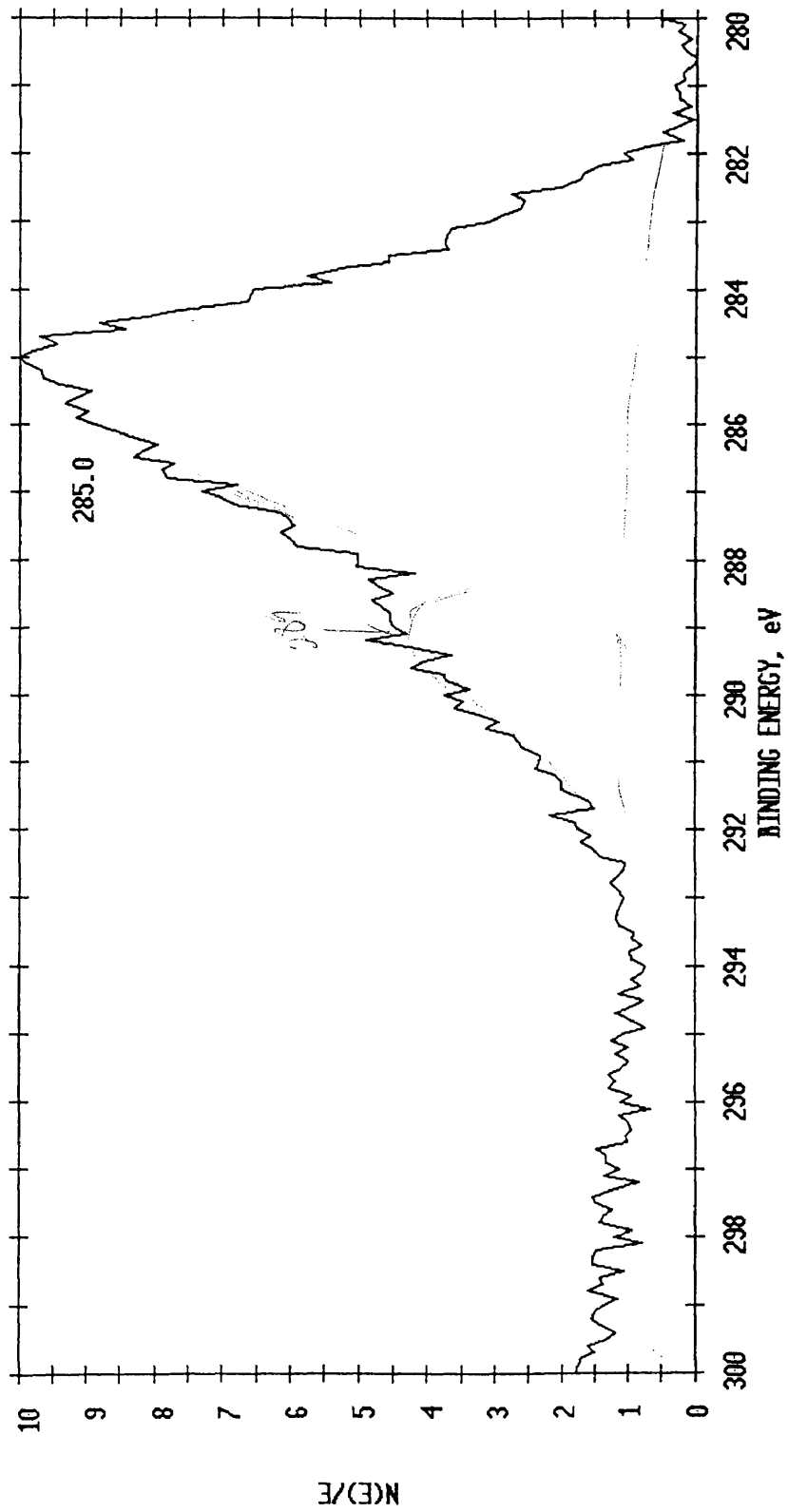


Figure 63: BPA-based CE + 10 wt. % B<sub>4</sub>C Back Surface Oxygen Peak AO Exposed

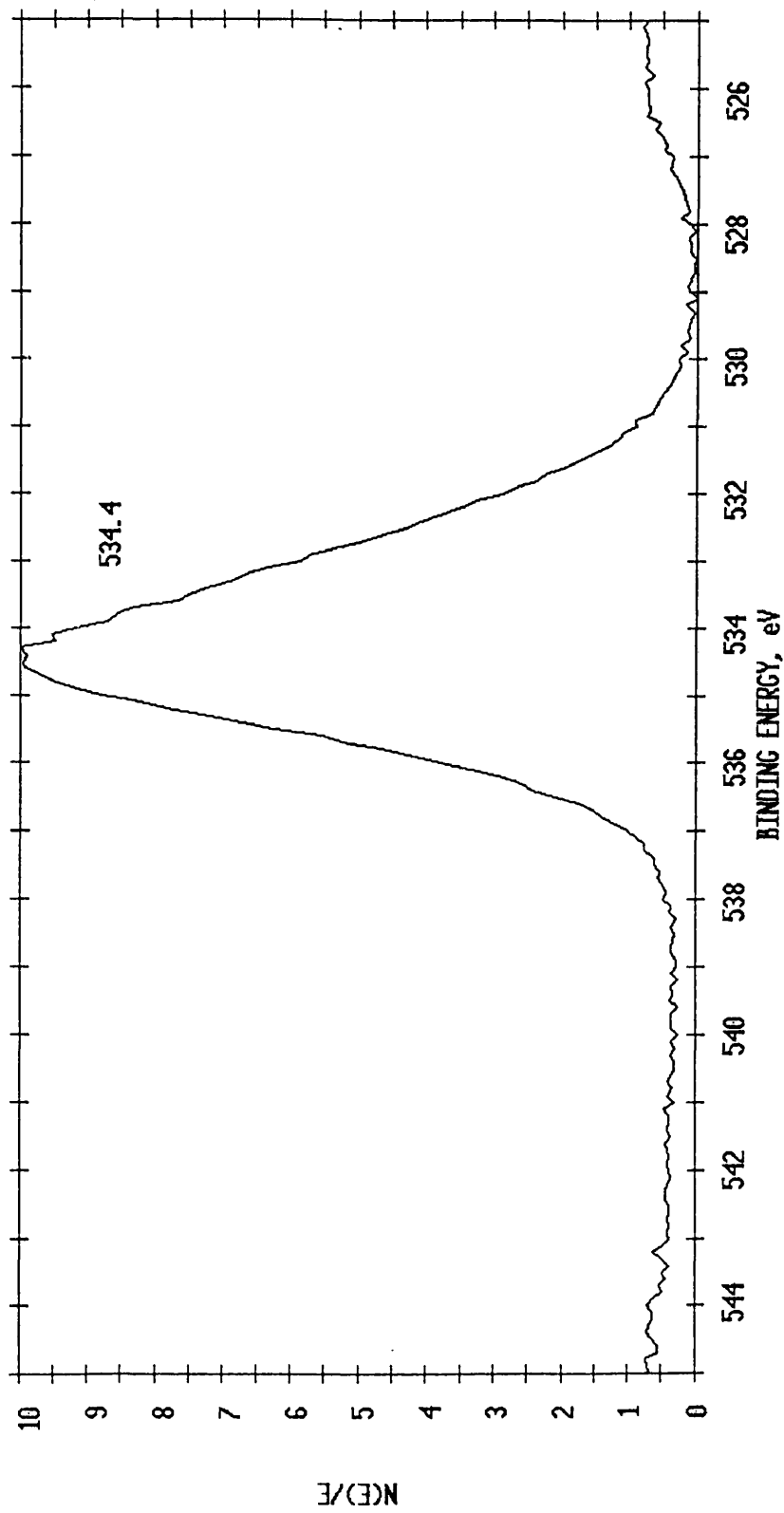


Figure 64: BPA-based CE + 10 wt. % B<sub>4</sub>C Back Surface Nitrogen Peak AO Exposed

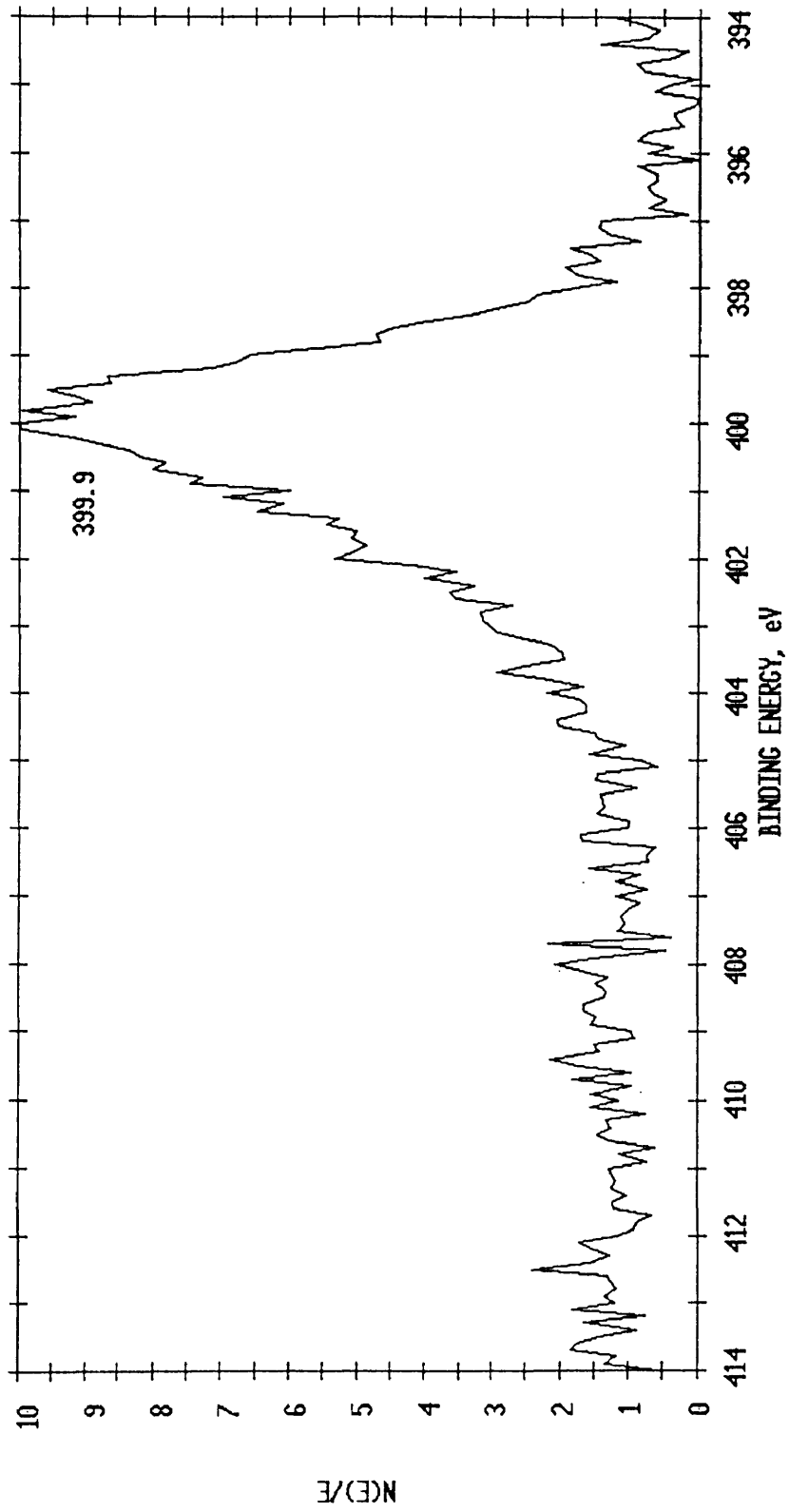


Figure 65: BPA-based CE + 10 wt. % B<sub>4</sub>C Back Surface Boron Peak AO Exposed

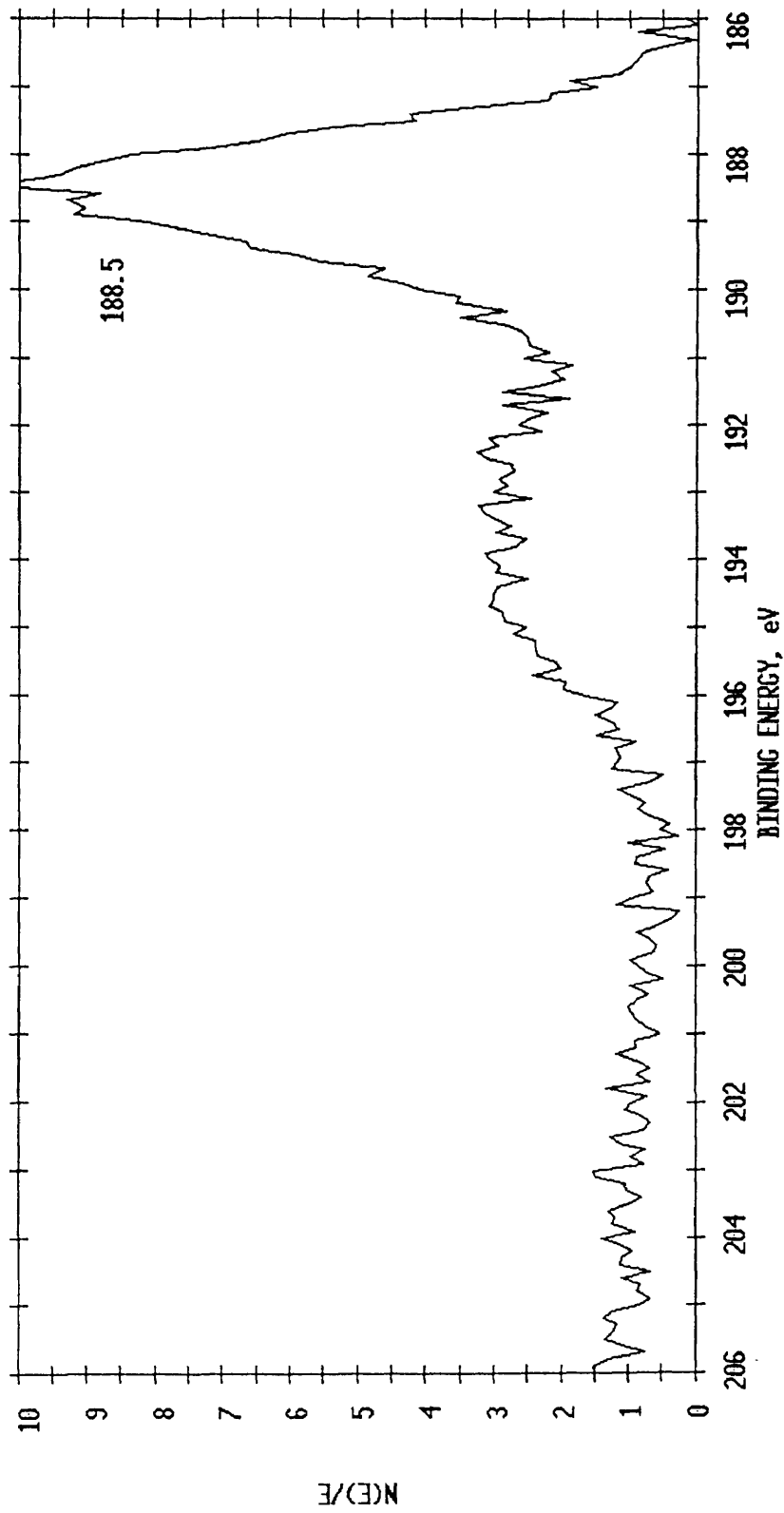


Figure 66: BPA-based CE + 10 wt. % B<sub>4</sub>C Front Surface Carbon Peak Control

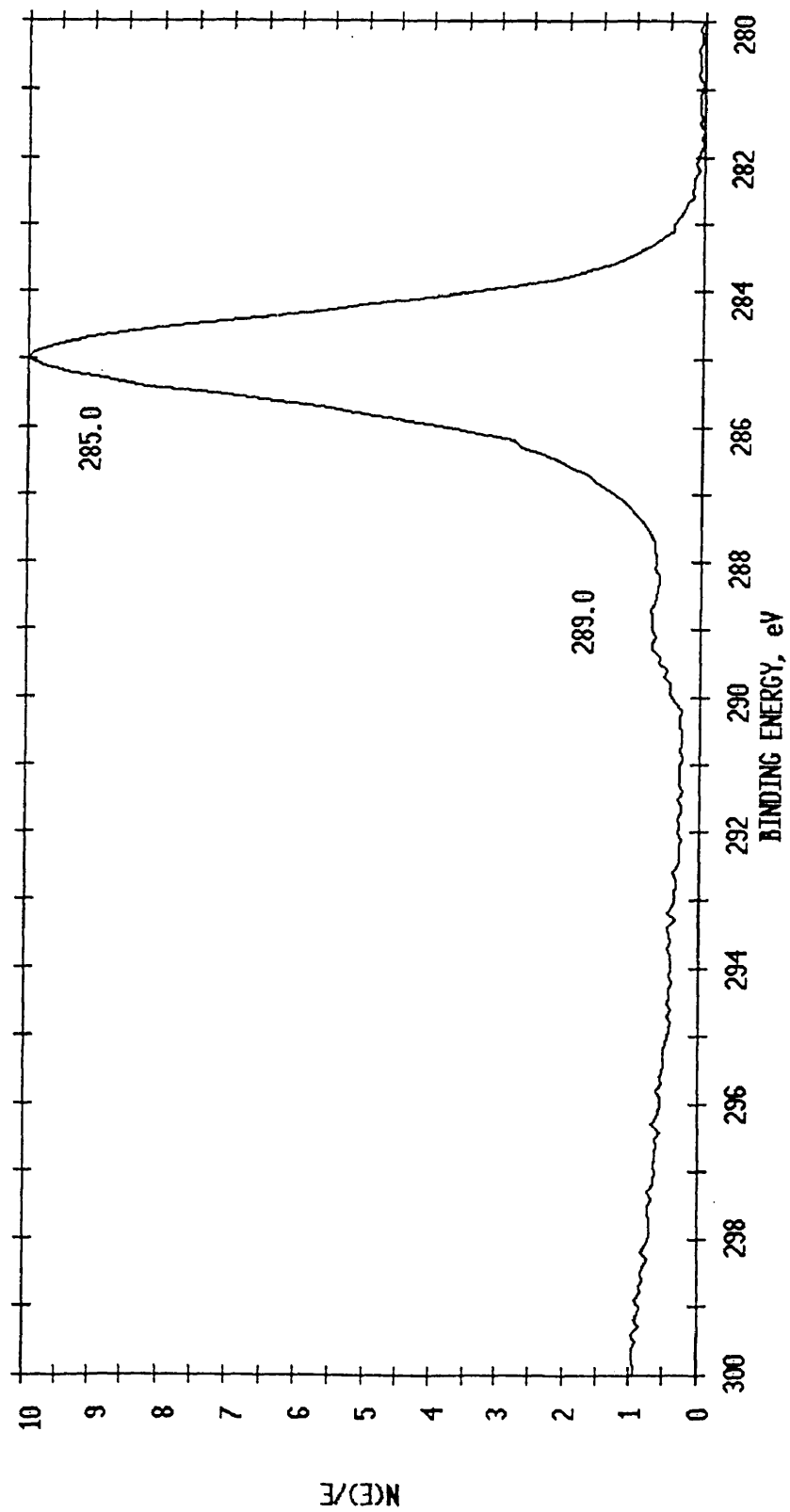


Figure 67: BPA-based CE + 10 wt. % B<sub>4</sub>C Front Surface Oxygen Peak Control

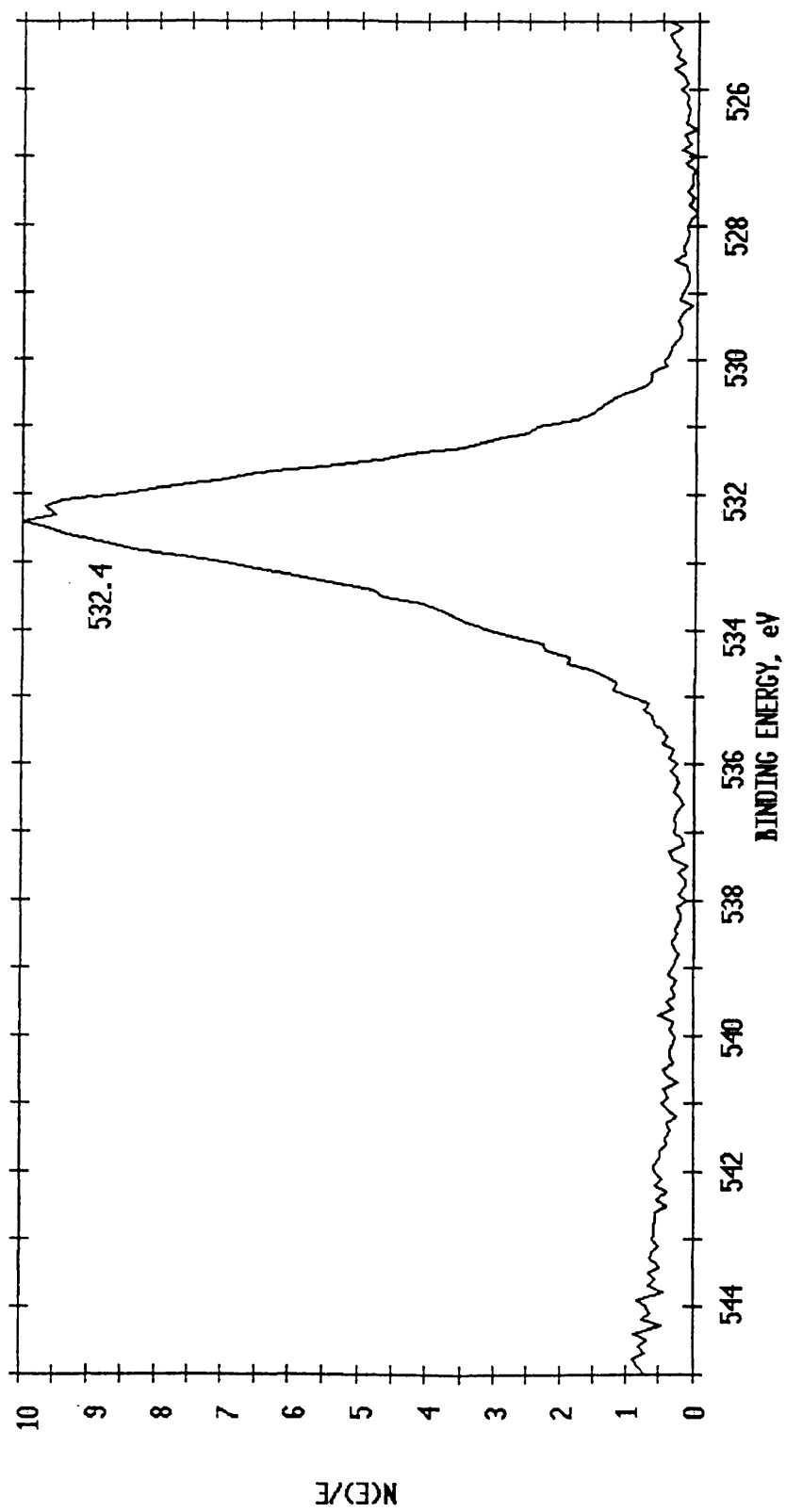


Figure 68: BPA-based CE + 10 wt. % B<sub>4</sub>C Front Surface Nitrogen Peak Control

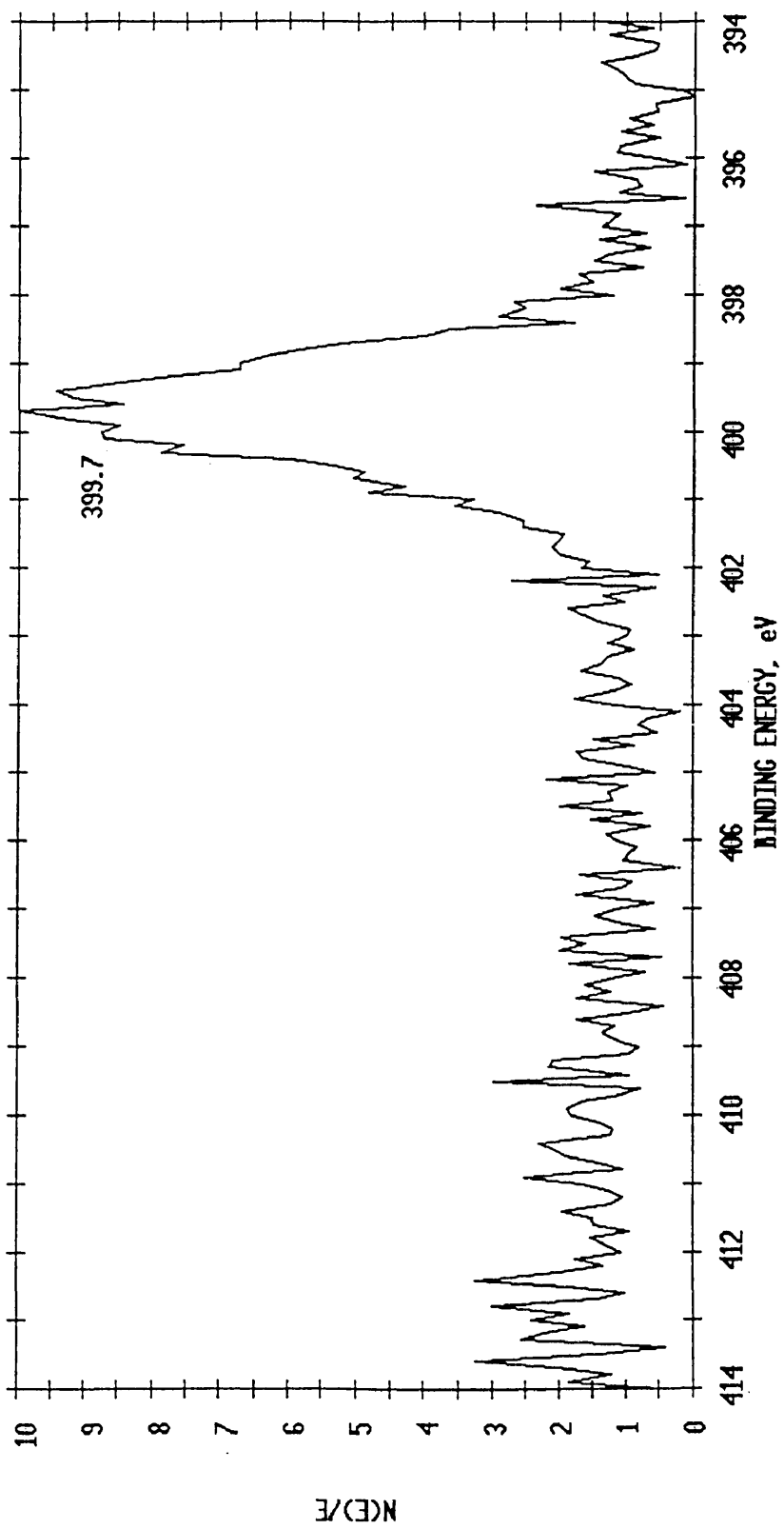


Figure 69: BPA-based CE + 10 wt. % B<sub>4</sub>C Front Surface Boron Peak Control

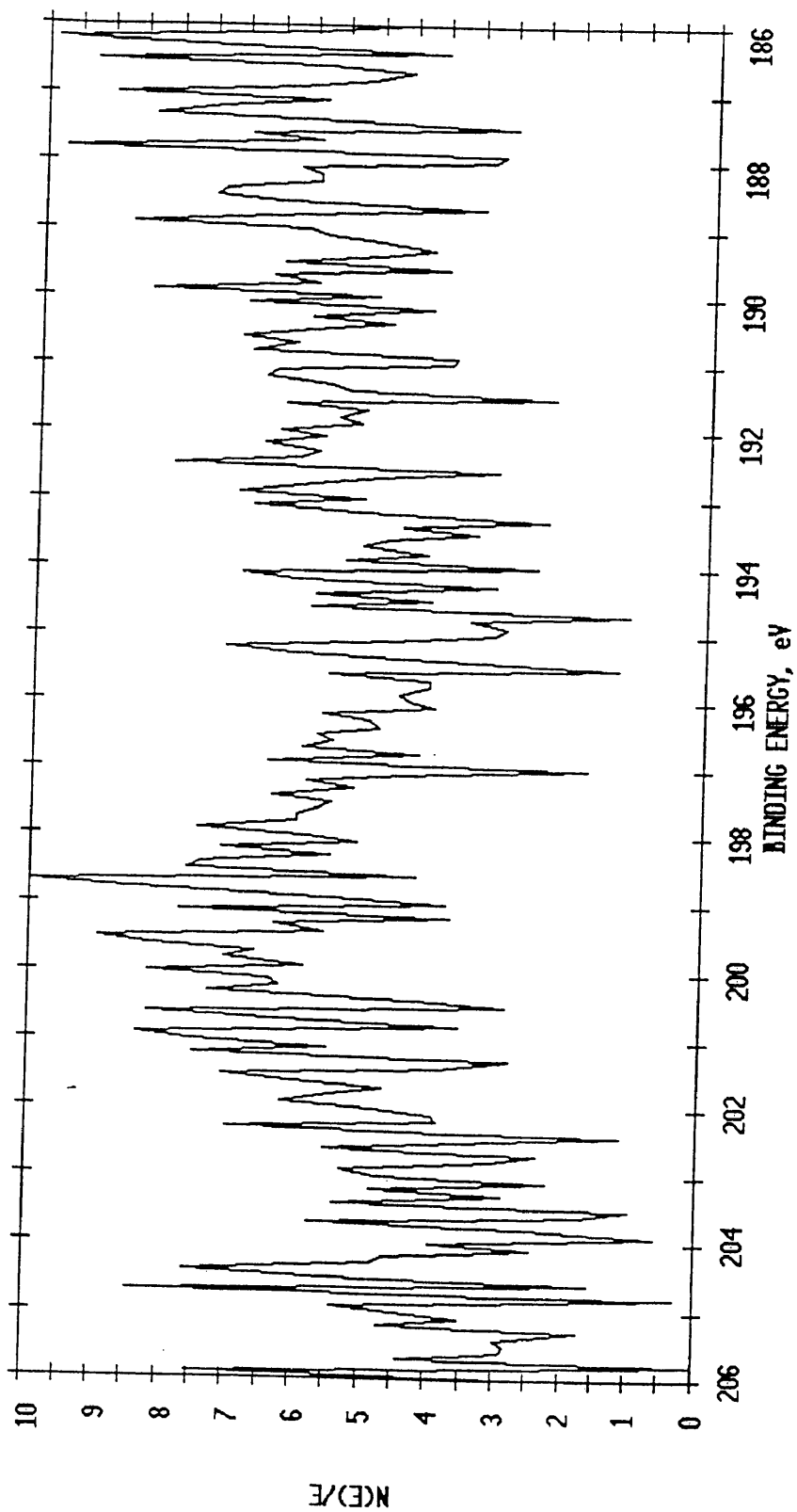


Figure 70: BPA-based CE + 10 wt. % B<sub>4</sub>C Front Surface Carbon Peak AO Exposed

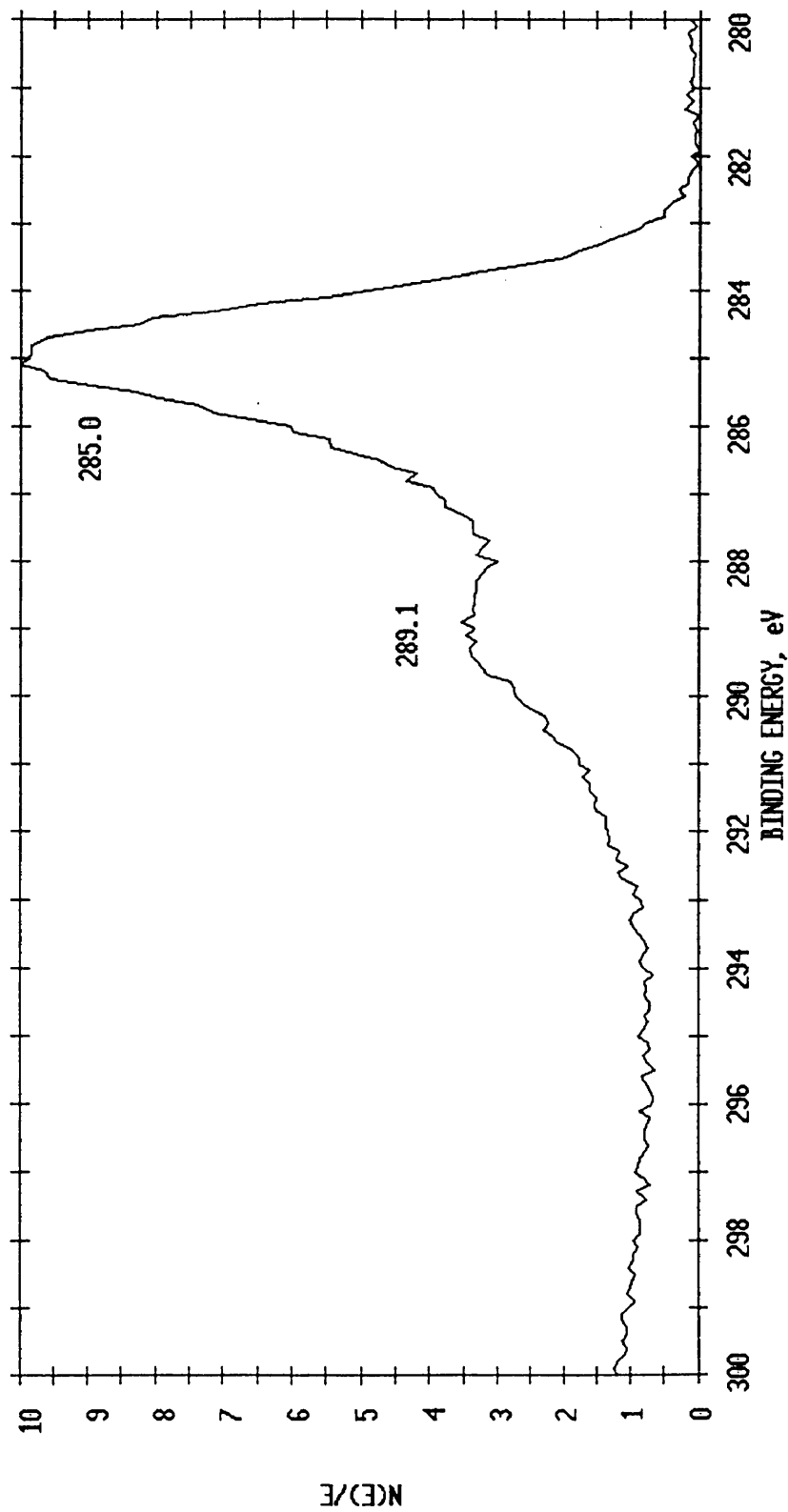


Figure 71: BPA-based CE + 10 wt. % B<sub>4</sub>C Front Surface Oxygen Peak AO Exposed

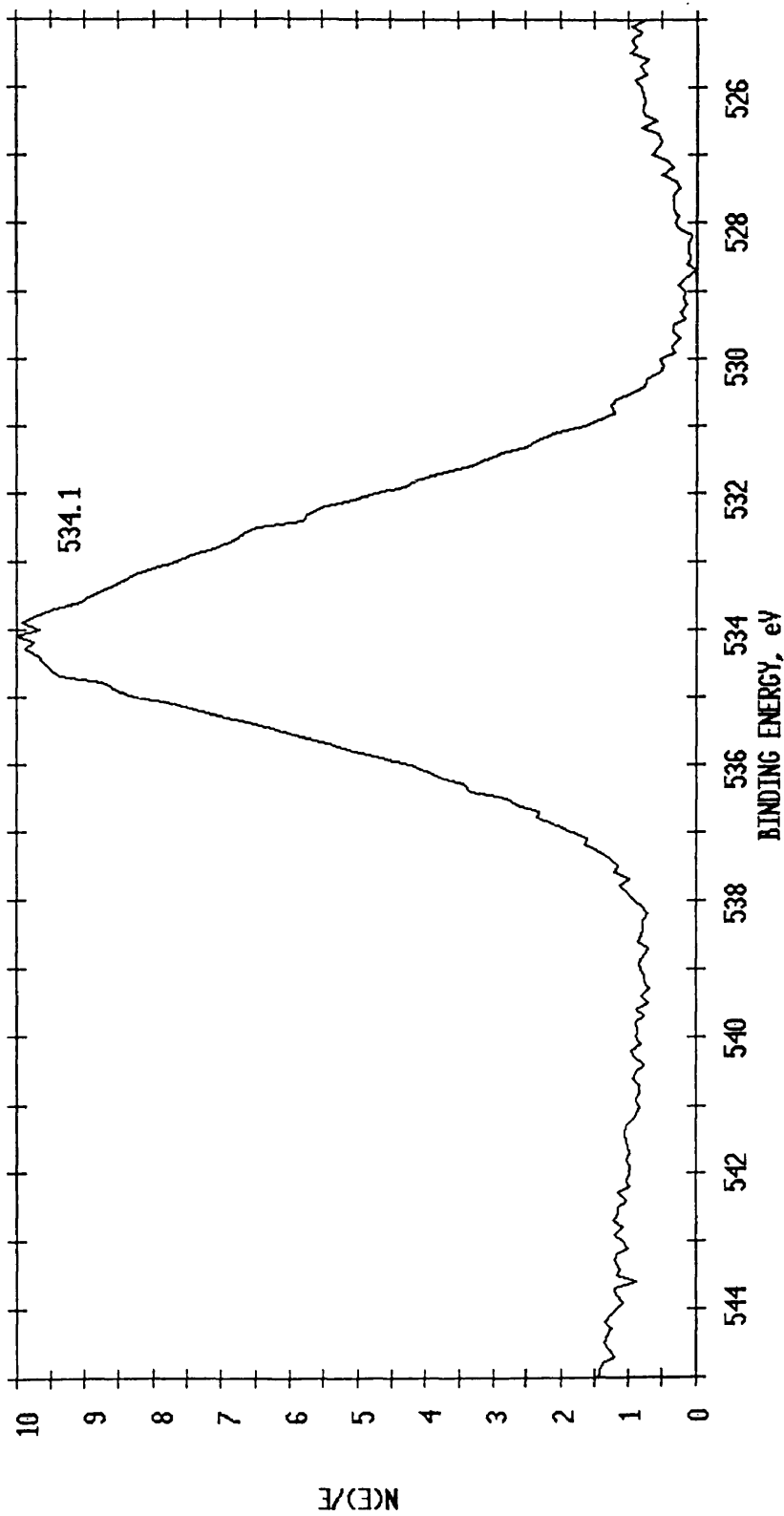


Figure 72: BPA-based CE + 10 wt. % B<sub>4</sub>C Front Surface Nitrogen Peak AO Exposed

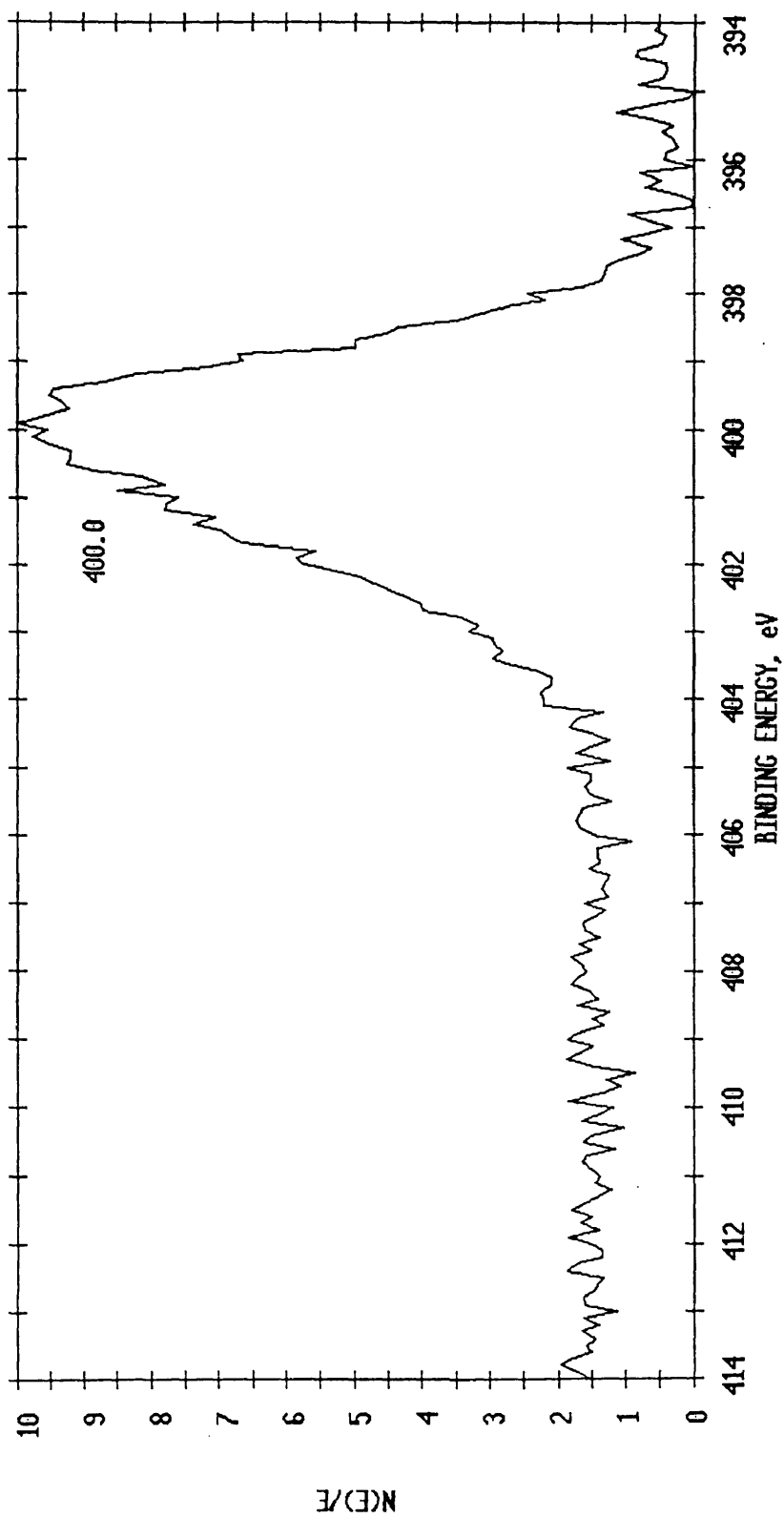


Figure 73: BPA-based CE + 10 wt. % B<sub>4</sub>C Front Surface Boron Peak AO Exposed

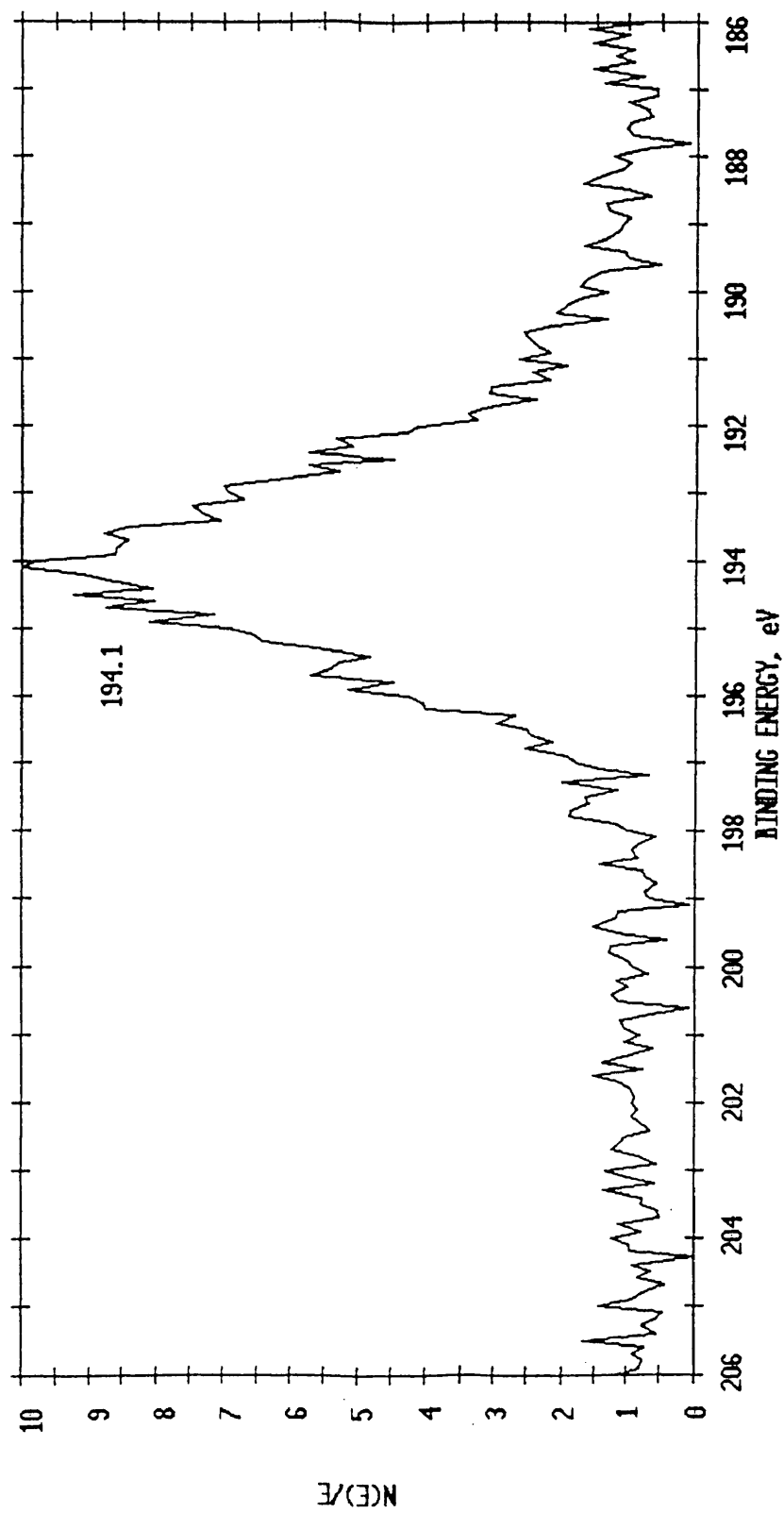


Figure 74: Pure Hexcel 954-3 CE Control

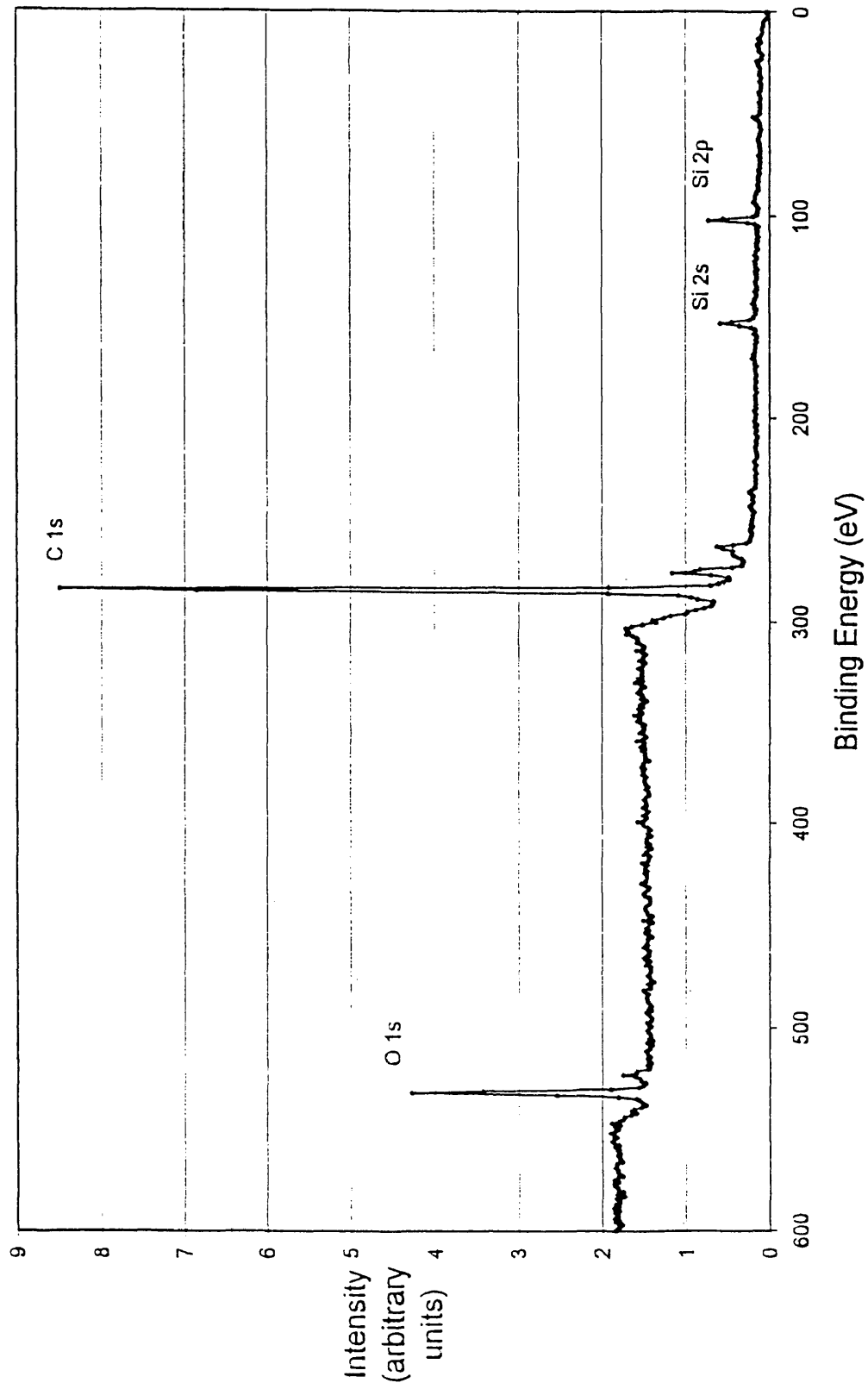


Figure 75: Pure Hexcel 954-3 CE AO Exposed 18 hours

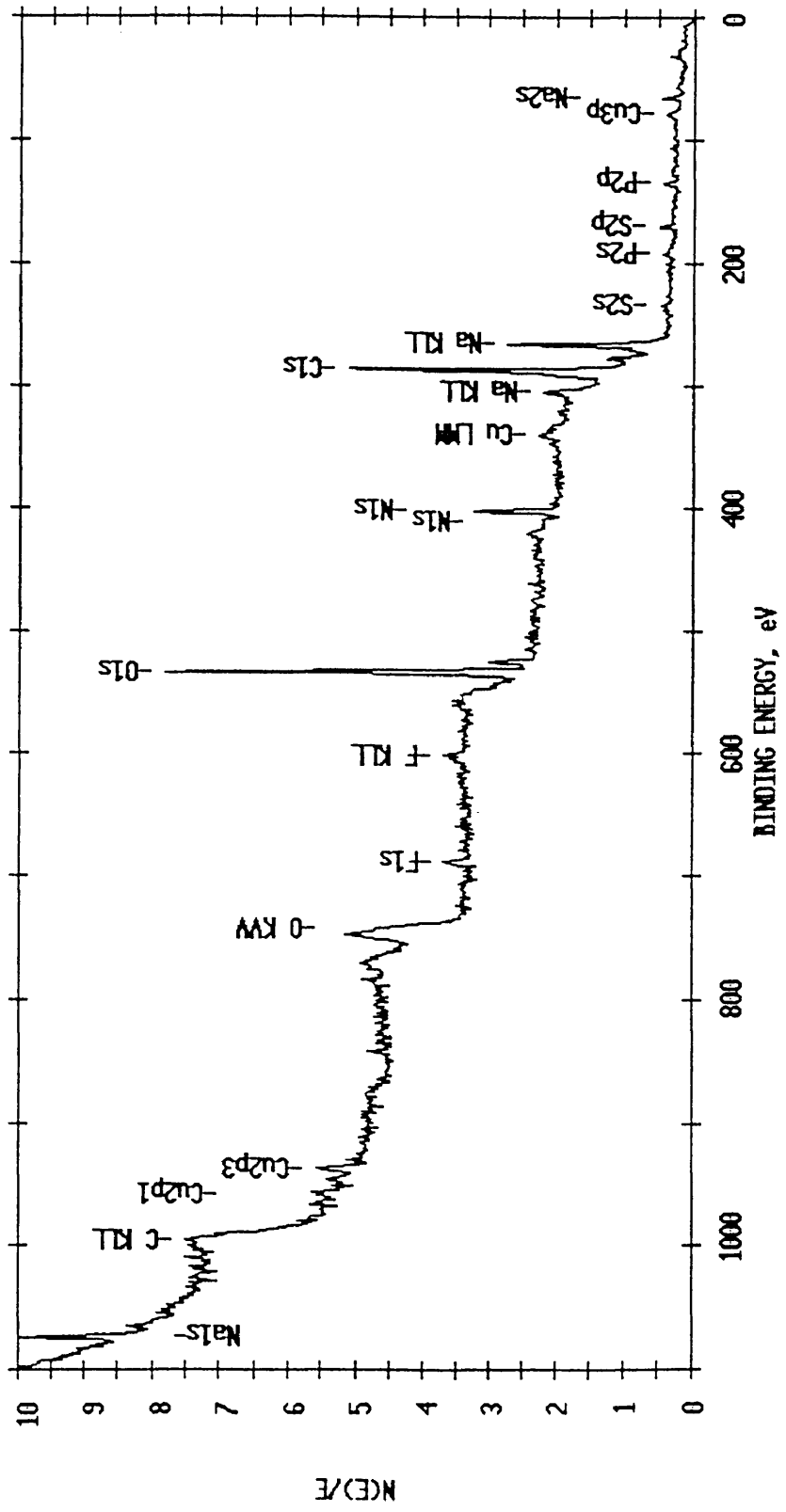


Figure 76: Pure Hexcel 954-3 CE AO Exposed 104 hours

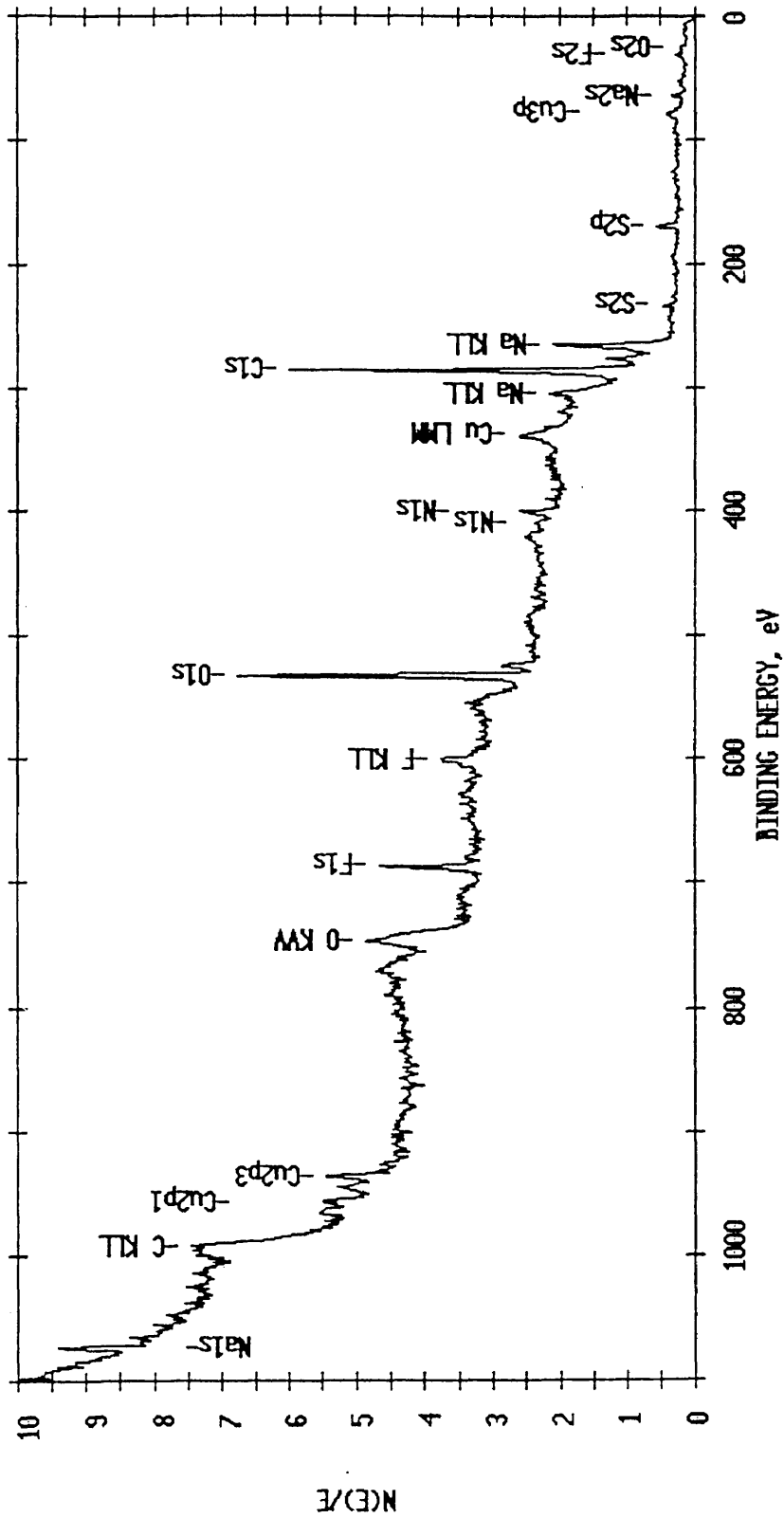


Figure 77: Hexcel 954-3 CE + 5 wt. % Boron AO Exposed 18 hours

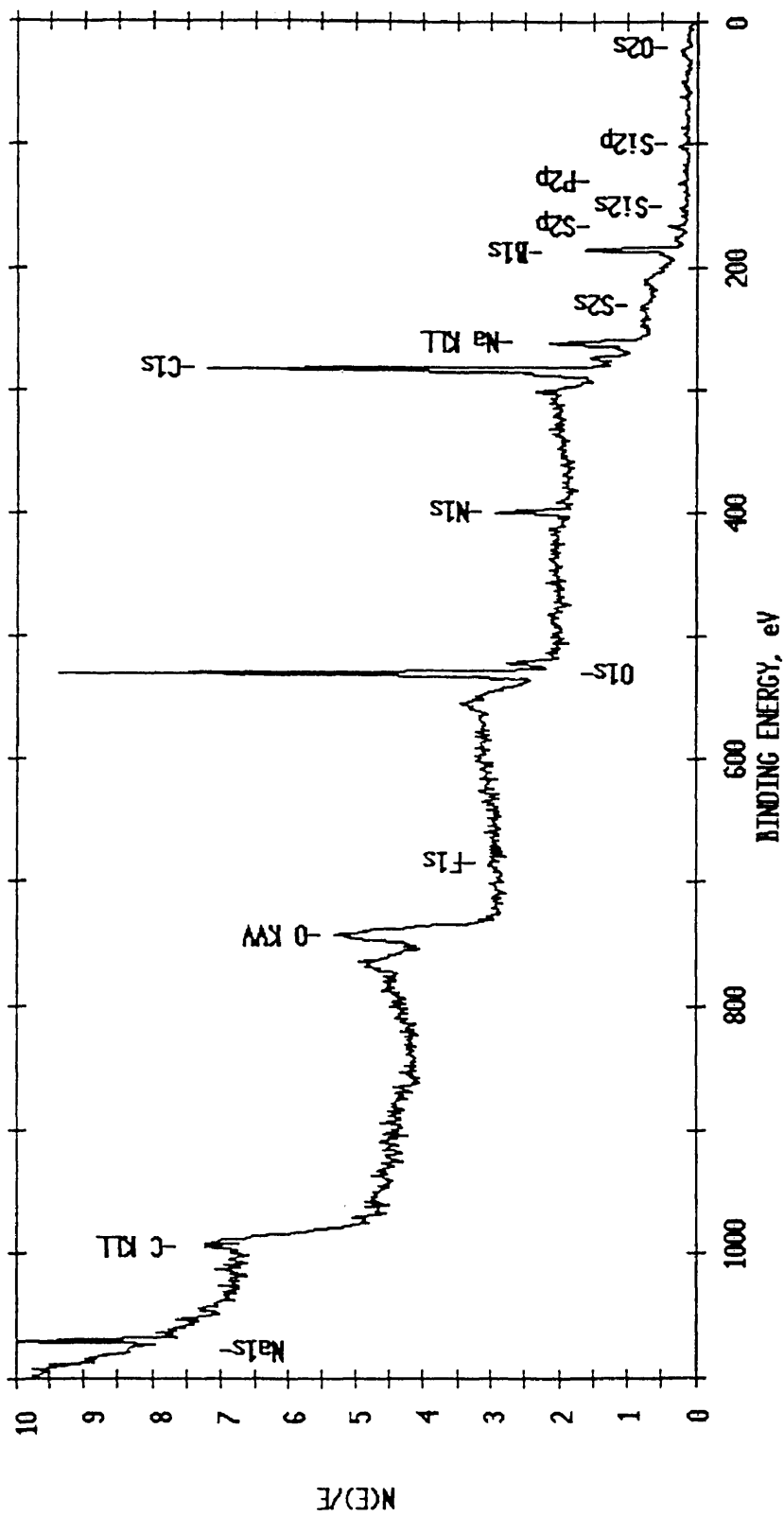




Figure 79: Hexcel 954-3 CE + 5 wt. % Boron AO Exposed 68 hours

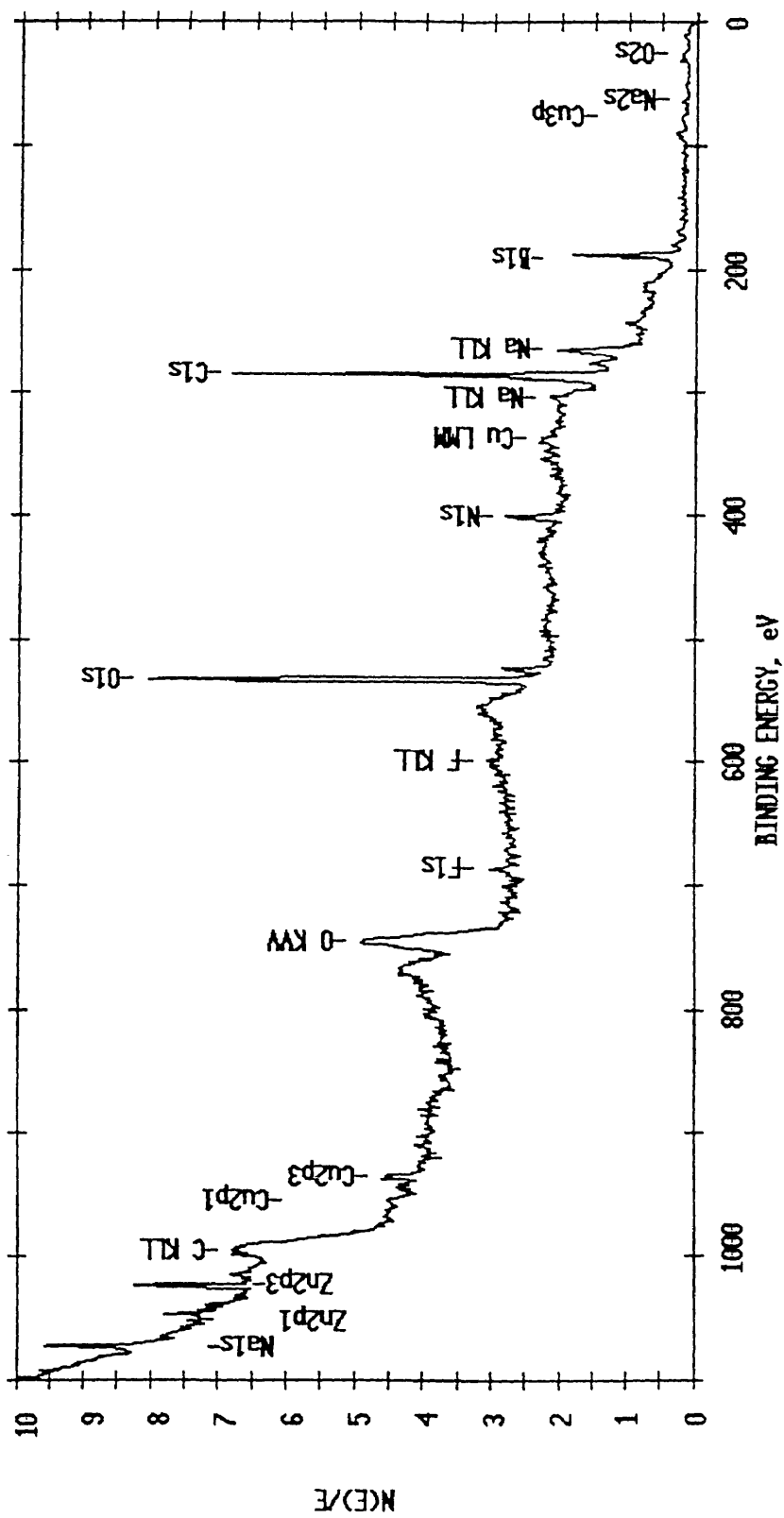


Figure 80: Hexcel 954-3 CE + 5 wt. % Boron AO Exposed 104 hours

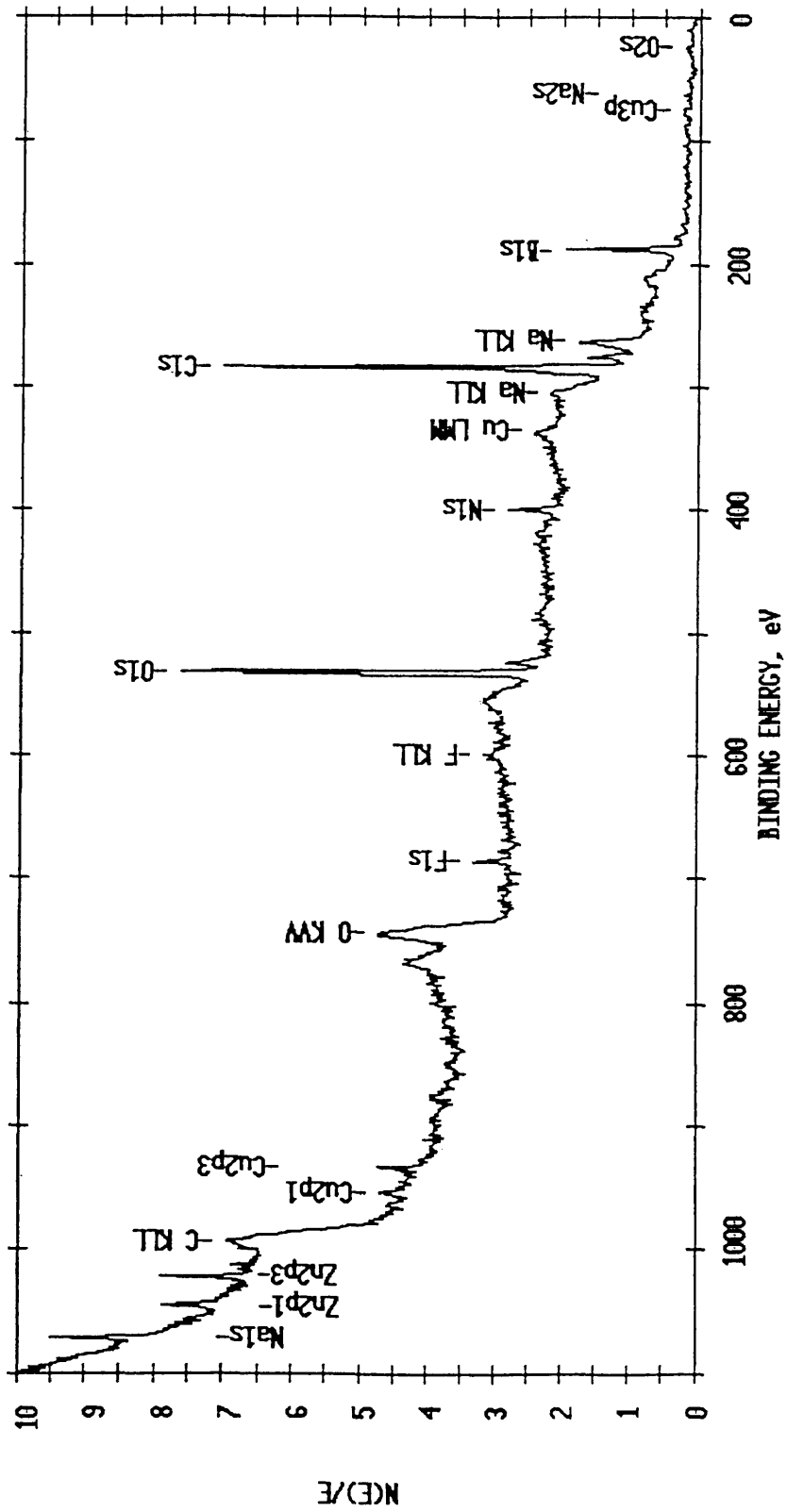


Figure 81: Pure Hexcel 954-3 CE Carbon Peak AO Exposed 18 hours

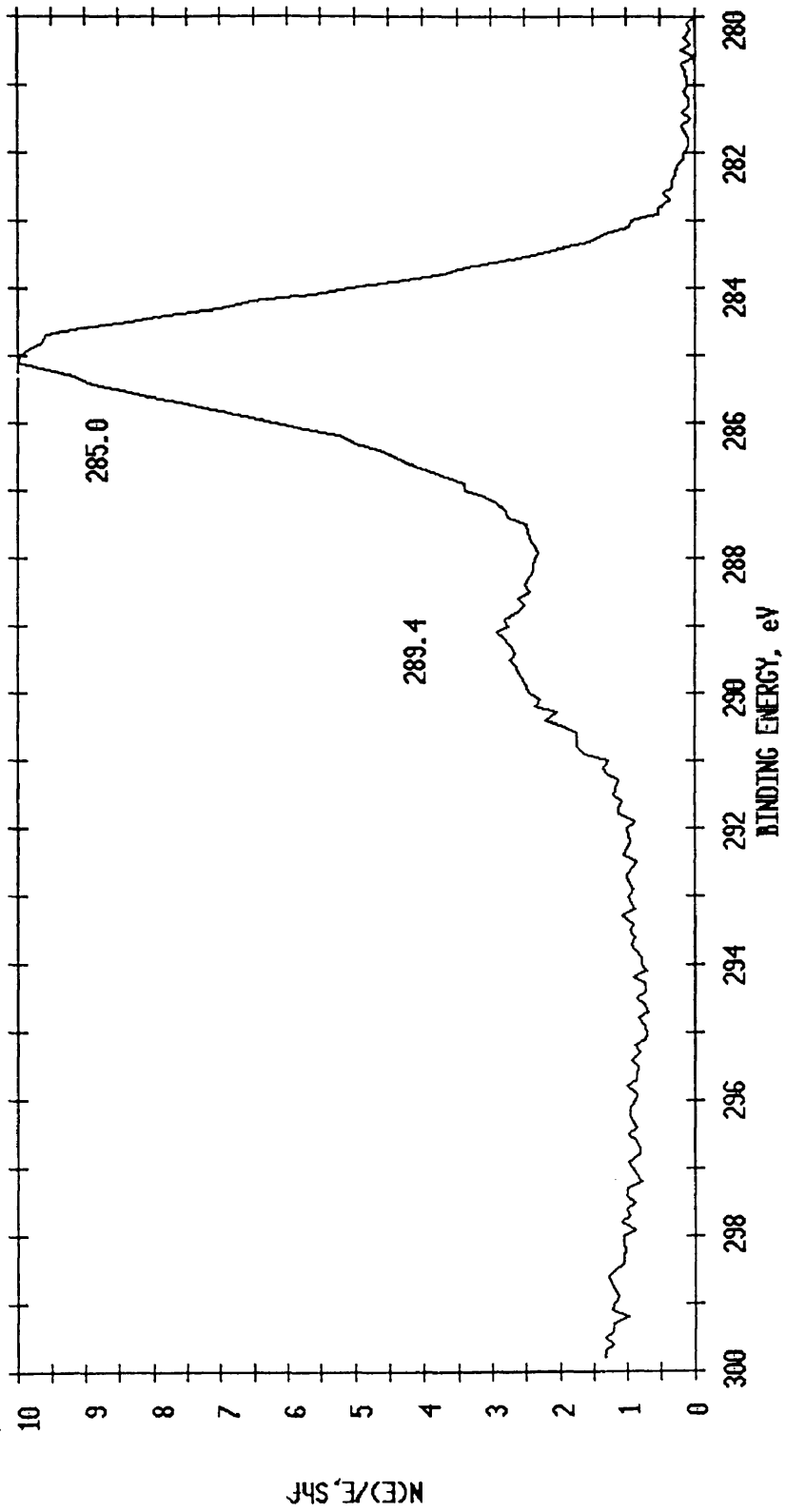


Figure 82: Pure Hexcel 954-3 CE Oxygen Peak AO Exposed 18 hours

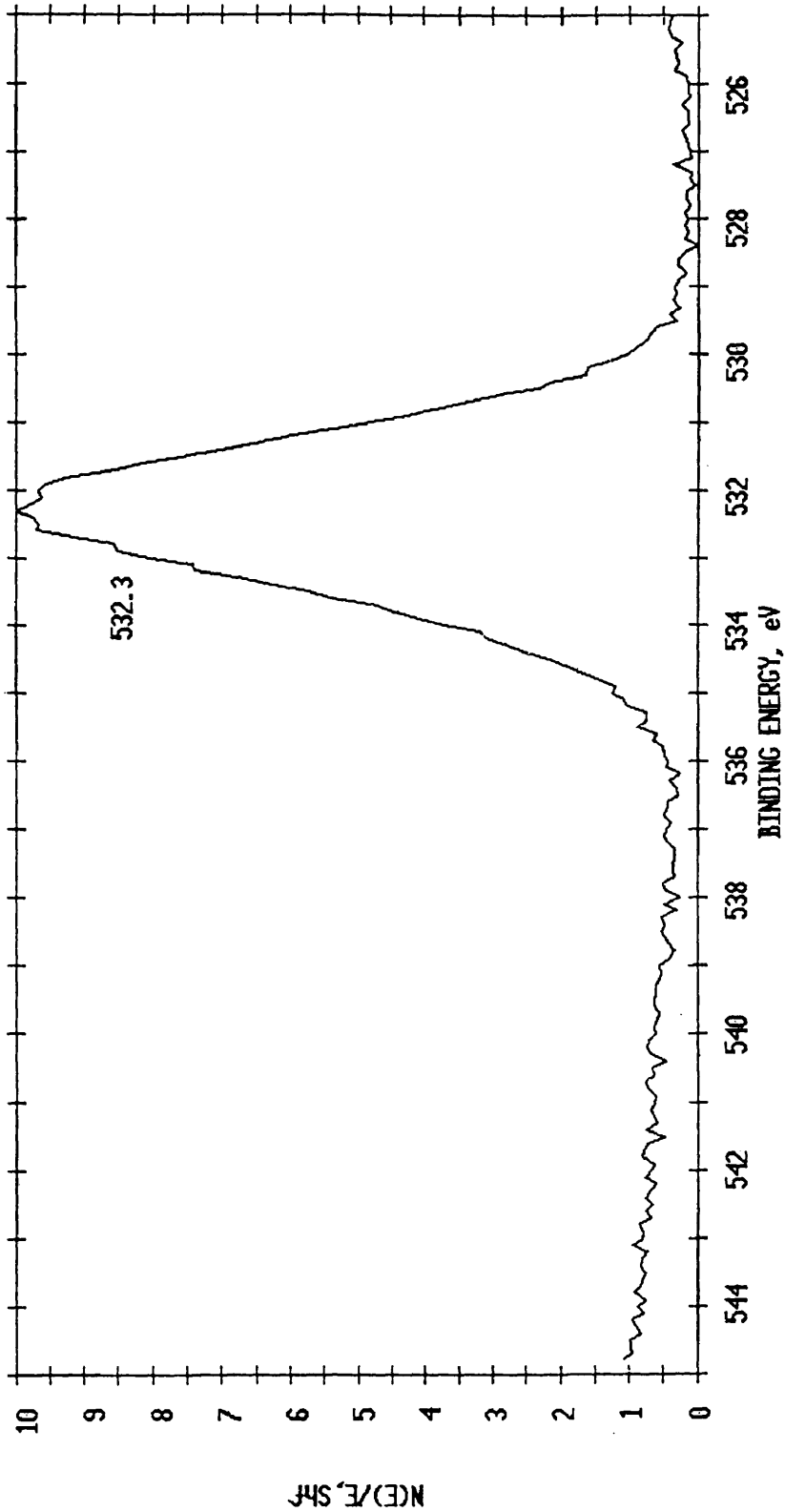


Figure 83: Pure Hexcel 954-3 CE Nitrogen Peak AO Exposed 18 hours

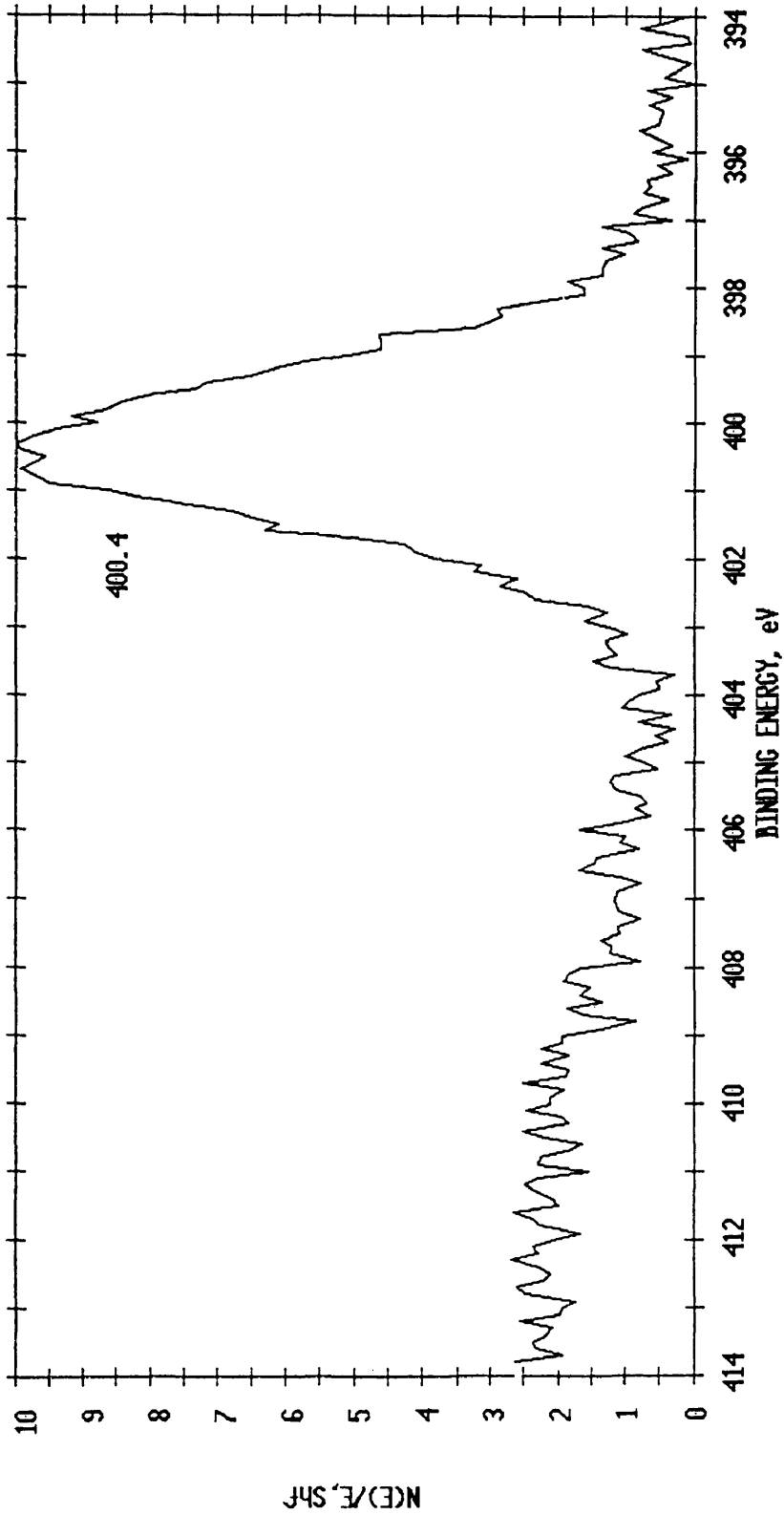


Figure 84: Pure Hexcel 954-3 CE Carbon Peak AO Exposed 104 hours

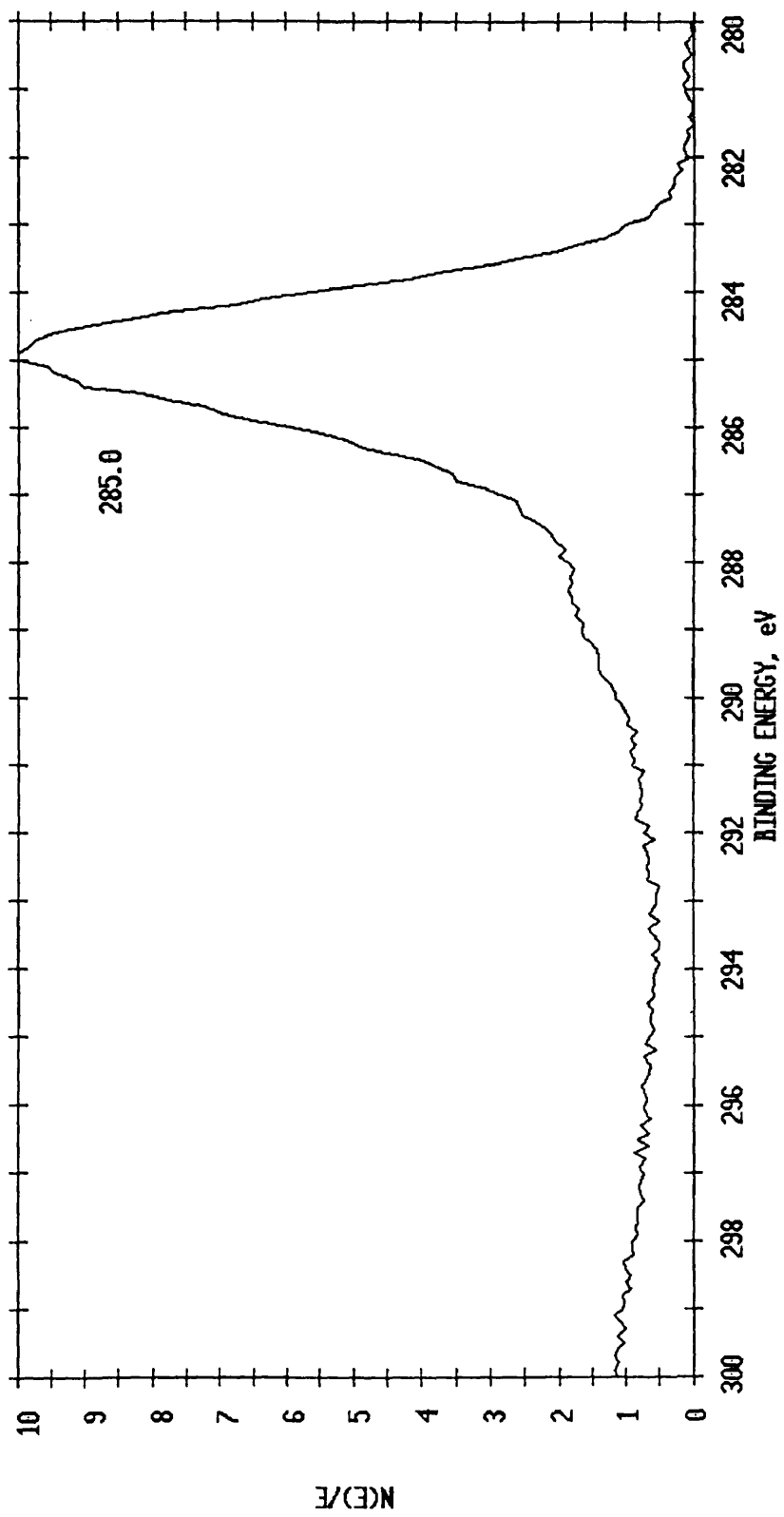


Figure 85: Pure Hexcel 954-3 CE Oxygen Peak AO Exposed 104 hours

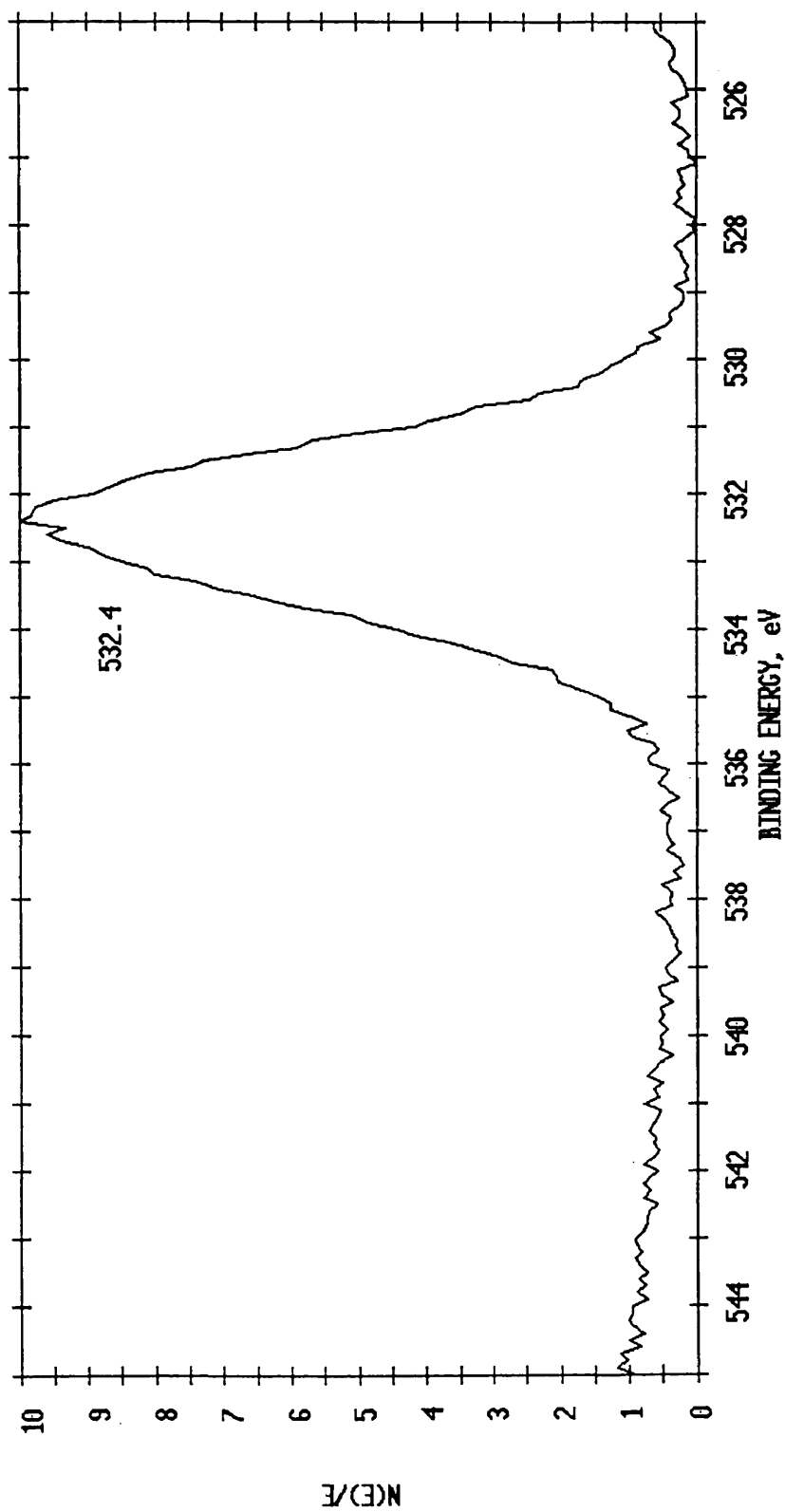


Figure 86: Pure Hexcel 954-3 CE Nitrogen Peak AO Exposed 104 hours

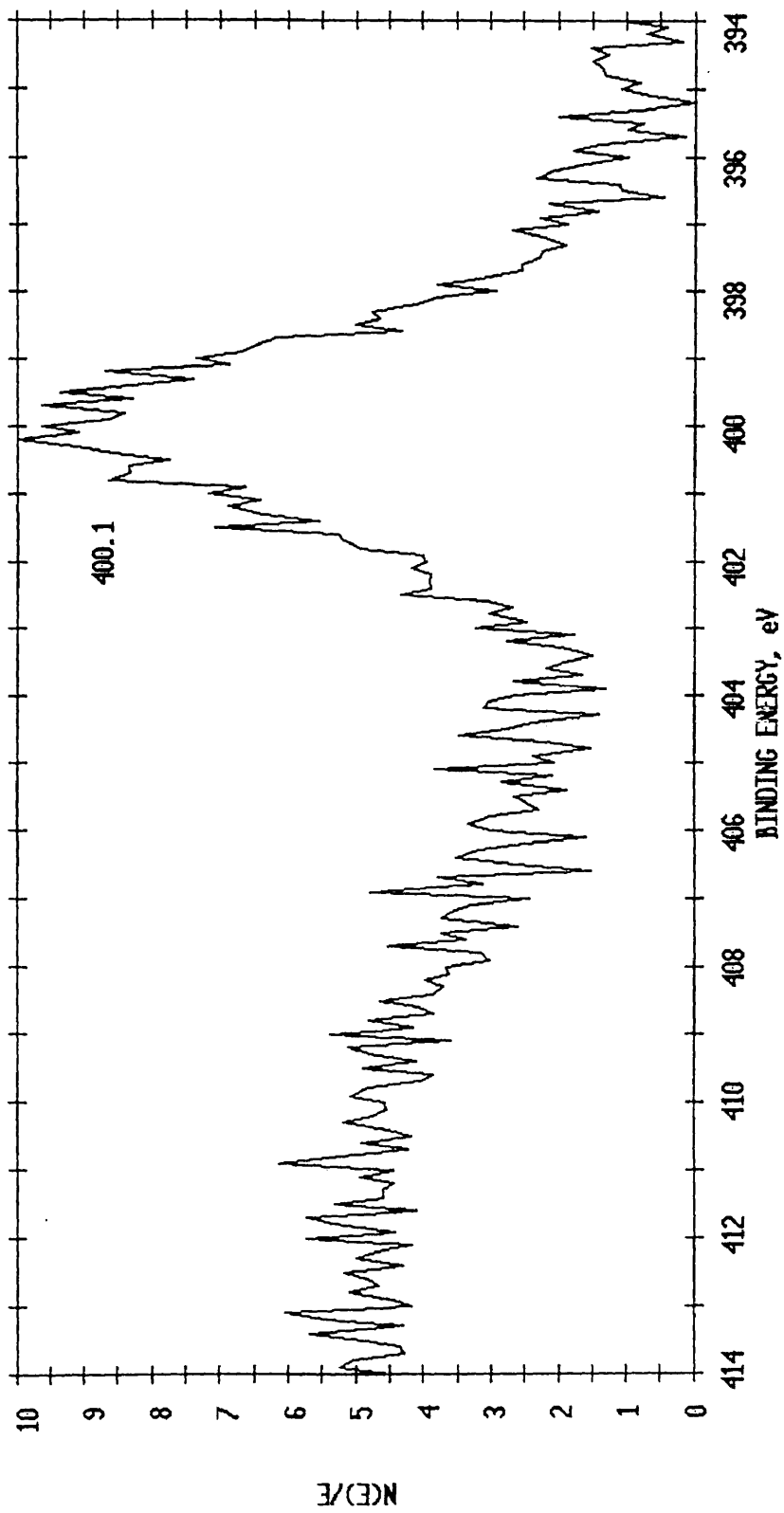


Figure 87: Hexcel 954-3 CE + 5 wt. % Boron Carbon Peak AO Exposed 18 hours

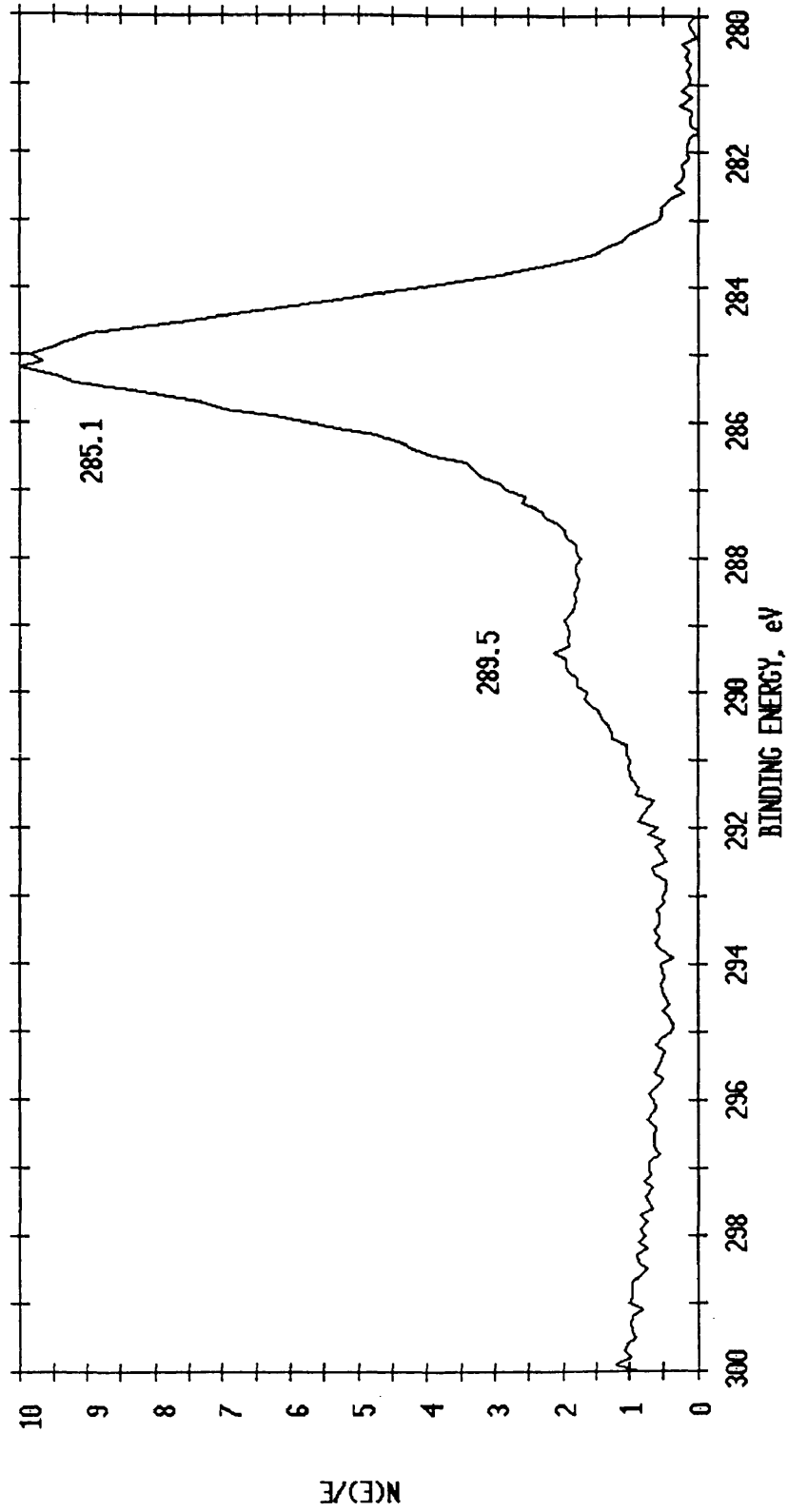


Figure 88: Hexcel 954-3 CE + 5 wt. % Boron Oxygen Peak AO Exposed 18 hours

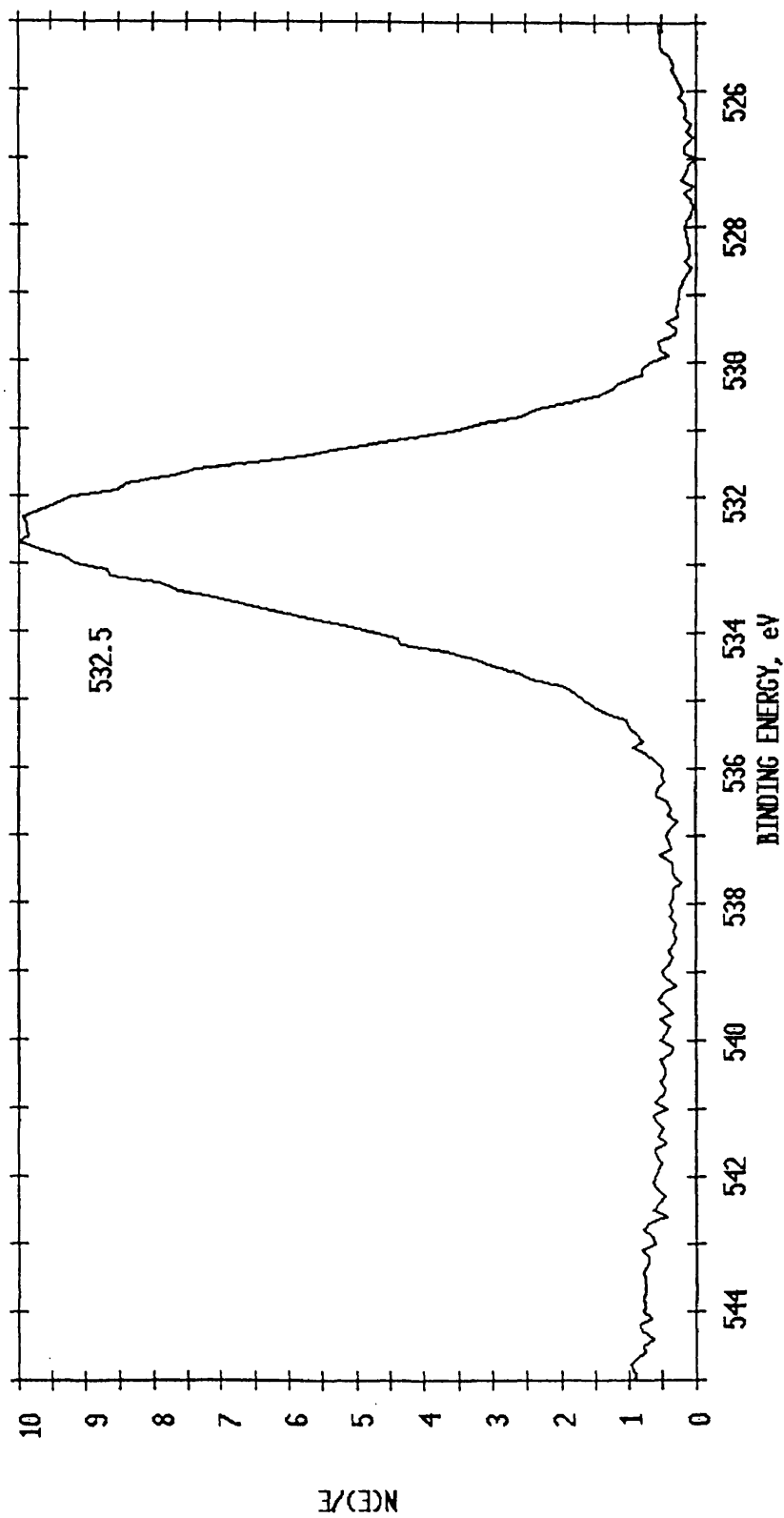


Figure 89: Hexcel 954-3 CE + 5 wt. % Boron Nitrogen Peak AO Exposed 18 hours

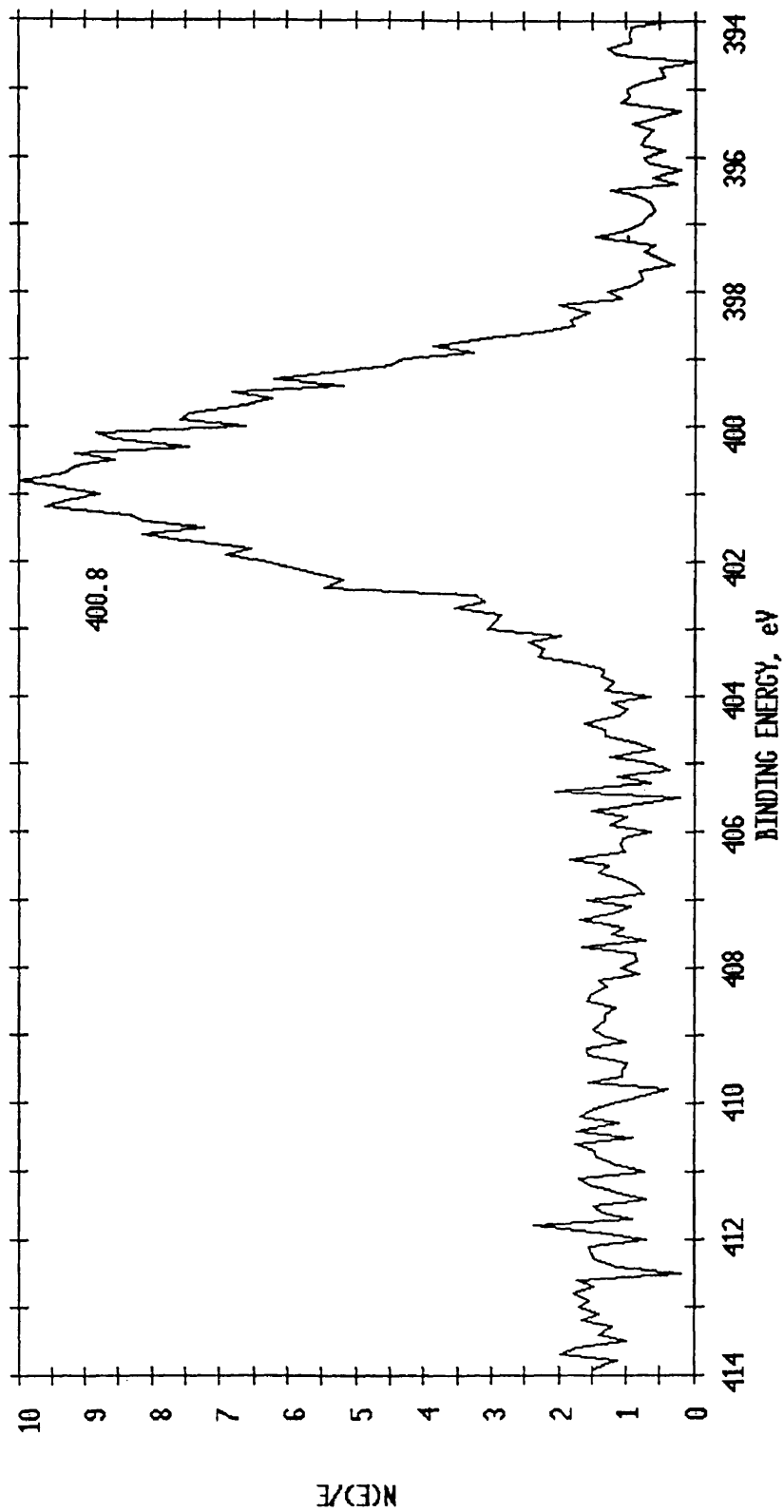


Figure 90: Hexcel 954-3 CE + 5 wt. % Boron Boron Peak AO Exposed 18 hours

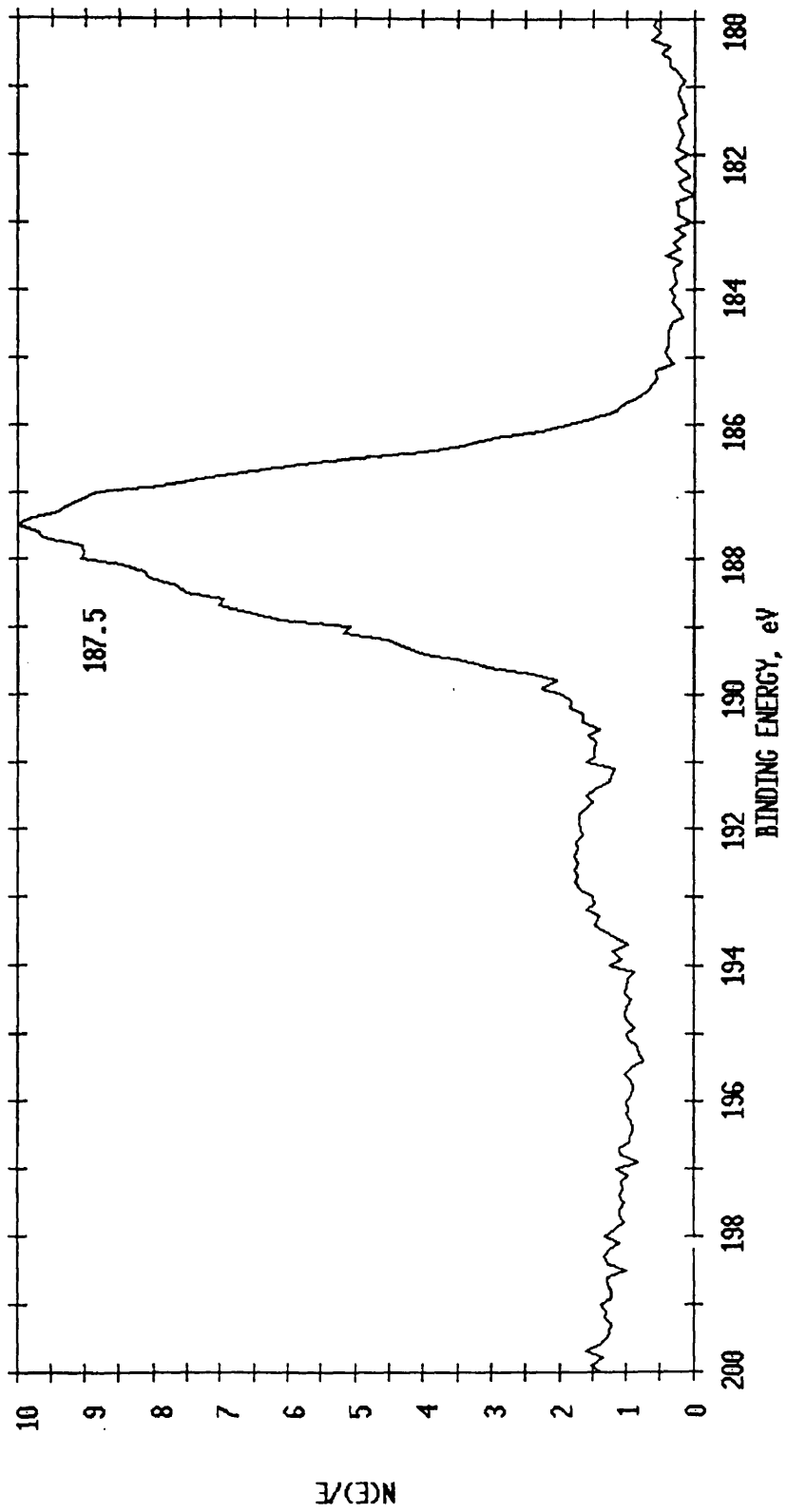


Figure 91: Hexcel 954-3 CE + 5 wt. % Boron Carbon Peak AO Exposed 36 hours

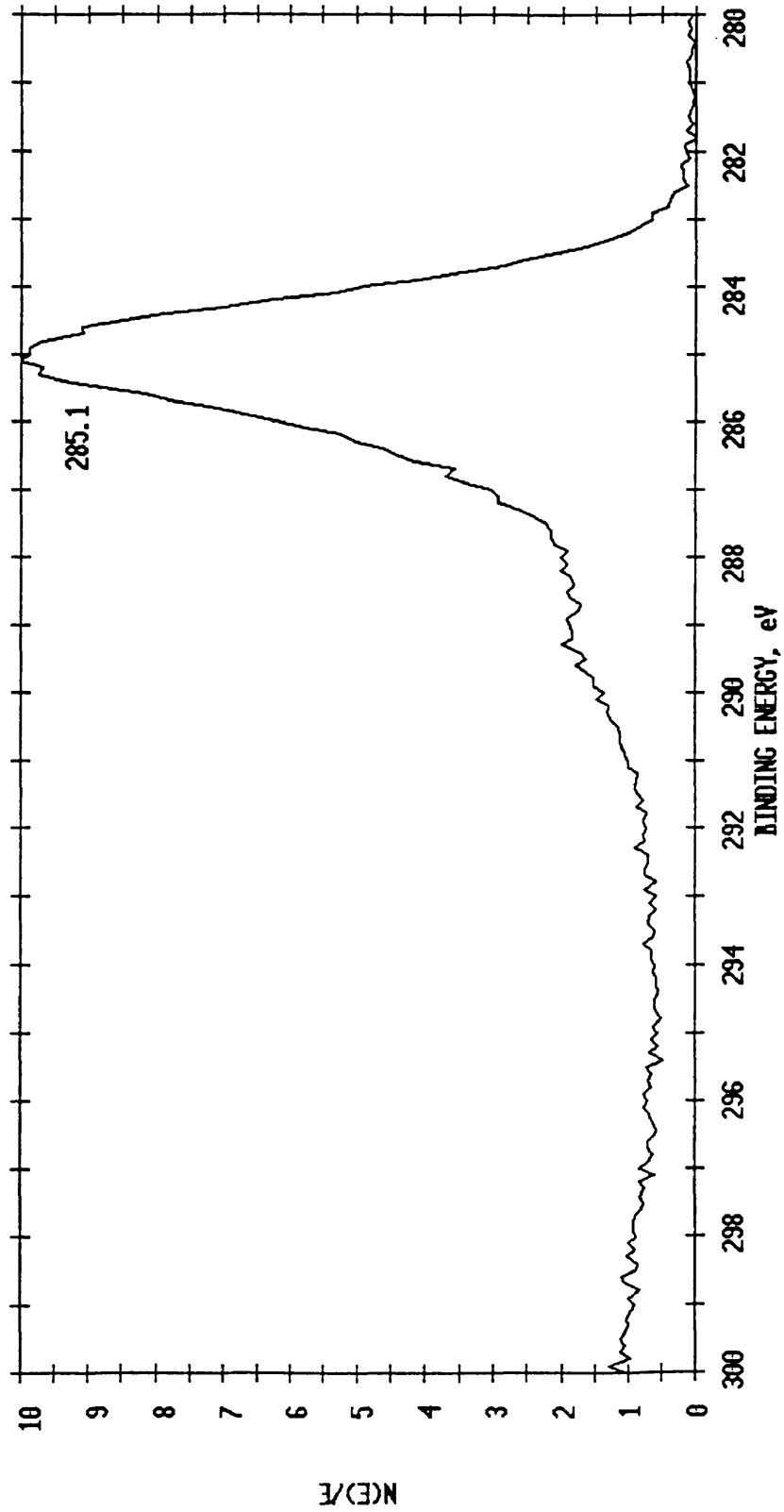


Figure 92: Hexcel 954-3 CE + 5 wt. % Boron Oxygen Peak AO Exposed 36 hours

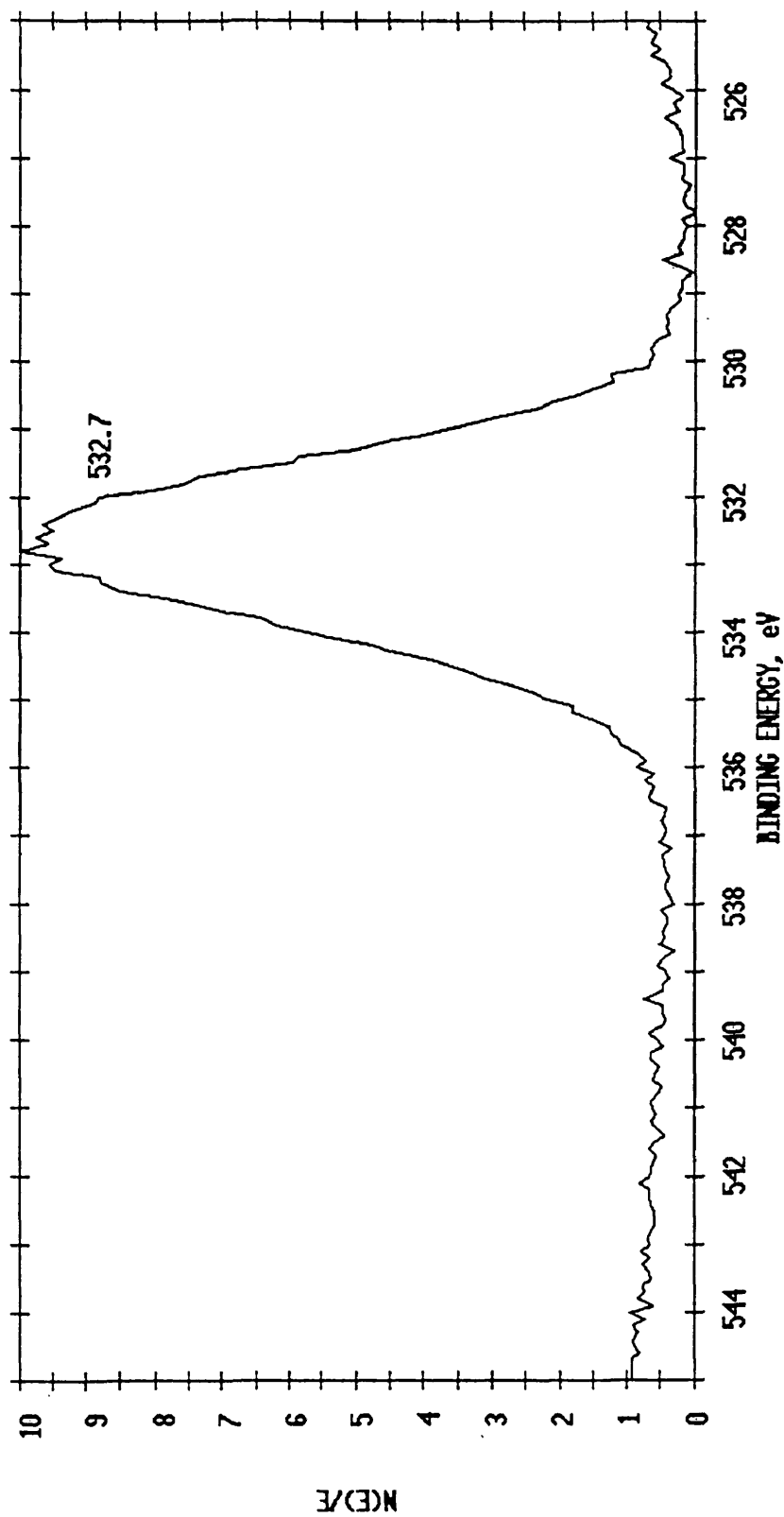


Figure 93: Hexcel 954-3 CE + 5 wt. % Boron Nitrogen Peak AO Exposed 36 hours

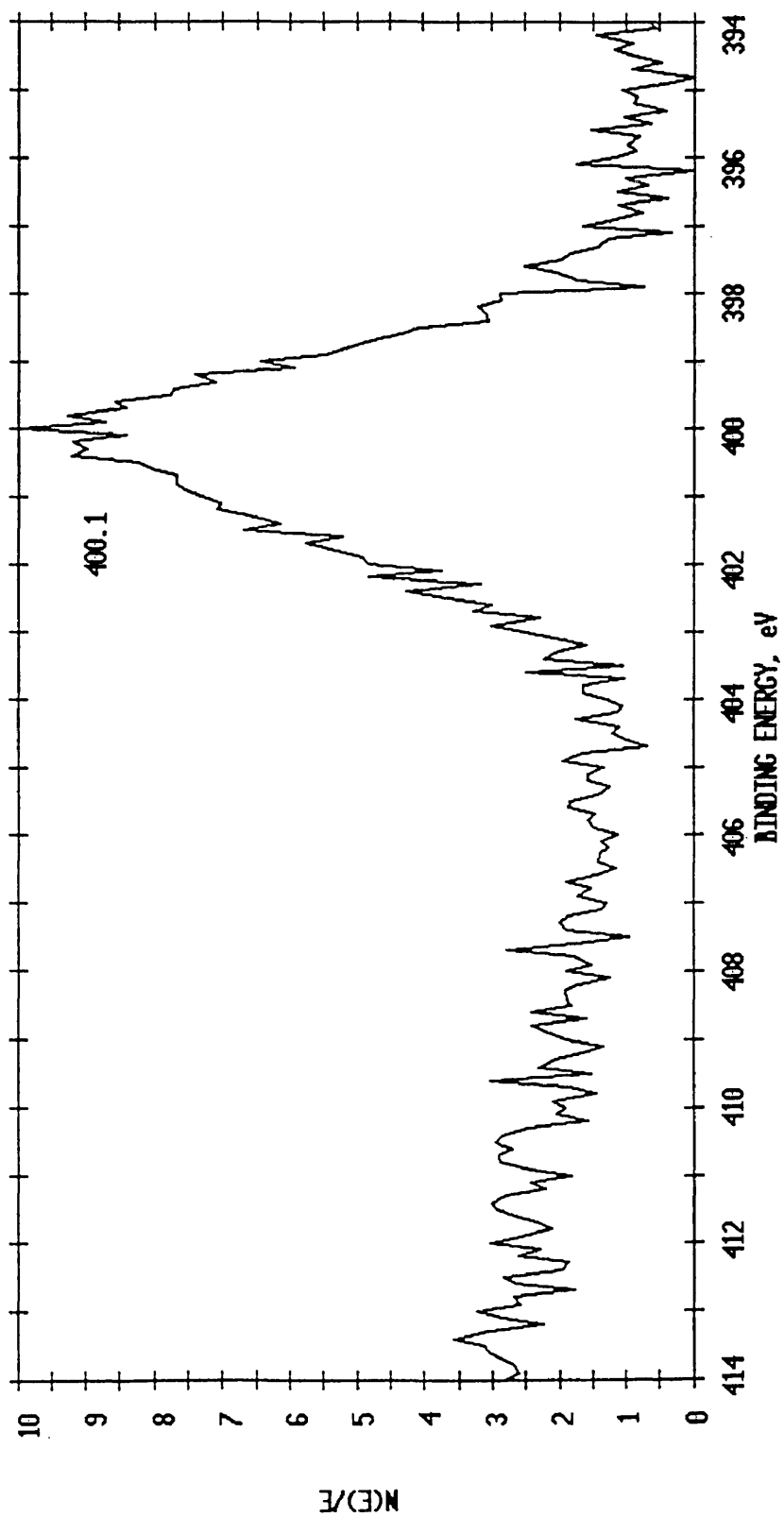


Figure 94: Hexcel 954-3 CE + 5 wt. % Boron Boron Peak AO Exposed 36 hours

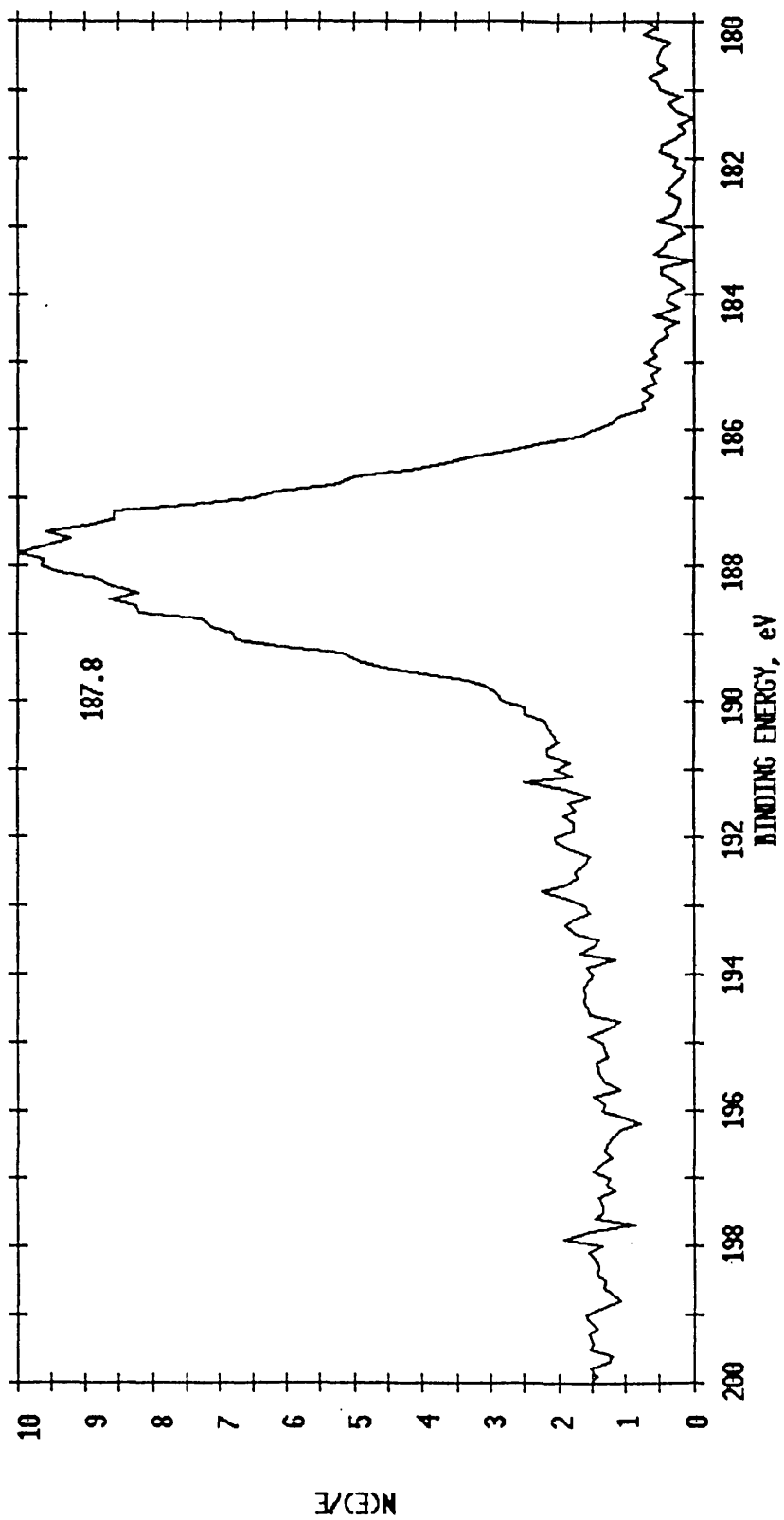


Figure 95: Hexcel 954-3 CE + 5 wt. % Boron Carbon Peak AO Exposed 68 hours

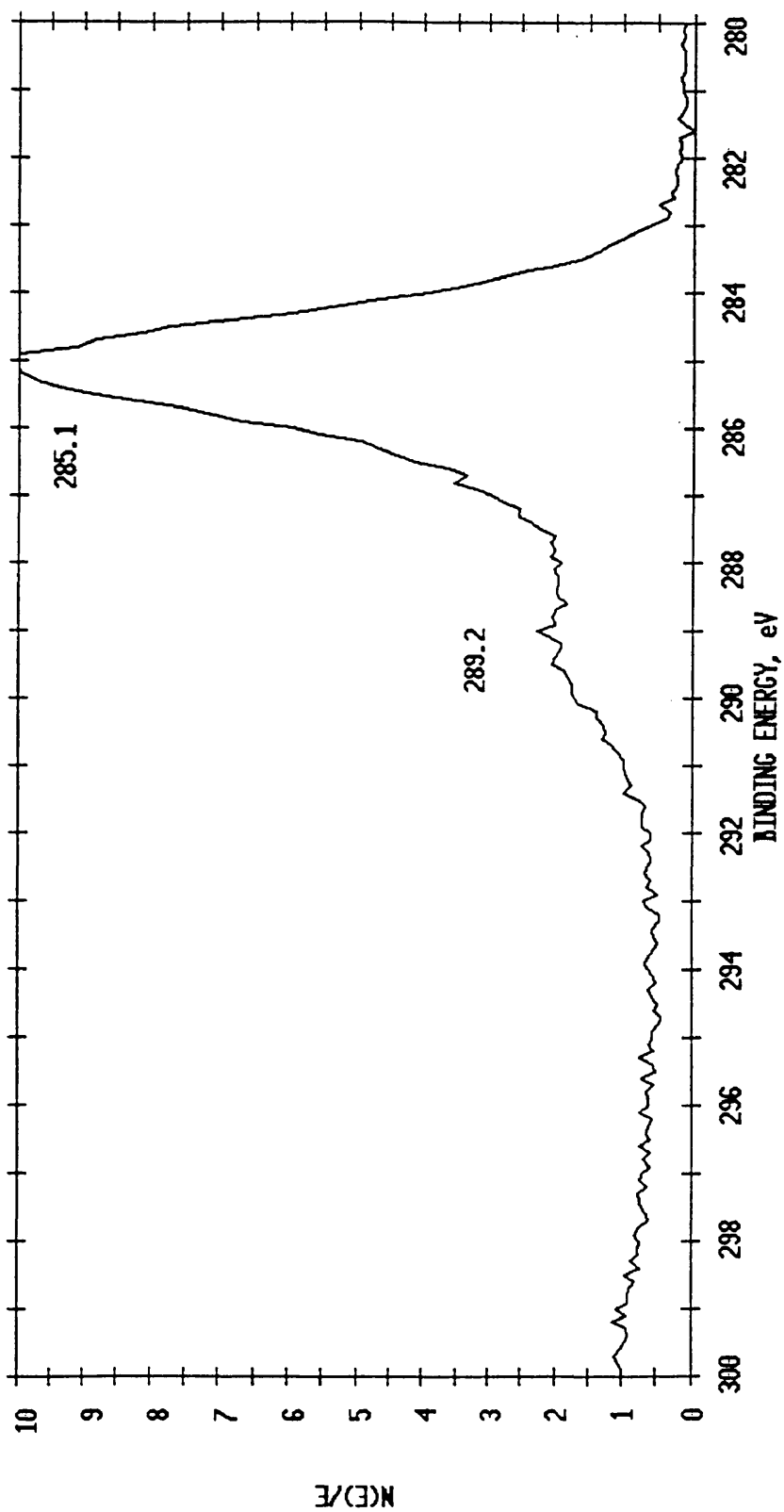


Figure 96: Hexcel 954-3 CE + 5 wt. % Boron Oxygen Peak AO Exposed 68 hours

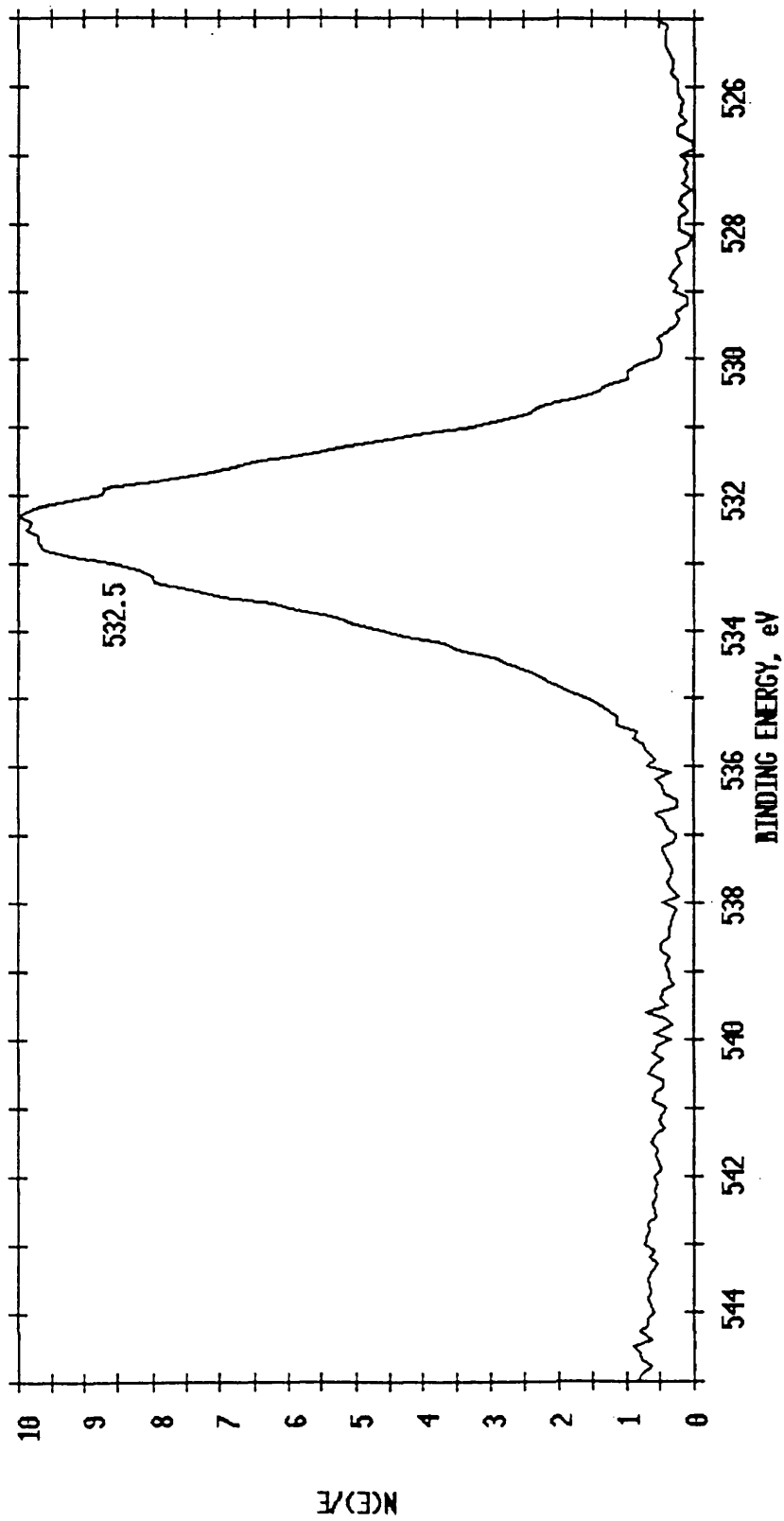


Figure 97: Hexcel 954-3 CE + 5 wt. % Boron Nitrogen Peak AO Exposed 68 hours

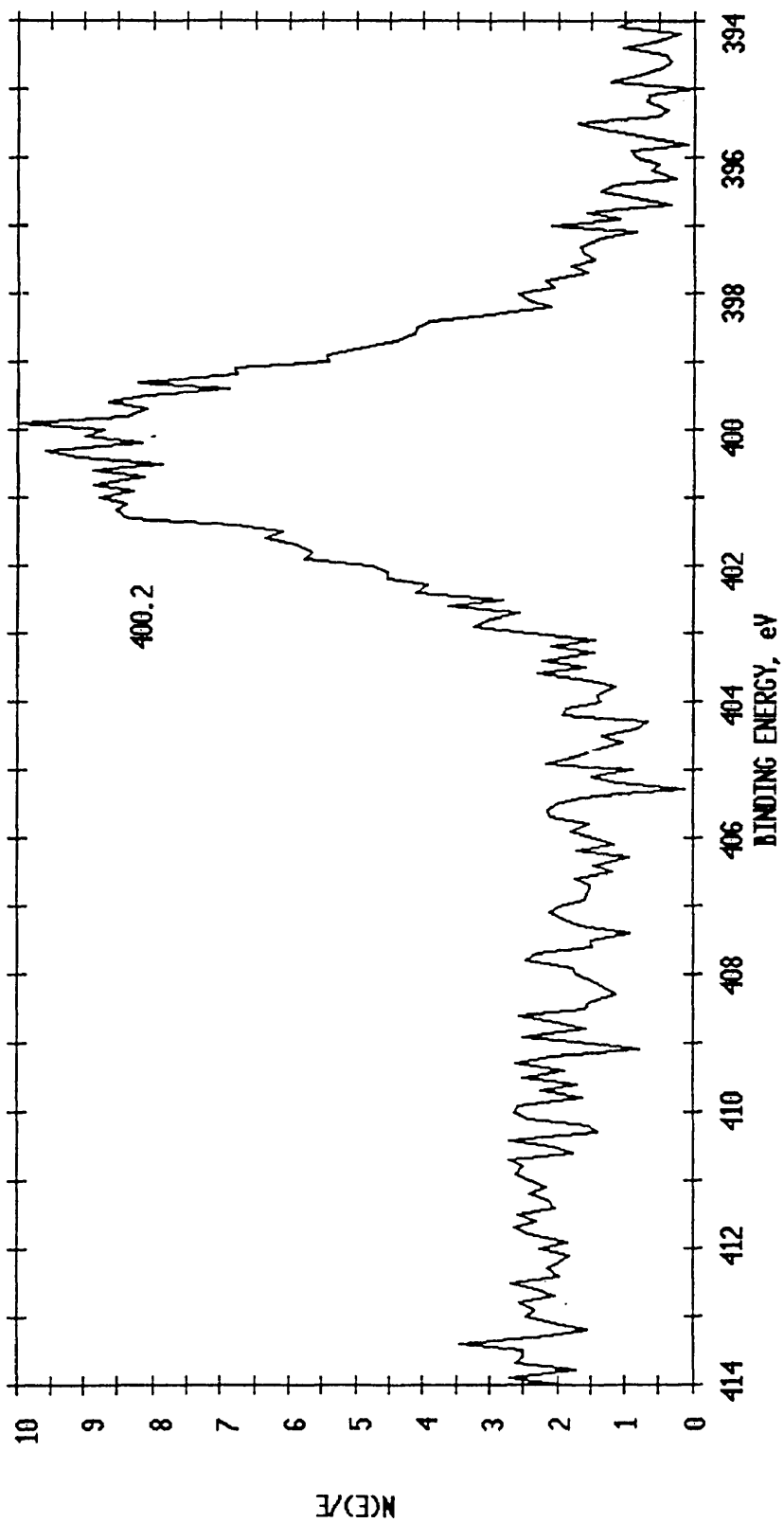


Figure 98: Hexcel 954-3 CE + 5 wt. % Boron Boron Peak AO Exposed 68 hours

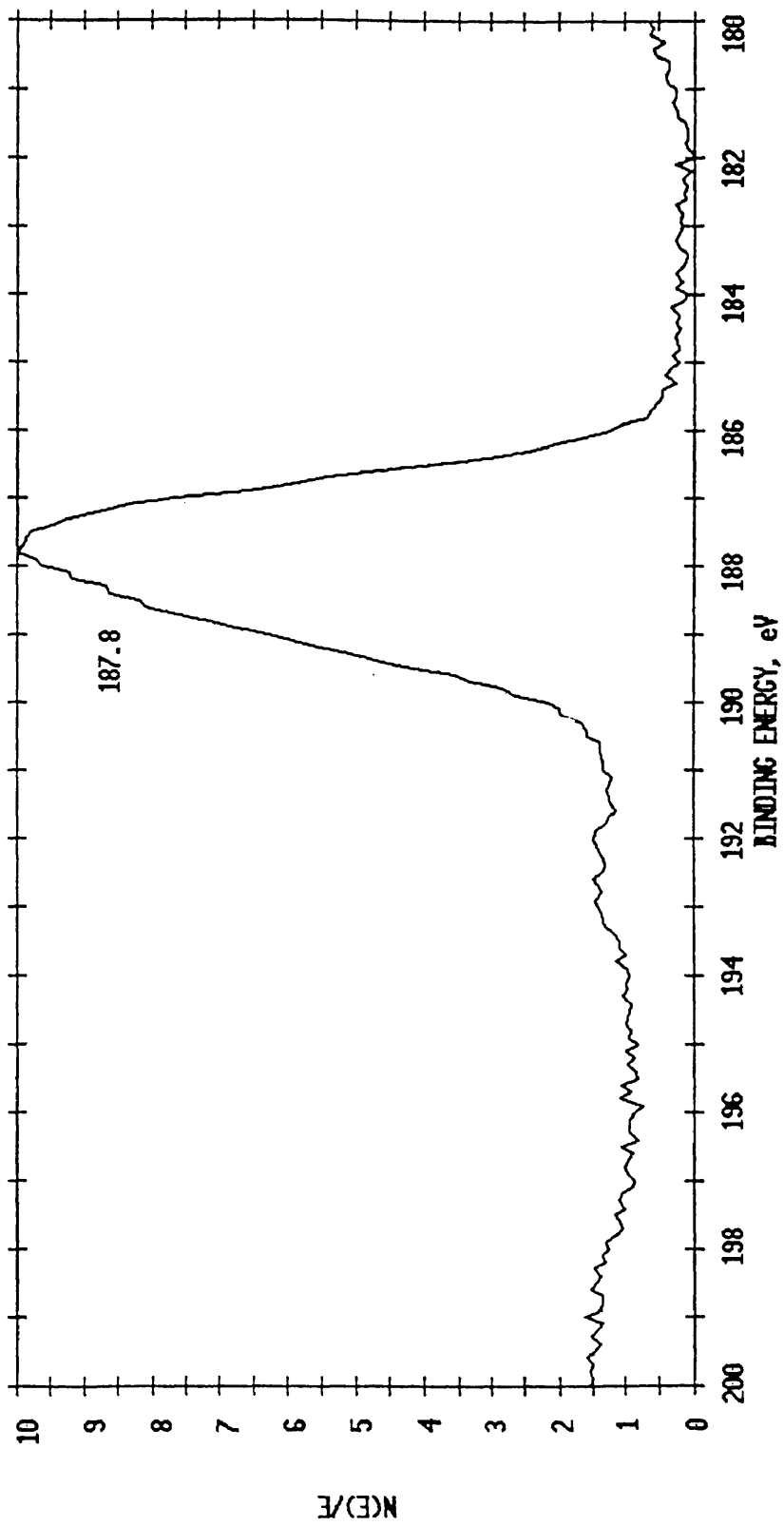


Figure 99: Hexcel 954-3 CE + 5 wt. % Boron Carbon Peak AO Exposed 104 hours

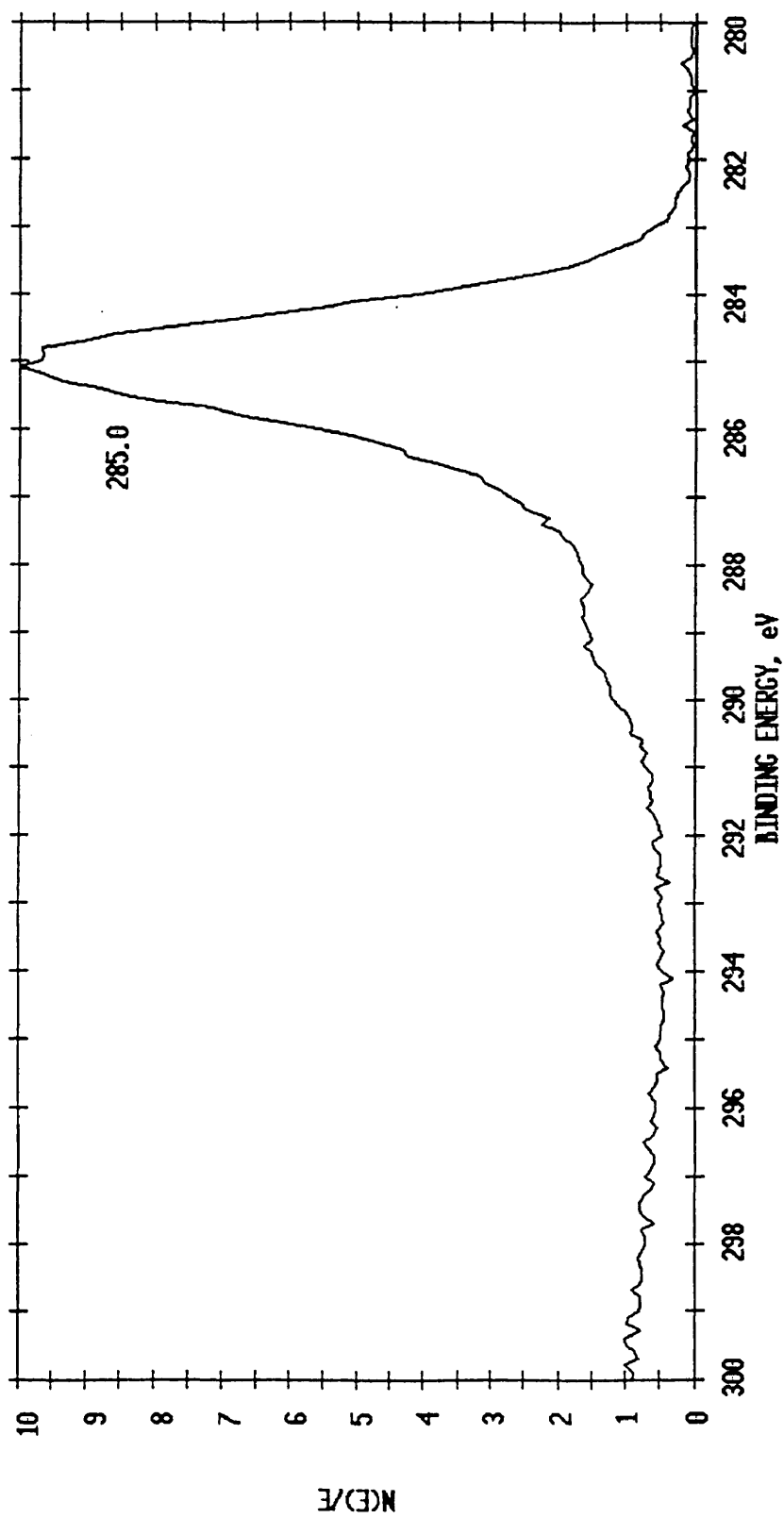


Figure 100: Hexcel 954-3 CE + 5 wt. % Boron Oxygen Peak AO Exposed 104 hours

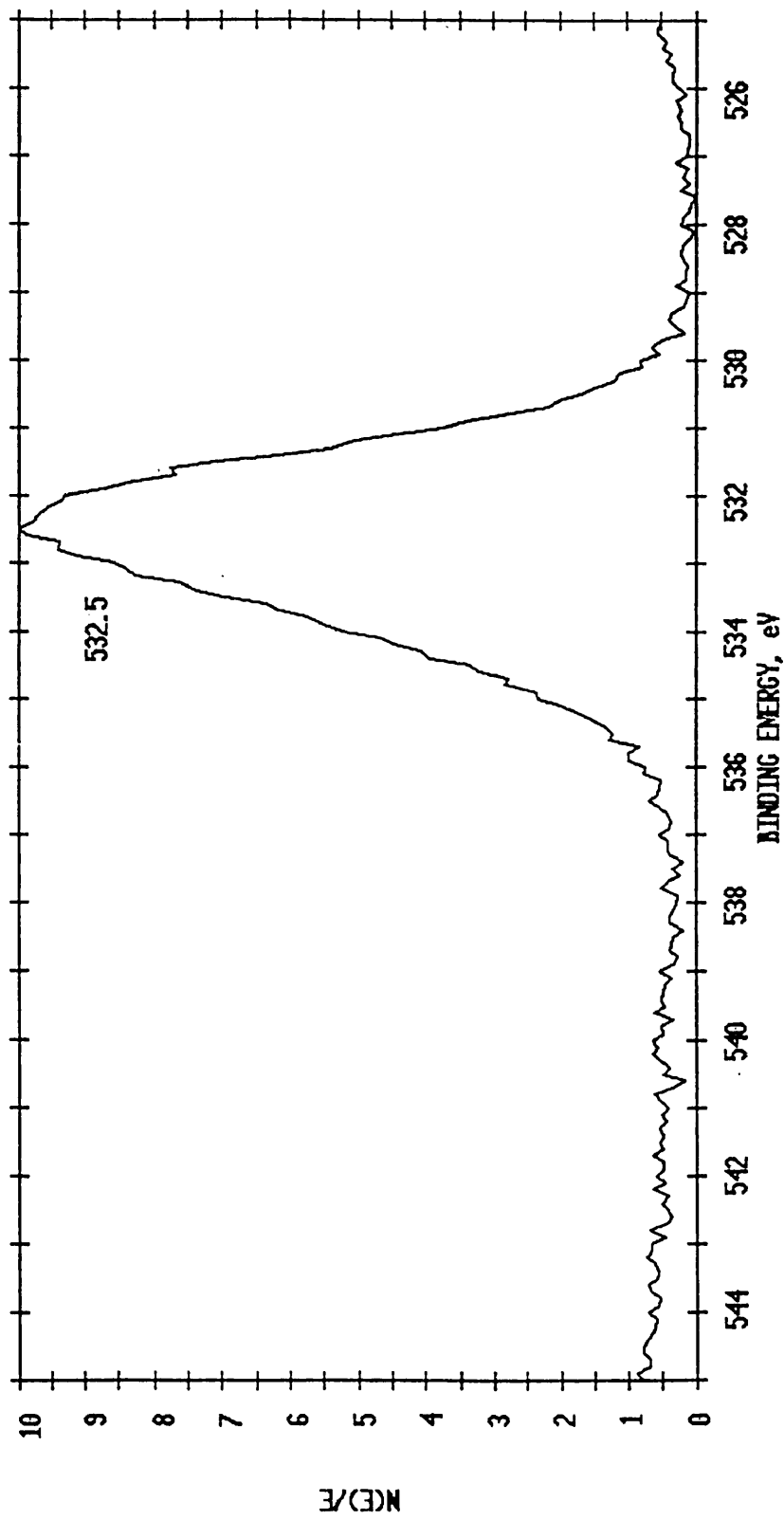


Figure 101: Hexcel 954-3 CE + 5 wt. % Boron Nitrogen Peak AO Exposed 104 hours

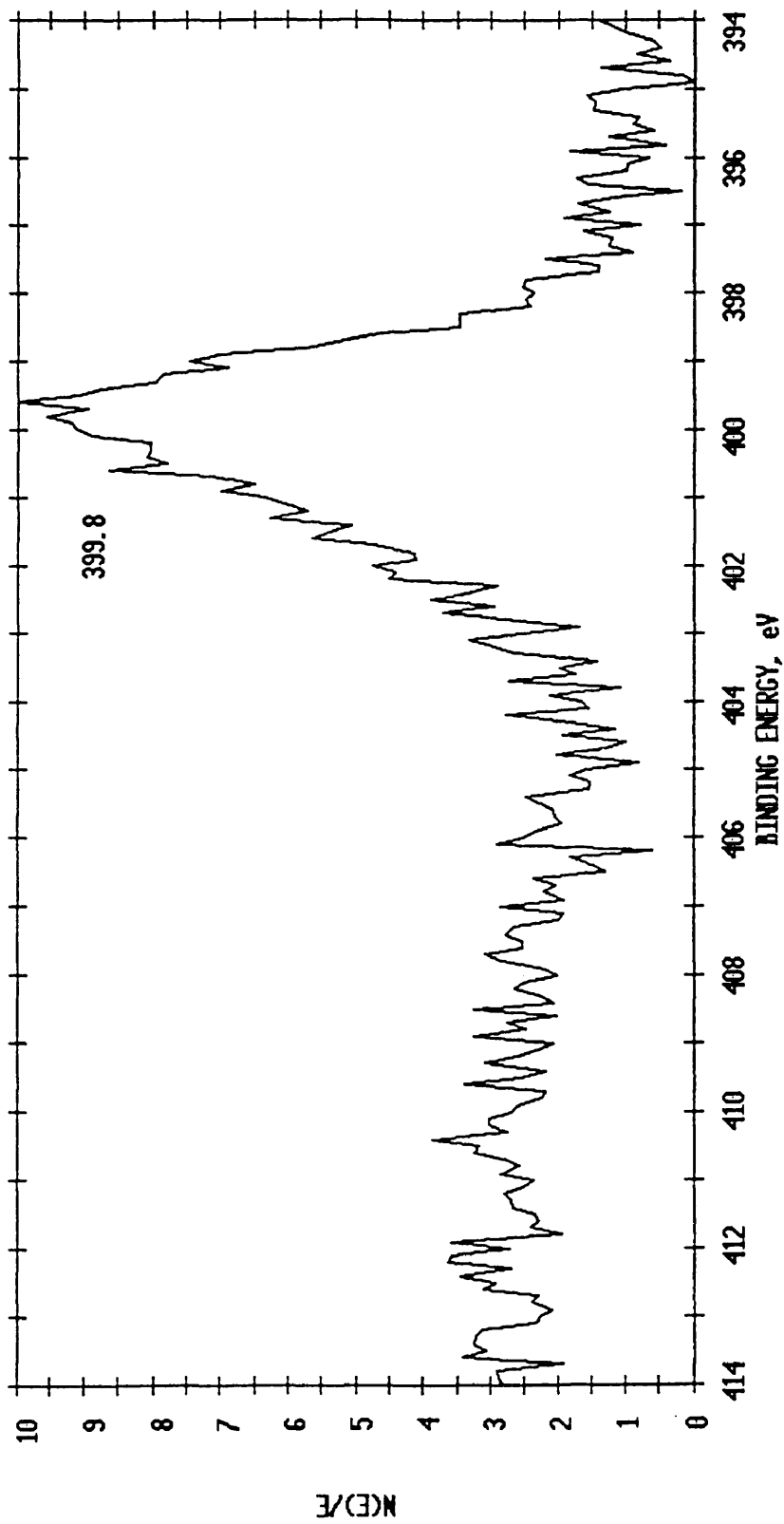
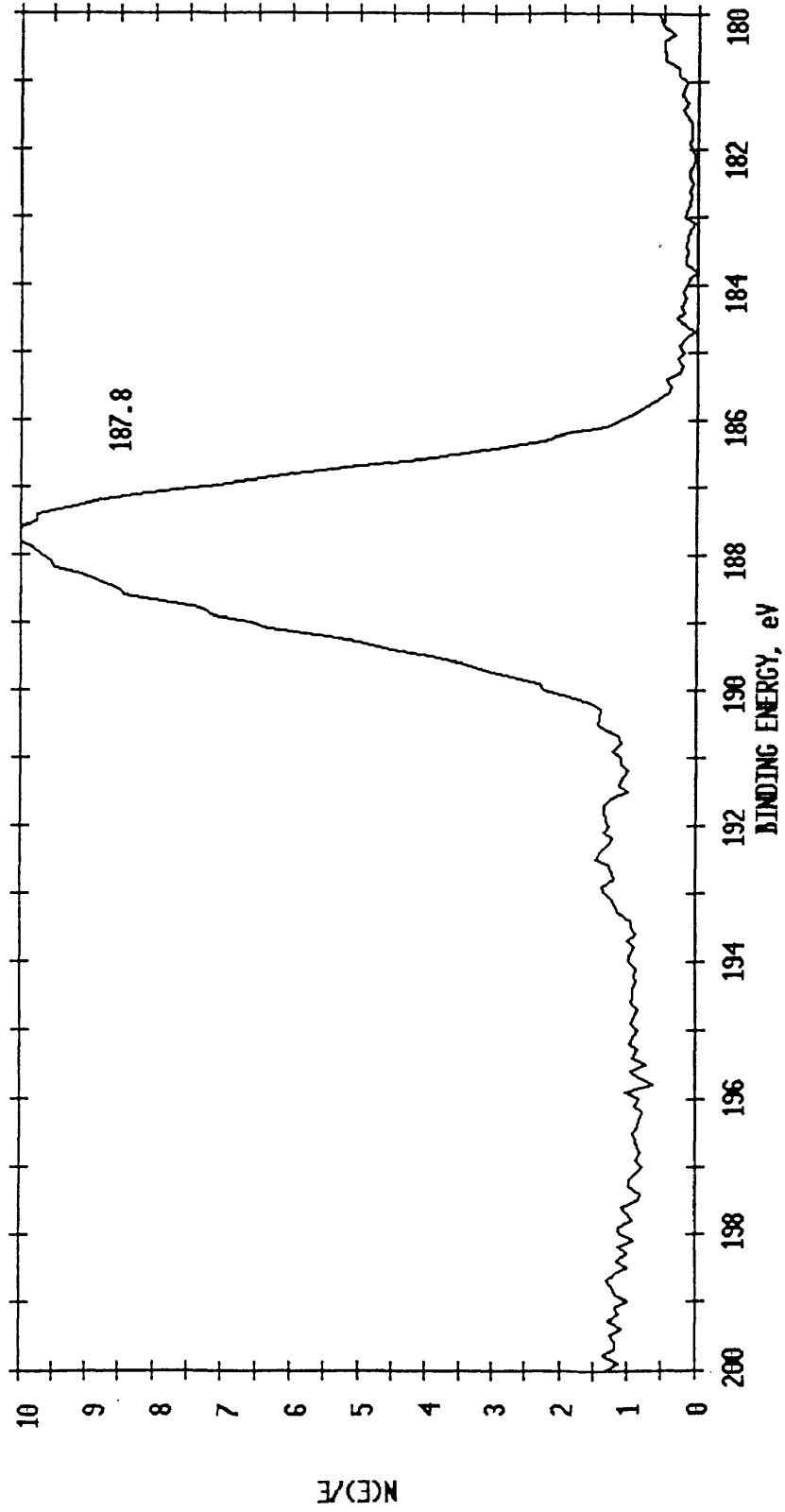


Figure 102: Hexcel 954-3 CE + 5 wt. % Boron Boron Peak AO Exposed 104 hours



## VITA

Sandeep Amar Saggar

Born in Salisbury, Maryland on May 27, 1977 to Deepak and Jyoti Saggar. He has one older brother, Suraj.

Upon graduation in 1995 from James M. Bennett Senior High School in Salisbury, Maryland, he attended the College of William and Mary and earned a Bachelor of Science degree in Chemistry in 1998. Subsequently he furthered his proficiency by pursuing a Master of Arts degree in Chemistry at the College of William and Mary with a focus on the area of Polymer Chemistry.

In December of 1999, the author will start work in the Department of Medicinal Chemistry at Merck Research Laboratories in West Point, Pennsylvania.